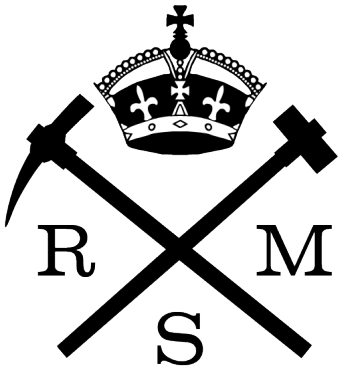
The Role of Conic Curvature and Surface-Wall Roughness in Gas Cyclones and Hydrocyclones



Arjun Kumar Pukkella

Department of Earth Science and Engineering
Royal School of Mines
Imperial College London

Supervisor: Prof Jan J. Cilliers
Co-supervisor: Dr Kathryn Hadler

submitted in partial fulfillment of the requirements for the degree of
Doctor of Philosophy in Engineering and
the Diploma of Imperial College

LONDON
28th February 2025

Abstract

Static centrifugal classifiers, such as gas cyclones and hydrocyclones, are widely used in mineral processing industries for particle separation and classification. However, while gas cyclones are typically employed as separators for the complete removal of particles from gas streams, hydrocyclones function as classifiers but often suffer from high bypass in ball-mill classifier circuits. This thesis investigates the influence of conic curvature and surface wall roughness on the performance of gas cyclones and hydrocyclones, with the aim of enhancing classification efficiency and reducing bypass.

The study employs Computational Fluid Dynamics (CFD) simulations and laboratory-scale experiments, utilizing 3D-printed prototypes with varying surface wall roughness. A novel particle collection method using expandable chambers was developed to measure particle size distributions. Initial CFD simulations in 31 mm gas cyclones reveal that convex conic designs yield coarser cut sizes compared to standard and concave designs, favoring classification operations. Response Surface Methodology (RSM) and Monte Carlo simulations further confirm these findings, identifying convex designs as the most effective for achieving coarser cut sizes.

Experimental validation supports these results, demonstrating that convex gas cyclones achieve lower separation efficiency for fine particles while enhancing classification performance with coarser cut sizes. The study extends these insights to hydrocyclones (75 mm), where convex designs reduce fines bypass, offering significant cost-saving potential in ball-mill classifier circuits by reducing re-grinding costs.

Additionally in gas cyclones, the effects of surface wall roughness are examined, showing that rough surfaces lower tangential velocities and reducing separation efficiency. For hydrocyclones, increased flow rates with rough surfaces enhance solids recovery and concentration ratios, highlighting their potential for dewatering applications.

This thesis presents novel approaches to gas cyclone and hydrocyclone design, supported by rigorous CFD simulations and experimental validation. The findings pave the way for more efficient classification and separation systems in mineral processing and the development of industrial-scale designs.

Copyright

The copyright of this thesis rests with the author. Unless otherwise indicated, its contents are licensed under a Creative Commons Attribution-Non Commercial 4.0 International Licence (CC BY-NC). Under this license, you may copy and redistribute the material in any medium or format. You may also create and distribute modified versions of the work. This is on the condition that: you credit the author and do not use it, or any derivative works, for a commercial purpose. When reusing or sharing this work, ensure you make the license terms clear to others by naming the license and linking to the license text. Where a work has been adapted, you should indicate that the work has been changed and describe those changes. Please seek permission from the copyright holder for uses of this work that are not included in this license or permitted under UK Copyright Law.

Plagiarism declaration

I hereby declare that all of the work presented in this thesis – except that which is appropriately acknowledged and referenced as such – is my own, and that it has not been submitted in fulfilment of the requirements of any other degree at Imperial College London or elsewhere.

Arjun Kumar Pukkella

28th February 2025

Acknowledgements

I am deeply grateful to Professor Jan Cilliers and Dr. Kathryn Hadler for their unwavering support and guidance throughout my PhD journey. Their encouragement and insights have been invaluable. A heartfelt thanks to Professor Cilliers, whose kindness and generosity in providing me with this incredible opportunity will always remain close to my heart.

I would like to thank my friends and colleagues, both past and present, in the Advanced Mineral Processing Research Group at large. In particular, I would like to extend my sincere gratitude to Dr. Joshua Rasera, for his support throughout this journey. His practical advice, support, and willingness to share his own experiences uplifted me during my low phases.

I am also deeply thankful to Dr. Avalos-Patino Jorge for his invaluable assistance with scripting Fluent simulations on HPC, which significantly contributed to accelerate my computational research.

My thanks also go to Dr. Lampret Borut from the Design Engineering Department for his invaluable assistance in facilitating 3D printers for prototyping the devices needed for my experiments. His expertise and suggestions on 3D printing greatly enhanced the success of my research. A big thank you to Gary Jones and the Hackspace team at Imperial College for their support in developing the prototype devices essential for my experiments.

I am very thankful to Dr. Dennis Vega-Garcia and Professor Fernando Betancourt, Head of the Metallurgical Engineering Department from the University of Concepción, Chile, for their generosity in sharing their lab space to conduct my hydrocyclone experiments. I am especially grateful to their lab supervisors, Christine and Elgardo, whose kindness and full support ensured that I could perform my experiments with ease — a gesture I will never forget.

I gratefully acknowledge the support and encouragement of Mr. Ananth Krishnan, Ex-

CTO of Tata Consultancy Services, who approved a sabbatical to allow me to pursue my doctoral studies. I extend my heartfelt thanks to Dr. Venkataramana Runkana (Chief Scientist, TCS Research) and Dr. Sivakumar Subramanian (Principal Scientist, TCS Research) for their continued mentorship and support throughout this journey.

On a personal note, I owe everything to my wife, Himabindu. Her unwavering support, sacrifices, and resilience made this journey possible. She endured challenges with grace and stood by me in every possible way. To my son, Mohansh — your smiles, kisses, and hugs lightened my burdens and gave me the strength to carry on.

To my Amma, Pushpalatha, whose vision and determination to see me succeed despite all odds have shaped the person I am today, and to my Daddy, Chalapathi Rao, whose life is a constant source of inspiration — I am eternally grateful. To my sister, Deepthi, and my nephew, Chinnu, thank you for your boundless love and encouragement. To my in-laws, thank you for your prayers and unwavering support, which have given me strength throughout this journey.

Lastly, I want to express my gratitude to the universe for manifesting my childhood dream of pursuing a PhD at one of the world's top institutions. This journey has been a fulfillment of that dream, and I am profoundly thankful for all the support and serendipity that made it possible.

For my family

Research is to see what everybody else has seen, and think what nobody has thought.

Nobel-Prize-winning physiologist Albert Szent-Györgyi

Contents

Acknowledgements

List of Figures **iv**

List of Tables **viii**

1 Introduction **1**
1.1 Research Context 2
1.2 Motivation and Objectives 3
1.3 Thesis Structure 4
1.4 Scientific Dissemination 5
1.4.1 Journal Publications 5
1.4.2 Conference presentations 6

2 Literature Review **7**
2.1 Dry classifiers: Classification based on particle separation 12
2.2 Centrifugal Air Classifiers 15
2.2.1 Static Centrifugal Classifiers: Cyclone Separators 17
2.2.2 Dynamic Centrifugal Classifiers: Rotary classifiers 21
2.3 Gas Cyclones 30
2.4 Hydrocyclones 32
2.5 Effect of roughness in gas cyclone and hydrocyclones 34
2.5.1 Roughness studies in gas cyclones 34
2.5.2 Roughness studies in hydrocyclones 35
2.6 Research Gaps 36
2.7 Summary and Thesis Objectives 37

3 Design of Parabolic Conic Gas Cyclones for Coarse Particle Classification: A CFD Study with Response Surface Methodology **39**
3.1 Background 41
3.2 CFD Modelling Methodology 42
3.2.1 Modelling of airflow and selection of turbulence model 42
3.2.2 Modelling of particle motion 43
3.2.3 Geometry and Boundary conditions 45
3.2.4 Grid Independency and Model Validation 47
3.3 Response Surface Methodology: Theory 49
3.3.1 Design of Experiments: 49
3.3.2 Variables and Responses 50
3.3.3 Response Surface Methodology Model 54
3.4 Results and Discussion 54
3.4.1 CFD Analysis: Standard design model validation 54
3.4.2 CFD analysis of parabolic designs 57
3.4.2.1 Axial Velocity 58
3.4.2.2 Tangential Velocity 59
3.4.2.3 Static Pressure 59

3.4.2.4 Particle Separation Characteristics . . . 61
3.4.3 Response Surface Methodology: Results . . . 65
3.4.3.1 Analysis of Variance . . . 65
3.4.3.2 Analysis of Responses . . . 69
3.4.3.3 Monte Carlo Simulations . . . 69
3.5 Summary . . . 72

4 Impact of Conic Curvature and Wall Roughness on Gas Cyclones: A Computational and Experimental Study 74
4.1 Background . . . 75
4.2 Experimental Methodology . . . 76
4.2.1 Novel method to capture the overflow particles . . . 77
4.3 CFD Modelling Methodology . . . 78
4.3.1 Turbulence Modelling . . . 78
4.3.2 Geometry and Boundary conditions . . . 80
4.4 Results and Discussion . . . 81
4.4.1 Experimental Analysis: Effect of Conic Curvature . . . 81
4.4.2 CFD Analysis: Understanding the influence of roughness . . . 83
4.4.2.1 Axial Velocity . . . 84
4.4.2.2 Tangential Velocity . . . 85
4.4.2.3 Static Pressure . . . 86
4.4.3 Cyclone Performance Analysis . . . 87
4.5 Summary . . . 89

5 Influence of Conic Shape on Bypass and cut size in Hydrocyclones 91
5.1 Background . . . 92
5.2 CFD Modelling Methodology and Experimental Methods . . . 94
5.2.1 Capturing the Turbulence . . . 94
5.2.2 Air-Core Formation: Volume of Fluid (VOF) Theory . . . 95
5.2.3 Discrete Phase Particle Motion . . . 96
5.2.4 Simulation Details . . . 97
5.2.4.1 Geometry and Boundary conditions . . . 97
5.2.4.2 Meshing and Grid Independency . . . 99
5.2.5 Model Validation . . . 101
5.2.6 Experimental setup and Methods . . . 103
5.3 Results and Discussion . . . 105
5.3.1 CFD Analysis: Understanding the flow-field . . . 105
5.3.1.1 Axial Velocity . . . 106
5.3.1.2 Tangential Velocity . . . 107
5.3.1.3 Radial Velocity . . . 107
5.3.1.4 Static Pressure . . . 109
5.3.1.5 Air-Core formation . . . 109
5.3.2 CFD Analysis: Particle separation characteristics . . . 109
5.3.3 Experimental Analysis: Water-only . . . 112
5.3.4 Experimental Analysis: Particle Separation . . . 113
5.3.4.1 Industrial case study . . . 117
5.4 Summary . . . 118

6 The Influence of Surface-Wall Roughness on Hydrocyclone Performance 120
6.1 Background . . . 121
6.2 CFD Modelling Methodology and Experimental Methods . . . 122
6.2.1 CFD Modelling theory . . . 122
6.2.1.1 Capturing the Turbulence . . . 122
6.2.1.2 Modelling air-core formation: Volume of Fluid (VOF) Theory 123

6.2.1.3 Modelling of discrete phase particle motion . . . 124
6.2.2 Simulation Set-up . . . 125
6.2.2.1 Geometry and Boundary conditions . . . 125
6.2.3 Meshing and grid independecy . . . 127
6.2.4 Experimental setup and Methods . . . 130
6.3 CFD Results and Analysis . . . 132
6.3.1 Effect of surface-wall roughness . . . 132
6.3.2 Flow-field Analysis . . . 133
6.3.2.1 Axial Velocity . . . 134
6.3.2.2 Tangential Velocity . . . 135
6.3.2.3 Radial Velocity . . . 136
6.3.2.4 Pressure . . . 137
6.3.3 CFD particle separation characteristics . . . 138
6.4 Experimental results . . . 139
6.4.1 Water-only flow splits . . . 139
6.4.2 Experimental particle separation analysis . . . 141
6.5 Conclusions . . . 147

7 Conclusions and Future Work **148**
7.1 Thesis Summary . . . 149
7.2 Conclusions . . . 151
7.3 Study Limitations & Future Work . . . 152

Bibliography **154**

Appendices **171**

Appendix A Literature Review **173**
A.1 Gravitational and Inertial Air Classifiers . . . 173
A.1.1 Gravitational Classifiers . . . 173
A.1.2 Inertial Air Classifiers . . . 176
A.2 Fluidizers . . . 180

Appendix B Supplemental Data for Chapter 4: "Impact of Conic Curvature and Wall Roughness on Gas Cyclones: A Computational and Experimental Study" **184**
B.1 . . . 184

Appendix C Supplemental Data for Chapter 5: "Influence of Conic Shape on Bypass and Cut-Size in Hydrocyclones" **188**
C.1 Empirical Models from Industrial Data: . . . 188
C.1.1 Plitt Model: For prediction of Bypass through underflow recovery. . . . 189
C.1.2 Nageswara Rao Model: For Cut size determination . . . 190
C.1.3 Feed Flowrate model: Non-linear regression model . . . 190
C.2 Experimental Conditions . . . 192
C.3 Hydrocyclones Predictive models for Monte Carlo simulations . . . 192

Appendix D Publications **195**

List of Figures

2.1 Flow sheet of a classifier with its performance evaluation curve 10
2.2 Broad classification of dry classifiers based on their particle separation mechanism 15
2.3 Schematic diagrams of centrifugal static and dynamic classifiers. 16
2.4 Separation efficiency curve depicting the trend of d_{50} vs apex cone clearance area as a function of blow-up ratio - Bu = Blow up, S = Cone clearance (Image Source: Yoshida [1]) 19
2.5 Design of coarser particle cyclone classifier with improved collection boxes (Image Source: Oshitari *et al.* [2]) 19
2.6 Schematic of spiral air classifier developed by Rumpf and Leschonski [3] (Image Source: Leschonsi and Legenhausen [4]) 21
2.7 Deflecting wheel classifier (Image Source: Leschonski [5, 6]) 21
2.8 Schematic depicting the cut-point diameter as a function of radial distance for free and forced vortex sink flows 23
2.9 Design of Impeller Wheel Classifier - MicroCut MC (Image Source: Galk *et al.* [7]) 24
2.10 Design of Ultrafine classifier (Image Source: Morimoto and Shakouchi [8]) . 24
2.11 A typical tromp curve in an Ultrafine Classifier depicting sub-micron size particle classification (Image Source: Morimoto and Shakouchi [8]) 25
2.12 Effect of rotor speed and air flow rate on the tromp curve for an O-SEPA High-Efficiency Separator (Image Source: William and Craig[75]) 26
2.13 Typical turbo-air classifiers a) Vertical b) Horizontal arrangement of rotor cage (Image Source: Sun *et al.* [9]) 27
2.14 BLMT Classifier with a BLMT filter installed below the vortex finder (Image Source: Worthen [10]) 28
2.15 Dry classifiers based on their centrifugal force mechanism 29
2.16 Compounded chart depicting all the dry classifiers discussed above 36
2.17 A research contour plot highlighting the gaps in centrifugal air classifiers . . 37

3.1 Geometrical design of cyclones under study 46
3.2 Hexahedral mesh for the standard design gas cyclone. a) Top view b) Isometric View 48
3.3 Variation of measured quantities on a centre-line (Height Z = 46 cm - measured from the bottom). a) Tangential Velocity b) Axial Velocity 48
3.4 Comparison of the experimental LDA measurements of tangential and axial velocities Hoekstra (2000), with the CFD predictions of Reynolds stress model (RSM) model and SST $k\omega(cc)$ model. (The radial distance is scaled by the cyclone radius and the axial and tangential velocity are scaled by the inlet velocity.) 49
3.5 CFD analysis of standard design: Radial profiles of scaled axial, tangential velocities, and static pressure measured at three locations (L1, L2, and L3) as a function of inlet flowrate. 55

3.6 CFD validation of experimental particle classification studies for flowrates of 30, 40, 50, and 60 lpm, respectively in the standard design [Experimental data source: Xiang *et al.* [11]]. 56
3.7 Axial velocity profiles as a function of conic design for a flowrate of 60 lpm: a) Contour Plots b) Radial profiles predicted at three axial locations L1, L2, and L3 58
3.8 Tangential velocity profiles inside the cyclones as a function of conic design for a flowrate of 60 lpm: a) Contour Plots b) Radial profiles predicted at three axial locations L1, L2, and L3 60
3.9 Pressure distribution profiles inside the cyclones as a function of conic design for a flowrate of 60 lpm: a) Contour Plots b) Radial profiles predicted at three axial locations L1, L2, and L3 60
3.10 Effect of conic curvature shape on the particle separation characteristics as a function of inlet air flowrate. a) 30 lpm, b) 40 lpm, c) 50 lpm, and d) 60 lpm. [Experimental data source: Xiang *et al.* [11]] 61
3.11 Single particle tracking of particles representing their respective cut size diameters for the flowrate of 30 lpm, in 1) Standard (a - 2.36 μm), 2) Convex (b - 3.38 μm), and 3) Concave (c - 4.91 μm) design cyclones 63
3.12 Contours of turbulent kinetic energy (k-$\frac{m^2}{s^2}$) for the flow rate of 60 lpm: a) Standard design b) Concave design c) Convex design 64
3.13 Contour plots from response surface methodology a) Cut size - Du vs Do, b) Sharpness - Du vs Do, c) Cut size - S vs Do b) Sharpness - S vs Do 70
3.14 The design space of cut size and sharpness of classification generated by Monte Carlo simulations as a function of cyclone design 71
3.15 Trends of response variables in terms of certainty bands (From Monte Carlo simulations). 72

4.1 (a) 3D printed complete assembly of gas cyclone, (b) Smooth conics and (c) Rough conics 76
4.2 (a) Laboratory experimental rig, and (b) Schematic of experimental setup . 77
4.3 Geometrical design of cyclone under study. a) Side-view: Cyclone with dimensions b) Top view, c) Profiles to conic curvature (Standard and Convex) 80
4.4 Solids recovery as a function of flowrate and conic design. 82
4.5 Comparison of Separation Efficiency curves for Standard (S) and Convex (C) Gas cyclone Designs across different Flowrates. 83
4.6 Effect of roughness and conic design on axial velocity profiles at the center XZ plane (Y=0) for a flowrate 30 lpm a) Contour plots b) radial profiles at three axial locations (L1, L2, and L3) 84
4.7 Effect of roughness and conic design on scaled tangential velocity profiles at the center XZ plane (Y=0) for a flowrate 30 lpm a) Contour plots b) radial profiles at three axial locations (L1, L2, and L3) 85
4.8 Effect of roughness and conic design on Pressure distribution profiles at the center XZ plane (Y=0) for a flowrate 30 lpm 86
4.9 Comparion of experimental pressure differential between the taps with the computational measured values as a function of flowrate and turbulence modelling technique. (a) Standard Design (b) Convex Design 88
4.10 Comparison of separation efficiency curves for rough gas cyclone designs across varying flow rates, with results for smooth designs overlaid for reference. 88

5.1 Ballmill classifier circuit with recycle, the classifier can be either Derrick screens or Hydrocyclone 93
5.2 Geometrical design of hydrocyclones under study. a) The standard design b) The novel convex bottom design 98

5.3 Unstructured hexahedral mesh for both standard and convex hydrocyclone designs. 100
5.4 Variation of measured quantities on a center-line for an inlet flowrate of 200 kg/s (Height Z = 140 cm, measured from the bottom). a) Pressure drop b) Tangential Velocity scaled with the inlet velocity. 101
5.5 Comparison of the experimental LDA measurements of tangential and axial velocities reported by Hsieh [12] and Ghodrat *et al.* [13], with the CFD predictions of RSM - VOF model. 102
5.6 Validation of separation efficiency curve for the classification of limestone at feed solids concentration 4.88% (by volume) reported by Hsieh [12], with the CFD predictions by Vysyaraju *et al.* [14] model (LES - VOF) and the current simulation (RSM - VOF). 102
5.7 (a) 3D printed hydrocyclones, (b) Casing, and (c) Schematic of flow domain. 104
5.8 (a) Laboratory experimental rig, (b) Schematic of experimental setup, and (c) Feed particle size distribution. 104
5.9 Effect of conic design on axial velocity profiles inside hydrocyclones at 1500 mL/s flowrate: a) Contour plots b) radial profiles at three axial locations (L1, L2, and L3) 106
5.10 Effect of hydrocyclone design on the flow quantities for a flowrate of 1500 mL/s: a) Tangential velocity, b) Radial velocity, c) Pressure distribution, and d) Water volume fraction. 108
5.11 Comparison of CFD predictions for particle separation characteristics in standard and convex hydrocyclone designs as a function of inlet flowrate. . 110
5.12 Effect of conic design on turbulent intensity profiles inside hydrocyclones at 1500 mL/s flowrate 111
5.13 (a) Underflow spray profiles as a function of design and flowrate (b) Effect of flowrate on underflow water recoveries as a function hydrocyclone design 112
5.14 Underflow solids recovery as a function of flowrate and design. 114
5.15 Comparison of Separation Efficiency curves for Standard (S) and Convex (C) Hydrocyclone Designs across different Flowrates. 115
5.16 Understanding the effect of flowrate as a function of hydrocyclone design on bypass and cut size (D_{50}). 115
5.17 Industrial scale hydrocyclone data: Influence of hydrocyclone design and inlet flowrate on bypass and cut size relationship 118

6.1 (a) Geometrical design of hydrocyclones with dimensions. (b) Unstructured hexahedral mesh 126
6.2 Grid independence study: (a) Variation of scaled tangential velocity on a center-line for an inlet flowrate of 1500 mL/s (Height (Z) = 217 mm, measured from the bottom). (b) The measured quantities i.e., pressure drop, and turbulent dissipation rate as a function of the number of cells. . . 128
6.3 (a) Microscopic images of 3-D printed hydrocyclones with three levels of roughness, (b) Hydrocyclone and casing, (c) Schematic of flow domain . . 130
6.4 (a) Silica feed PSD (b) Schematic of the experimental setup to test the hydrocyclone 131
6.5 Effect of surface wall roughness on the underflow water recovery for a flowrate of 1000 mL/s and roughness constant of 0.5 133
6.6 Effect of surface-wall roughness on axial velocity profiles inside hydrocyclones at 1500 mL/s flowrate: a) Contour plots at center XZ plane (Y=0) b) radial profiles at three axial locations (L1, L2, and L3) 134
6.7 Effect of surface-wall roughness on flow quantities at the center XZ plane (Y=0) for a flow rate of 1500 mL/s: (a) Tangential velocity, (b) Radial velocity, (c) Pressure distribution, and (d) Water volume fraction. 136

6.8 Comparison of CFD predicted separation efficiency curves for smooth and rough designs as a function of flowrate. (a) 1000 mL/s, (b) 1250 mL/s, (c) 1500 mL/s 138
6.9 Underflow discharge spray profiles for flowrate of 1500 mL/s as function of surface-wall roughness: (a) Smooth, (b) Medium, (c) Rough. 140
6.10 Effect of surface roughness on experimental water recoveries as a function of flow rate, with CFD predictions overlaid for trend comparison. 141
6.11 Effect of flowrate and wall roughness on the solids recovery and concentration ratio 143
6.12 Comparison of Separation Efficiency curves for Standard smooth, rough, and Convex rough designs as a function of flowrate. (a) 1000 mL/s, (b) 1250 mL/s, (c) 1500 mL/s 144
6.13 Effect of flowrate on surface roughness and the interplay between roughness and conic design in relation to bypass and water recovery. 144

7.1 Summary of key findings from the thesis 151

A.1 Horizontal Cross-flow classifier: Particle tracks as a function of particle size (Image Source: Wang *et al.* [15]) 174
A.2 Inertial Air-Classifiers. Image Source: Johansson and Evertsson [16, 17] . . 177
A.3 A schematic of Throat Classifier (Image Source: Petit and Irassar [18]) . . . 178
A.4 Elbow jet classifier: Particle tracks as a function of particle size (Image Source: Liang *et al.* [19]) 179
A.5 Saidi *et al.* depicted the segregation of particles based on the size (Blue - 920 μm, white - 330 μm) from the mixed feed Saidi *et al.* [219] 181
A.6 Continuous Fluidized bed particle classifier Yoshihiro *et al.* [20] 182
A.7 Charts depicting the operational characteristics for Gravitational and Inertial air classifiers 183

B.1 Free fall of particles into the flowing stream of air results in accumulation of particles on the cyclone walls. 185
B.2 A particle dispersion chamber is incorporated before the cyclone inlet to generate an aerosol for dispersing solids in air. However, particles tend to adhere to the chamber walls and accumulate in the dead zones. 185
B.3 A compact aerosolization chamber eliminates the problem of particle agglomeration along the walls. However, the pressure inside the system could not be maintained due to hair-line leaks. 186
B.4 Figure depicting the novel method to capture the particles exiting through the dust outlet using expandable chamber. 187

C.1 Parameters used to predict hydrocyclone performance and the models/methodology used for their prediction. 189
C.2 Bypass model: Bypass is predicted indirectly using water recovery (Rf) using Plitt model 190
C.3 Cut size as a function of hydrocyclone design is modelled using Nageswara Rao model 191
C.4 Feed solids flowrate is modeled using our own Non-linear regression model as a function of hydrocyclone design is modelled using Nageswara Rao model 191

List of Tables

2.1 Grouping of dry classifiers based on size and density of particle 14
2.2 Performance characteristics of Centrifugal-air classifiers Source: Fives FCB and Yardi[65] 17
2.3 Few studies reported the design changes on gas cyclones 20

3.1 Geometric design parameters of the standard 31 mm diameter cyclone. . . . 45
3.2 Grid independence analysis for an inlet flow rate of 60 lpm: Pressure drop as a function of grid refinement, compared to the experimentally reported value of 595 Pa. 48
3.3 The high and low-level settings of the factors along with categoric and response variables defined in the DOE study 51
3.4 List of simulations performed for the input design space and their corresponding output response variables. 51
3.5 Performance comparison of standard, concave, and convex design gas cyclones for key parameters 62
3.6 Fit statistics comparing the quadratic and modified models for cut size and sharpness 66
3.7 p-values of reduced quadratic model (Modified model) 67
3.8 Model equations for cut size and sharpness as a function of design. 68
3.9 Summary statistics for Monte-Carlo simulations for the response variable . . 71

4.1 Comparative analysis of performance metrics as a function of flowrate for smooth cyclones 81
4.2 Comparative analysis of performance metrics as a function of rough cyclone designs 88

5.1 Details of grid convergence study calculations using GCI method 100
5.2 Quantitative comparison of flow parameters between the experiments and predicted results 103
5.3 CFD model comparative analysis of performance metrics as a function of hydrocyclone design 106
5.4 Experimental observations of underflow recoveries for different flow conditions as a function of hydrocyclone design. Water-only data is explicitly labeled; all other data corresponds to 5% solids experiments. 113
5.5 Key metrics of particle separation characteristics from experiments 114

6.1 Details of grid convergence study calculations using GCI method 128
6.2 Comparative analysis of CFD model performance metrics as a function of hydrocyclone surface-wall roughness and flowrate. 134
6.3 Key performance metrics from slurry experimental results comparing rough and smooth-surface hydrocyclones across various flowrates 142

C.1 Statistics of non-linear regression model for feed solids flowrate 192
C.2 Design and operating conditions for the plant trails 193
C.3 Monte Carlo model input variables and output predictions 194

Chapter 1

Introduction

1.1 Research Context 2
1.2 Motivation and Objectives 3
1.3 Thesis Structure 4
1.4 Scientific Dissemination 5
1.4.1 Journal Publications 5
1.4.2 Conference presentations 6

1.1 Research Context

This thesis explores the influence of curved conic design modifications and surface wall roughness on the classification efficiency of gas cyclones and hydrocyclones. Through a combination of computational fluid dynamics (CFD) simulations and experimental studies, it addresses key gaps in understanding particle classification processes.

Gas cyclones and hydrocyclones are ubiquitous in mineral processing industries for applications requiring particle removal or classification. Both devices depend on induced centrifugal forces to segregate particles from the fluid medium based on size or density. Traditionally, gas cyclones are designed for complete removal of solids from gas streams; research exploring their potential for particle classification has been limited [1, 2, 21, 22]. The successful development of gas cyclones for classification applications could significantly reduce reliance on water. Coupled with growing water scarcity due to climate change and stricter regulations on water use and discharge, there is increasing pressure to rethink water-intensive mineral processing practices [23]. Gas cyclones have smaller cut sizes, as they are typically designed for fine separation. Hence, they cannot be directly deployed in these circuits. To achieve the objective of classification, novel designs should aim to achieve coarser cut sizes.

Hydrocyclones are extensively used in wet processing applications, such as mineral ore beneficiation and ball mill classifier circuits. However, they typically suffer from higher fine bypass in their underflow streams. Research in shifting classification operations from water-based hydrocyclones to air-based gas cyclones may take years to demonstrate practical use, while efforts to improve hydrocyclone designs may see an immediate benefit and industrial implementation.

An additional challenge common to both gas cyclones and hydrocyclones is the effect of surface wall roughness on their performance. Wall roughness, which is acquired by operational wear over time, can alter the flow patterns and particle dynamics within these devices. Understanding the impact of roughness on the performance is critical for improving and sustaining the efficiency of these systems.

Computational modeling and experimental methods provide opportunities for enhancing the performance of cyclonic devices. While numerous studies report improvements in gas cyclone and hydrocyclone designs using Computational Fluid Dynamics (CFD), the lack of experimental validation often limits their adoption in industry. This thesis bridges this gap by combining CFD simulations with laboratory-scale experiments to investigate and validate novel design modifications, including the role of surface wall roughness. The findings advance the understanding of particle classification mechanisms and offer practical solutions for industrial applications.

1.2 Motivation and Objectives

Numerous studies have investigated the influence of design variables such as inlet dimensions, cyclone diameter, vortex finder dimensions, dust outlet diameter, and operational parameters on the performance of gas cyclones [1, 24–30]. However, these studies consistently report cut sizes below 3 μm; therefore, the cyclone functions as a separator rather than a classifier. Although some attempts have been made to adapt cyclones for classification, they primarily rely on external modifications such as introducing blow-up airflow or constricting the apex outlet [2, 22]. No prior research has explored inherent design modifications tailored to transform gas cyclones into effective classifiers.

In contrast, several Computational Fluid Dynamics (CFD) studies on hydrocyclones suggest that curved conic designs can significantly influence cut sizes [31–34]. Yet, similar investigations on gas cyclones remain limited, with the notable exception of Pandey and Brar [35], which focused on larger gas cyclones (210 mm diameter) with less pronounced conic curvatures, which reported conic curvature has an insignificant effect on the cut size. Interestingly, Ghodrat *et al.* [31] specifically noted that a higher degree of conic curvature in hydrocyclones correlates with coarser cut sizes. This observation motivates the exploration of pronounced conic curvature effects in smaller-diameter gas cyclones. A 31 mm diameter was selected as a basis, leveraging the availability of particle separation data in the literature [11] to facilitate comparisons and validations.

Hydrocyclones, on the other hand, often face challenges such as high fines bypass in the underflow, which leads to lower recovery of valuable minerals in the overflow stream and increased grinding loads in ball mill-classifier circuits. This has led to a shift toward incorporating screens in these circuits, as screens enhance mill capacity and reduce the over-grinding of fines due to their lower bypass [36, 37]. However, the integration of screens necessitates significant plant modifications and incurs high maintenance costs, including frequent screen replacements. A more cost-effective solution is optimizing hydrocyclone designs to reduce bypass. Thus insights gained from the study of gas cyclones regarding the effects of pronounced conic curvatures are transferred to hydrocyclones and systematically explored through CFD simulations and in-house experiments.

Another critical aspect influencing cyclone and hydrocyclone performance is surface wall roughness. For both, wall roughness alter the internal flow patterns and affect particle separation behavior. Understanding the influence of surface wall roughness, both in isolation and combined with novel conic designs, can provide insights to optimize the performance of these devices for classification and separation applications.

To address these knowledge and research gaps, the specific objectives of this thesis are as follows:

- Design and Evaluation of Gas Cyclones for Coarse Particle Classification. Utilize CFD simulations coupled with Response Surface Methodology (RSM) to design and evaluate parabolic conic gas cyclones targeting coarser cut sizes.
- Experimentally validate the performance of these novel designs to bridge the gap between computational predictions and practical outcomes. Investigate the effects of surface wall roughness on gas cyclone performance through controlled experiments using 3D-printed prototypes.
- Application of Gas Cyclone Insights to Hydrocyclones. Transfer design insights from convex gas cyclones to hydrocyclones and evaluate their impact on classification behavior through CFD and experimental studies. Quantify the changes in cut size and bypass for convex hydrocyclone designs compared to standard designs.
- Examine the influence of surface wall roughness on hydrocyclone performance, focusing on underflow solids recovery and concentration.

1.3 Thesis Structure

This thesis comprises seven chapters, including this Introduction and five main chapters, and the Conclusions chapter. Five main chapters are adapted from five journal articles, of which two are under review.

Chapter 2 provides a comprehensive review of classification equipment used for particle separation based on size, with a focus on centrifugal air classification technologies. It highlights gas cyclones, traditionally employed as separators rather than classifiers, and discusses hydrocyclones, emphasizing challenges such as fines bypass and existing design modifications aimed at mitigating these issues. This chapter is based partly on published peer-reviewed journal articles [21, 38, 39] and an additional journal article currently under review [40].

Chapter 3 examines the impact of conic curvature in 31 mm diameter gas cyclones using Computational Fluid Dynamics (CFD) simulations. The study validates previously published results at various flow rates [11] and employs Response Surface Methodology (RSM) with a D-optimal design to investigate interaction effects between design variables. The resulting RSM models are further subjected to Monte Carlo simulations to identify trends and assess the potential for achieving coarser particle classification as a function of conic curvature design. This chapter is a full reproduction of published peer-reviewed journal article [38].

Chapter 4 presents the experimental validation of CFD findings, focusing on the impact of surface wall roughness on gas cyclone performance. An innovative particle size measurement technique for the dust outlet using expandable collection chambers is introduced,

addressing challenges in previous measurement attempts, which are detailed in Appendix B. Supporting CFD analyses comparing smooth and rough designs are provided to explain trends observed in the experiments. The results indicate that convex gas cyclones yield coarser cut sizes with a lower separation efficiency for fine particles (i.e., reduced fines bypass) compared to standard designs. These findings motivate the application of similar design principles to hydrocyclones, discussed in subsequent chapters, 5 and 6. This chapter is a complete reproduction of a peer-reviewed journal article currently under review [41].

Chapter 5 explores the application of convex conic design principles, derived from gas cyclone studies, to hydrocyclones. CFD simulations comparing convex and standard hydrocyclone designs are analyzed using flow profiles and discrete phase modeling (DPM) simulations to evaluate performance differences. Experimental results, including water-only and 5% solids slurry tests, are presented to validate the CFD findings, demonstrating that the convex hydrocyclone design reduces fines bypass while achieving coarser cut sizes. This chapter is a complete reproduction of a peer-reviewed journal article [40].

Chapter 6 examines the impact of surface wall roughness on hydrocyclone performance through CFD simulations. The findings from these simulations are validated using experimental methods similar to those outlined in Chapter 5, ensuring consistency in the approach. However, additional rough hydrocyclones design are 3D printed to consider the effect of roughness in the experiments. This chapter is based partly on published peer-reviewed journal article [39].

Chapter 7, Conclusions, summarizes the thesis, presents main findings, and concludes by study limitations and future work.

1.4 Scientific Dissemination

1.4.1 Journal Publications

Four peer-reviewed journal articles have been published directly from this doctoral study (A, B, C, and D). Further, one more additional peer-reviewed journal articles were under review in Powder Technology journals (E). These articles are as follows:

(A) A. K. Pukkella, J. J. Cilliers and K. Hadler, 'A comprehensive review and recent advances in dry mineral classification,' *Minerals Engineering*, vol. 201, p. 108 208, 2023

(B) A. K. Pukkella, J. Cilliers and K. Hadler, 'Design of parabolic conic gas cyclones for coarse particle classification: A cfd study with response surface methodology,' *Powder Technology*, vol. 433, p. 119 217, 2024

(C) A. K. Pukkella, D. Vega-Garcia, K. Hadler and J. Cilliers, 'Influence of conic shape

on bypass and cut-size in hydrocyclones,' *Separation and Purification Technology*, vol. 361, p. 131 224, 2025

(D) A. K. Pukkella, D. Vega-Garcia, K. Hadler and J. Cilliers, 'The influence of surface-wall roughness on hydrocyclone performance,' *Separation and Purification Technology*, vol. 360, p. 131 109, 2025

(E) A. K. Pukkella, J. Rasera, K. Hadler and J. Cilliers, 'Impact of conic curvature and wall roughness on gas cyclones: A computational and experimental study,' *Powder Technology - Under Review*,

The mapping of the content of this thesis to these publications is as follows:

1. **Chapter 2** and **Appendix A**: Primarily from paper A, additional content from papers B-E.
2. **Chapter 3**: reproduction of paper B.
3. **Chapter 4**: reproduction of paper C.
4. **Chapter 5**: reproduction of paper D.
5. **Chapter 6**: reproduction of paper E.

1.4.2 Conference presentations

Four oral presentations were given at national and international conferences and congresses during this PhD.

1. **World Congress on Particle Technology**, Spanish Association for Chemist and Chemical Engineers, Madrid, September 2022. *Design of Novel Small Diameter Gas Cyclone for Accurate Particle Classification*.
2. **9th UK-China Powder Technology Forum**, Particle Technology Early Career Forum (PTECF), Greenwich, August 2023. *Effect of Curved Conical Wall Shape on Particle Classification in Gas Cyclones: Insights from CFD Analysis*.
3. **POWDER TECHNOLOGY CONCLAVE & EXHIBITION**, Thapar Institute of Engineering & Technology, India, MArch 2024. *Design of parabolic conic gas cyclones for coarse particle classification: A CFD study with Response Surface Methodology*.
4. **ESE Annual Conference**, Imperial College London, London, September 2024. *Enhancing Closed Ball-Mill Classifier Circuits: A Comprehensive Study on Bypass Mitigation through Hydrocyclone Design Modifications, CFD Analysis, and Experimental Validation*.

Chapter 2

Literature Review

2.1 Dry classifiers: Classification based on particle separation 12
2.2 Centrifugal Air Classifiers 15
2.2.1 Static Centrifugal Classifiers: Cyclone Separators 17
2.2.2 Dynamic Centrifugal Classifiers: Rotary classifiers 21
2.3 Gas Cyclones 30
2.4 Hydrocyclones 32
2.5 Effect of roughness in gas cyclone and hydrocyclones 34
2.5.1 Roughness studies in gas cyclones 34
2.5.2 Roughness studies in hydrocyclones 35
2.6 Research Gaps 36
2.7 Summary and Thesis Objectives 37

Introduction

Water is critical to the performance of most mineral processing circuits. Huge quantities of water are consumed daily in various unit operations like comminution (grinding), flotation, slurry transportation, and all hydrometallurgical operations [42]. It has been estimated that around 1 kiloliter of water is required to process a tonne of ore [43]. There is a significantly increased demand for water for the basic needs of a growing population, agriculture, and other industries. These needs, combined with growing water scarcity due to climate change, and stricter regulatory standards for water abstraction and disposal places the future of water-based mineral processing under scrutiny.

Dry mineral processing offers reduced mining water demand. It is considered to be economically viable due to lower capital and operational costs with a smaller plant footprint [42]. For example, Franks *et al.* [44] have reported that a Dry Sand Fluidized Bed (DSFB) in combination with heap leaching may have economic benefits with reduced energy and water requirements in a copper ore processing flow sheet. Dry mineral processing methods are classified broadly into size reduction (comminution) and separation. Dry separation uses forces generated by gravity, centrifuges, magnetics, electricity, and so forth to separate a collection of particles into groups of different sizes and compositions. Classification is a specific operation that deals solely with particle separation into sized fractions. Size classification is affected by particle physical properties such as size, shape, and density. Particle size classification is broadly grouped into two classes; those that take advantage of carrier fluid to create differences in particle trajectory, which is strongly dependent upon the size and density of the particles because of fluid dynamic interaction forces. In dry separation, this fluid is generally air. The second class of classifier is based on the particle's ability (or probability) to pass through an aperture, such as a screen. This is not generally efficient for fine particles ($<$300 μm), and will not be reviewed in detail.

Size classification can be carried out wet or dry. In mineral processing, wet classification techniques are generally preferred over dry technologies [45]. However, with an increasing focus on reducing water consumption in the minerals industry, dry technologies are receiving more attention. Dry separation technologies present a range of challenges, including low throughput rates, narrow cut size ranges, high operating costs, and the need for dust mitigation. Furthermore, efficient dry classification requires low moisture content to avoid blocking equipment. Although wet classification technologies address many of the above challenges it also presents difficulties. There are significant costs associated with accessing water and water handling, tailings dams and their management and the elimination of harmful chemicals before disposal. Wet processing is often not possible in very arid climates and sub-zero conditions.

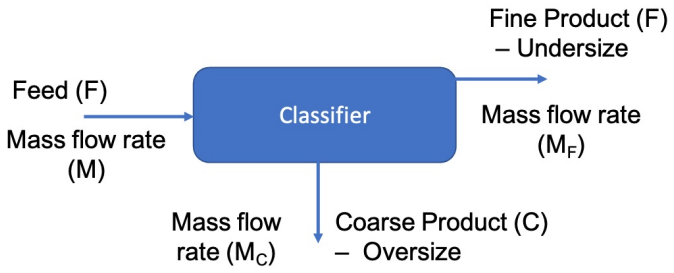
Dry size-based particle classification has important applications in a variety of indus-

tries, such as minerals and cement, agriculture, food processing, pharmaceuticals, and resource recycling. The world consumption of cement is around 4.08 billion tonnes per annum [46]. Comminution is a key operation in cement production; there are specific targets for milling limestone (90% finer than 90 μm) and clinker nodules (100% finer than 90 μm). It is estimated that 110 kWh of electrical energy is consumed to produce a tonne of cement, of which 30% is used in raw material preparation and 40% in clinker grinding [47]. Size classifiers are used in closed-milling circuits to remove fine particles. This avoids their unnecessary over-grinding, increasing throughput capacity and energy efficiency. Dry particle classification is a key operation also in powder preparation. The demand for various mono-dispersed products, i.e. particles within a narrow size range, is high due to their product utility value [48]. For example, in the microelectronic packaging industries, Tin-Silver-Copper (SAC) alloys are widely used in the manufacturing of the solders used in microelectronics. These solder powders have to meet strict particle characteristics such as sphericity, average size, and narrow particle size distribution [49]. The particle size range 25-40 μm is the industrial-grade standard for SAC305 alloy powders [50]. The major application of air classification in the food industry is "protein shifting" in pea or wheat flours [51]. The endosperm cells ($\approx$ 40 μm) in the grains are an ensemble of hard starch granules and a protein matrix. By milling and size classification the protein content in the fine fraction ($<$17 μm) is enriched to 19% from a feed containing 8% leaving the coarser fraction (25-35 μm) containing 7% protein [51].

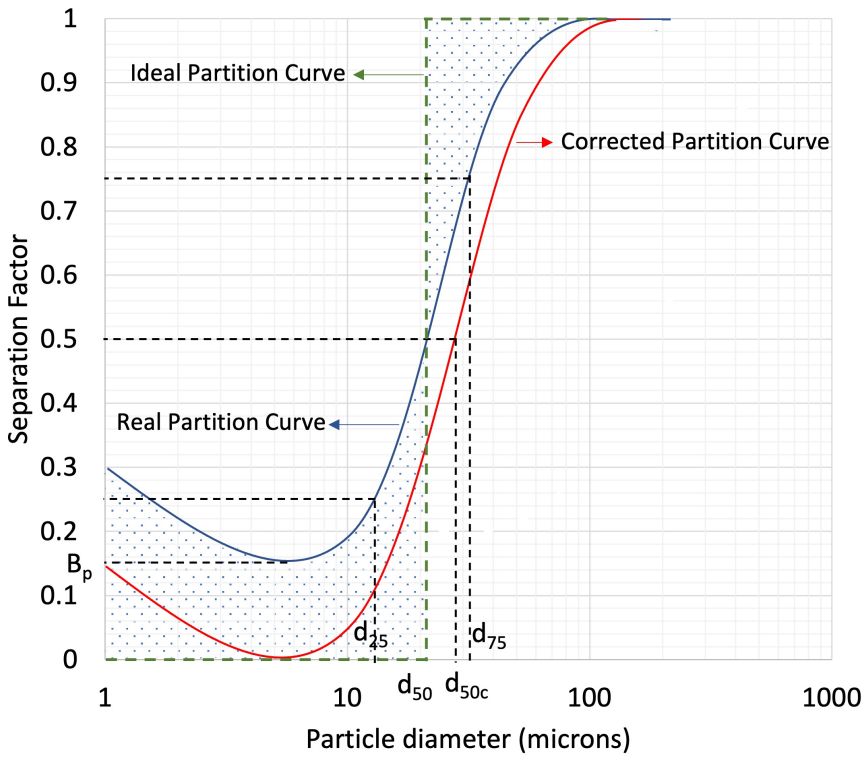
Quantifying separation for classifiers

The following example is for a generic air classifier to illustrate the classification process. As shown in Figure 2.1a, the general mechanism of an air classifier is: The feed material (F) is dispersed in air and is separated into coarser (C) and finer streams (F). The probability of a particle reporting to either the coarse or fine stream depends on the net force balance, which includes the drag and centrifugal forces. For small particles, the drag force exerted by the air stream dominates and carries the particle to the fine fraction. Larger particles are less influenced by the aerodynamic drag force, and the particle is removed through the coarse fraction.

The effectiveness of the particle size classification can be evaluated quantitatively using the partition or Tromp curve. The separation factor (S_i) for i^{th} size fraction is defined as the ratio of the mass of i^{th} size fraction present in coarse fraction to the mass of feed of that size fraction into the classifier. Particle size is plotted on log scaled x-axis and particle recovery values (i.e., separation factor) are on the y-axis. A semi-log graph is chosen to emphasize the fine particle classification behavior. A typical separation efficiency curve is shown in Figure 2.1b. The operational performance of an air classifier can be determined in terms of three major parameters: (1) the cut size (d_{50}), (2) the bypass (B_p), and (3)



(a) A schematic representing the operation of a general classifier



(b) A representative Separation Efficiency Curve

Figure 2.1: Flow sheet of a classifier with its performance evaluation curve

the sharpness of separation.

Particles at the cut size (d_{50}) have an equal probability to report to the coarse stream or the fine stream. In an ideal scenario, particles larger than the cut size i.e., d $> d_{50}$ should entirely report to the coarse stream ($S_i = 1$), and all particles below the cut size i.e., d $< d_{50}$ particles should report to the fine stream ($S_i = 0$) [52]. This trend is indicated by the green dotted line in Figure 2.1b. However, real classifier behavior differs from the ideal classifier as some of the fine particles may get trapped in the aerodynamic wake formed behind the coarse fraction (bypass), or by agglomeration. Less commonly, some coarse particles may enter the fine product (short-circuiting). Typically, industrial separation efficiency curves takes an '***S***' shape curve as shown in Figure 2.1b. The value of particle recovery remains constant at a particular level for lower particle sizes, which is referred to as the bypass (B_p). This value corresponds to the fraction of the feed stream that bypasses or escapes the classification process [53]. Often, bypass increases with an increase in solids loading and throughput rates [54]. For convenience, the bypass can be corrected mathematically to zero for smaller particle sizes by scaling the recovery using the following equation [53, 55]:

$$C_i = \frac{S_i - B_p}{1 - B_p} \tag{2.1}$$

It is observed from Figure 2.1b, the corrected cut sizes (d_{50c}) are coarser than the true cut sizes (d_{50}). As shown in Figure 2.1b, the area between the true separation efficiency curve and the ideal curve is known as the "error area", which indicates the measure of the degree of misplacement of particles to the wrong product streams [56].

Further, the sharpness of separation which indicates the quality of separation can be determined using the sharpness index (β), which is determined by the following relation [52]:

$$\beta = \frac{d_{25}}{d_{75}} \tag{2.2}$$

The parameters d_{25} and d_{75} correspond to respective particle diameters against the particle recovery values of 25% and 75%. The sharpness of separation can also be expressed using other means, for example, the probable error of separation also known as the *Ecart probable (Ep)* or by the imperfection index (I) respectively. The probable error of separation (Ep) is defined as half the distance between the particle diameters corresponding to recovery values of 75% and 25%, which can be represented by the following equation:

$$Ep = \frac{1}{4 \times \text{Slope of } S \text{ curve}} = \frac{d_{75} - d_{25}}{2} \tag{2.3}$$

Where, the imperfection index is defined by the following relation,

$$I = \frac{Ep}{d_{50}} = \frac{d_{75} - d_{25}}{2 \times d_{50}} \tag{2.4}$$

Lower the values of I, the sharper the separation, indicating an efficient operation. Conversely, higher values of I indicate a broader particle size distribution, leading to lower separation sharpness. For an ideal classifier, the sharpness index value is unity i.e., β = 1, whereas I =0. However, for all real classifiers, β is less than 1 and I is $>$ 0. When separation efficiency curves are similar, i.e., partition curves parallel to each other, they have the same sharpness and imperfection index values, but their Ep values differ due to logarithmic abscissa. Therefore, analyzing the sharpness of separation for separation efficiency curves using Ep is only meaningful when their d_{50}'s are approximately in the same range [57]. Ep is generally used in characterizing the separation efficiencies for Dense Medium Separations (DMS). Perhaps a separation index based on the "error area" is more meaningful in quantifying the separation for systems having higher bypass values ($B_p \geqslant$ 25 %).

The dispersion of particles in the air is a major contributor to the sharpness of classification [58]. In an ideal classifier, each particle experiences flow field conditions that are independent of other particles. To reduce agglomeration, particles are well dispersed before entering classifiers using external mechanical means (e.g. rotors). Moisture often plays a major role in forming agglomerates, and in dry processing, the relative humidity is usually maintained at around 50 to 70% [59]. Very low humidity is often undesired as particles become electrostatically charged, which hinders the separation and can cause a risk of explosion [59, 60]. The particle size being treated also affects the dispersion; as the particle size decreases, the attractive forces between the particles increase. This increase in particle-particle attraction makes it difficult to disperse particles less than 1 μm in size. Further, the random movement of fine particles due to brownian motion and turbulence effects makes it more difficult to deviate the particles from the mean flow. High tangential velocities are therefore required to act on the particles in order to overcome the fluidic forces and to classify accurately [5].

2.1 Dry classifiers: Classification based on particle separation

The major contributing separation mechanisms for dry classification are 1) Centrifugal Forces, 2) Gravitational forces, 3) Inertial forces, 4) Screens, 5) Fluidization, and 6) Surface forces (friction). Table 2.1 lists the majority of dry classifiers which separate the particles based on size, density, or the combination of both under the influence of the above-listed mechanisms. The separation of particles is further enhanced by modifying the surrounding environment or equipment design i.e., by providing inclination, vibration,

fluidizing the medium, and by other miscellaneous mechanisms. The primary interest of this review paper is to highlight the gaps and limitations in dry classifiers that separate the particles purely based on size. Hence, the class of equipment under magnetic separators, electrostatic classifiers, and air jigs/Tables are excluded from the discussion.

We introduce a novel schematic plot to illustrate and compare the range of application of each class of dry classification equipment, by shading their ranges of particle cut size d_{50} (μm) and throughput rates (kg/h), as shown in Figure 2.2. This data is collated from the literature sources for the equipment given in Table 2.1. A log scale is used to emphasize smaller cut sizes and capture the higher throughput values. We observe that the equipment which uses centrifugal forces to separate particles spans the broadest range for cut sizes i.e., up to $\leqslant$ 200 μm. Centrifugal classification technology not only achieves smaller cut sizes but is also adaptable to scale for higher throughput rates. It is evident that equipment based on inertial forces is overlaid by those based on centrifugal forces. Excluding gravitational classifiers, there is a broad overlap of the classifiers between 20 to 300 μm; hence the selection of equipment requires consideration of further criteria such as energy use, stable operation, ease of cut size control, product recoveries, and so forth [61].

Table 2.1: Grouping of dry classifiers based on size and density of particle

<table>
<tr><th></th><th>Centrifugal force</th><th>Gravitational force</th><th>Inertial force</th><th>Surface</th><th>Vibration</th><th>Fluidization</th><th>Other forces</th></tr>
<tr><td rowspan="3">Size</td><td rowspan="5">Cyclones,

Vortex air classifiers,

Rotor/Rotating wheel classifiers,

High-Efficiency separators,

Circulating air classifiers,

Turbo-air classifiers,</td><td rowspan="3">Counter Flow vertical raise classifiers,

Zig-Zag classifiers</td><td rowspan="5">Franken/Buell gravitational-inertial classifier,

Vortex classifier,

Gravitational-Centrifugal classifier,

Throat classifier</td><td>Sieves</td><td>Vibration sieves</td><td>Air Fluidizers</td><td rowspan="5">Elbow classifier,

Packed-bed classifier,

Electrostatic classifier,

Tribo-cyclone</td></tr>
<tr><td colspan="2">Inclined vibrational sieves,

Inclined vibrational plate (IVP)</td><td rowspan="2"></td></tr>
<tr><td colspan="3">Reflux classifier,

Inclined air fluidizers</td></tr>
<tr><td>Density</td><td>Cross Flow classifiers with horizontal air stream</td><td colspan="3">Air Tables,

FGX separator,

Air Jiggs (Fluidization + Hindered settling + Suction - Consolidation tickling)</td></tr>
</table>

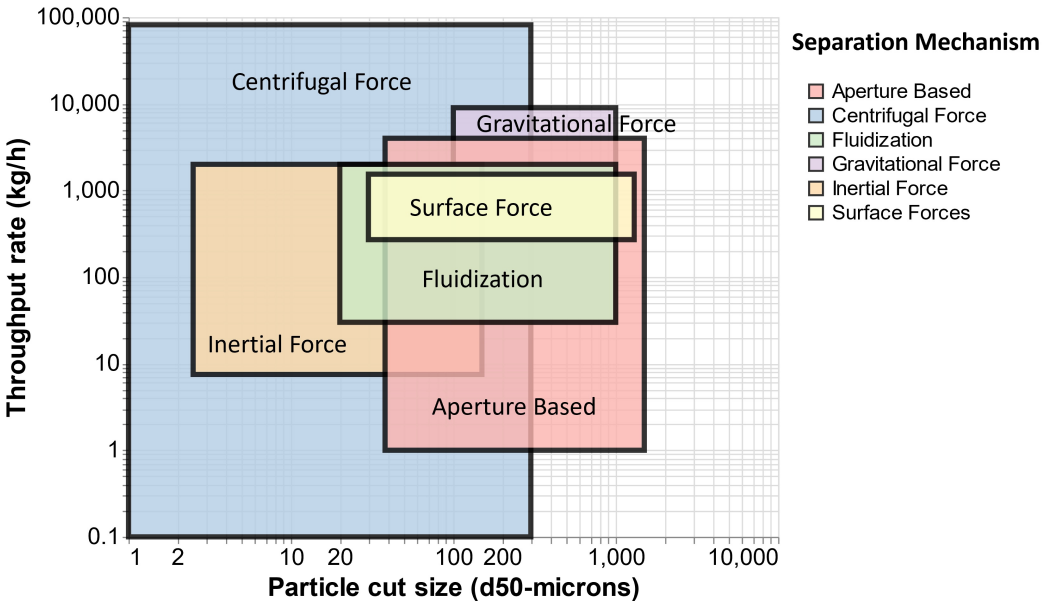


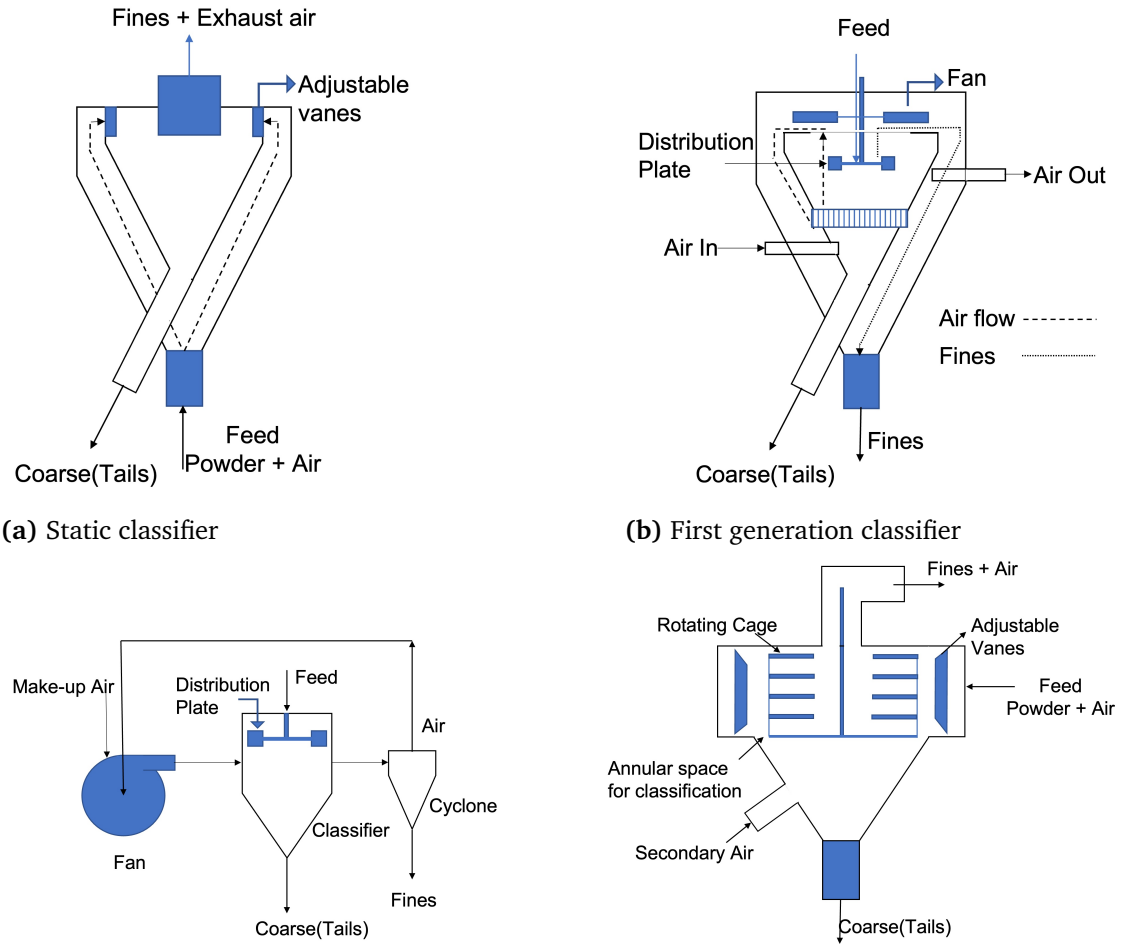
Figure 2.2: Broad classification of dry classifiers based on their particle separation mechanism

The following sections will review each class of classifier, and compare the performance of various types of equipment within that class using a schematic of the form shown in Figure 2.2.

2.2 Centrifugal Air Classifiers

Centrifugal air classifiers can be divided into Static and Dynamic classifiers. Figure 2.3 shows the general schematic diagram of both static and dynamic classifiers, depicting their general principle of operation. Table 2.2 captures the information on performance metrics; cut size, bypass, and sharpness of static and dynamic centrifugal classifiers. Static centrifugal classifiers have design features similar to cyclone separators, as shown in Figure 2.3a. They induce centrifugal forces using a flowing air stream into a cylindro-conical section of the classifier which classifies the particles. The cut size is fixed for the given design of static classifiers and can only be altered by changing the flow magnitude and direction of flow into the classifier. It is observed from Table 2 that static classifiers suffer from high bypass ($> 60\%$) with low sharpness values.

In contrast, dynamic classifiers have a variable speed rotating cage which allows adjustment of the cut size [62]. Since their introduction in 1885, Altun and Benzer [63] dynamic centrifugal air classifying equipment has evolved through three generations. In the first generation classifiers, as shown in Figure 2.3b, an integrated centrifugal rotor is placed inside the device to disperse the particles towards the wall of the separator. Further, rising air exerts a drag force on the particles which carries the fine particles [63]. The major challenge with first-generation devices are the high bypass of fines, and which



(a) Static classifier

(b) First generation classifier

(c) Second generation classifier

(d) Third generation classifier

Figure 2.3: Schematic diagrams of centrifugal static and dynamic classifiers.

Table 2.2: Performance characteristics of Centrifugal-air classifiers Source: Fives FCB and Yardi[65]

	Static Classifier	First-Generation (1890)	Second-Generation (1960)	Third-Generation (1980)
Cut size Diameter (d_{50}) microns	Not Applicable	>20	15-20	10-15
Bypass	>60	>50	15-35	5-15
Sharpness (d_{25}/d_{75})	0.3-0.35	0.4-0.45	0.5-0.55	0.6-0.7

was addressed in the second-generation classifiers, where the centrifugal rotor is replaced by an external air circuit. These are operated in tandem with cyclones in order to improve the fines collection efficiency, reduce the bypass and increase the sharpness of separation [62]. Though this proved effective when compared with the first-generation equipment, they required large space, particularly because of their auxiliary equipment. In third-generation classifiers, a rotating cage is placed in the upper portion of the classifier to disperse particles radially outward, whereas the air enters radially inwards, allowing the particles to classify. Particles are subjected to two counteracting forces: centrifugal force due to turbine rotation, and drag force because of the centripetal gas flow [64, 65]. Coarser particles have sufficient inertia to enter the rotating cage and get impacted by the internal rods and settle to the bottom, thereby leaving behind the fines to be removed by the gas stream.

2.2.1 Static Centrifugal Classifiers: Cyclone Separators

Gas cyclones are the major static equipment type that uses induced centrifugal forces for particle classification. Cyclone separators have lower throughput rates because of their inability to scale by size, as the separation efficiency is inversely proportional to the radius of the cyclone. Table 2.3 reports a number of studies on cyclone design changes. It shows that there has been extensive research on modifications to improve efficiency by reducing pressure drop or adjusting the cut size. Most of these studies focus on the use of gas cyclones as a particle separator (e.g. removing the dust; hence $d_{50} \leqslant 3\ \mu m$).

The early studies of Iinoya *et al.* [66] focused on achieving cut point values at the sub-micron level by using the blow-down method (i.e., free collection of the particles at underflow rather than into a closed collection chamber). Later Yoshida *et al.* [25] explained the particle separation mechanism in blow-down operation using computational fluid dynamics (CFD). Yoshida *et al.* [24] installed a movable guide plate at the inlet to control the cut point diameter between 0.45-0.75 μm. Wang *et al.* [30] numerically investigated the effect of the flow field inside gas cyclones on particle classification. The turbulence inside the cyclone is captured using the Reynolds Stress Model (RSM) with

reasonable accuracy, as the flow field and pressure profiles were in good agreement with the reported experimental values. It was observed that particle injection location from the inlet plane has a major influence on the separation efficiency. Interestingly, when the particles were injected from the top of the inlet plane, a higher separation values was obtained compared with particles released from the bottom of the inlet. Yoshida *et al.* [27] studied the influence of secondary flow injection location and inlet guide plate on classification performance. It was observed from the CFD simulations that the overall tangential velocity profiles improved when the main flow inlet is located slightly lower than the secondary flow inlet; resulting in a cut size of 0.5 μm. However, when both the secondary flows and inlet guide plates are used it is observed that the cut point is reduced from 0.97 μm to 0.5 μm [26, 27, 29]

As shown in Table 2.3, Yoshida [1] and his co-workers performed extensive research on modifying the design of various parts of the cyclone (Vortex finder, Apex section, Conical section, Inlet section, and a combination of these) to control the cut point diameter in the sub-micron range. Most of the above-mentioned studies focused on improving the tangential velocity components near the cylindrical wall, as it enhances the centrifugal force acting on the particle, thereby improving the classification efficiency in terms of cut size (d_{50}) and sharpness.

Very few studies [1, 2, 22] have been carried out on gas cyclones which can classify coarse particles, requiring d_{50} values of at least 30 μm. For a conventional cyclone separator, any attempts at increasing the cut size to coarser sizes require a decrease in swirling flow in order to reduce the tangential velocity components of the flow. This lowers the centrifugal forces acting on the particle to classify. Yoshida [1] modified the apex region with a movable apex cone which enables the cut size to be varied between 2 to 38 μm. Figure 2.4 depicts the shift in the separation efficiency curve due to the change in the position of the apex cone and the effect of the blow-up flow into the dust collection chamber. Installing an apex cone upstream of a dust box dampens the rotational and upward fluid velocities, thereby reducing the re-entrainment of particles from the dust box [1]. Oshitari *et al.* [2] changed the design of a conventional cyclone by installing a Controlled Surface (CS) sloped wall surface in the apex section where particles passing through the inner and outer collection boxes are classified. The design developed by Oshitari *et al.* [2] is shown in Figure 2.5 which contains a channel that derives additional air (blow-up flow) through the tangential inlet which creates a confluent flow with the swirling main flow of the cyclone. Larger particles, for which centrifugal forces dominate, are collected in the outer box, while fine particles are carried by the air drag and removed through the inner box. Cut size strongly depends on the main flow and it is varied between 15-30 μm by changing the main flow conditions. Blow-up flow has a negligible effect on the cut size as it increases both drag and centrifugal forces acting on the particle to the same extent,

however, the sharpness of the classification curve is improved significantly by increasing the blow-up flow [2, 22]. The interesting observation is both of the studies focusing on the coarser particle classification in cyclones attempted to modify the design at the apex section. Any attempts made to alter the design of cyclones other than at the apex are likely to hamper the classification efficiency, as they reduce the tangential flow velocity component.

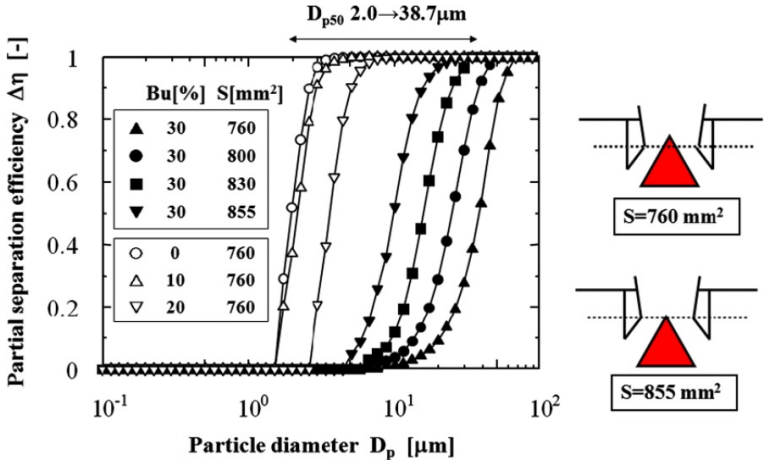


Figure 2.4: Separation efficiency curve depicting the trend of d_{50} vs apex cone clearance area as a function of blow-up ratio - Bu = Blow up, S = Cone clearance (Image Source: Yoshida [1])

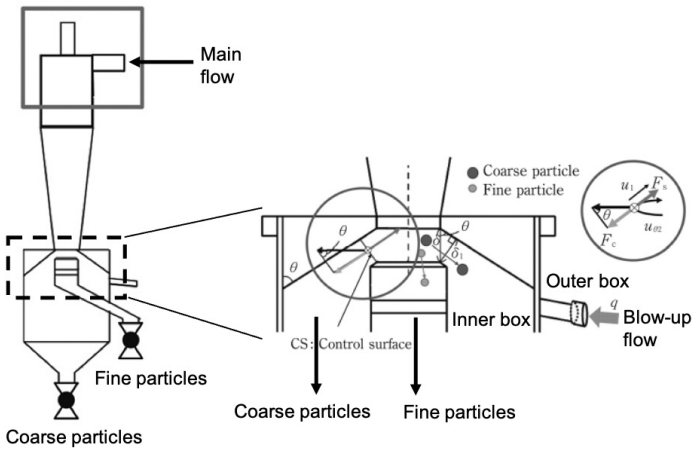


Figure 2.5: Design of coarser particle cyclone classifier with improved collection boxes (Image Source: Oshitari *et al.* [2])

As observed from Table 2.3, the design changes made on gas cyclones were able to increase the maximum cut size to 30 μm, however, the challenge of low throughput rate persists. By adding external rotors, it is possible to achieve higher throughput rates and a wider cut size range; this is discussed in the following section on dynamic centrifugal classifiers.

Table 2.3: Few studies reported the design changes on gas cyclones

Article	Target Part	Design Modification	d_{50} Range (μm)	Summary of Findings
Design changes on a cyclone to function as a Particle Separator ($d_{50} \leqslant 3\,\mu$m)				
Yoshida *et al.* [24]	Inlet	Inlet guide plate	0.45–0.75	Controlled cut point by adjusting guide plate location to alter inlet clearance
Yoshida *et al.* [26]	Inlet	Secondary injection flow	0.7–1.25	Secondary flow injection was placed in proximity of the upper plate. High tangential velocities are reported in region close to secondary injection flow.
Hiraiwa *et al.* [67]	Inlet	Compressed air injection. Secondary flow	1.1–1.75	Higher tangential and axial velocities are reported in upper cylindrical part because of secondary flow injection.
Huang *et al.* [68]	Inlet	15 horizontal laminarizer cylinders inserted in the inlet	1.4–2.07	Laminarizer induces higher gas velocities near outer part of inlet. Increased pressure drop and higher particle separation efficiency were reported as a greater number of particles was found in outer part of entrance.
Misiulia *et al.* [69, 70]	Inlet	Inlet angle with a helical-roof inlet	1.2–3.75	An increase in inlet angle increases cut size with a reduction in cyclone efficiency and pressure drop coefficient.
Yoshida *et al.* [28]	Conic	Double cone for Iinoya cyclone	0.8–0.95	10% lower pressure drop than compared with conventional designs.
Huang *et al.* [71]	Conic	Various splits on the conical section	0.83–1.35	Fine particles are removed before they exit through overflow through split. Overall separation efficiency increased from 74.5 to 80.7%.
Wakizono *et al.* [72]	Vortex finder	Optimised the ring structure on the vortex finder	0.67–2	Modified design eliminates re-circulation zones near vortex finder area. Thus, high particle collection efficiencies and lower pressure drop were reported.
Yoshida *et al.* [25]	Apex	Blow down	–	Performed CFD simulations to track the particle behavior in a blow-down cyclone. Observed reduction in cutpoint.
Design changes on a cyclone to function as a Particle Classifier (d_{50} 1–30 μm)				
Yoshida [1]	Apex	Apex cone shape + Blow-down	2–38.07	A movable apex cone reduces re-entrainment of particles from dust box.
Oshitari *et al.* [2, 22]	Apex	Particles are classified between sloppy channel of inner and outer collection boxes using blow-up air flow	18–29	It was demonstrated that cut size is a strong function of main inlet flow through entrance irrespective of blow-up flow rate. However with the increase in blow-up flow sharpness of separation increases.

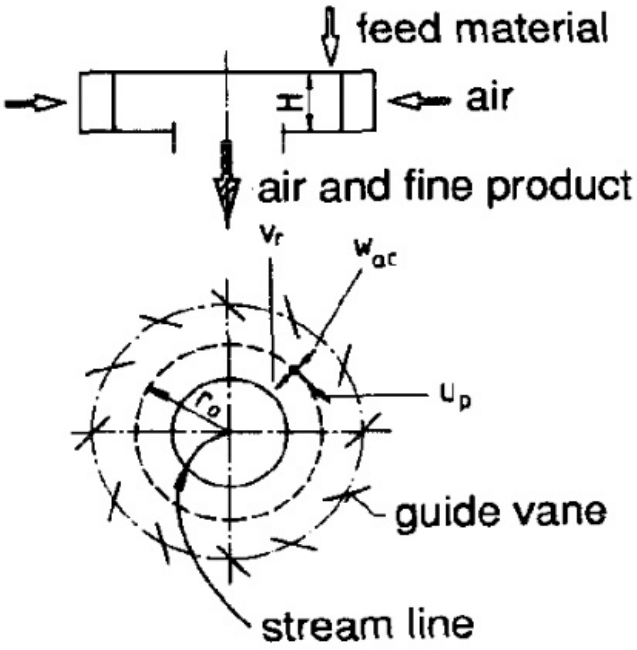
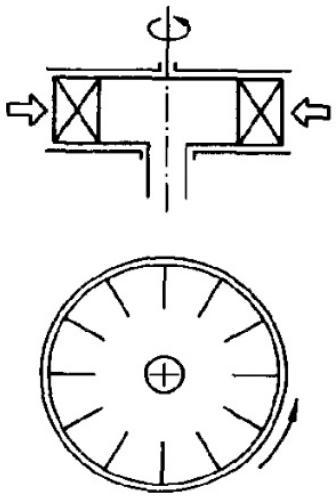
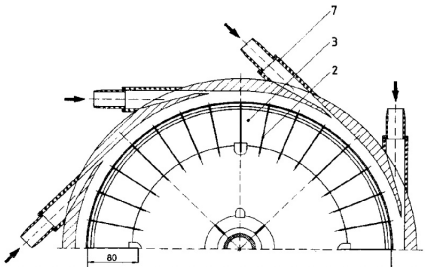


Figure 2.6: Schematic of spiral air classifier developed by Rumpf and Leschonski [3] (Image Source: Leschonsi and Legenhausen [4])



(a) A schematic representing the Deflecting Wheel Classifier



(b) Cross-sectional view of industrial deflecting wheel classifier

Figure 2.7: Deflecting wheel classifier (Image Source: Leschonski [5, 6])

2.2.2 Dynamic Centrifugal Classifiers: Rotary classifiers

A centrifugal counter-flow classifier with a free vortex sink flow, called a Spiral Classifier, was developed by Rumpf and Leschonski [3] and is shown in Figure 2.6. It consists of a short circular cylindrical classification chamber and a circumferential spiral casing with adjustable guide vanes. The air is introduced tangentially into the classification chamber, creating a spiral motion as it travels towards the center and exits axially. This motion

induces a free vortex sink flow. The feed particles enter at a defined radius into the classification chamber. The coarser particles move to the periphery and fines travel along with air.

For a given inlet flow rate of air, the tangential velocity decreases with solids loading (due to momentum exchange between the particles and air), decreasing the efficiency [3]. To address this limitation, deflecting wheel classifiers were developed [4, 73]. In the first generation classifier, as shown in Figure 2.7, a rotating wheel with radial blades induces a tangential gas velocity, creating a forced vortex (solid-body rotation) superimposed on the free vortex sink flow. In a free cylindrical vortex, the velocity is inversely proportional to the distance from the axis of rotation i.e., 'r' ($U \propto 1/r$), whereas, in a forced vortex regime, the fluid is forced to rotate at constant 'ω' ($U = r\omega$). By combining these two observations for rotational symmetrical flows it can be approximated that:

$$U_\theta r^m = U_{\theta 0} r_0^m = Constant \tag{2.5}$$

where, m = 1 for free vortex flow and m = -1 for forced vortex flow. Continuity yields the radial velocity component of the fluid as:

$$U_r r = U_{r0} r_0 = Constant \tag{2.6}$$

By applying the conservation of momentum on a particle at equilibrium between centrifugal and drag forces, the cut size diameter is expressed by the following equation [4]:

$$d_{50} = \left(\frac{18 \eta U_r r}{\rho_p U_\theta^2} \right)^{1/2} \tag{2.7}$$

Where d_{50}, η, r, and ρ_p represent the cut size diameter, the viscosity of the gas medium, the radial distance measured from the center, and the density of the particle. U_r and U_θ represent the radial and tangential velocity components of the airflow. By substituting the Equation 2.5 and 2.6 in the generalized cut-point equation which was derived earlier i.e., Equation 2.7, we obtain a relationship for cut size as a function of radial distance 'r' for the cases of free vortex sink flow (m=1) and forced vortex flow (m=-1), respectively:

$$d_{50} = \begin{cases} \left(\dfrac{18 \eta U_{r0}}{\rho_p U_{\theta 0}^2} \right)^{1/2} \dfrac{r}{r_0^{1/2}} = C \dfrac{r}{r_0^{1/2}}, & \text{for } m = 1 \text{ (Free vortex)} \\ \left(\dfrac{18 \eta U_{r0}}{\rho_p U_{\theta 0}^2} \right)^{1/2} \dfrac{r_0^{3/2}}{r} = C \dfrac{r_0^{3/2}}{r}, & \text{for } m = -1 \text{ (Forced vortex)} \end{cases} \tag{2.8}$$

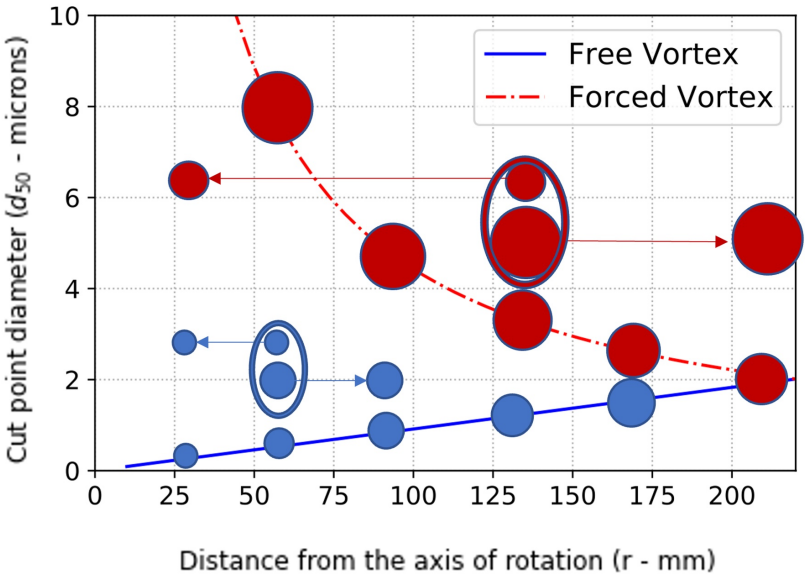


Figure 2.8: Schematic depicting the cut-point diameter as a function of radial distance for free and forced vortex sink flows

Figure 2.8 depicts the particle classification effect produced in free and forced vortex sink flows. This plot is reproduced for the conditions reported elsewhere [4]. The round spots on the red and blue lines represent the corresponding cut size diameters of forced and free vortex flows. According to equation 2.8, as observed from Figure 2.8, the cut size in a free vortex classifier is directly proportional to the radius of the classifier because velocity is inversely proportional to the radial distance. Theoretically, for the free-vortex condition a particle reaches its respective equilibrium radial position and continues to travel in a circular path in the classification chamber, thus producing the dispersion effect. Whereas, from equation 2.8 for a forced vortex flow the cut size reduces with an increase in the radial distance; hence at a given radial location the particles finer than their corresponding cut size travel towards the center and coarser particle moves toward the outer wall under the influence of centrifugal forces; thus producing the classification effect. Hence, forced vortex flow behavior is preferred over free vortex flow as it produces a classification effect. In forced vortex classifiers the circumferential velocities available in the classifier depend upon the rotor speed. The cut size is independent of the particle loading unlike free vortex classifiers [74].

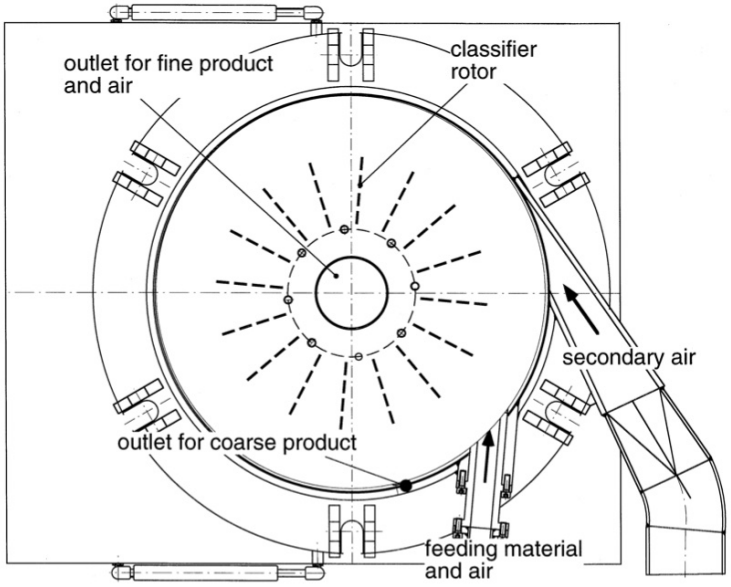


Figure 2.9: Design of Impeller Wheel Classifier - MicroCut MC (Image Source: Galk *et al.* [7])

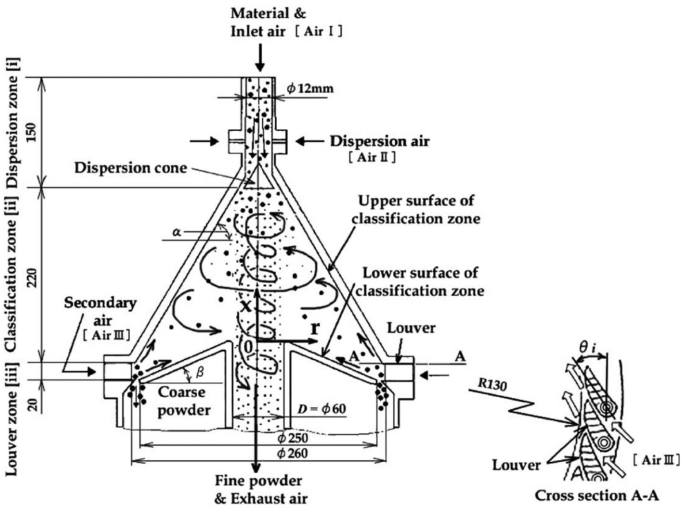


Figure 2.10: Design of Ultrafine classifier (Image Source: Morimoto and Shakouchi [8])

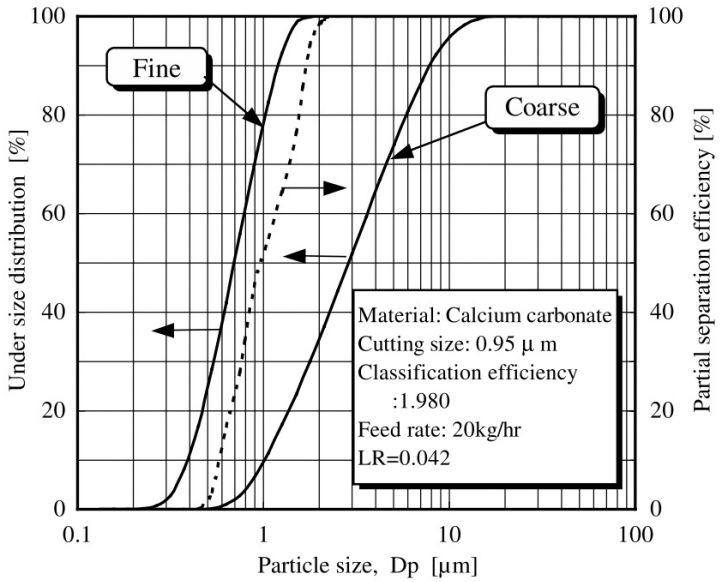


Figure 2.11: A typical tromp curve in an Ultrafine Classifier depicting sub-micron size particle classification (Image Source: Morimoto and Shakouchi [8])

Galk *et al.* [7] have developed an impeller wheel classifier *'Microcut MC'* that uses a forced vortex to achieve high classification efficiencies. The operating principle is similar to the deflecting wheel classifier except that the feed enters through a tangential inlet and a provision is made for a secondary air inlet to improve the classification efficiency. The design of the MicroCut MC classifier is shown in Figure 2.9. The high rotating speeds of the rotor classifiers (100 m/s) produce the centrifugal acceleration, of the order 1500 **g**, used to classify particles in the sub-micron range, with a throughput rate of up to 500 kg/h.

Morimoto and Shakouchi [8] have performed experimental flow field studies on a novel pneumatic ultrafine powder classifier. The static device develops a swirling flow from inclined guide vanes (louvers) in an inverted circular-conical classification chamber, as shown in Figure 2.10. The strength of the swirling flows intensifies upwards as the swirling radius decreases, creating the high centrifugal force required to classify ultrafine particles. The feed particles, inlet air, and dispersion air are introduced from the top and enter the classification zone. The centrifugal forces in the upper region of the cone force the coarser particles radially outwards and collect them through the slit at the bottom. Fine material is removed through the central descending flow exit. The major proportion of the air, up to 90%, enters through the louvers, and suction removes the air from the classifier through bag filters. This is typical for second-generation air classifiers which operate on negative pressure. The device classifies powders with cut sizes of $\leqslant 3$ μm with throughput rates up to 20 kg/h. A typical Tromp curve for this ultrafine classifier is shown in Figure 2.11 with cut size and sharpness index (d_{25}/d_{75}) values of 1.98 μm and 0.95 respectively.

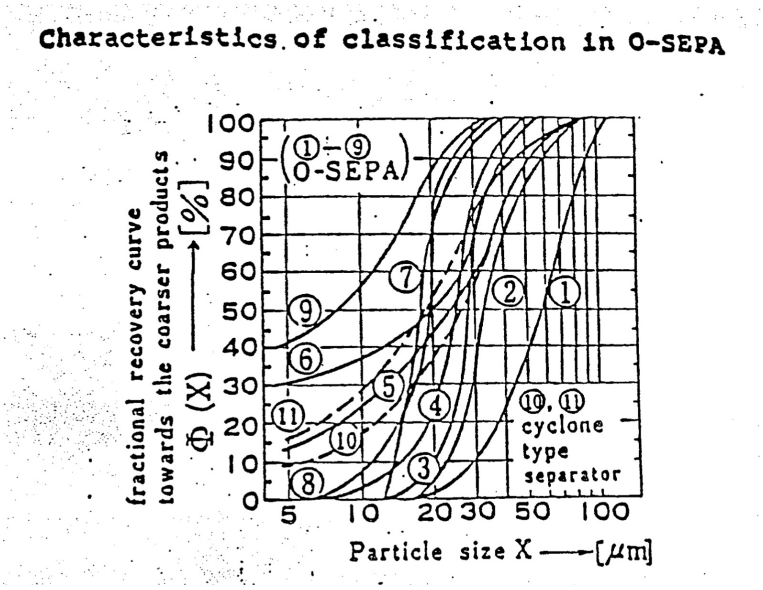


Figure 2.12: Effect of rotor speed and air flow rate on the tromp curve for an O-SEPA High-Efficiency Separator (Image Source: William and Craig[75])

Nied [74] developed a novel CFS-HD classifier that operates on the combination of free and forced vortex flows which produces the cut sizes of $\leqslant 2\ \mu m$ having throughput rates of 100-400 kg/h. Static vanes surrounding the rotor cage help in generating the free vortex flow which is used to efficiently disperse the particles. The dispersed particles are effectively classified by the forced vortex created by the rotor cage.

The following section details classifiers that enhance their performance with an external rotating mechanism; either to disperse the solid particles or to induce the required flow. These third generation classifiers include Circulating Air classifiers, O-SEPA High-Efficiency Separator, Rotor air classifier, Circulating air classifiers, Turbo-air classifiers, and Ultrafine classifiers.

As discussed earlier, the general form of a cut-point diameter of the centrifugal air classifier is given by Equation 2.7, where the radial and tangential velocity components of the fluid U_r and U_θ are dependent upon the mode of centrifugal forces generated. For a given volumetric flow rate (Q) of a turbo/rotor-air classifier, the radial and tangential velocities can be calculated as:

$$U_r = \frac{Q}{120\pi Rh} \tag{2.9}$$

$$U_\theta = \frac{2\pi Rn}{60} \tag{2.10}$$

Where R, h, and n are the radius, height, and rotations per minute of the rotor cage placed inside the classifier. Therefore, by substituting Equation 2.9 and 2.10 in Equation 2.7, a relationship of cut-point diameter as a function of design and operating parameters of the rotor is obtained:

$$d_{50} = \left(\frac{135 Q \eta}{\pi^3 R^2 n^2 h \rho_p} \right)^{1/2} \tag{2.11}$$

The vortical flow separator, commercially known as the O-SEPA High-Efficiency Separator, was introduced to the cement industry in 1984 to provide narrow size distributions. The classification mechanism balances the centrifugal and air tangential velocities. The feed material is distributed through the rotating dispersion plate at the top. Cut sizes and particle size distributions are controlled by a variable speed rotor (dispersion plate) and air flow rates [75]. As shown in Figure 2.12, cut size can be varied from 6 to 60 μm by changing the operating flow conditions, and has a production capacity of 90 t/h.

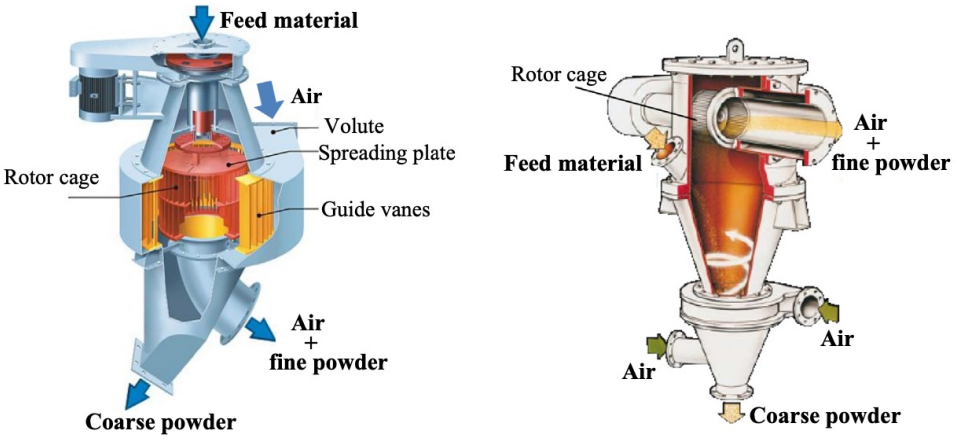


Figure 2.13: Typical turbo-air classifiers a) Vertical b) Horizontal arrangement of rotor cage (Image Source: Sun *et al.* [9])

As shown in Figure 2.13, Turbo-air classifiers are either vertical or horizontal depending on the direction of the rotor cage. Turbo-air classification operates by dispersion followed by separation. Feed particles are either pre-dispersed before entering the classifier or dispersed inside the classifier. In turbo-air classifiers; feed particles are distributed onto the rotating spreading plate, dispersing them into the cross-flow air stream. Coarser particles are deflected by the rotating cage towards the wall and are collected through the coarse particle chamber. Fine particles are removed through the central exit pipe.

The cut-point in High-Efficiency Separators can be controlled using three methods:

- By varying the inlet air flow rate; higher flowrates produce coarser cut-points d_{50}
- By adjusting the speed of the rotor cage, the higher the speed of the rotor, the finer the cut-point, and
- By adjusting the angle of the vanes; radially aligned vanes produce a coarser product while tangential vanes yield a finer product.

The effects of operating and structural parameters such as rotor speed, rotor blade angle, inlet air velocity, and material feed rate have been studied using Laser Doppler Velocimetry (LDV), Particle Image Velocimetry (PIV), and computational fluid dynamic (CFD) simulations [76–78].

Karunakumari *et al.* [79] have studied the rotating air classifier which is a complex design consisting of rotating fan blades and stationary guide vanes. They performed CFD analysis to understand the internal flow field and the effect of geometric features. They observed that the type of stationary guide vanes (radial or angular) has a significant influence on the secondary re-circulation pattern inside the classifier which in turn affects the classification efficiency. The secondary flows intensify with an increase in the speed of the fan thus increasing the cut size. Interestingly, the higher centrifugal forces adversely affect the collection efficiency for higher particle sizes as the particles tend to escape through the fines outlet. In contrast; for a constant rotational speed with an increase in particle loading the classification efficiency improves because of the loss of momentum to solid particles (momentum exchanged between the fluid and solid), reducing the strength of secondary flows.

Though the rotor wheel and vane classifiers offer the advantages of variable cut point diameter and increased throughput rates, particle-rotating wall collisions lead to significant particle attrition and breakage of a fragile material. Ito *et al.* [80] have studied particle attrition in centrifugal air classifiers with rotor blades. They observed powder particles are broken in the classifier, producing two size fractions: a coarser range and fines from submicron to a few microns in size. The amount of breakage increases with an increase in rotor speed, inlet air flowrate, and a reduced solids mass flowrate.

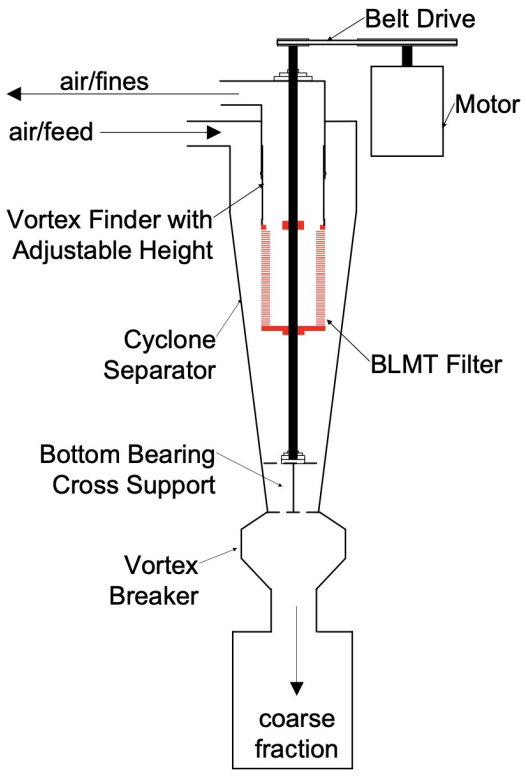


Figure 2.14: BLMT Classifier with a BLMT filter installed below the vortex finder (Image Source: Worthen [10])

Worthen [10] developed the Boundary Layer Momentum Transfer (BLMT) classifier, which is a combination of the BLMT filter and a cyclone separator with a modified inlet, as shown in Figure 2.14. The BLMT filter is a set of closely spaced, co-axially stacked rotating cylinders that transfer angular momentum to the fluid in the boundary layer between them, creating a forced vortex region. This causes the coarse particles to move radially outward against the main inward flow due to the centrifugal forces. Finer particles are carried by the radially entering air through the disks and axially exit out at the top. Worthen [10] found experimentally that installing a BLMT filter into a cyclone separator increases the sharpness of the classifier for a broader range of cut sizes (4-30 μm) than a conventional cyclone. Further, the BLMT classifier is more effective at classifying fragile particles as rotating vane collisions are eliminated.

Centrifugal air classifiers are widely used in various industries for particle size and granularity control, with the added benefit of adjustable cut sizes and high classification efficiency [81]. Internal protective liners allow the economic treatment of abrasive powders, such as silica, fly ash, and ceramics. However, these systems can suffer from clogging and maintenance issues when surface moisture is high [82] and are not suitable for processing materials that are particularly sticky or oily. They are unsuitable for fragile or friable materials and can generate fines due to particle-rotor interactions at high throughputs. They exhibit high energy consumption from the particle dispersion devices. Despite these challenges, centrifugal air classifiers are used for a wide range of applications, such as classifying coal particles from fly ash, grinding circuits, recycling plants, protein shifting, and chemical processing of polymers, pigments, and toner, among others [81].

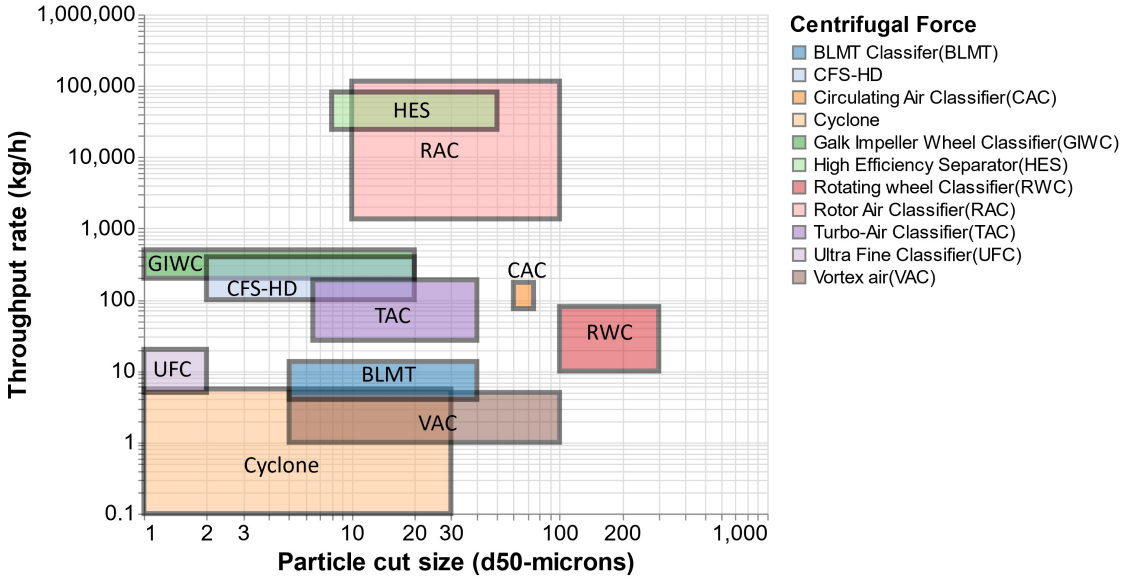


Figure 2.15: Dry classifiers based on their centrifugal force mechanism

To summarise, the throughput rate (kg/h) and particle cut sizes (d_{50}) of centrifugal

air classifiers are collated and the maximum and minimum values of these parameters are presented in Figure 2.15. The static centrifugal classifier- ie., cyclone appears at the bottom of the chart. In general, cyclone separators have a cut size less than $< 3\mu m$, but we have also considered design modification studies on cyclones that facilitate its functionality as a classifier having coarser cut sizes. The Boundary layer Momentum Classifier (BLMT) appeared close to the cyclone. BLMT is in principle a cyclone with a rotating element (i.e., stacked rotating cylinders with annular gap to flow) located at the vortex finder for achieving coarser cut sizes. Further, dynamic air classifiers such as Turbo Air classifier (TAC), Circulating Air Classifier (CAC), Rotating Wheel Classifier (RWC), and Rotor Air Classifier (RAC) have different classification principles that enable the cut size range to be extended to $5 \leqslant d_{50} \leqslant 300\ \mu m$, with throughput ranging from few ten's to several thousand tph. High-Efficiency Separator (HES) and Rotor air classifiers (RAC), third-generation air classifiers, can be found at the top of the chart. Owing to their robust design and high operational rotor speeds they possess the ability to scale for larger throughput rates.

More details related to gravity and inertial air classifiers can be found at the Appendix A.

2.3 Gas Cyclones

Cyclones are used ubiquitously in industry for the removal of particles from the carrier gas stream. Including applications such as in internal combustion engines for cleaning the oil mist from the blow-by-gases [83], vacuum cleaners [84], viral and bacterial detection and removal kits [85, 86], and personal cyclone samplers to evaluate airborne particulate matter and its adverse health effects [87].

There have been numerous studies on the influence of design and operational parameters on the performance efficiency of gas cyclones. Elsayed and Lacor [88] studied numerically the effect of inlet dimensions (inlet height and width) on the pressure drop and cut-off diameter. It is reported that inlet width has a greater influence on cut-off diameter than inlet height. Zhao *et al.* [89] reported that a double spiral inlet configuration produces a more symmetrical flow field than the conventional tangential inlet design; which improves separation efficiency. Studies reported the effect of vortex finder design changes on pressure drop and particle separation performance [90, 91]. Misiulia *et al.* [69, 70] studied the influence of the inlet angle of a helical-roof cyclone. An increase in inlet angle increases the cut size (1.2-3.75 μm) reducing the cyclone efficiency and lowering pressure drop losses. Raoufi *et al.* [90] numerically evaluated various vortex finder designs (converging, diverging, stepped cylinder) and reported that the angle of converging and diverging vortex finders determine the separation. Wang *et al.* [30] studied numerically

the effect of vortex finder length of the flow field inside the cyclone. By examining the axial and tangential flow profiles at various locations they found that vortex finder length has an insignificant effect on the flow field.

Xiang *et al.* [11] experimentally studied the effect of the cone dimensions, specifically the bottom apex diameter on the cyclone performance characteristics. They found flow rate has a strong influence on the particle cut-off diameter. Safikhani *et al.* [92] numerically studied the ratio of cylinder length to conic section length. It was observed that a longer conic section design has greater separation efficiency. Recently, Pandey and Brar [35] conducted a numerical investigation on the impact of conic curvature on a 205 mm diameter gas cyclone. Their study explored convex, concave, and other hybrid curved designs. The results indicate that the conic curvature has a negligible effect on particle separation characteristics, but it does have an impact on the pressure drop.

All these design changes produce cut sizes $<3\ \mu m$, with the objective of the cyclone to function as a particle separator. There are very few studies that focus on design modification of the gas cyclone for use as a particle classifier. Yoshida [1] studied the effect of apex cone angle and the clearance between the cone and collection on the particle separation characteristics. Blow-up flow is introduced near the dust box chamber to strengthen the classification effect. It was observed that an adjustable apex cone reduces the re-entrainment of particles from the dust box. The cut size reported was in the range of 2-38.07 μm. Oshitari *et al.* [2, 22] observed that secondary particle classification is induced by blow-up flow introduced. They demonstrated that cut size is a strong function of the main flow through the inlet irrespective of the blow-up flow rate. However with the increase in blow-up flow the sharpness of the separation increases. The cut size of classification is increased up to 18-29 μm depending upon the flow conditions. Caliskan *et al.* [93] designed a cyclone with internal collector rings. It is demonstrated that particles can be classified into 4 size classes [93]. Interestingly, these are the only research studies on gas cyclones that function as a classifier rather than as a separator.

CFD simulations can predict the flow field and separation characteristics accurately and can be used to build multi-objective optimization. Natural vortex length is one of the key parameters that influence the separation efficiency and surface erosion inside the cyclone [94]. Qian and Zhang obtained the relation between the natural vortex length and the cyclone design and process parameters. The Response Surface Methodology (RSM) was used to optimize the cyclone design by performing CFD simulations at the design points [94]. Safikhani [95] performed multi-objective optimization on Karagoz cyclones to improve collection efficiency and reduce pressure drop. Elsayed and Lacor [96] lowered the pressure drop, using the RSM model to capture the interaction effects between design parameters. The optimized design lowered the pressure drop by 25% compared to the Stairmand design. In cyclones, significant pressure is lost (up to 50% of total pressure

drop) in the swirling flow that exits through the vortex finder [97]. To recover the energy lost design modifications such as deswirlers and slotted vortex finders are used [98–100]. Misiulia *et al.* [97] optimized the design of a deswirler, using CFD simulations with a combination of genetic algorithms-based optimization techniques. It was reported that the overall pressure drop was reduced by 43% compared to the standard design [97]. Guo *et al.* [101] optimized the design of a slotted vortex finder cyclone, using CFD simulations to find the effect of the number of slots, slot length, span, and inclination angle of the slots. Singh *et al.* [102] used surrogate-based model optimization methods rather than conventional genetic algorithms. They optimized seven design parameters to reduce the pressure drop.

2.4 Hydrocyclones

Hydrocyclones have established themselves as integral components in a wide range of industrial processes, facilitating efficient particle separation and classification. These devices find applications in ore processing, chemical engineering, and mineral beneficiation due to their simple design and capability to separate solid particles from liquid suspensions [103, 104]. Hydrocyclones are employed in mill-classifier circuits in mineral industries where, the coarse fraction (*i.e.*, underflow) is sent back for further milling. Nonetheless, within a conventional hydrocyclone, the intricacies of the internal flow field invariably result in a compromised classification process, whereby fine particles become entrained in the underflow. These fine particles, evading proper separation and finding themselves misallocated to the underflow, are known as 'bypass'. Importantly, the presence of these bypassed fine particles enhances the yield of particles in the underflow, while reducing water recovery. This aspect holds particular significance for dewatering operations. Roldanvillasana *et al.* assert that the bypass effect should be regarded as a prevalent occurrence rather than an incidental anomaly [105].

Bypass reduction in hydrocyclones in mill-classifier closed circuits can improve separation efficiency, reduce power consumption due to overgrinding, and improve product quality by restricting the flow of fine particles to the underflow stream. Research has shown that bypass reduction can lead to significant improvements in mill circuit performance and should be considered an important operational parameter in such circuits [106]. As noted by Napier-Munn *et al.*, reducing the bypass can increase the circuit capacity and improve the grinding performance in a closed circuit.

From past research, it is understood that the bypass is influenced by the change in either operating conditions or by the design modifications. Cilliers *et al.* have studied the effect of temperature on the classification and dewatering characteristics of 10 mm hydrocyclones. They reported that the bypass increased with the temperature of the suspension

(studied range: 10-60°C) [107]. Frachon and Cilliers [108] observed that bypass increases with an increase in pressure and stays relatively constant at higher feed flowrates. Banerjee *et al.* also observed that bypass increases with feed pressure and decreases with solids loading [109].

The separation of particles in the hydrocyclone primarily begins in the conical section and many researchers have investigated various design modifications. For a conventional straight-cone hydrocyclone, Fu *et al.* has investigated the effects of cone angle, and was observed that separation efficiency was influenced more strongly for a fixed cylindrical diameter than for a fixed total hydrocyclone length [110]. Yang *et al.* reported that tapering the cylindrical body can effectively reduce the fine particle's misplacement to the underflow [111]. Jiang *et al.* increased the cone angle to 180°, creating a flat-bottomed, cylindrical hydrocyclone. It was observed that the flat-bottomed structure had lower axial velocities and increased particle residence times, thereby reducing the bypass behavior [112]. Jiang *et al.* reported that the effect of the 'W'-shaped apex structure reduced the bypass by increasing the axial velocity of the inner vortex while reducing the outer vortex [113]. According to Hou *et al.* [114], enlarging the upper diameter of the spigot in a cylindrical hydrocyclone has been found to reduce the misplacement of fines into the underflow. This is attributed to the enhanced circulating flow within the spigot region when using larger upper-diameter spigots compared to their smaller counterparts [114]. Vysyaraju *et al.* reported that concentric rings along the conic surface aid in disengaging the fines that are locked between the coarse particles, thereby reducing the bypass of fines to underflow [14].

It has been reported that multi-cone hydrocyclones may offer adaptability in terms of cut size and bypass [115–117]. It is reported that the angle of individual cones significantly impacts the particle separation characteristics [118]. This observation has led to exploring the curved conic designs which offer a smother internal flow; minimizing the turbulent environment in the flow domain. Chu *et al.* [119] investigated experimentally different structural modifications of the conical part on the cyclone performance. It is reported that both the parabola (convex) and hyperbola (concave) designs lead to sharper separation with coarser cut sizes compared to conventional designs. Concave hydrocyclones have a relatively lower internal volume, enhancing consequently the centrifugal flow field. Motin and Bénard [32] and Vega-Garcia *et al.* [33] reported promising separation performance for these concave curved cones through numerical simulations and experimental investigations, respectively.

Ghodrat *et al.* studied numerically the effect of cone shape (concave to convex) on particle classification at various loadings on a 75 mm hydrocyclone. It has been observed that both the curved conical designs (convex and concave) yield coarser cut sizes with relatively lower bypass compared to the standard design. Furthermore, as the solids loading

increases, the cut sizes also increase. When the loading increases from 4.14% to 30% for a given feed rate, the cut size increases from 35 μm to 87 μm for the convex design, while it ranges from 23 μm to 68 μm for the concave design and 19 μm to 57 μm for the standard design. Additionally, a novel hydrocyclone design with an elongated and slightly convex (n=1.4) cone has been suggested. This design exhibits enhanced sharpness, leading to reduced particle bypass into the underflow [31]. It is reported that a larger diameter convex design hydrocyclone (1000 mm) yields superior classification performance with a better sharpness index yielding lower cut sizes for all the densities studied than compared to the standard [13]. However, this observation contradicts the previously reported results of Ghodrat *et al.* [31], where coarser cut sizes are observed for convex designs on a smaller hydrocyclone.

Li *et al.* studied numerically a novel hydrocyclone with bisymmetric involute inlets and a parabolic cone, comparing it with standard single tangential, involute, and bisymmetric tangential inlet designs. The novel design showed superior separation performance, benefiting from the doubled feed input [120]. Jiang *et al.* conducted experiments comparing particle misplacement in overflow and underflow using a new compound curve conical design hydrocyclone versus a standard straight cone design in a 50 mm diameter cyclone. They have explored the effects of apex diameter, solids loadings (<20%), and feed pressure. Results showed that apex diameter significantly impacted cut size and solids bypass. Increasing apex diameter from 6 mm to 10 mm decreased cut size from 40 μm to 18 μm and raised bypass from 8% to 22%. Feed pressure and loading had minor effects on cut size and bypass [34].

2.5 Effect of roughness in gas cyclone and hydrocyclones

2.5.1 Roughness studies in gas cyclones

Wall roughness, an inevitable feature of industrial cyclones due to operational wear, has long been a subject of investigation for its influence on gas cyclone performance. Initial attempts to incorporate surface roughness into empirical models considered factors such as friction factor and solids loading, aiming to assess its impact on tangential velocities, pressure drop, and collection efficiency [121, 122]. It has been demonstrated by CFD analysis that variations in surface-wall roughness impact significantly tangential velocity, vortex length, and pressure drop in gas cyclones, ultimately affecting separation efficiency [123–125]. Moreover, Zhou *et al.* highlighted the critical value of wall roughness, where deviations above or below this threshold adversely influence total separation efficiency. Zhou *et al.* [127] experimentally and numerically studied the effect of surface wall roughness in swirling gas-particle flows. It is observed that the mean and fluctuating components of tangential velocities are dampened due to wall roughness.

Recent studies have increasingly focused on the impact of surface wall roughness in specific gas cyclone components, such as the vortex finder and cone walls [128–130]. Zhou *et al.* [128] demonstrated that increased roughness on the outer surface of the vortex finder leads to a rise in the average diameter of deposited particles. Interestingly, the effect of cone wall roughness on cut-off diameter varies with the number of inlet configurations, while roughness increases the cut size diameter in single-inlet cyclones, reverse trends are observed in two- and three-inlet designs [129]. Further analyses have extended this work by examining non-uniform roughness, where cyclone walls are divided into sections with varying roughness levels. These studies reveal that although rough-walled gas cyclones generally exhibit increased cut size compared to smooth designs, specific roughness distributions can enhance classification sharpness compared to the smooth cyclone [130].

2.5.2 Roughness studies in hydrocyclones

In prior research on hydrocyclones, the focus has predominantly been on understanding the impacts of design geometry and operational parameters on key performance metrics such as cut size, recovery, separation efficiency, pressure, and capacity. However, these studies typically operate under the assumption of smooth wall surfaces, overlooking the changing internal wall surface roughness due to wear during operation. Despite its significant influence on the hydrocyclone's flow field, wall roughness effects have not been studied comprehensively.

Fontein *et al.* first documented the influence of wall roughness on the reduction in tangential velocities and pressure drop. In his study involving 30 mm diameter hydrocyclones, compared the smooth cyclone with an artificially roughened cyclone (roughness height parameter (ks) = 110-150 microns). It was observed that, for a constant pressure drop the flow rate increased from 13.2 lpm to 18.8 lpm with an increase in underflow solids recovery from 10.4% to 24.3% [131]. Bradley reported that no differences were observed between 'machined' and 'highly polished' hydrocyclones. This finding suggests that wall roughness must surpass a certain threshold to have a significant effect on cyclone performance [104]. Zhao *et al.* studied the effect of surface wall roughness in hydrocyclones under equal flow rate and equal inlet pressure conditions. Their CFD model was validated experimentally on a hydrocyclone with a 150 mm diameter and a roughness height of 117 microns. It is reported that equal pressure conditions can provide superior separation results with higher capacity than equal flow rate conditions. However, the roughness adversely affects the separation and flow field in both cases [132]. Hou *et al.* studied the effect of wall roughness on a flat-bottom 200 mm cylindrical hydrocyclone using CFD simulations. It was observed that as the wall structure changes from smooth to rough-wall, with a roughness height of 100 microns, the fines bypass increases from 9 to

12%, making the cut size coarser, from 77 to 88 microns [114].

Though surface roughness in hydrocyclones has not been explored extensively, it has been well-researched in gas cyclones. The insights gained from studying surface roughness effects in gas cyclones are particularly valuable, as they can be applied to hydrocyclones due to the similarities in their flow patterns and particle separation mechanisms.

2.6 Research Gaps

A consolidated chart of throughput rate (kg/h) vs particle cut size ie., d_{50} (μm) was prepared by including all the above-discussed types of dry classifiers available in the literature; as shown in Figure 2.16. This chart helps in selecting the equipment that can be deployed for the process requirements in dry mineral processing circuits for classification. In Figure 2.16 each classifier is identified with an abbreviated code for clarity and their full names are given in the legend.

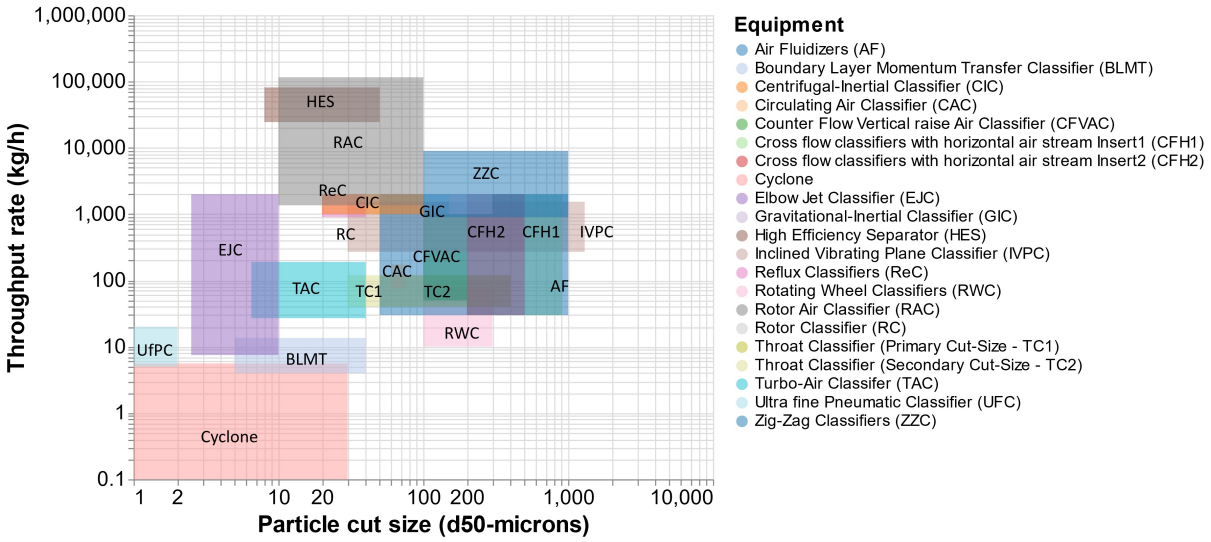


Figure 2.16: Compounded chart depicting all the dry classifiers discussed above

Selection from overlapping technologies: It is observed from Figure 2.16 there are many competing equipment of both across and within different class of classifiers that can be deployed for a given task. Hence selection of the right equipment to be deployed requires taking various process and operational parameters into consideration.

From Figure 2.16 it is understood that the majority of the classifiers fall under centrifugal classification technology. Figure 2.17 shows all the centrifugal classifiers and also highlights the three technology gaps which are further discussed below.

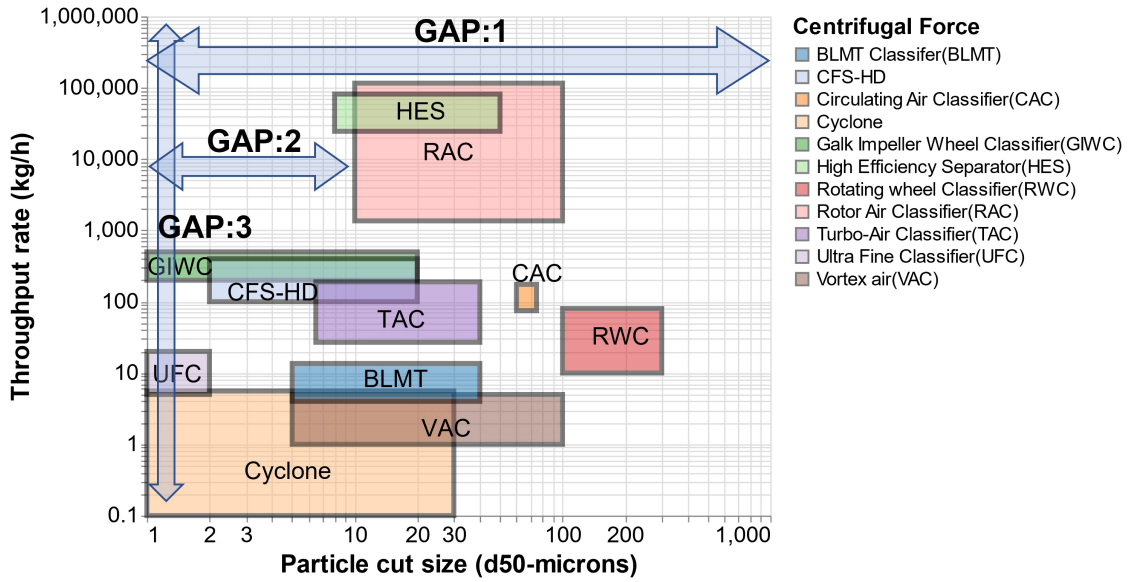


Figure 2.17: A research contour plot highlighting the gaps in centrifugal air classifiers

- Gap 1: Higher throughput devices that can adapt and operate over a broad range of cut size with high sharpness.
- Gap 2: Fine particle high throughput classification devices which can efficiently classify sizes $\leqslant 10\ \mu m$. As the particle becomes finer (ie., $\leqslant 10\ \mu m$) it is challenging to efficiently disperse the particles in the gas medium, hence an efficient solids dispersion mechanism that can handle larger throughput has to design.
- Gap 3: Particle classifier to separate sub-micron size particles which can scale the classification process for varied throughput rates
- Some potential research directions are outlined below.
  - Design modifications to handle the higher throughput rates.
  - Design changes which result in lower pressure drop and efficient performance.
  - Design modifications for coarser particles and tight size classification.

2.7 Summary and Thesis Objectives

In this review chapter, we have discussed the various dry classification equipment and their modes of operation and the research progress to date. A new graphical illustration of throughput rate vs cut size identifies three major gaps in the centrifugal classifiers. Due to its simple construction and operation, there is an opportunity for research on gas cyclones to extend the particle separation characteristics from separator to classifier.

The literature highlights that conic curvature in hydrocyclones significantly affects particle classification, with coarser cut sizes for both convex and concave shapes. Conic curvature also influences particle misplacement, particularly bypass, but most studies rely

on CFD simulations without experimental validation. In gas cyclones studies related to conic curvature are very few and limited to CFD analysis. Furthermore, while surface-wall roughness is common across these classifiers; it remains an under-researched topic in the existing literature.

This research addresses gaps by combining CFD analysis with experimental validation using 3D-printed gas cyclone and hydrocyclone designs.

To achieve these goals, the objectives of this thesis are as follows:

- Perform CFD analysis on gas cyclones to understand the effect of conic curvature on the particle classification, and explore its interaction effects with other parameters using response surface methodology.
- Experimentally validate the trends observed in the gas cyclone and further investigate the combined effects of surface-wall roughness and conic design.
- Extend the findings to hydrocyclones; Study the effect of conic curvature on the classification performance in hydrocyclones through CFD simulations and experiments.
- Understand the effect of surface-wall roughness and its interplay on conic design in hydrocyclones using both CFD simulations and experiments.

Chapter 3

Design of Parabolic Conic Gas Cyclones for Coarse Particle Classification: A CFD Study with Response Surface Methodology

3.1 Background . . . 41
3.2 CFD Modelling Methodology . . . 42
3.2.1 Modelling of airflow and selection of turbulence model . . . 42
3.2.2 Modelling of particle motion . . . 43
3.2.3 Geometry and Boundary conditions . . . 45
3.2.4 Grid Independency and Model Validation . . . 47
3.3 Response Surface Methodology: Theory . . . 49
3.3.1 Design of Experiments: . . . 49
3.3.2 Variables and Responses . . . 50
3.3.3 Response Surface Methodology Model . . . 54
3.4 Results and Discussion . . . 54
3.4.1 CFD Analysis: Standard design model validation . . . 54
3.4.2 CFD analysis of parabolic designs . . . 57
3.4.2.1 Axial Velocity . . . 58
3.4.2.2 Tangential Velocity . . . 59
3.4.2.3 Static Pressure . . . 59
3.4.2.4 Particle Separation Characteristics . . . 61
3.4.3 Response Surface Methodology: Results . . . 65
3.4.3.1 Analysis of Variance . . . 65
3.4.3.2 Analysis of Responses . . . 69

3.4.3.3 Monte Carlo Simulations 69
3.5 Summary 72

Chapter Introduction

This chapter investigates the influence of conic curvature, ranging from parabolic concave to convex designs, on the performance of gas cyclones. Computational Fluid Dynamics (CFD) and Response Surface Methodology (RSM) are employed to optimize key performance parameters such as particle cut size and sharpness of separation.

The chapter begins with a brief review of the reason for choosing to investigating curved cyclone designs. This is followed by Section 3.2 which introduces the CFD modeling methodology, which details the selection of turbulence models, particle motion modeling approaches, and boundary condition specifications. To ensure simulation reliability, grid independency studies and model validation are presented in Section 3.2.4. Further, the Response Surface Methodology (RSM) is introduced as a statistical approach to evaluate the interaction between design variables and performance metrics.

Section 3.4 presents results and discussion, where the performance of the proposed parabolic cyclone designs is rigorously evaluated. Key findings from CFD simulations are presented, including analyses of axial and tangential velocity profiles, static pressure distributions, and particle separation characteristics. Additionally, RSM results are interpreted using Analysis of Variance (ANOVA) and Monte Carlo simulations to provide deeper insights into design trends in yielding sharper and coarser cut sizes.

This chapter serves as a foundation for understanding the interaction between conic curvature, fluid dynamics, and separation performance. It offers a detailed framework for combining CFD simulations and statistical methods to design and optimize gas cyclones for enhanced efficiency. The findings presented here contribute significantly to the broader objectives of this thesis, paving the way for further exploration in subsequent chapters.

The content of this chapter has been published in: A. K. Pukkella, J. Cilliers and K. Hadler, 'Design of parabolic conic gas cyclones for coarse particle classification: A cfd study with response surface methodology,' *Powder Technology*, vol. 433, p. 119 217, 2024. Minor modifications have been made to the original text to improve clarity and readability in this thesis.

3.1 Background

The literature on hydrocyclone studies, as reviewed in Chapter 2, extensively explored the impact of conic curvature on particle classification (Ghodrat *et al.* [31], Motin and Bénard [32], Vega-Garcia *et al.* [33] and Jiang *et al.* [133]). Ghodrat *et al.* [31] specifically noted that a higher degree of conic curvature leads to a coarser cut size for both convex and concave shapes. However, in the context of gas cyclones, despite Pandey and Brar [35] numerical investigation, there is a notable absence of further studies on the effect of

conic curvature in the literature. In this chapter, we aim to bridge this gap by exploring whether similar findings can be observed in the smaller scale of gas cyclones. Our focus is on a 31 mm diameter gas cyclone with pronounced conic curvatures, diverging from Pandey and Brar [35] investigation, which centered on larger gas cyclones (210 mm) with less pronounced curved conic sections. To assess the effect of conic curvature on particle classification in small-scale (31 mm) gas cyclones, we utilize experimental data reported by Xiang *et al.* [11] to validate our CFD model predictions. Subsequently, we analyze predictions based on parabolic concave and convex conic curvatures, comparing them to the standard design. Additionally, we construct an RSM model using a D-Optimal design to unravel the interaction effects between parameters. Exploring the design space through Monte Carlo simulations based on the RSM models provides further insights. It is noteworthy that literature indicates an increase in cut size with the diameter of the cyclone [134]. Therefore, the potential impact of the conic curvature observed in smaller gas cyclones is expected to have positive implications for large-scale industrial applications.

3.2 CFD Modelling Methodology

3.2.1 Modelling of airflow and selection of turbulence model

The swirling flow inside the cyclone is resolved using a CFD model. It is well known that turbulence models such as Reynolds Stress Model and Large Eddy Simulation (LES) models accurately capture the Rankine vortex flow and pressure drop inside the cyclone separator [135–137]. Though, the conventional Eddy Viscosity Models (EVM) such as $k-\epsilon$, RNG $k-\epsilon$, $k-\omega$ are computationally less expensive when compared to the Reynolds Stress Model, but are not suitable for systems having strong swirling flows and streamlined curvature. The conventional EVM models predicted an unrealistic distribution of axial and tangential velocities inside the cyclone flow domain [138, 139]. The limitations of the EVM-based models can be attributed to their inherent assumptions, notably their lack of response to rotation and streamline curvature effects, as well as their assumption of isotropic eddy viscosity [139].

Spalart and Shur [140] adapted the $k-\omega$ model to account for rotation and streamline curvature. Dhakal *et al.* [139] and Alahmadi and Nowakowski [141] evaluated this modified $k-\omega$ Shear Stress Transport model with Curvature Correction (SSTCC) for modeling cyclone separators. They reported that predictions from the $k-\omega$ SSTCC model closely agreed with predictions from the Reynolds Stress Model at a lower computational cost. In recent studies, researchers have successfully captured the swirling flow inside the cyclone using this turbulence model [142, 143]. Therefore, considering the robustness, accuracy, and computational cost we use the $k-\omega$ SSTCC turbulence model for all the simulations performed. We assumed that the particle concentration is dilute, hence gas-particle

interaction is captured using one-way coupling through discrete particle modeling.

For incompressible fluid flow, the equation of continuity and momentum is expressed as follows:

$$\frac{\partial \overline{u}_i}{\partial x_i} = 0 \tag{3.1}$$

$$\frac{\partial(\rho\overline{u}_i)}{\partial t} + \frac{\partial(\rho\overline{u}_i\overline{u}_j)}{\partial x_j} = -\frac{\partial p}{\partial x_i} + \frac{\partial \sigma_{ij}}{\partial x_j} - \frac{\partial \tau_{ij}^{sgs}}{\partial x_j} \tag{3.2}$$

$$\sigma_{ij} = \mu\left(\frac{\partial \overline{u}_i}{\partial x_j} + \frac{\partial \overline{u}_j}{\partial x_i}\right) - \frac{2}{3}\mu\frac{\partial \overline{u}_l}{\partial x_l}\delta_{ij} \tag{3.3}$$

$$\tau_{ij}^{sgs} = \overline{u_i u_j} - \overline{u}_i\overline{u}_j \tag{3.4}$$

where $\overline{u}_i$ is i^{th}-component of velocity, ρ is fluid density, μ is molecular viscosity, and p is pressure of the fluid. σ_{ij} is the stress tensor due to molecular viscosity and δ_{ij} is the Kronecker delta. Needless to say, i, j, k represent the cartesian coordinate indices, when used as subscripts the corresponding component of the vector.

$$\tau_{ij}^{sgs} - \frac{1}{3}\tau_{kk}\delta_{ij} = 2\mu_t\overline{S}_{ij} \tag{3.5}$$

where μ_t is subgrid-scale turbulent viscosity and $\overline{S}_{ij}$ is the rate of strain tensor for resolved scales defined as:

$$\overline{S}_{ij} = \frac{1}{2}\left(\frac{\partial \overline{u}_i}{\partial x_j} + \frac{\partial \overline{u}_j}{\partial x_i}\right) \tag{3.6}$$

The turbulent kinetic energy (k) and specific dissipation rate (ω) are given by the following equations:

$$\frac{\partial(\rho k)}{\partial t} + \frac{\partial(\rho k\overline{u}_i)}{\partial x_i} = \frac{\partial}{\partial x_j}\left(\left(\mu + \frac{\mu_t}{\sigma_k}\right)\frac{\partial k}{\partial x_j}\right) + \tilde{G_k} - Y_k + S_k \tag{3.7}$$

$$\frac{\partial(\rho\omega)}{\partial t} + \frac{\partial(\rho\omega\overline{u}_i)}{\partial x_i} = \frac{\partial}{\partial x_j}\left(\left(\mu + \frac{\mu_t}{\sigma_\omega}\right)\frac{\omega}{\partial x_j}\right) + \tilde{G_\omega} - Y_\omega + S_\omega \tag{3.8}$$

where σ_k and σ_ω are the turbulent Prandtl numbers for k and ω, respectively. The turbulent viscosity is given by μ_t, Further details of the modeling equations are provided in the appendix.

3.2.2 Modelling of particle motion

Lagrangian Particle Tracking (LPT) is used to predict the behavior of particles in a dilute system. The motion is determined by drag, gravitational, buoyancy, centrifugal, and other forces. The method is represented mathematically as follows:

$$\frac{d\vec{u_p}}{dt} = F_D(\vec{u} - \vec{u}_p) + \frac{\vec{g}(\rho_p - \rho)}{\rho_p} + F_x \tag{3.9}$$

where $\vec{u}_p$ represents the velocity of a particle, $\vec{u}$ the velocity of the fluid phase, ρ_p the particle density, and d_p the particle diameter. The term F_x encompasses any additional forces that may play a role in determining the particle motion. This could include the added mass force resulting from the relative acceleration of the particulate phase, pressure gradient force, Brownian motion, thermophoretic force, Saffman's lift force, and others. Song *et al.* [144] have investigated particle motion including these forces in gas cyclones, it was determined that the pressure gradient force and the added mass force were at least three orders of magnitude smaller than the dominant drag force. Similarly, the Saffman lift force was at least 15 orders of magnitude smaller. Hence, we neglect these forces in our study. Further, as the entire computational domain is at a constant temperature, thermophoretic forces are negligible under these conditions. The drag force is given by:

$$F_D = \frac{18\mu}{d_p^2 \rho_p} C_D \frac{Re_p}{24} \tag{3.10}$$

In the above equation, C_D is the drag coefficient and Re_p is the particle Reynolds number, defined as:

$$Re_p = \frac{\rho d_p \mid \vec{u}_p - \vec{u} \mid}{\mu} \tag{3.11}$$

The drag coefficient C_D for smooth spherical particles is a function of particle Reynolds number Re_p, given by with the following equation [145]:

$$C_D = a_1 + \frac{a_2}{Re_p} + \frac{a_3}{Re_p^2} \tag{3.12}$$

Here, a_1, a_2, and a_3 represent constants applicable across various ranges of particle Reynolds numbers. In turbulent flow conditions, the motion of particles is significantly impacted by fluctuating instantaneous velocities. The dispersal of particles, due to turbulence in the fluid phase, is tracked using a stochastic method known as the 'Discrete Random Walk' (DRW). Individual particle paths are obtained by integrating the trajectory equation using the instantaneous fluid velocity, $\overline{u} + u'(t)$. The DRW model specifically assumes that the fluctuating fluid velocities follow a Gaussian distribution. A characteristic fluctuating velocity can be represented by the following equation:

$$u_i^{'} = \xi \sqrt{2k/3} \tag{3.13}$$

where $u_i^{'}$ is the normally distributed random number and k is the turbulent kinetic energy. The DRW model in ANSYS FLUENT 2021 R1 was used in the current study.

3.2.3 Geometry and Boundary conditions

This study investigates the impact of conic section curvature on the classification performance in a gas cyclone. As a reference geometry, the 31 mm diameter gas cyclone design reported by Xiang *et al.* [11] is used. Figure 3.1a depicts the standard design of the cyclone geometry, which highlights all seven design parameters required for its construction, and Table3.1 lists the dimensions of each variable. The design equations required to construct the conic section geometries for the cyclone are given below. Figure 1b shows the conic profile shapes of the standard, parabolic convex, and parabolic concave shapes. It can be observed from Figure 3.1b that the profile shapes of the concave and convex structures are inverted mirror images of each other. Further, the final designs constructed for the CFD analysis, i.e., the standard design and the parabolic convex and concave shape structural designs as shown respectively in Figure 3.1. The lines L1, L2, and L3 highlighted in Figure 3.1a are created at heights of Y = 23 mm, 46 mm, and 60 mm when measured from the bottom of the cyclone to perform post-processing activities.

Design equations of conic curvatures:

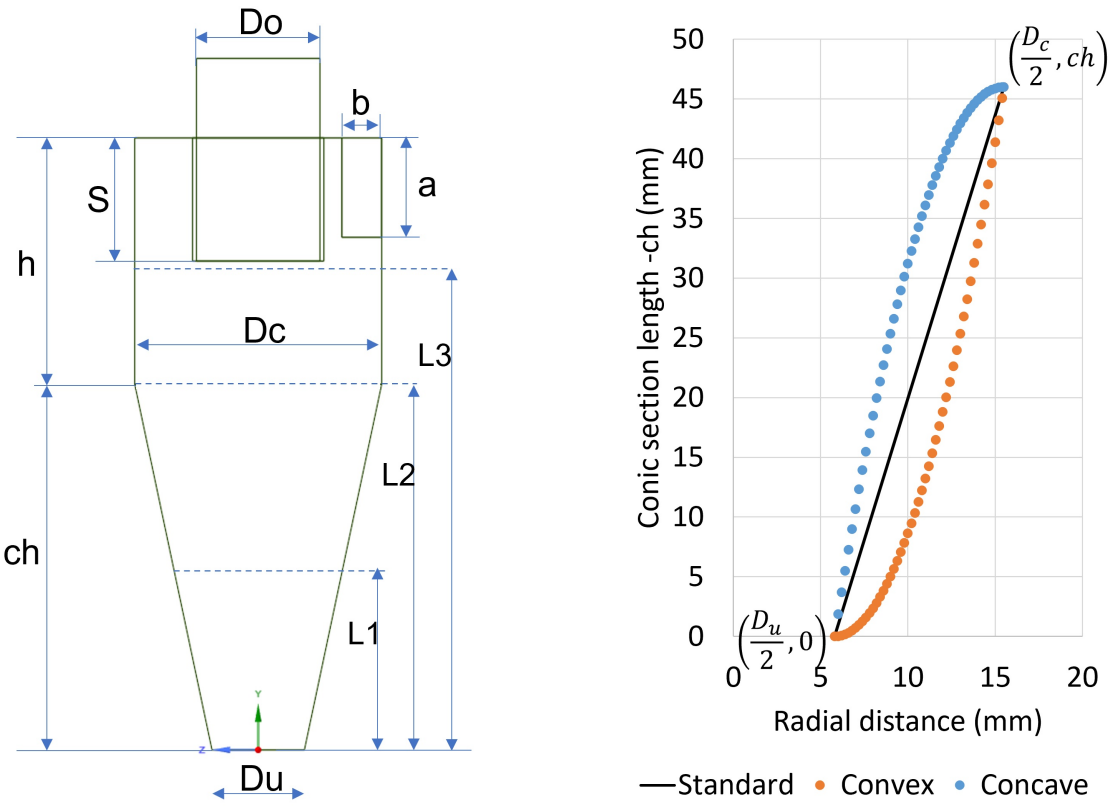
$$\begin{aligned}
&\text{Parabolic Convex Design} : (x-h)^2 = 4P(y-k), \text{ where P>0}; (h,k) = \left(\frac{Du}{2}, 0\right) \\
&\text{Parabolic Concave Design} : (x-h)^2 = 4P(y-k), \text{ where P<0}; (h,k) = \left(\frac{Dc}{2}, ch\right) \\
&\text{Standard Design: Straight line passing through } \left(\frac{Du}{2}, 0\right), \text{ and } \left(\frac{Dc}{2}, ch\right).
\end{aligned} \tag{3.14}$$

Where D_u, D_c, and ch are the bin diameter, cyclone diameter, and conic cylinder height.

Table 3.1: Geometric design parameters of the standard 31 mm diameter cyclone.

Design Variable (mm)	a	b	S	Do	Du	h	ch
Standard Design ([11])	5	12.5	15.5	15.5	11.6	31	46

The first objective is to validate the experimental particle separation reported by Xiang *et al.* for the standard design. Conducted CFD simulations for inlet air flow rates of 30, 40, 50, and 60 lpm. Despite the use of 'flow rate' in the text for consistency with experimental reports, it is important to clarify that the simulations were based on inlet velocity conditions. The inlet of the cyclone was modeled as a velocity inlet with uniform normal velocities of 8, 10.66, 13.33, and 16 m/s for their respective flow rates. The gas outlet was modeled as an outflow boundary condition, and all remaining surfaces as walls with no-slip boundary conditions. The density and dynamic viscosity of air was assumed to be 1.225 kg/m^3 and 1.8*$10^{-5} kg/(ms)$, respectively. To evaluate the particle separation characteristics, Discrete Phase Modeling (DPM) predictions were compared to the experimental grade efficiency curves. The particles were assumed to be spherical, mono-



(a) Standard cyclone geometry

(b) Conic profiles including parabolic convex and concave shapes

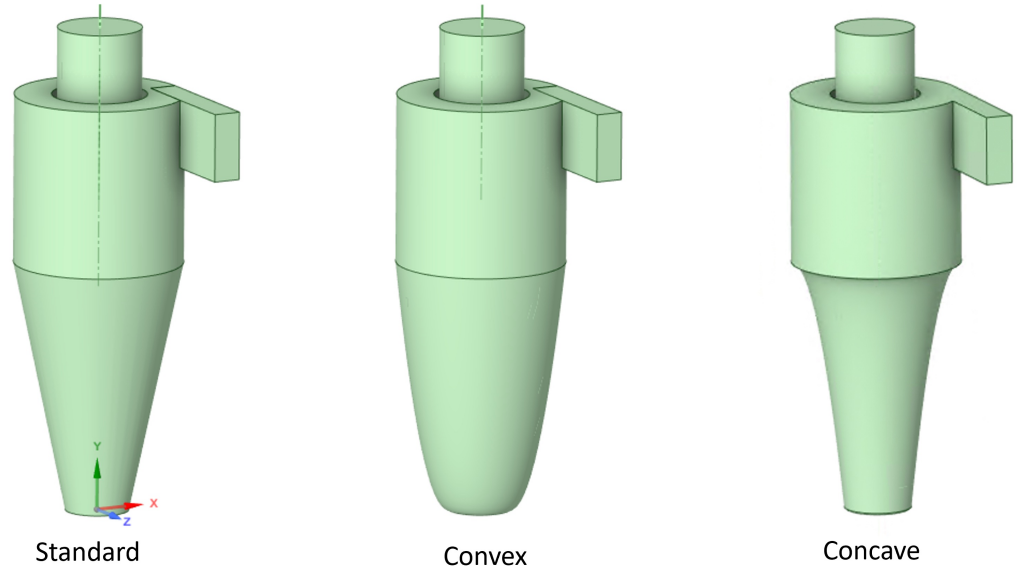


Figure 3.1: Geometrical design of cyclones under study

disperse, and have diameters ranging from 0.5-10 μm, with specific sizes reflecting the experimental particle sizes reported by Xiang *et al.* [11]. These sizes include 0.5, 0.8, 1.05, 1.53, 2, 2.5, 3.1, 4.18, 5.28, 6.18, and 8.09 microns, respectively. They were in a dilute regime with concentration ($\frac{\text{volume of particles}}{\text{volume of gas flow through}}$) $<10^{-6}$ and their density was set to 1055 kg/m^3 to mimic the density of the polystyrene latex beads (PSL) used in the experiments. An escape boundary condition was applied to the gas outlet, and a trap boundary condition was used to model the dust outlet. The collisions between the wall and particles were assumed to be perfectly elastic, with a coefficient of restitution of 1. Particle-particle collisions were neglected resulting from dilute particle concentrations. The separation efficiency was defined as the ratio of the number of particles trapped in the dust outlet to the number of particles released from the inlet.

To ensure robustness, a pressure-based coupled solver (PBCS) algorithm was used for pressure-velocity coupling, and the Quadratic Upstream Interpolation for Convective Kinetics (QUICK) scheme was selected for discretizing the momentum terms. The Pressure Staggered Option (PRESTO) pressure interpolation scheme was used to accurately capture the sharp pressure gradients in the high swirling flows. A second-order upwind discretization was used for both the turbulent kinetic energy and the specific dissipation rate. A time step of 10^{-4} s was used in all transient simulations. The convergence criteria for all scaled residuals were set at 10^{-5}.

3.2.4 Grid Independency and Model Validation

Meshing and Grid Independency

In this study, an unstructured hexahedral grid was generated using the blocking technique in ANSYS ICEM CFD. The mesh was refined near the walls for accurate capture of wall effects (Figure 3.2). While higher mesh density (number of cells) improves accuracy, it also increases computational cost. A grid independence test was conducted using four meshes (M1, M2, M3 and M4) with varying cell counts listed in Table 3.2. CFD simulations were performed with an inlet flow rate of 60 lpm, and the overall pressure drop was measured and recorded in Table 3.2. The radial profiles of axial and tangential velocities were also measured on the central plane at a height of Z = 46 mm from the bottom and are shown in Figure 3.2. Based on the observations reported in Figure 3.3 and Table 3.2, it was concluded that mesh M2 was optimal for capturing the swirling flows inside the cyclone with reasonable accuracy and producing grid-independent results. Thus, mesh M2 was selected for all further simulations and similar mesh densities were used for other design configurations.

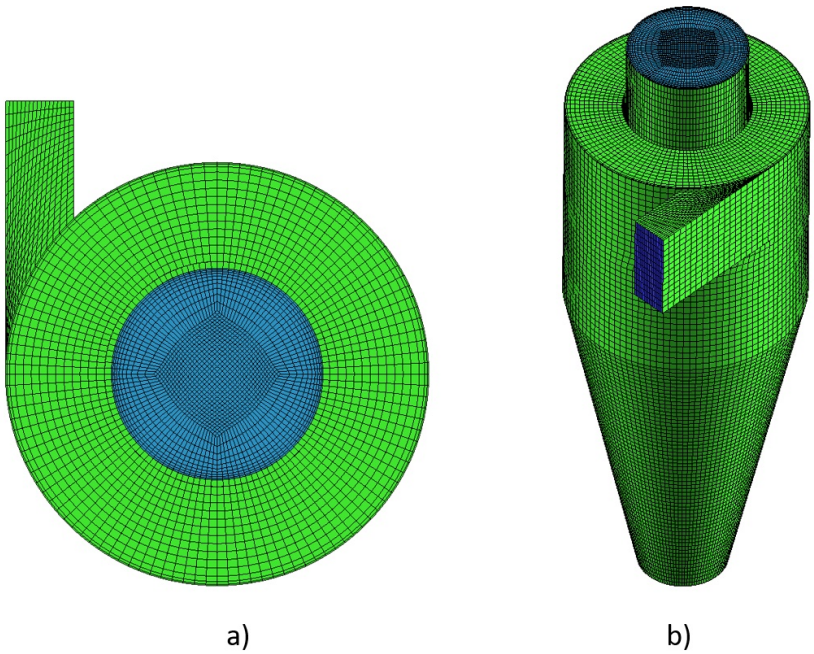


Figure 3.2: Hexahedral mesh for the standard design gas cyclone. a) Top view b) Isometric View

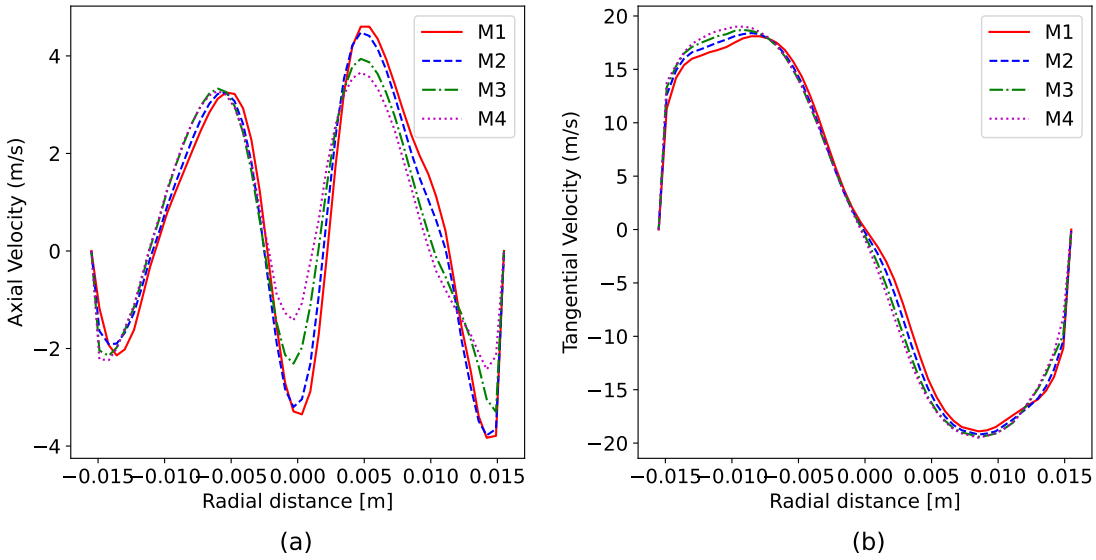


Figure 3.3: Variation of measured quantities on a centre-line (Height Z = 46 cm - measured from the bottom). a) Tangential Velocity b) Axial Velocity

Table 3.2: Grid independence analysis for an inlet flow rate of 60 lpm: Pressure drop as a function of grid refinement, compared to the experimentally reported value of 595 Pa.

Mesh Name	Number of Cells	Pressure Drop (Pa)
M1	966746	593
M2	703288	591
M3	502418	571
M4	308945	552

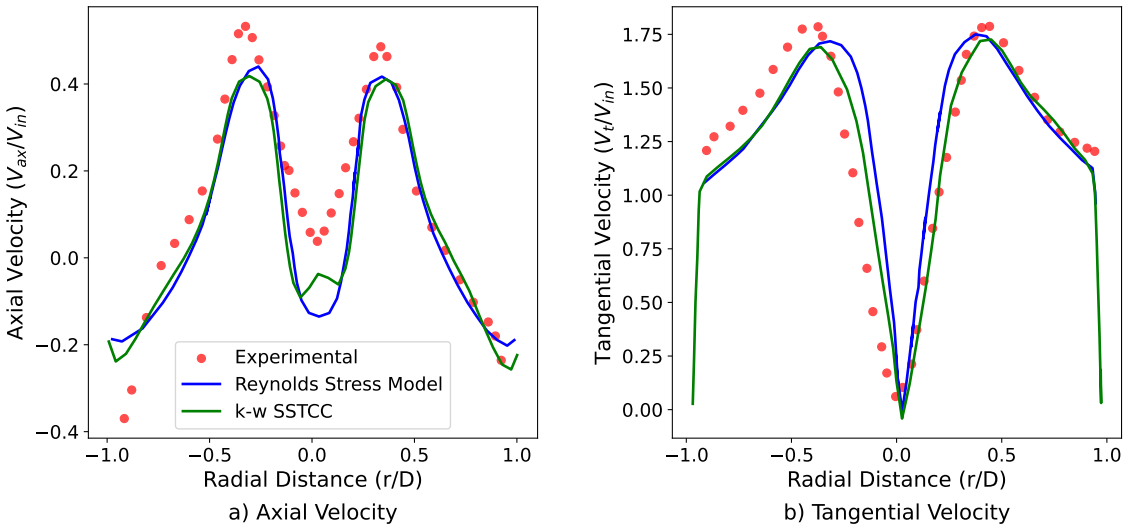


Figure 3.4: Comparison of the experimental LDA measurements of tangential and axial velocities Hoekstra (2000), with the CFD predictions of Reynolds stress model (RSM) model and SST $k\omega(cc)$ model. (The radial distance is scaled by the cyclone radius and the axial and tangential velocity are scaled by the inlet velocity.)

Model Validation

To validate the results obtained from the $k-\omega$ (SSTCC) turbulence model, we compared them with experimental measurements by Hoekstra [146]. These measurements were obtained using Laser Doppler Anemometry (LDA) on a stairmand gas cyclone design. We compared our predictions with those from the well-established Reynolds Stress Model and the experimental measurements. Figure 3.4 shows the comparison of the radial profiles of axial and tangential velocity measured at the location of z=94.5 cm from the bottom of the cyclone (with D_o/D_c = 0.5) as obtained from the LDA measurements and the predictions from the Reynolds Stress Model and $k-\omega$ (SSTCC) models. The predictions from both models are in good agreement with the experimental results and follow similar trends. Hence, considering the accuracy, robustness, and computational cost, we use the $k-\omega$ (SSTCC) turbulence model for all the simulations in this study.

3.3 Response Surface Methodology: Theory

3.3.1 Design of Experiments:

Experiments are designed to understand the influence of controlled variables (X) on the quantity of interest (Y). A systematic Design of Experiments (DOE) provides a robust framework to realize the response and interaction effects through a multivariate parametric study [147]. DOE provides the optimized factors (X_i) to be selected from the design space based on statistical criteria. All the responses (Y_i) are tabulated for the DOE experiment factors (X_i).

Various classical DOE methods are available to construct the sampling design space such as the Full/Fractional factorial method, Box-Behnken designs (BBD), Central Composite Design (CCD), Orthogonal arrays, etc, [101]. These methods are widely used in the industry for well-posed problems [148]. However, in special scenarios like; a limited number of experiments can only be performed due to practical constraints, too many factors or levels, and the presence of categorical factors (discrete variables) makes the classical designs fail to apply. To circumvent these challenges, Atkinson and Donev [149] have developed optimal design methods (classed by letter) based on several statistical criteria.

The optimal designs build a minimum and optimal set of experiments to be performed to fit a model by minimizing the variance of the β estimators in an information matrix (XX^T) using an iterative search algorithm. Here, X is the design matrix with p rows; each row indicates the experimental run performed in the design and q columns represent the model coefficients (i.e., β estimators) for that experimental run in the model fit. Optimal designs are flexible and can be augmented by adding design points to further improve the fit. The D-Optimal design was used in the current study as it is widely used for industrial problems [150, 151]. D-optimal design minimizes the overall variance of the estimated regression coefficients by maximizing the determinant of the information matrix (XX^T).

3.3.2 Variables and Responses

A total of 8 quantitative independent variables (numeric) including the seven geometric variables identified in Figure 3.1, as well as inlet velocity, and an additional one qualitative variable (i.e., categorical variable), the type of cyclone design were chosen to perform the optimization study. The lower and upper limits of each variable are listed in Table 3.3. It has to be noted that these factors are scaled with cyclone diameter (D_c). The response variables (Y) of interest are cut size (D_{50}) and the sharpness of separation. To determine the cut size diameters, we read the values directly from the separation efficiency curves. Specifically, the cut size corresponds to the particle diameter at which the separation efficiency value equals 50%. Similarly, the metric sharpness, which indicates the quality of separation is determined by the ratio of D_{25} to D_{75}. Where the parameters D_{25} and D_{75} correspond to respective particle diameters against the particle separation values of 25% and 75% [152].

The D-Optimal design can consider both Quantitative (Numerical) and Qualitative (Categorical) variables in the design. Overall, we have performed 27 CFD simulations for each category to build the model, i.e. Standard-27, Concave-27, and Convex-27 simulations. The list containing the factors for all 81 design points generated by the D-optimal design in the DesignExpert tool is listed in Table 3.4. Further, we performed CFD simulations and particle tracking studies to quantify the response variables (cut size and sharpness). The final data containing the factors and responses are subjected to an RSM Model

Table 3.3: The high and low-level settings of the factors along with categoric and response variables defined in the DOE study

Quantitative Variables:	**8 Numeric**	
Independent Variables (X)	**Low**	**High**
Underflow Diameter (Du/Dc = A)	0.2	0.6
Gas Outlet Diameter (Do/Dc = B)	0.25	0.75
Inlet Height (a/Dc = C)	0.2	0.7
Inlet width (b/Dc = D)	0.1	0.3
Vortex finder height (S/Dc = E)	0.3	1
Cylinder height (h/Dc = F)	0.5	1.5
Cone height (ch/Dc = G)	0.5	2.5
Inlet velocity (V-$\frac{m}{s^2}$ = H)	4	16
Qualitative Variables:	**1 Categoric**	
Design	Standard	
	Concave	
	Convex	
Response Variables (Y):	**2**	
Cut-point Diameter (D_{50} microns) (Y1)		
Sharpness (Y2)		

to fit models for cut size and sharpness of classification.

Table 3.4: List of simulations performed for the input design space and their corresponding output response variables.

Run	**Factors**									**Response 1** **Cutsize** (μm)	**Response 2** **Sharpness**
	A: Du	**B: Do**	**C: a**	**D: b**	**E: S**	**F: h**	**G: ch**	**H: V**	**J: Design**		
1	0.2	0.25	0.2	0.3	1	0.5	2.5	4	Concave	4.8	0.8019
2	0.2	0.75	0.2	0.2	0.3	0.5	2.5	16	Concave	3.8	0.7771
3	0.6	0.75	0.7	0.3	1	1.5	1.5	4	Convex	8	0.4231
4	0.2	0.75	0.7	0.3	0.3	1	2.5	4	Convex	12.5	0.2500
5	0.3	0.375	0.575	0.15	0.475	0.75	1	13	Concave	1.93	0.7072
6	0.2	0.25	0.7	0.1	0.3	1.5	2.5	4	Convex	5.8	0.7536
7	0.2	0.75	0.45	0.1	0.3	0.5	0.5	4	Concave	8.5	0.6075
8	0.6	0.25	0.2	0.1	0.3	1.5	0.5	4	Standard	8.1	0.5044
9	0.2	0.25	0.7	0.1	0.3	1.5	2.5	4	Standard	5.65	0.7813
10	0.6	0.25	0.7	0.3	0.3	1.5	2.5	4	Convex	5.1	0.7826
11	0.2	0.5	0.7	0.1	0.3	1.5	2.5	16	Convex	2.3	0.7170

Run	Factors									Response 1	Response 2
	A: Du	B: Do	C: a	D: b	E: S	F: h	G: ch	H: V	J: Design	Cutsize (μm)	Sharpness
12	0.3	0.375	0.575	0.25	0.825	1.25	1	13	Concave	1.87	0.6828
13	0.3	0.625	0.325	0.25	0.825	1.25	2	10	Standard	4.4	0.7755
14	0.5	0.375	0.325	0.25	0.475	0.75	2	13	Standard	2.75	0.7188
15	0.6	0.75	0.2	0.1	0.65	1.5	0.5	16	Convex		0.6238
16	0.6	0.75	0.45	0.1	1	1.5	2.5	4	Concave	9.5	0.6967
17	0.5	0.375	0.575	0.15	0.825	1.25	1.5	7	Convex	1.7	0.7568
18	0.4	0.625	0.325	0.25	0.825	1.25	2	7	Standard	4.9	0.8077
19	0.6	0.25	0.7	0.2	1	0.5	2.5	4	Concave	5.05	0.8036
20	0.6	0.5	0.7	0.1	1	1.5	0.5	4	Convex	6.75	0.7097
21	0.2	0.25	0.7	0.1	1	1.5	1.5	4	Convex	6.15	0.7103
22	0.2	0.75	0.2	0.1	0.3	1.5	0.5	4	Concave	12	0.5167
23	0.3	0.625	0.325	0.15	0.475	0.75	2	7	Concave	4.6	0.7379
24	0.3	0.625	0.325	0.25	0.475	1.25	1	13	Concave	2.05	0.7390
25	0.3	0.625	0.575	0.25	0.825	1	1	13	Standard	3.3	0.5926
26	0.4	0.75	0.2	0.1	1	1.5	2.5	16	Standard	5.3	0.7627
27	0.5	0.375	0.325	0.25	0.65	0.75	1	13	Concave	2	0.7623
28	0.6	0.75	0.2	0.1	0.3	1.5	1.5	16	Concave	4.5	0.6174
29	0.2	0.75	0.45	0.1	1	1.5	2.5	4	Convex	9.2	0.5280
30	0.5	0.375	0.325	0.25	0.825	1.25	1	7	Concave	4.7	0.8465
31	0.6	0.25	0.7	0.3	1	1	0.5	4	Standard	3.75	0.5385
32	0.2	0.5	0.7	0.1	0.3	1.5	2.5	16	Convex	2.6	0.8182
33	0.2	0.75	0.2	0.3	0.65	0.5	0.5	16	Concave	3.75	0.4870
34	0.6	0.75	0.7	0.1	0.3	1.5	0.5	10	Standard	4	0.3929
35	0.6	0.75	0.7	0.3	0.3	1.5	0.5	16	Concave	5.5	0.2426
36	0.5	0.625	0.325	0.25	0.825	1.25	1.5	13	Convex	2.2	0.6981
37	0.6	0.25	0.7	0.3	0.65	0.5	2.5	4	Concave	4.75	0.8000
38	0.6	0.75	0.2	0.1	1	0.5	0.5	4	Standard	12	0.5987
39	0.2	0.75	0.2	0.3	0.3	1.5	1.5	4	Concave	10.5	0.3684
40	0.2	0.75	0.7	0.3	0.65	1.5	0.5	4	Convex	8.32	0.4601
41	0.2	0.25	0.2	0.3	0.3	1.5	0.5	4	Convex	5.25	0.7966

Run	Factors									Response 1	Response 2
	A: Du	B: Do	C: a	D: b	E: S	F: h	G: ch	H: V	J: Design	Cutsize (μm)	Sharpness
42	0.6	0.75	0.45	0.1	0.3	0.5	2.5	16	Standard	2.8	0.8254
43	0.5	0.375	0.45	0.15	0.475	0.75	2	7	Convex	5	0.7328
44	0.3	0.625	0.575	0.15	0.825	1	1	13	Convex	2.15	0.7500
45	0.2	0.25	0.2	0.1	1	0.5	2.5	10	Convex	15	0.6667
46	0.2	0.75	0.7	0.1	1	0.5	2.5	10	Convex	4.8	0.8654
47	0.6	0.25	0.7	0.3	1	1.5	2.5	16	Concave	1.73	0.7895
48	0.2	0.75	0.2	0.1	0.3	1.5	0.5	4	Standard	11.5	0.3428
49	0.4	0.375	0.325	0.25	0.475	0.75	2	13	Standard	2.7	0.8276
50	0.2	0.25	0.7	0.3	0.3	0.5	0.5	4	Standard	3.5	0.4381
51	0.6	0.25	0.2	0.1	0.3	1.5	0.5	4	Standard	7.25	0.3364
52	0.5	0.625	0.575	0.15	0.475	0.75	1.5	13	Standard	1.85	0.7727
53	0.2	0.75	0.2	0.3	0.3	0.5	0.5	10	Concave	9	0.3378
54	0.5	0.375	0.325	0.25	0.475	0.75	1	13	Convex	1.65	0.7222
55	0.3	0.375	0.575	0.2	0.825	0.75	2	13	Convex	2.6	0.8036
56	0.6	0.75	0.2	0.1	1	0.5	0.5	4	Standard	11	0.3750
57	0.6	0.5	0.2	0.3	1	0.5	2.5	4	Convex	8	0.6915
58	0.4	0.75	0.2	0.3	0.3	0.5	0.5	4	Standard	10	0.4580
59	0.3	0.375	0.575	0.15	0.475	1.25	1	10	Convex	2	0.7556
60	0.5	0.5	0.575	0.15	0.825	0.75	2	7	Concave	3.8	0.7791
61	0.5	0.375	0.325	0.15	0.475	0.75	1.5	13	Standard	1.7	0.6500
62	0.2	0.25	0.2	0.1	1	1.5	0.5	16	Standard	2.25	0.8320
63	0.5	0.5	0.325	0.15	0.475	0.75	2	13	Concave	1.75	0.6829
64	0.6	0.75	0.7	0.3	1	0.5	1.5	16	Standard	3.5	0.2563
65	0.6	0.75	0.7	0.3	0.3	1.5	0.5	16	Concave	5.4	0.3840
66	0.2	0.75	0.7	0.1	1	0.5	2.5	10	Convex	5	0.7500
67	0.6	0.5	0.2	0.3	1	0.5	2.5	4	Convex	8	0.6913
68	0.3	0.625	0.325	0.25	0.825	0.75	2	13	Standard	2.72	0.7372
69	0.4	0.5	0.45	0.2	0.475	1	1.5	10	Convex	3.5	0.7500
70	0.5	0.625	0.325	0.25	0.825	1.25	1	7	Concave	4.85	0.7963
71	0.2	0.25	0.2	0.1	0.65	0.5	0.5	4	Standard	5.65	0.7308

Run	Factors									Response 1	Response 2
	A: Du	B: Do	C: a	D: b	E: S	F: h	G: ch	H: V	J: Design	Cutsize (μm)	Sharpness
72	0.6	0.25	0.7	0.3	1	1	0.5	4	Concave		0.5909
73	0.3	0.625	0.575	0.25	0.825	0.75	1	7	Convex	4	0.6373
74	0.6	0.75	0.7	0.3	0.3	0.5	2.5	4	Standard	9	0.2778
75	0.5	0.625	0.575	0.15	0.825	1	2	13	Convex	2.15	0.7292
76	0.4	0.5	0.45	0.2	0.65	1	1	10	Standard	2.75	0.8000
77	0.3	0.375	0.575	0.2	0.825	0.75	1	13	Standard	2.68	0.7516
78	0.2	0.75	0.7	0.1	0.65	1.5	0.5	4	Concave	8.1	0.7135
79	0.3	0.5	0.575	0.25	0.825	0.75	1	13	Standard	2.8	0.6973
80	0.3	0.5	0.575	0.15	0.825	1.25	2	7	Concave	4.1	0.5893
81	0.4	0.25	0.2	0.3	1	0.5	0.5	16	Concave	1.52	0.7143

3.3.3 Response Surface Methodology Model

An RSM Model is built by fitting a second-order polynomial function between the independent variables X_i and dependent responses (Y_i) as follows:

$$Y = \beta_0 + \sum_{i=1}^{n} \beta_i X_i + \sum_{i=1}^{n} \beta_{ii} X_i^2 + \sum_{i} \beta_{ij} X_i X_j + e \tag{3.15}$$

where β_0, β_i, β_{ii}, and β_{ij} are the regression coefficient terms of the model for the constant term, linear effects, quadratic effects, and the interaction effects between the factors. While *e* accounts for both measurement error and lack of fit response error. The fitness functions for response variables are obtained based on mathematical statistics and least squares error methods.

3.4 Results and Discussion

3.4.1 CFD Analysis: Standard design model validation

Initially, the flow parameters, including pressure distribution, axial and tangential velocity radial profiles, were analyzed to understand the flow behavior inside the gas cyclone. Subsequently, the particle separation characteristics of a standard design cyclone were validated at different flow rates reported in the literature by Xiang *et al.* [11].

In addition to the gravitational force, axial velocities are responsible for conveying particles into the collection bin, while tangential velocities directly impart centrifugal

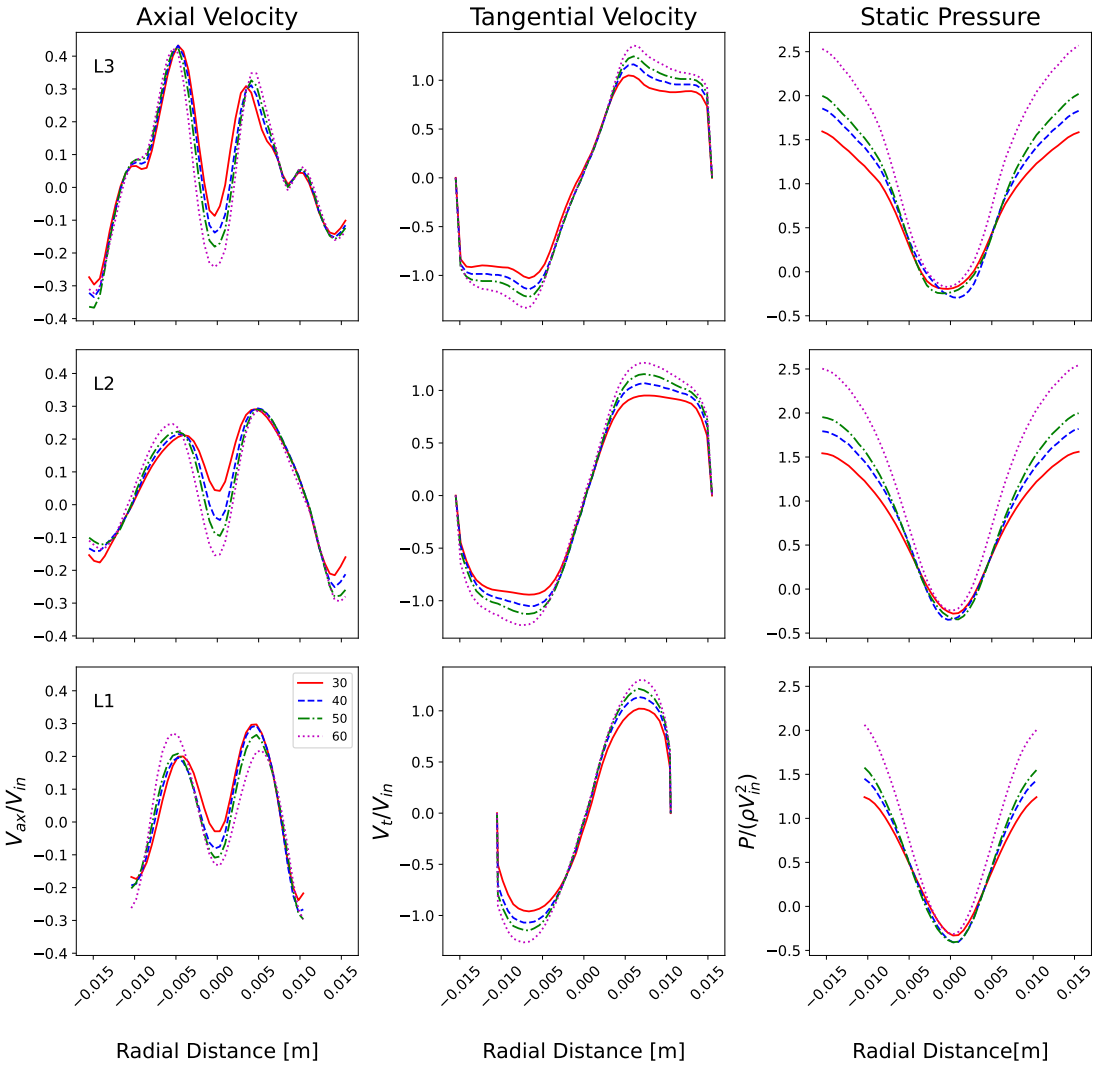


Figure 3.5: CFD analysis of standard design: Radial profiles of scaled axial, tangential velocities, and static pressure measured at three locations (L1, L2, and L3) as a function of inlet flowrate.

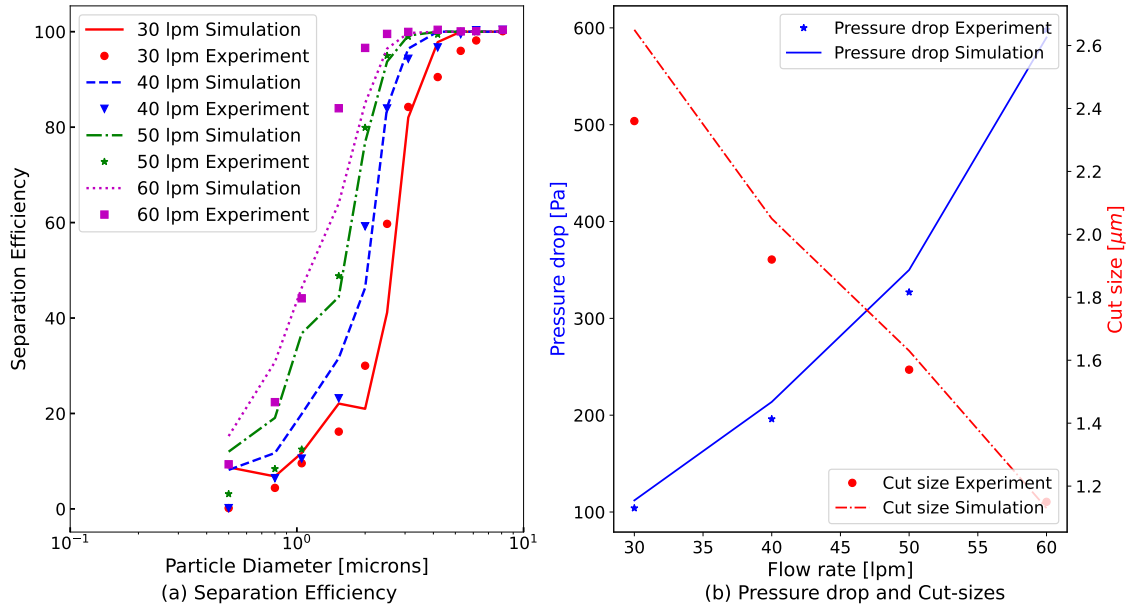


Figure 3.6: CFD validation of experimental particle classification studies for flowrates of 30, 40, 50, and 60 lpm, respectively in the standard design [Experimental data source: Xiang *et al.* [11]].

forces that are necessary for separating the particles from the gas medium [153]. Figure 3.5 displays the radial profiles of time-averaged axial and tangential velocity at three axial positions (L1, L2, and L3, Figure 3.1) for all the flow rates under study. The tangential and axial velocities are scaled with the inlet velocities.

The axial velocity profiles in Figure 3.5 resemble the standard inverted 'W' shape. The dip in the profile occurs near the central axis of the cyclone body. The swirling motion inside the cyclone generates a strong radial pressure gradient with a low-pressure region near the core and high pressure towards the outer wall. Due to frictional losses, the exit gas swirl intensity attenuates in the vortex finder, leading to the formation of an adverse pressure gradient axially in the inner core. This gradient drives less swirling fluid from the exit to the core. Although the swirl attenuation occurs in the vortex finder, the reverse flow is dominant across the cyclone near the central core [154]. This explains the presence of a dip at the center of the axial velocity profiles in Figure 3.5. Further, the dip at the center increases with increasing flow rate at all axial locations. The extent of the dip in axial velocity profiles is more significant in the cylindrical body at L3, closer to the vortex finder than in the conic section location (L1). Negative axial velocities towards the walls help slide particles into the collection bin.

The simulated tangential velocities exhibit a standard Rankine vortex nature, with the inner core having solid-body-like rotation and outer free vortex flow. The tangential velocity profiles in the inner core remain unchanged with the flow rate and preserve their shape at different sections. However, there is a sharp drop in velocity near the wall. These trends have been reported elsewhere in the literature [88, 155]. It is also observed

that maximum tangential velocities appear at the boundary between the inner and outer vortex zones and increase with an increase in flow rate. The tangential velocity profiles indicate that the inner core occupies a larger portion in the conic section (L1) than in the cylindrical body (L2 and L3).

Similarly, the static pressure radial profiles are scaled with the kinetic energy per volume of flow to represent a form similar to the Euler number (Eu), which corresponds to energy losses in the flow. It is observed from the Figure 3.5 static pressure profiles at locations L1, L2, and L3 that the pressure gradient is more predominant in the radial direction than in the axial direction for all the flowrates under study. The pressure distribution profiles in the cylindrical section are almost constant as there is an insignificant variation in pressure distribution profiles between L3 and L2 locations. The lowest values of pressure are reported in the center-core region and increase its values towards the wall of the cyclone, this behavior is more pronounced as the flowrate increases. Further, the overall pressure drop between the simulated and experimentally reported values is discussed below.

Figure 3.6a compares the simulated separation efficiency of a standard 31mm diameter cyclone with the experimentally reported values by Xiang *et al.* [11]. The simulation predictions are in close agreement with the experimental values, and it is observed that as the flow rate increases, the separation efficiency curve shifts to the left, indicating smaller cut sizes due to increased centrifugal forces acting on the particles. Additionally, Figure 3.6b compares the trends of overall pressure drop and cut size as a function of the inlet air flow rate, with the experimental values. The overall pressure drop is observed to increase with an increase in flow rate. For a flowrate of 30 lpm the pressure drop is observed to be 109.3 Pa and it increases to 590.1 Pa for a flow rate of 60 lpm. Whereas the cut size increases from 1.25 μm to 2.25 μm as the flow rate decreases from 60 lpm to 30 lpm. As observed from Figure 3.6b both the cut size and pressure drop are in agreement with experimental observations. In the later part of the work, we will provide a detailed discussion on the comparison of cut sizes and pressure drop between the standard design and parabolic designs.

In conclusion, the CFD model developed captures the flow field and particle separation characteristics accurately and can be used to study convex and concave conic cyclones.

3.4.2 CFD analysis of parabolic designs

The flow field inside the parabolic designs are compared to the standard design. The time-averaged contour plots and radial profiles of axial velocity, tangential velocity, and pressure distribution inside the flow domain are compared at three axial locations L1, L2, and L3 for a flowrate of 60 liters per minute. Further, particle separation characteristics

are compared, based on separation efficiency curves and particle tracks.

3.4.2.1 Axial Velocity

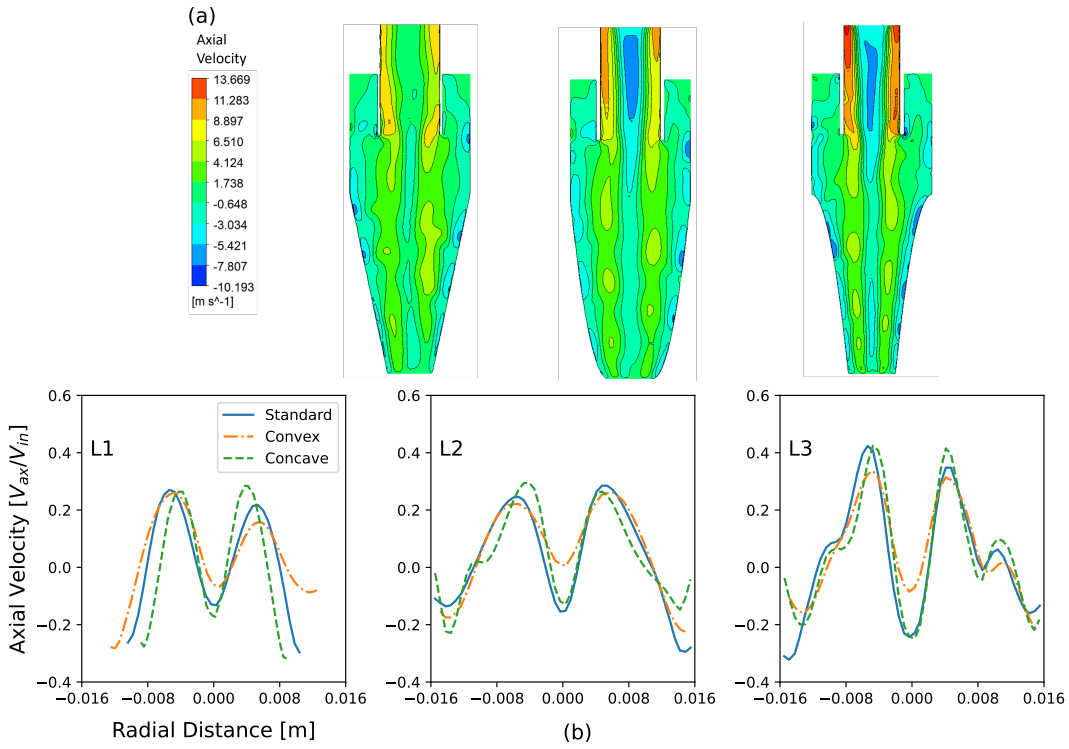


Figure 3.7: Axial velocity profiles as a function of conic design for a flowrate of 60 lpm: a) Contour Plots b) Radial profiles predicted at three axial locations L1, L2, and L3

The contour plots in Figure 3.7(a) show that the distribution of axial velocities is broader for curved conic design cyclones than for the standard design. Additionally, high axial velocities are seen near the inner wall of the vortex finder, while negative axial velocities (i.e., backward flow) occur in the core region of the vortex finder. This pattern is most pronounced in concave designs, followed by convex and standard designs. Nevertheless, the radial profiles of velocities in Figure 3.7(b) highlight that the strength of backward flow in convex-design cyclones deteriorates rapidly moving towards the dust outlet in the axial direction.

Figure 3.7(b) reveals that all three cyclones have similar inverted 'W' shaped axial velocity profiles. The concave design follows the trend of the standard design axial velocity more closely than the convex design. The concave design also exhibits slightly higher maximum axial velocities. At all three locations, the central dip in the axial velocity of the convex design is less pronounced compared to the other two designs. This is due to the lower pressure distribution inside the convex design cyclone, as shown in Figure 3.9. As illustrated in Figure 3.7(b), the magnitude of maximum axial velocities is higher in the cylindrical section (at location L3) than in the conic sections. The symmetry in the profiles at location L3 is disrupted on the right side due to the presence of an inlet. It is

important to note that the radial distance for the measurement location at L1 is greatest for the concave design cyclone, followed by standard and convex design cyclones. This difference in radial distance explains the disparities in the abscissa values in the radial profiles shown in Figure 3.7(b) L1.

3.4.2.2 Tangential Velocity

The contour plots in Figure 3.8(a) demonstrate that the intensity of tangential velocity is greater in the standard design than in the convex and concave designs, with particularly low intensity in the convex design. The distribution of lower tangential velocities can also be seen in the vortex finder region in the concave and convex conic design cyclones compared to the standard cyclone. It is observed that the tangential flow field inside the convex and concave designs resembles the Rankine vortex structure similar to the standard design. The radial profiles show that the maximum value peaks at the boundary between the inner quasi-vortex flow zone and the outer quasi-free vortex flow zone. The concave design closely follows the profile of the standard design, while the tangential velocity profiles of the convex design are lower compared to the standard design. This could be due to the higher internal volume of the convex design, which decreases the available flow velocities for a given flow rate. As shown in Figure 3.8(b) - L3, there is a slight flattening of the tangential velocity profile in the outer vortex zone for the convex design beneath the vortex finder. It is noteworthy that the radial location of maximum axial velocity is closer to the central axis than the radial location of maximum tangential velocity.

3.4.2.3 Static Pressure

The contour plots of the static pressure distribution on a center plane for all three designs are presented in Figure 3.9(a). It is observed that, except for the central core region, the pressure distribution profiles are similar. The magnitude of pressure increases with an increase in radial distance from the wall, resulting in a negative pressure core in the central core region. This negative pressure drives the backward flow from the gas outlet. The concave and convex designs have lower pressure distribution inside the vortex finder region, which contributes to the higher backflow, compared to the standard design. As seen in Figure 3.9(b), the standard design has higher pressure values near the walls than the other designs. Conversely, the convex design has the least pressure formation.

The pressure drop is calculated by determining the difference in total pressure between the inlet and gas outlet for each case. As observed from Table 3.5, there is a close agreement between the estimated values for the standard design and the experimentally reported values Xiang *et al.* For low flow rates ($\leqslant$ 50 lpm), the differences in overall pressure drop among the conic designs are negligible. However, for higher flow rates, the concave and convex designs have a lower pressure drop compared to the standard design. There-

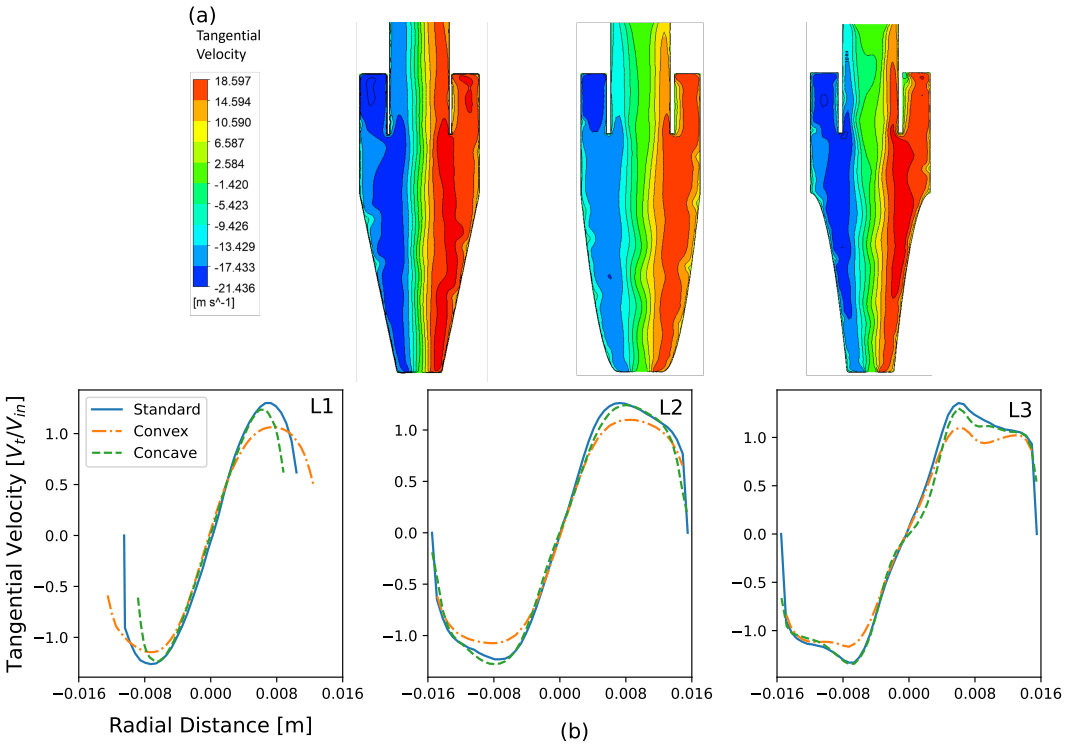


Figure 3.8: Tangential velocity profiles inside the cyclones as a function of conic design for a flowrate of 60 lpm: a) Contour Plots b) Radial profiles predicted at three axial locations L1, L2, and L3

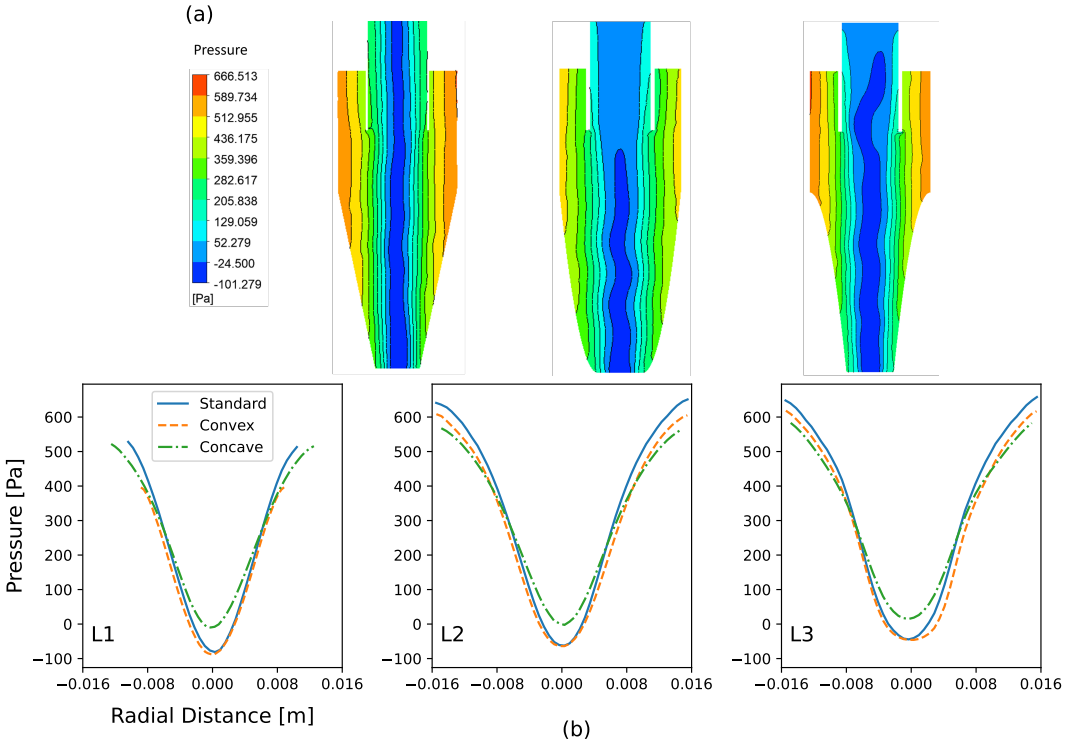


Figure 3.9: Pressure distribution profiles inside the cyclones as a function of conic design for a flowrate of 60 lpm: a) Contour Plots b) Radial profiles predicted at three axial locations L1, L2, and L3

fore, lower flow rates result in coarser cut sizes (discussed in detail in the next section), and lower pressure drops if particle classification, rather than separation, is the goal.

3.4.2.4 Particle Separation Characteristics

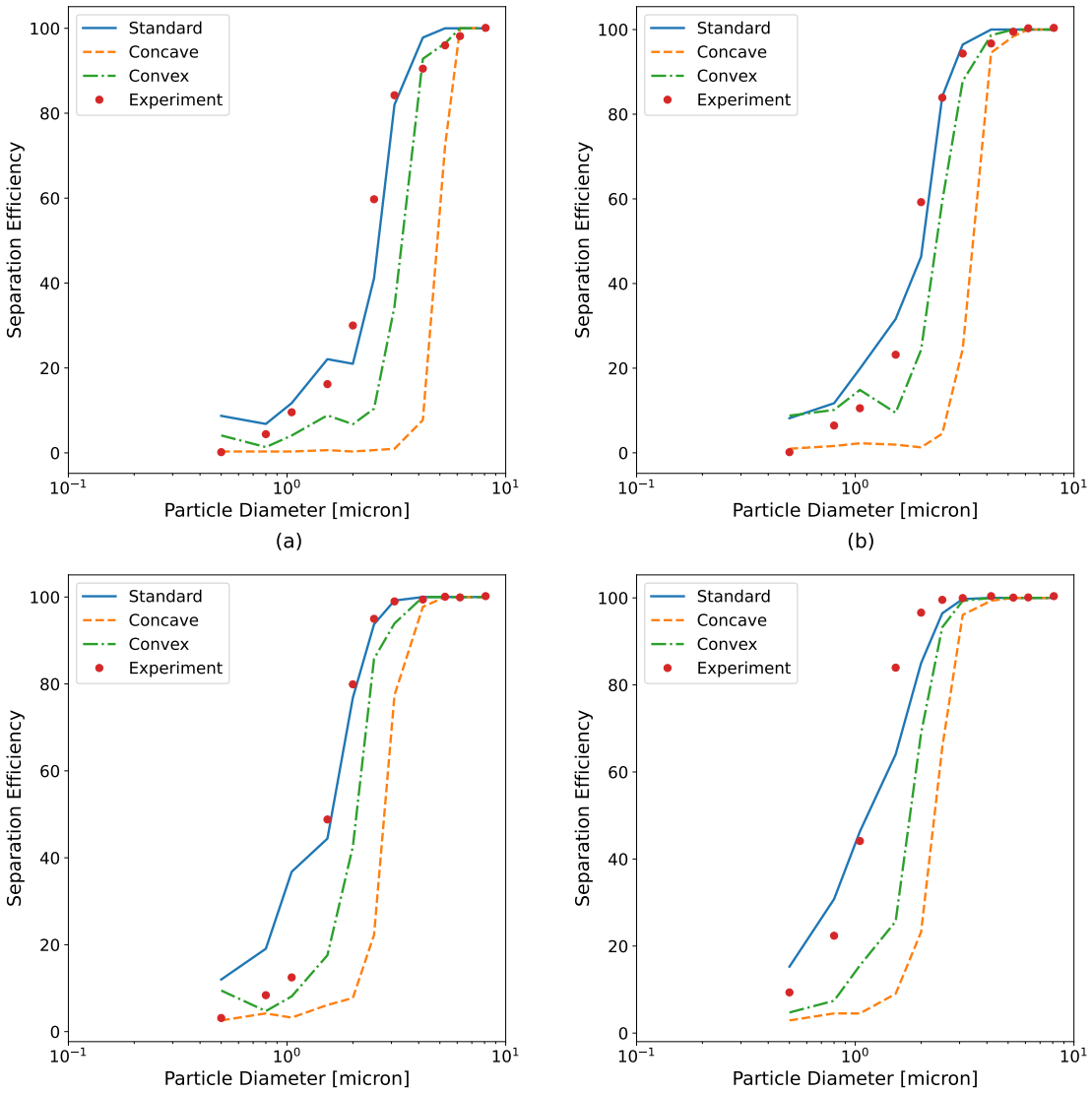


Figure 3.10: Effect of conic curvature shape on the particle separation characteristics as a function of inlet air flowrate. a) 30 lpm, b) 40 lpm, c) 50 lpm, and d) 60 lpm. [Experimental data source: Xiang *et al.* [11]]

Figure 3.10 illustrates the impact of conic curvature on particle separation characteristics as a function of the inlet air flow rate. It is consistently observed that, at any given flow rate, the concave and convex conic cyclones produce coarser cut sizes compared to the standard conic design. Additionally, the concave conic shape produces even coarser cut sizes with a sharper classification profile. As the flow rate increases, all the separation efficiency curves shift to the left, decreasing the particle cut size (D_{50}). As observed from Table 3.5 there is good agreement between the predicted cut sizes and the experimentally reported values for the standard design cyclone at all flow rates under study. As the flow rate increases, the cut size decreases for all conic designs. For example, as the flow rate

Table 3.5: Performance comparison of standard, concave, and convex design gas cyclones for key parameters

	Cut Size (microns)				Sharpness				Pressure Drop (Pa)			
Flowrate (lpm)	Standard Exp.	Standard	Convex	Concave	Standard Exp.	Standard	Convex	Concave	Standard Exp.	Standard	Convex	Concave
30	2.36	2.65	3.38	4.91	0.63	0.72	0.77	0.85	104	109.3	93.7	115.9
40	1.92	2.05	2.35	3.45	0.66	0.53	0.72	0.82	196	213.7	189.2	230.4
50	1.57	1.63	2.08	2.76	0.61	0.45	0.72	0.83	327	350	325.7	357.3
60	1.15	1.13	1.8	2.31	0.57	0.39	0.73	0.77	595	591.1	492.3	540.6

increases from 30 to 60 lpm, the average cut size decreases from 2.65 μm to 1.13 μm for the standard design cyclone. At a flow rate of 30 lpm, the concave design cyclone produces a particle cut size of approximately 5 μm, while the standard design cyclone produces 2.65 μm. The particle separation characteristics of the convex design are intermediate between the standard and concave designs. Although lower flow rates result in coarser cut sizes, after an optimal value, the effective centrifugal force acting on the particle decreases, which decreases the sharpness of classification, which is not desirable.

Similarly, it is observed from Table 3.5 that standard design shows a slight decrease in sharpness with an increase in flow rates ($\geqslant$ 40 lpm) in experimentally reported values, which is more pronounced in CFD estimates. On the other hand, the concave and convex conic designs exhibit better sharpness values at all flow rates studied. The CFD results indicate that the concave and convex designs enhance the axial velocities near the inner wall of the vortex finder and intensify the negative axial velocities (backward flow) in the core region. This pattern plays a crucial role in improving the sharpness of particle classification efficiency by acting as a secondary classification zone. The negative axial velocities in the vortex finder's core prevent particles from easily escaping through the gas outlet, increasing their classification by entering the main flow stream. As a result, the classification sharpness is improved, with the concave designs exhibiting the most pronounced improvement, followed by the convex designs, compared to the standard design cyclones. Hence, higher sharpness values are expected for concave-design cyclones.

Further, we present single particle tracks for the case of 30 liters per minute flowrate to understand the particle behavior inside the cyclone. Particles with diameters of 2.36, 3.38, and 4.91 μm are introduced into the center of the inlet at a flow rate of 30 liters per minute. These particle diameters represent the respective cut size diameters for the standard, convex, and concave designs. Figure 3.11 displays the single particle tracking of these injections, which allows for better visualization of the cut size diameter and cyclone design.

The particle of the cut size has an equal probability to either report to a dust outlet or gas outlet. In the standard design cyclone, as shown in Figure 3.11-1a, the particle with a diameter equal to the cut size diameter (ie., 2.36 μm) travels up to the conical section

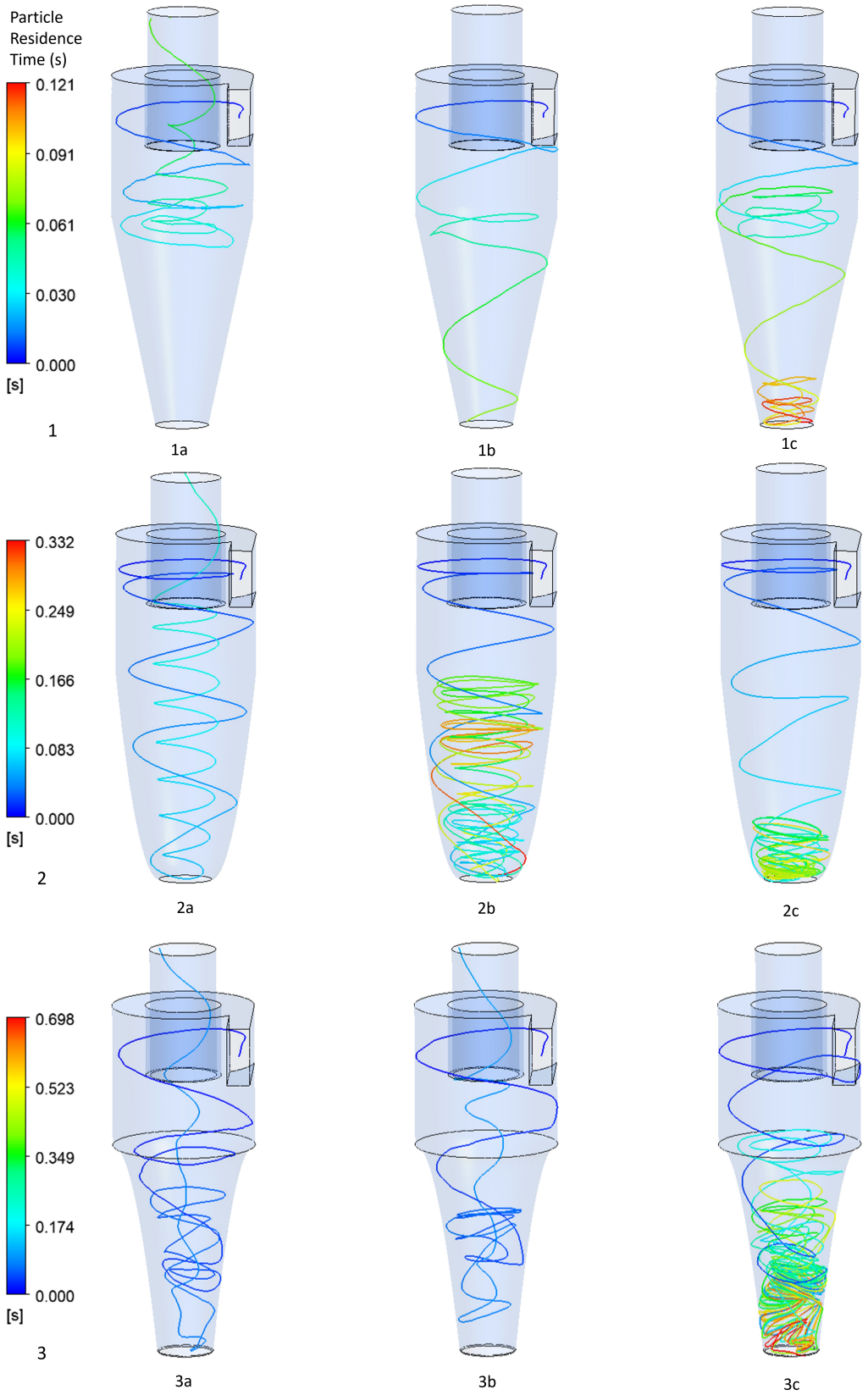


Figure 3.11: Single particle tracking of particles representing their respective cut size diameters for the flowrate of 30 lpm, in 1) Standard (a - 2.36 μm), 2) Convex (b - 3.38 μm), and 3) Concave (c - 4.91 μm) design cyclones

and is carried away by the upward vortex flow to the gas outlet. Whereas, particles of 3.38, and 4.91 μm report to the dust outlet as seen from Figure 3.11-1b and 1c. However, for the convex design, as seen in Figure 3.11-2a, the particle with a diameter less than the cut size diameter exits through the gas outlet. Meanwhile, the particle with a diameter equal to the cut size diameter, as shown in Figure 3.11-2b, travels to the bottom and is caught by the upward vortex, reversing its direction and ending up at the dust outlet. Coarser particles, as depicted in Figure 3.11-2c, are collected through the dust outlet. The concave design cyclone shows similar trends in particle tracking. Figures 3.11-3a and 3b show that particles with diameters less than the cut size diameter escape through the gas outlet, while the particle with a diameter equal to the cut size diameter, as shown in Figure 3.11-3c, has an uncertain path before finally exiting through the dust outlet. It is worth noting that the particle tracks in the concave and convex designs have longer residence times and particles tend to reach the bottom of the cyclone more frequently compared to the standard design.

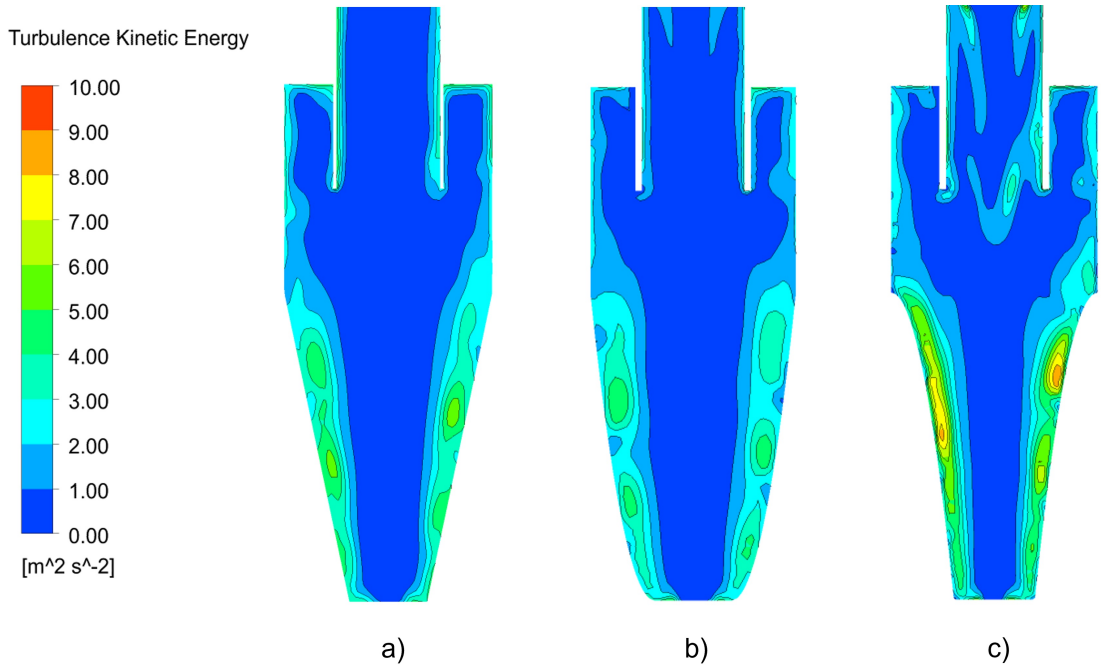


Figure 3.12: Contours of turbulent kinetic energy (k-$\frac{m^2}{s^2}$) for the flow rate of 60 lpm: a) Standard design b) Concave design c) Convex design

In turbulent flow conditions, particles move preferentially from regions of high turbulence intensity to those of low intensity, a process known as “Turbophoresis” [156, 157]. This leads to faster particle dispersion in areas of high turbulence intensity compared to low-intensity regions. The regions of high intensity of turbulent kinetic energy act as a resistance for the particles to pass through; resulting in particle classification [158, 159]. Figure 3.12 displays the contour plots of turbulent kinetic energy for all three design configurations at an inlet flow rate of 60 lpm. It can be observed from Figure 3.12 that turbulent kinetic energy distribution is predominant in the conic section of the gas cyclones.

Figure 3.12 shows that the standard design has a lower turbulent intensity distribution when compared with the convex and concave designs. Hence, particles that reach the conic wall in the standard design are more likely to slide along the wall and collect at the bottom bin, while in the convex and concave designs, intense turbulence leads to a particle filtering mechanism. Only larger particles have a high likelihood of overcoming the turbulence barrier along the conic wall. Thus more particles get caught by the secondary vortex and exit through the vortex finder, resulting in coarser cut sizes.

The conic curvature of a cyclone significantly affects the coarser particle classification. Because of higher turbulence intensity near the conic section in curved conic designs, ie., concave and convex designs, particles move toward the center of the cyclone where the velocity of the fluid decreases. This leads to a longer residence time as reflected in the particle tracks (Figure 3.11). Based on the above analysis we can conclude that the decrease in the tangential velocity field, higher negative axial velocities near the vortex finder core, and increase in turbulence intensity near the vicinity of conic section for concave and convex designs cyclones help in achieving the coarser and sharper cut sizes than compared to those achieved by the standard gas cyclones.

3.4.3 Response Surface Methodology: Results

3.4.3.1 Analysis of Variance

Analysis of variance (ANOVA) is used to evaluate the significance of coefficients of estimators in the quadratic polynomial fit. It is an ensemble of statistical procedures to analyze the RSM fitted model representing the experimental data [96]. The error analysis followed by the F-test (p-values; p<0.05 indicates 95% confidence) to evaluate the significant effects of interactions is discussed here. The accuracy of RSM model is evaluated using R^2, adjusted R^2 (R^2_{adj}), predicted R^2 (R^2_{pred}), and Adeq Precision terms. The detailed definitions and mathematical expressions for the indices mentioned above are defined as follows: R^2 is a measure of the amount of variation around the mean explained by the model.

$$R^2 = 1 - \frac{RSS}{TSS} = 1 - \frac{\sum_{i=1}^{n}(y_i - \hat{y_1})^2}{\sum_{i=1}^{n}(y_i - \bar{y_i})^2} \tag{3.16}$$

Where RSS is the residual sum of squares and TSS is the total sum of squares for the response. R^2_{adj} is the measure of the amount of variation around the mean explained by the model, adjusted for the number of terms in the model.

$$\text{Adjusted } R^2 \ (R^2_{adj}) = 1 - \frac{RSS/(n-p-1)}{TSS/(n-1)} = 1 - \frac{(1-R^2)(n-1)}{n-p-1} \tag{3.17}$$

Table 3.6: Fit statistics comparing the quadratic and modified models for cut size and sharpness

Parameter	Std. Dev.		R2		Adjusted R2		Predicted R2		Adeq. Precision	
	Quadratic	Modified	Quadratic	Modified	Quadratic	Modified	Quadratic	Modified	Quadratic	Modified
cut size	0.585	0.486	0.992	0.989	0.965	0.975	0.3438	0.9231	25.97	37.93
Sharpness	0.09	0.062	0.902	0.907	0.6991	0.855	-0.721	0.7485	8.43	17.28

R^2_{pred} is a measure of the amount of variation in new data explained by the model.

$$\text{Predicted } R^2 \ (R^2_{pred}) = 1 - \frac{PRESS}{TSS} \tag{3.18}$$

Where PRESS is the predicted residual error sum of squares, it accounts for one point deletion squared residual error. Adequate Precision (Adeq Precision) measures the signal-to-noise ratio. A ratio greater than 4 is desired to differentiate between the signal and noise.

$$\text{Adeq. Precision} = \frac{max(\hat{Y}) - min(\hat{Y})}{\sqrt{\frac{p\hat{\sigma^2}}{n}}} \tag{3.19}$$

The model fit in terms of adjusted R^2 values is improved by selecting the variables that are truly contributing to the accuracy. We use the Bayesian information criterion (BIC) with the backward selection of variables in the model [160]. In a system having 'p' parameters, we remove the variable with the largest p-value as it is statistically insignificant and the resultant 'p-1' variable model is fit. This process is repeated until the threshold between the R^2 and Adjusted R^2 is reached.

Table 3.6 contains the list of fit statistics for both the quadratic model and the modified models for cut size and sharpness respectively. Though the R^2 and adjusted R^2 values for the quadratic model of cut size indicate a good fit, the predicted R^2 values are low. This indicates over-fitting parameters in the model. These excess model parameters are removed using the BIC criterion with the backward selection of parameters containing high p-values. The modified model fit statistics are improved significantly as shown in Table 3.6. The model for cut size and sharpness have a Predicted R^2 of 0.9231, and 0.7485. These are in reasonable agreement with the Adjusted R^2 of 0.9759, and 0.8553; as the difference is less than 0.2. Adeq Precision measures the signal-to-noise ratio. A ratio greater than 4 is desirable. The ratios of 37.93 and 17.28 indicate an adequate signal. All the above fit-statistics parameters indicate a good agreement between the final RSM model predictions and simulation results for cut size and sharpness. Table 3.7 lists the p-values of the reduced quadratic model (i.e., modified model) and helps to identify the significant parameters ($p<0.05$) that influence the response variables. Further, Table 3.8 depicts the model equations developed for cut size and sharpness as a function of the design of cyclones for the modified model. Additionally, it is crucial to acknowledge

Table 3.7: p-values of reduced quadratic model (Modified model)

Cut size		Sharpness	
Source	p-value	Source	p-value
Model	<0.0001	Model	<0.0001
A-Du	0.6934	A-Du	0.5081
B-D0	<0.0001	B-D0	<0.0001
C-a	<0.0001	C-a	0.1762
D-b	0.0306	D-b	0.0005
E-S	0.0057	E-S	0.0425
F-h	0.0059	F-h	0.6787
G-ch	0.0022	G-ch	<0.0001
H-V	<0.0001	H-V	0.0136
J-Design	0.0125	J-Design	0.8761
AB	<0.0001	AJ	<0.0001
AC	<0.0001	BD	0.0015
AF	<0.0001	BF	<0.0001
AH	<0.0001	CD	0.0036
BD	0.0002	CF	0.0235
BE	<0.0001	CH	0.0326
BF	0.0533	CJ	0.0335
BG	0.0012	DE	0.0422
BH	<0.0001	DF	<0.0001
BJ	<0.0001	DG	0.0131
CD	<0.0001	EH	<0.0001
CE	<0.0001	HJ	0.0023
CF	0.0238	A^2	<0.0001
CJ	<0.0001	E^2	0.0002
DE	<0.0001	F^2	0.0004
DJ	<0.0001	G^2	0.0008
EF	<0.0001		
FG	<0.0001		
FH	<0.0001		
FJ	0.0010		
GH	0.0037		
GJ	<0.0001		
HJ	<0.0001		
A^2	0.0002		
C^2	0.0016		
F^2	0.0002		
G^2	0.0034		
H^2	0.0236		

Table 3.8: Model equations for cut size and sharpness as a function of design.

Cut size	Standard	Convex	Concave	Sharpness	Standard	Convex	Concave
Intercept	9.197	25.556	20.724	***Intercept***	-0.329	-0.377	-0.271
Du	-37.176	-37.176	-37.176	***Du***	4.680	5.114	5.321
D0	9.235	8.481	1.921	***D0***	0.576	0.576	0.576
a	-39.349	-48.999	-37.298	***a***	0.903	0.757	0.554
b	-20.016	-40.977	-19.175	***b***	-1.048	-1.048	-1.048
S	9.347	9.347	9.347	***S***	1.567	1.567	1.567
h	14.456	11.418	12.223	***h***	-0.974	-0.974	-0.974
ch	-3.862	-4.288	-5.672	***ch***	-0.404	-0.404	-0.404
V	0.086	-0.234	-0.320	***V***	0.046	0.042	0.030
Du * D0	22.273	22.273	22.273	***D0 * b***	-1.656	-1.656	-1.656
Du * a	-21.535	-21.535	-21.535	***D0 * h***	-0.585	-0.585	-0.585
Du * h	7.355	7.355	7.355	***a * b***	-1.780	-1.780	-1.780
Du * V	-0.684	-0.684	-0.684	***a * h***	-0.265	-0.265	-0.265
D0 * b	22.143	22.143	22.143	***a * V***	-0.019	-0.019	-0.019
D0 * S	-11.909	-11.909	-11.909	***b * S***	0.682	0.682	0.682
D0 * h	1.865	1.865	1.865	***b * h***	1.423	1.423	1.423
D0 * ch	-1.979	-1.979	-1.979	***b * ch***	0.377	0.377	0.377
D0 * V	-0.579	-0.579	-0.579	***S * V***	-0.041	-0.041	-0.041
a * b	68.840	68.840	68.840	***Du²***	-6.473	-6.473	-6.473
a * S	11.128	11.128	11.128	***S²***	-0.966	-0.966	-0.966
a * h	3.587	3.587	3.587	***h²***	0.588	0.588	0.588
b * S	-28.137	-28.137	-28.137	***ch²***	0.125	0.125	0.125
S * h	-4.835	-4.835	-4.835				
h * ch	1.859	1.859	1.859				
h * V	-0.337	-0.337	-0.337				
ch * V	0.084	0.084	0.084				
Du²	42.119	42.119	42.119				
a²	22.066	22.066	22.066				
h²	-7.185	-7.185	-7.185				
ch²	1.148	1.148	1.148				
V²	0.025	0.025	0.025				

the inherent challenges in predicting sharpness in the particle classification process, as highlighted by the complexities observed in hydrocyclone models [161].

3.4.3.2 Analysis of Responses

A few of the significant pair interaction effects as a function of cyclone design are shown in Figure 3.13 in the form of 2D contour plots. It depicts the interaction effects of dust outlet and gas outlet diameters (A-B) and vortex finder length and gas outlet diameter (E-B) on the response variables cut to size and sharpness of classification. In Figure 3.13a, it is observed that higher Do and Du yield coarser cut sizes. However, the same combination produces lower sharpness values which are shown in Figure 3.13b. Further, lower values of this combination (Do-Du) yield smaller and sharper cut sizes as observed in figures 3.13a and 3.13b. This observation is more predominant in standard design than compared with concave and convex conic-shaped cyclone designs. From Figure 3.13b, it is observed that sharper cut sizes are achieved for lower gas outlet diameters around the central values of dust outlet diameters. From Figure 3.13c, it is observed that coarser cut sizes are achieved for a combination of higher gas outlet diameter and smaller lengths of vortex finder. As seen from Figures 3.13c and 3.13d the effect of vortex finder length is relatively low when compared with the gas outlet diameter on cut size, whereas, this trend is in contrast to the sharpness of classification. From Figure 3.13d, it is observed that an optimum length of vortex finder is desired for sharper classification. It is understood from the above discussion there exists interacting and contrasting effects between the variables. Hence a full optimization study has to be performed to obtain the optimal designs that produce coarser cut sizes.

Monte Carlo simulations are carried out using the RSM models developed in order to probabilistically determine the influence of variables on the cut size and sharpness of classification. The possible outcomes in response variables were analyzed for the randomly generated input variables within the feasible input design space which is discussed in the following section.

3.4.3.3 Monte Carlo Simulations

Monte Carlo simulations calculate the probability of a particular outcome at the randomly created ensemble of samples within the design space [162]. We use the fitted equations of response variables (ie., models for cut size and sharpness) for each design derived from the RSM study. Numerous predictions based on the randomly created ensemble of factors within the design space are generated. This process yields confidence in establishing the design in terms of its classification capability [163]. A continuous uniform distribution is assumed for all the factors under study with the same lower and upper limits as given in Table 3.4. Monte Carlo simulations were performed for 25,000 runs in Oracle Crystal

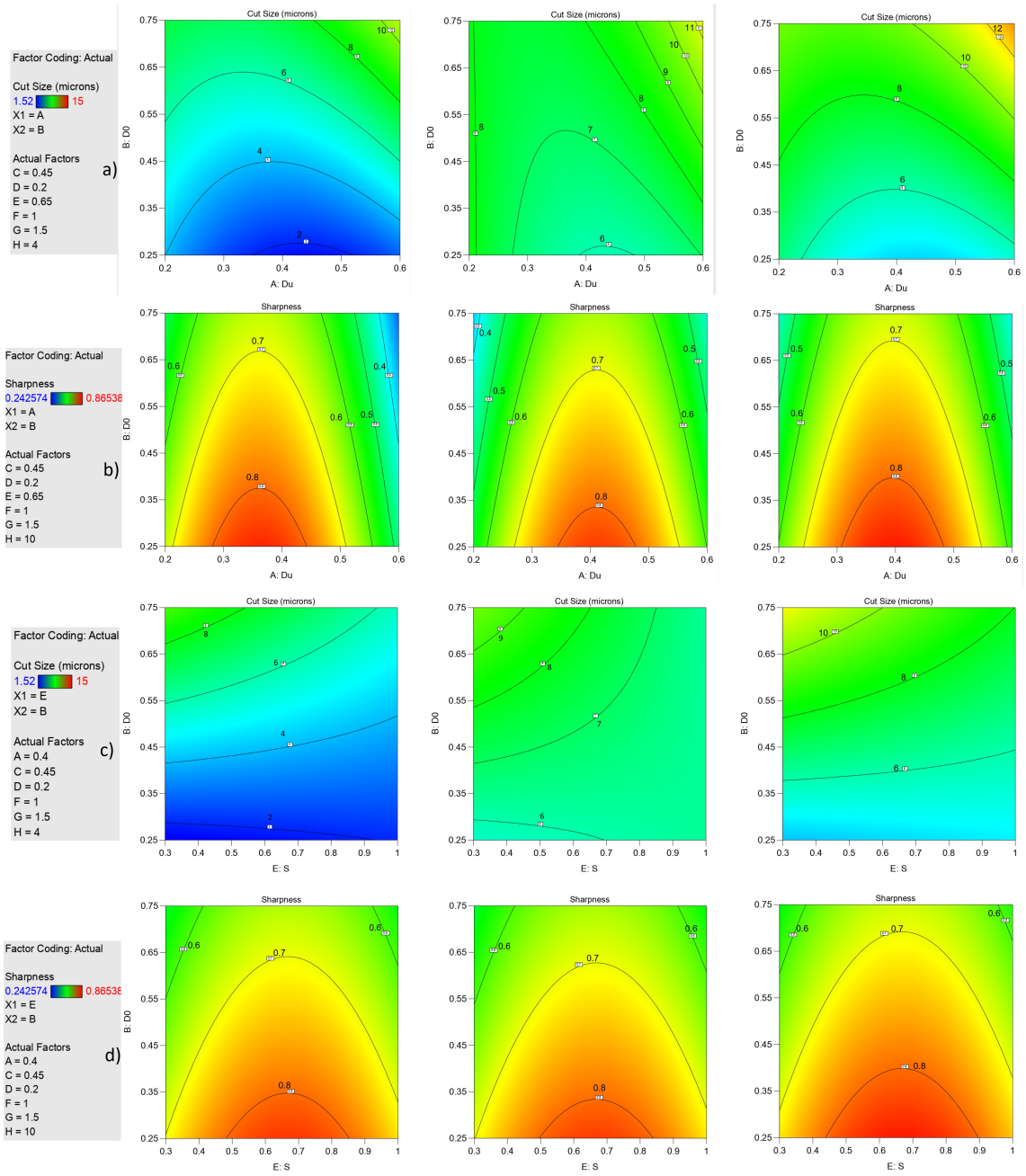


Figure 3.13: Contour plots from response surface methodology a) Cut size - Du vs Do, b) Sharpness - Du vs Do, c) Cut size - S vs Do b) Sharpness - S vs Do

Table 3.9: Summary statistics for Monte-Carlo simulations for the response variable

	Cut size - (6-12 μm)			Sharpness - (0.7-0.9)		
	Standard	Concave	Convex	Standard	Concave	Convex
Mean	3.9	4.1	4.9	0.71	0.71	0.73
Standard Deviation	2.16	2.7	3.2	0.14	0.13	0.13
Certainty (%)	16.6	20.8	30	47.7	47.3	51.6

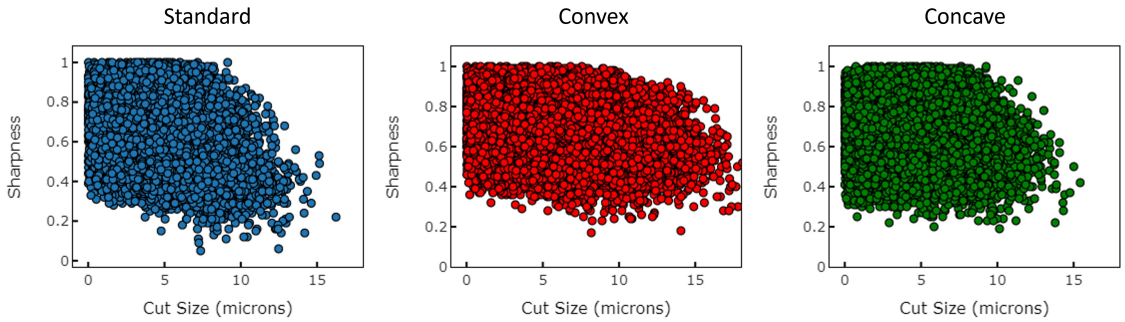
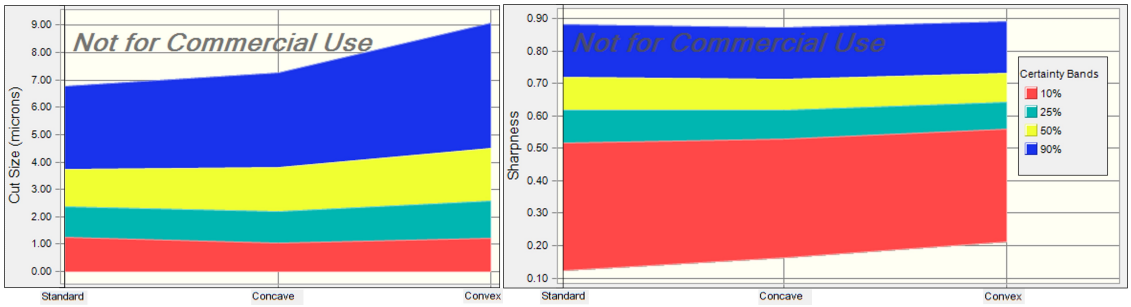


Figure 3.14: The design space of cut size and sharpness of classification generated by Monte Carlo simulations as a function of cyclone design

Ball version 11 software. To determine the satisfactory number of runs, we employed a procedure based on confidence intervals. Initially, 20,000 simulations were conducted and subsequently increased to 25,000. Comparing the widths of the 95% confidence intervals for cut size and sharpness between the two simulations showed no significant difference. Thus, the precision achieved with 20,000 simulations is deemed sufficient. However, we used the data from 25,000 simulations for added accuracy. Table **??** presents the summary of statistics for the Monte Carlo simulations of the response variables. It is observed that the overall mean for the cut size of the Convex design cyclone is higher than those of the Standard and Concave designs. Although the mean cut sizes of Standard and Concave designs are close, there is a reasonable degree of standard deviation between them. Similarly, based on the metric of certainty (%) of cut size between 6-12 μm, it is understood that the Convex design has the highest certainty with 30% compared to 20.8% and 16.6% for the Concave and Standard designs, respectively. Therefore, it can be concluded that the Concave design and the Convex design cyclone can be deployed for coarse particle classification. It is also observed that the effect of cyclone design has an insignificant contribution to the sharpness of classification. The overall mean and standard deviation of predictions from Monte Carlo simulations are around 0.71 and 0.13 regardless of cyclone design type. As shown in Figure 3.14 the design space is evaluated by plotting the sharpness and cut size responses generated by Monte Carlo simulations as a function of cyclone design type to understand their classification performance. It is observed that in standard design the sharpness of classification falls sharply after cut



(a) Cut Size **(b)** Sharpness

Figure 3.15: Trends of response variables in terms of certainty bands (From Monte Carlo simulations).

size values cross 7 μm. However, in the Concave design, this trend slightly shifts towards the right and this behavior is even more pronounced for the Convex cyclone design. It is observed that Convex design cyclones can yield cut sizes up to 15 μm with the sharpness of classification as high as 0.7.

Figure 3.15 captures the trends of response variables as a function of cyclone design type in terms of percentage certainty bands. It is observed that there is a minimum improvement in cut size when the design is varied from Standard to Concave. However, for Convex design, the 90% certainty band of cut size has increased to 9 μm without compromising in terms of sharpness of classification as shown in Figure 3.15b.

3.5 Summary

The CFD analysis of the parabolic designs showed that the conic curvature has a significant impact on the particle classification inside the gas cyclone. It has been found that the k-ω - (SSTCC) model is equally as accurate as the well-established Reynolds Stress Model in capturing the flow field inside gas cyclones, and has a lower computational cost.

The CFD model successfully predicts the particle separation characteristics for the standard design against the experimentally reported values of a 31 mm diameter gas cyclone. For a standard design, as the flow rates increase from 30 to 60 liters per minute, the cut size decreases from 2.65 to 1.13 μm, whereas the pressure drop increases from 109 to 590 Pa which is in good agreement with the experiments. It has been observed that both convex and concave conic design cyclones offer coarser cut sizes at all flow rates studied. At a flow rate of 30 liters per minute, the cut size increases to 4.91 μm for a parabolic concave design, compared to 3.38 μm and 2.65 μm for the parabolic convex and standard design cyclones, respectively. It is argued that turbophoerosis plays a crucial role in achieving coarser cut sizes in curved conic designs compared to the standard design. The total pressure drop in both the concave and convex designs has been found to be in the same range as the standard design, to some extent on the lower side, for

all flow rates studied. The average sharpness of classification is higher for concave conic design cyclones followed by convex and standard designs. The increased negative axial velocities in the center region of the vortex finder strengthen the secondary classification zone for curved conic designs, compared to the standard design cyclone. Based on Monte Carlo simulations using the certainty metric (%) of cut size ranging from 6-12 μm, it is evident that the Convex design exhibits the highest certainty at 30%, while the Concave and Standard designs, have values of 20.8% and 16.6%, respectively.

Overall, the CFD analysis with RSM study provides valuable insights into the flow field and particle separation characteristics of the parabolic designs, suggesting their potential for coarser classification. While our study focuses on a 31 mm gas cyclone, we aim to conduct scalability studies through experiments and simulations. Further development and optimization of these designs for specific applications are to be evaluated. It is interesting to observe the trends of Monte Carlo simulations, as the predictions indicate that convex conic design has greater capability in achieving a coarser and sharper classification. This leaves scope for design optimization in future studies.

Chapter 4

Impact of Conic Curvature and Wall Roughness on Gas Cyclones: A Computational and Experimental Study

4.1 Background . . . 75
4.2 Experimental Methodology . . . 76
4.2.1 Novel method to capture the overflow particles . . . 77
4.3 CFD Modelling Methodology . . . 78
4.3.1 Turbulence Modelling . . . 78
4.3.2 Geometry and Boundary conditions . . . 80
4.4 Results and Discussion . . . 81
4.4.1 Experimental Analysis: Effect of Conic Curvature . . . 81
4.4.2 CFD Analysis: Understanding the influence of roughness . . . 83
4.4.2.1 Axial Velocity . . . 84
4.4.2.2 Tangential Velocity . . . 85
4.4.2.3 Static Pressure . . . 86
4.4.3 Cyclone Performance Analysis . . . 87
4.5 Summary . . . 89

Chapter Introduction

The chapter begins with a discussion of the background, providing a framework and context for the study (Section 4.1). The experimental methodology is then detailed in Section 4.2, including the novel approach developed to capture particles leaving dust outlet to determine particle size distributions (Section 4.2.1). This is followed by the CFD modeling methodology in Section 4.3, which includes descriptions of the turbulence modeling approach along with description of sand grain models to capture the effect of wall roughness (Section 4.3.1) and the geometry to mimic the in-house experimental domain and boundary conditions used in the simulations (Section 4.3.2).

The results and discussion are presented in Section 4.4. Experimental analysis focuses on the effect of conic curvature on cyclone performance (Section 4.4.1). CFD analysis investigates the impact of surface roughness on flow fields, and pressure differential values comparing with experiments (Section 4.4.2). The combined experimental and CFD insights are synthesized in the cyclone particle separation performance analysis (Section 4.4.3), providing a deeper understanding of the interactions between design parameters and cyclone behavior.

The chapter concludes with a summary of the key findings (Section 4.5). The content of this chapter are currently under peer review in the Powder Technology journal. Minor modifications have been made to the original text to improve clarity and readability within the context of this thesis.

4.1 Background

The literature review in Chapter 2 highlights the critical role of conic design and wall roughness in cyclone performance, primarily explored through CFD simulations, with limited experimental investigations. Also in the previous chapter 3, it was concluded that a convex cyclone design has a higher probability of achieving coarser cut sizes compared to the standard design gas cyclones. Additionally, insights from the Response Surface Methodology (RSM) model revealed that lower flowrates favor coarser cut sizes. Building on these findings, this chapter aims to validate experimentally the trends identified earlier. Further investigations are conducted to examine the role of surface-wall roughness and roughness-conic interplay on the classification behavior of cyclones. To elucidate the underlying physics of the observed experimental trends, CFD simulations are employed to mimic the in-house experimental domain, allowing a comparative analysis between smooth and rough cyclone designs.

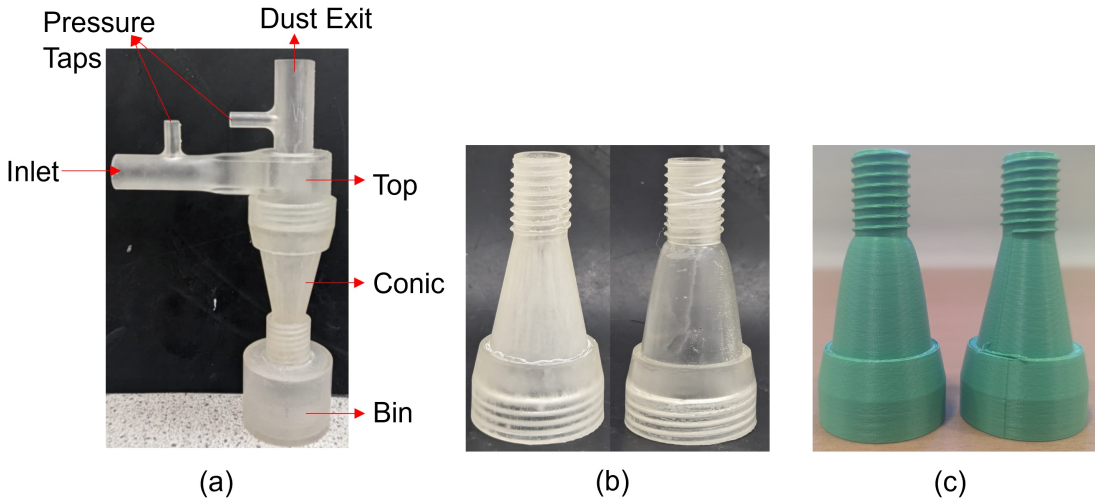


Figure 4.1: (a) 3D printed complete assembly of gas cyclone, (b) Smooth conics and (c) Rough conics

4.2 Experimental Methodology

We employed rapid prototyping to 3D print the cyclones. The cyclones were fabricated using high-resolution stereolithography (SLA) technology with a FormLabs Form 3 printer to achieve a smooth surface finish and a Stratasys 3D printer was used to achieve a coarser surface finish, with a layer height of 300 microns. The final gas cyclone assembly, including the collection bin, is shown in Figure 4.1a. Figures 4.1b and 4.1c display the conical sections of the standard and convex designs, featuring both smooth and rough surface finishes.

Figure 4.2a illustrates the laboratory setup for evaluating the performance of the gas cyclones. Figure 4.2b provides a schematic diagram of the experimental setup. Dry compressed air is first passed through an air filter to remove any condensables, and its flow rate is measured using a digital gas flowmeter (SMC-PFM series) with a range of 2–100 lpm. In the experiments, Eskal-500 plus particles made of calcium carbonate are used, with D_{10}, D_{50}, and D_{90} values of 1.75 μ m, 5.10 μ m and 10.10 μ m, respectively.

The air then passes through a pressure-regulating valve connected to a filter before entering the aerosol generator - PALAS Rotating Brush Generator (PALAS RBG 1000), which is pre-loaded with particles to create an aerosol. The device is designed to aerosolize the non-cohesive powders, by delivering compacted powder from a reservoir onto a rotating brush, where a high-velocity air stream disperses the particles and ejects them through a dust-exit nozzle. The aerosol exits the generator and enters the gas cyclone. A digital manometer is used to measure the pressure differential across the cyclone taps. Separated particles slide down the cone and are collected in the bin, while the exit gas is routed through a rotameter and further drawn into a vacuum pump. Care was also taken to ensure that all line losses were either minimized by adopting tubes and their associate

connections of equal diameter and properly sealed to arrest any gas leaks through the system.

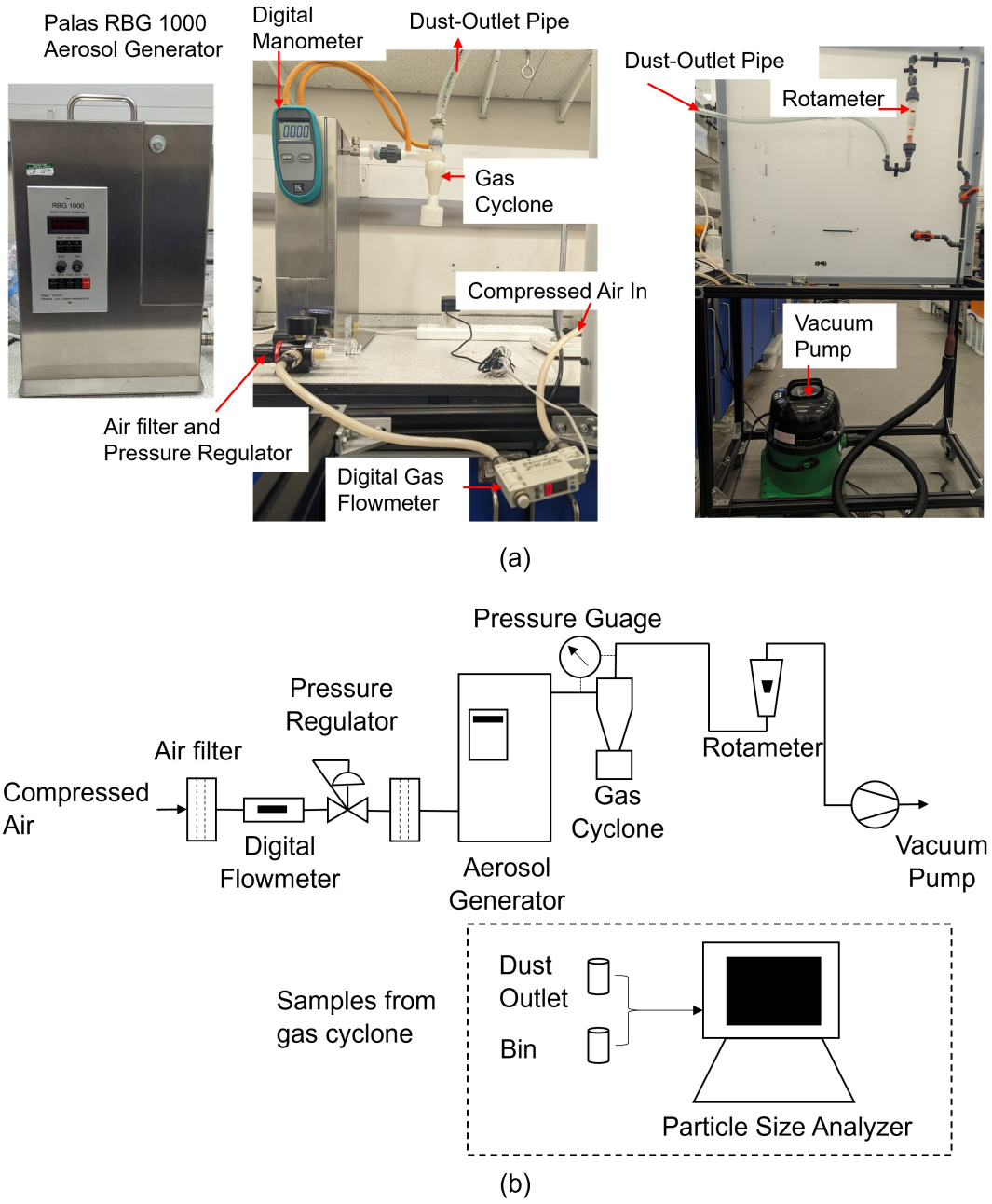


Figure 4.2: (a) Laboratory experimental rig, and (b) Schematic of experimental setup

4.2.1 Novel method to capture the overflow particles

To construct the partition curve, it is necessary to determine the particle size distribution (PSD) of both the samples in the collection bin and the dust outlet. While the collection bin samples are easily collected, obtaining a sufficient dust outlet sample poses a significant challenge. Since only a small fraction of the feed exits through the overflow, much of the material tends to settle in the piping, making it difficult to collect enough sample for PSD analysis. During method development, several potential solutions were considered, including sudden expansion chambers, filters, and other collection mechanisms; however,

many of these approaches proved impractical or ineffective in capturing and recovering sufficient particles for analysis. To overcome this issue, we devised a novel method involving the use of an expandable collection chamber made of latex rubber, which successfully captured the dust outlet particles for PSD analysis.

It was found that the expandable collector imposed no significant changes to the pressure drop across the cyclone. The Mach number for the operating conditions was well below 0.3, indicating that the gas could be treated as incompressible. As a result, the chamber expanded without generating back pressure, which was continuously monitored using a digital manometer. Once the collector had been filled to approximately 80% of its capacity, the system was shut down. The air inside the collector was then released slowly in a controlled manner, preventing the particles from being discharged abruptly. The particles trapped inside the balloon were then washed out using ethanol, and the resulting sample was analyzed to determine the particle size distribution (PSD). Both the samples from dust outlet and solids collected in the bin were analyzed using a Malvern Mastersizer 3000. The solid particles adhering to the cone walls are weighed, thoroughly washed with ethanol, and then combined with the solids in the bin for PSD measurement. To ensure accuracy, the solids concentration measurements and PSD analyses were performed in triplicate. A standard deviation error of less than 10% was observed and is indicated by the error bars in the figures presented in the following section.

4.3 CFD Modelling Methodology

4.3.1 Turbulence Modelling

The swirling flow inside the cyclone is resolved using CFD. While Reynolds Stress Model (RSM) and Large Eddy Simulation (LES) accurately capture Rankine vortex flow and pressure drop, they are computationally intensive. Conventional Eddy Viscosity Models (EVM), like $k-\epsilon$, are less suitable for strong swirling flows due to limitations in handling rotation and streamline curvature [138, 139].

In this study, we apply the $k-\omega$ Shear Stress Transport model with Curvature Correction (SSTCC), shown to align closely with RSM results while reducing computational cost [139, 141]. When comparing experimental pressure differential values with simulations using various turbulence models, we found that the $k-\omega$ SSTCC model predicted values closer to the experimental observations, whereas the RSM tended to overestimate the pressure differential. Based on this, we opted for the $k-\omega$ SSTCC model for all simulations in the study.

The governing equations consist of the continuity and momentum equations for in-

compressible flow:

$$\frac{\partial \overline{u}_i}{\partial x_i} = 0, \quad \frac{\partial(\rho \overline{u}_i)}{\partial t} + \frac{\partial(\rho \overline{u}_i \overline{u}_j)}{\partial x_j} = -\frac{\partial p}{\partial x_i} + \frac{\partial \sigma_{ij}}{\partial x_j} - \frac{\partial \tau_{ij}^{sgs}}{\partial x_j},$$

where $\overline{u}_i$ is the velocity, ρ is fluid density, p is pressure, and σ_{ij} and τ_{ij}^{sgs} are stress tensors due to viscosity and turbulence, respectively.

The $k-\omega$ SSTCC turbulence model employs transport equations for turbulent kinetic energy (k) and specific dissipation rate (ω):

$$\frac{\partial(\rho k)}{\partial t} + \frac{\partial(\rho k \overline{u}_i)}{\partial x_i} = \frac{\partial}{\partial x_j}\left(\left(\mu + \frac{\mu_t}{\sigma_k}\right)\frac{\partial k}{\partial x_j}\right) + \tilde{G}_k - Y_k + S_k,$$

$$\frac{\partial(\rho \omega)}{\partial t} + \frac{\partial(\rho \omega \overline{u}_i)}{\partial x_i} = \frac{\partial}{\partial x_j}\left(\left(\mu + \frac{\mu_t}{\sigma_\omega}\right)\frac{\partial \omega}{\partial x_j}\right) + \tilde{G}_\omega - Y_\omega + S_\omega.$$

In the above equations, the first terms on the right-hand side represent the diffusion of k and ω due to both molecular and turbulent viscosity. The terms, $\tilde{G}_k$ and $\tilde{G}_\omega$, account for the generation of k and ω due to turbulence, while Y_k and Y_ω, represent the respective rates at which k and ω dissipate within the flow. For further details on these equations and model parameters, please refer to our previous work [38].

Surface-wall roughness increases flow resistance and alters the velocity profile, necessitating a modification of the law of the wall with a constant roughness adjustment, ΔB.

$$U^+ = \frac{u}{u^*} = \left(\frac{1}{\kappa}\right)\ln\left(\frac{y u^*}{v}\right) + \mathrm{B} - \Delta B$$

In the above equation, friction velocity (u^*) is defined as $\left(\frac{\tau_w}{\rho}\right)^{0.5}$, with τ_w representing wall shear stress and ρ fluid density. The von Karman constant κ is 0.41, and B equals 5.56 for smooth walls. The roughness effect can be accurately captured using the sandgrain model which is introduced long ago by Nikuradse [164]. In this model, it is assumed that the wall is covered by a packed layer of mono-dispersed sand grain spheres, resembling sandpaper. The diameter of spheres corresponds to the equivalent height of roughness elements. The roughness function ΔB depends on roughness shape (C_s) and size (k_s), expressed through the dimensionless surface roughness $k_s^+ = \frac{k_s u^*}{v}$. Nikuradse [164] observed that the roughness function increases with an increase in roughness height. He further noted that for uniform sand-grain roughness, the roughness function increases sharply when the roughness height transitions from the transitionally rough regime to the fully rough regime. Aditionally, the roughness function no longer exists below (k_s^+) 2.25.

This trend is mathematically represented in the below equation.

$$\Delta B = \begin{cases} 0, & k_s^+ \leqslant 2.25 \\ \frac{1}{\kappa}\ln\left(\frac{k_s^+ - 2.25}{87.75} + C_s k_s^+\right) & \\ \cdot \sin\left[0.4258\left(\ln k_s^+ - 0.811\right)\right], & 2.25 < k_s^+ < 90 \\ \frac{1}{\kappa}\ln\left(1 + C_s k_s^+\right), & k_s^+ > 90 \end{cases} \tag{4.1}$$

Assuming uniform sand grains, the roughness constant is 0.5. For hydrodynamically smooth pipes ($k_s^+ < 2.25$), roughness has minimal impact. Its influence becomes significant in transitional ($2.25 < k_s^+ < 90$) and hydrodynamically rough regimes ($k_s^+ > 90$). Similar approaches to model the effect of surface-wall roughness in gas cyclones and hydrocyclone using sand-grain models have been adopted by various researchers in the literature [114, 124–126, 128–130, 132].

4.3.2 Geometry and Boundary conditions

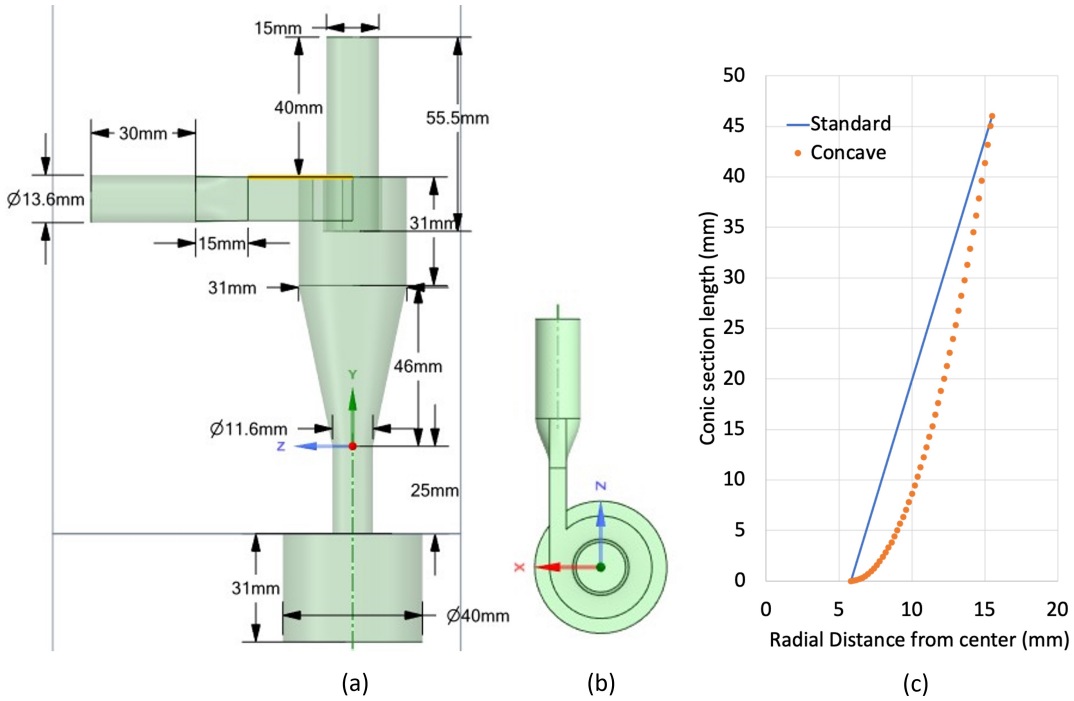


Figure 4.3: Geometrical design of cyclone under study. a) Side-view: Cyclone with dimensions b) Top view, c) Profiles to conic curvature (Standard and Convex)

Figure 4.3 depicts the flow domain of the entire cyclone assembly of the 3D-printed structure. The inlet pipe, which has an internal diameter of 13.6 mm, was chosen to match the internal diameter of the tubing and connectors, thereby eliminating any possible dead zones or recirculation areas. Additionally, the circular channel is extruded into a rectangular tangential inlet channel with dimensions of 12.5 mm in length and 5 mm in breadth, leading to a progression distance of 15 mm. Further, the cyclone apex region is extended into a dip leg which connects to the cylindrical dust collection bin. Figure 4.3c,

Table 4.1: Comparative analysis of performance metrics as a function of flowrate for smooth cyclones

Flowrate-(lpm) Velocity-[m/s]	Pressure (Pa)		Cut-Size (microns)		Bypass (%)		Sharpness		Imperfection Index	
Case	Standard	Convex	Standard	Convex	Standard	Convex	Standard	Convex	Standard	Convex
18 [2.087]	43	41	3.48	3.93	53	43	1.99	2.08	0.35	0.38
24 [2.788]	85	79	3.61	4.20	69	59	2.22	2.53	0.42	0.49
30 [3.480]	137	132	2.8	3.44	74	73	2.02	2.3	0.38	0.44

compares the conic curvature of the standard and parabolic convex shapes, the design equation can be found elsewhere in the literature [38].

The objective of the CFD study is to compare the effect of conic curvature and roughness effect for the experimental conditions. The experiments are conducted for the inlet flowrates of 18 lpm, 24 lpm and 30 lpm. For these conditions, the inlet velocities correspond to 2.087, 2.788, and 3.480 m/s, respectively. Despite the use of 'flow rate' in the text for consistency with experimental reports, it is important to clarify that the simulations were based on inlet velocity conditions. The inlet of the cyclone was modeled as a velocity inlet with uniform normal velocities. The gas outlet was modeled as an outflow boundary condition, and all remaining surfaces as walls with no-slip boundary conditions. However, for rough-surface simulations, the roughness height is assumed as 300 microns having a roughness constant value of 0.5. The density and dynamic viscosity of air was assumed to be 1.225 kg/m^3 and 1.8*$10^{-5} kg/(ms)$, respectively.

To ensure robustness, a pressure-based coupled solver (PBCS) algorithm was used for pressure-velocity coupling, and the Quadratic Upstream Interpolation for Convective Kinetics (QUICK) scheme was selected for discretizing the momentum terms. The Pressure Staggered Option (PRESTO) pressure interpolation scheme was used to accurately capture the sharp pressure gradients in the high swirling flows. A second-order upwind discretization was used for both the turbulent kinetic energy and the specific dissipation rate. A time step of 10^{-4} s was used in all transient simulations. The convergence criteria for all scaled residuals were set at 10^{-5}.

4.4 Results and Discussion

4.4.1 Experimental Analysis: Effect of Conic Curvature

As shown in Figure 4.4, the underflow solids recovery was analyzed as a function of cyclone design and flowrate. It was observed that with an increase in flowrate, the overall solids recovery improved for both cyclone designs. However, the convex design consistently exhibited lower underflow recoveries compared to the standard design across all flowrates studied. For the standard design, underflow recovery increased from 85% at 18

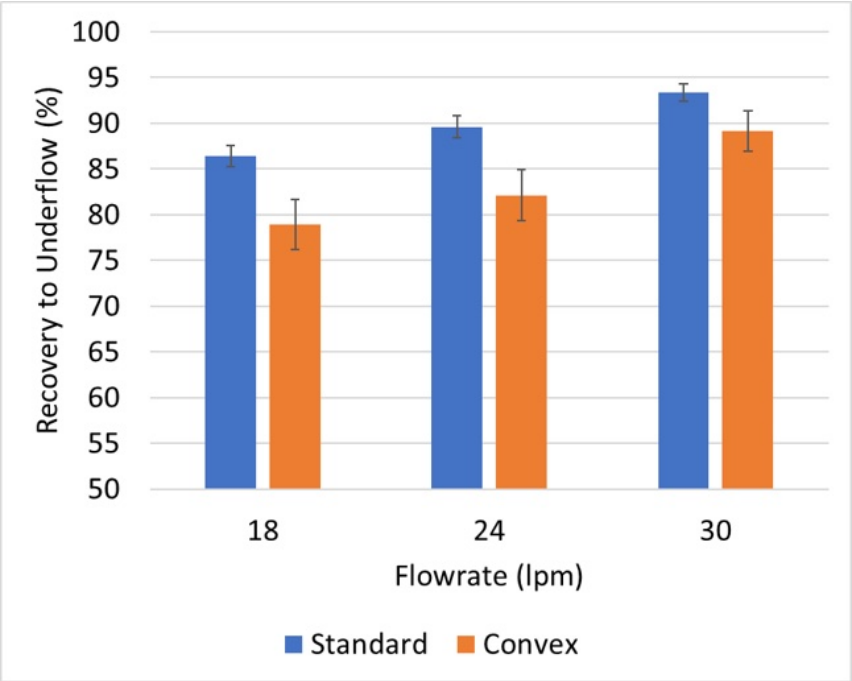


Figure 4.4: Solids recovery as a function of flowrate and conic design.

lpm to 94% at 30 lpm. In contrast, the convex design showed a recovery of 78% at 18 lpm, rising to 88% at 30 lpm. It is interesting to observe that the variance in solids recovery is higher for the convex design cyclone compared to the standard design cyclone. This could be attributed to the fact that overall solids recovery accounts for both the solids collected in the bin and those adhering to the cone walls. Since the convex design cyclone has a larger internal surface area than the standard design, it likely leads to greater variability in the amount of solids retained on the walls, resulting in higher variance in recovery.

The particle separation efficiency data, as a function of design and flowrate, are presented in Figure 4.5. It was observed that particle separation efficiency increased significantly with both particle size and flowrate for both cyclone designs. A fish-hook trend was consistently observed for smaller particles (i.e., less than 2 microns) across all flowrates for both designs. However, this fish-hook trend appeared to diminish (or flatten out) with increasing flowrate for both cyclones. Furthermore, bypass (i.e., the minimum separation efficiency) increased with rising flowrate, indicating that overall particle collection efficiency improved with increasing flowrate. Interestingly, the convex design cyclone exhibited a lower bypass compared to the standard design at all flowrates under study. Additionally, the separation efficiency curve of the convex design cyclone was shifted lower and to the right relative to the standard design, suggesting that a portion of the particles in the convex design, instead of being collected, escaped through the dust outlet, contributing to a classification effect.

Since the observed bypass values exceeded 0.5 for most cases under study, we constructed corrected separation efficiency curves by normalizing the true separation values

with the bypass (i.e., the minimum separation efficiency). From these curves, we extracted the values of D_{25}, D_{50}, and D_{75}, which represent the particle sizes corresponding to separation efficiencies of 0.25, 0.5, and 0.75, respectively. These values were used to calculate key metrics that quantify the quality of separation. The D_{50} represents the corrected cut-size, while sharpness is defined as the ratio of D_{75} to D_{25}. The imperfection index was calculated using the formula $\frac{D_{75}-D_{25}}{2 \cdot D_{50}}$.

Table 4.1 presents the pressure differential values and key metrics used to evaluate the quality of separation achieved in the cyclones as a function of design and flowrate. The corrected cut-size for the convex design cyclone was initially 3.48 microns at a flowrate of 18 lpm, increasing slightly to 4.2 microns at 24 lpm before decreasing to 3.44 microns at 30 lpm. A similar pattern was observed in the standard design cyclone, where the cut-size increased from 3.48 microns at 18 lpm to 3.61 microns at 24 lpm, then dropped to 2.8 microns at 30 lpm. A higher sharpness index indicates a more precise classification, with an ideal value of 1. It was observed that flowrate had no significant effect on sharpness; however, the convex design consistently exhibited lower sharpness compared to the standard design across all flowrates. Similarly, a lower imperfection index is preferred for better classification quality. The standard design cyclone demonstrated a relatively lower imperfection index than the convex design cyclone at all flowrates studied.

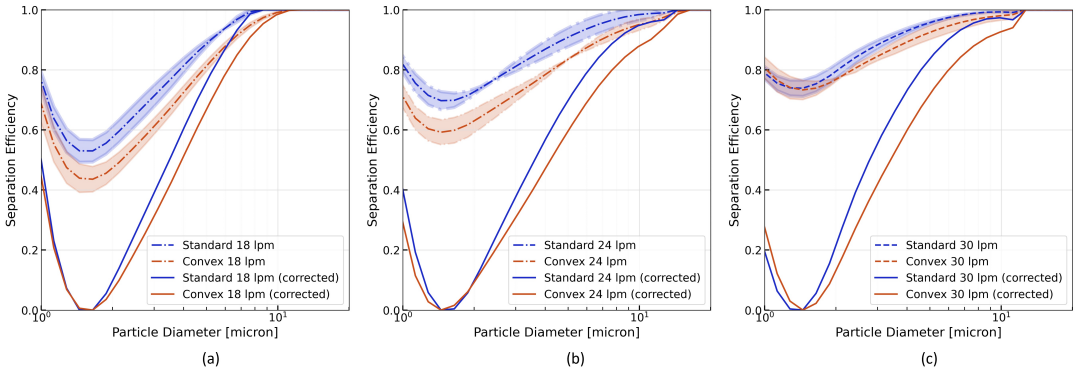


Figure 4.5: Comparison of Separation Efficiency curves for Standard (S) and Convex (C) Gas cyclone Designs across different Flowrates.

4.4.2 CFD Analysis: Understanding the influence of roughness

In this section, we present CFD results comparing key flow properties, including axial, and tangential velocities along with pressure distribution profiles in standard and convex design cyclones as a function of wall roughness. We observed that, when scaled with the inlet velocity, the flow velocities (tangential and axial) exhibit similar trends. Therefore, for the sake of brevity and clarity, we exclusively present results for the flow rate of 30 lpm. Table 4.1 reports particle separation performance metrics for both the cyclone designs as a function of inlet flowrate.

4.4.2.1 Axial Velocity

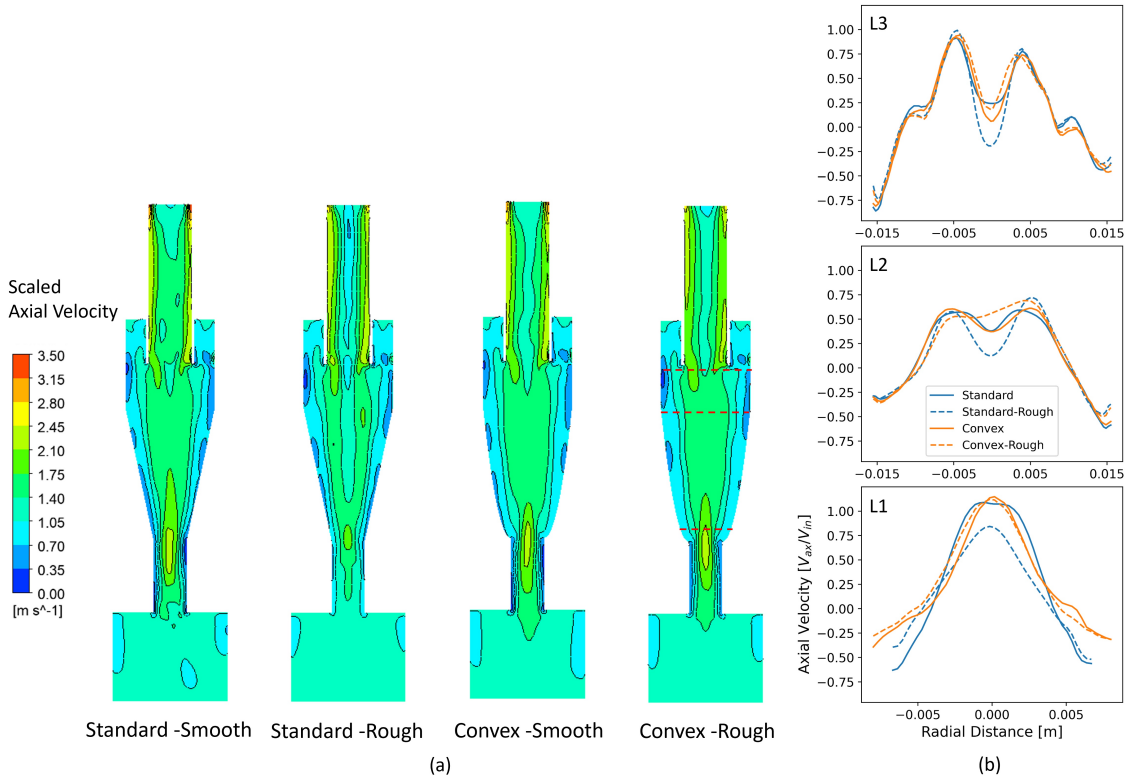


Figure 4.6: Effect of roughness and conic design on axial velocity profiles at the center XZ plane (Y=0) for a flowrate 30 lpm a) Contour plots b) radial profiles at three axial locations (L1, L2, and L3)

Figure 4.6 presents the axial velocity distribution (scaled with inlet velocity) contours and their radial profiles at selected locations, comparing the standard and convex designs as a function of wall roughness. The axial velocity distribution is characterized by a downward spiral motion near the wall (negative velocities) and an upward vortex flow near the center (positive velocities). Figure 4.6b illustrates how the axial velocity initially decreases due to the downward vortex flow, then gradually increases toward the cyclone core. Both smooth and rough cyclones irrespective of their conic design type, as shown in Figure 4.6b, exhibit similar inverted 'W'-shaped axial velocity profiles in the cylindrical section of the cyclone (L2 and L3). However, in the vicinity near the dip leg region (L1), the profile assumes an inverted 'U' shape due to the constriction of the collection bin, causing the gas flow to reverse and move upwards.

It can be observed from Figure 4.6b at L2 and L3 that there is no significant difference in axial velocity profiles between the standard and convex cyclone designs, as well as between their rough-surfaced counterparts, across most of the flow domain. However, in the core region, the rough convex cyclones display slightly higher axial velocity values compared to the standard design at both L2 and L3. In the apex region, as seen in Figure 4.6b at L1, the downward velocities near the wall are more pronounced for the standard design, in both smooth and rough configurations. These higher negative velocities are

beneficial as they contribute to increased collection efficiency. However, for classification purposes, the axial velocity patterns in the convex design are more favorable. The lower axial velocities in the convex design provide particles with more opportunities to participate in the classification process, increasing the likelihood that they will be entrained in the upward vortex and exit through the dust outlet.

4.4.2.2 Tangential Velocity

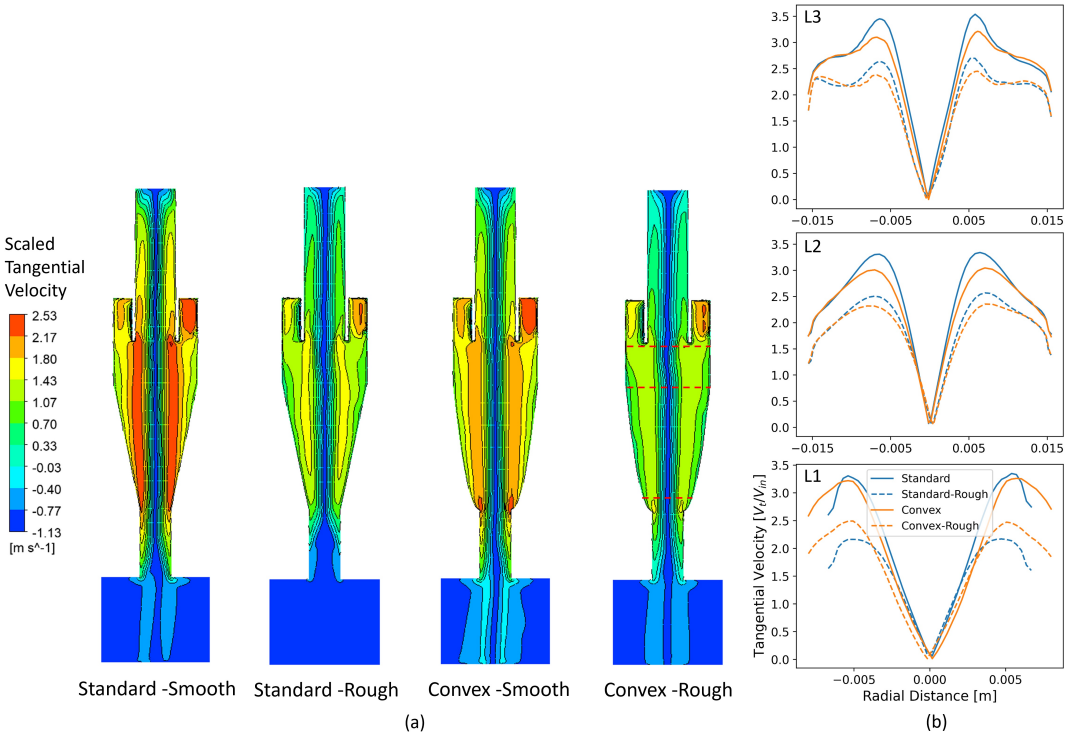


Figure 4.7: Effect of roughness and conic design on scaled tangential velocity profiles at the center XZ plane (Y=0) for a flowrate 30 lpm a) Contour plots b) radial profiles at three axial locations (L1, L2, and L3)

Tangential velocity is a key parameter that directly influences particle separation efficiency by determining the centrifugal forces acting on particles inside the cyclone. Figure 4.7a compares the tangential velocity profiles of standard and convex cyclone designs as a function of wall roughness. Among all configurations, the standard cyclone with a smooth surface consistently exhibits higher tangential velocities, particularly in the cylindrical and conical sections, resulting in stronger centrifugal forces acting on the particles. This higher tangential velocity leads to smaller cut sizes in the standard cyclone. In contrast, the smooth convex design shows relatively lower tangential velocities compared to the smooth standard design, generating weaker centrifugal forces and, consequently, larger cut sizes. The maximum tangential velocity in the smooth standard cyclone is approximately 3.5 times the inlet velocity, whereas in the smooth convex design, it is about 3 times the inlet velocity.

When wall roughness is introduced, some fluid momentum is lost due to friction,

resulting in reduced tangential velocities in both designs. Among all configurations, the rough convex cyclone shows the lowest tangential velocity profile in the flow domain. Figure 4.7b displays the radial profiles of tangential velocities at different locations (L1, L2, and L3). The tangential velocities across all configurations resemble Rankine vortex profiles, with the maximum values occurring at the boundary between the inner quasi-vortex flow zone and the outer quasi-free vortex flow zone. For the smooth surface configurations, as seen in Figure 4.7b at L2 and L3, the tangential velocities within the flow domain of the convex cyclone are lower compared to the standard design cyclone. However, near the apex region (Figure 4.7b at L1), the tangential velocity profiles for both designs are comparable. For the rough-surface configurations, the trends follow those observed in the smooth-surface configurations throughout the cylindrical section and much of the conical section. However, near the apex region (Figure 4.7b at L1), the rough convex cyclone exhibits higher tangential velocities compared to the rough standard cyclone.

4.4.2.3 Static Pressure

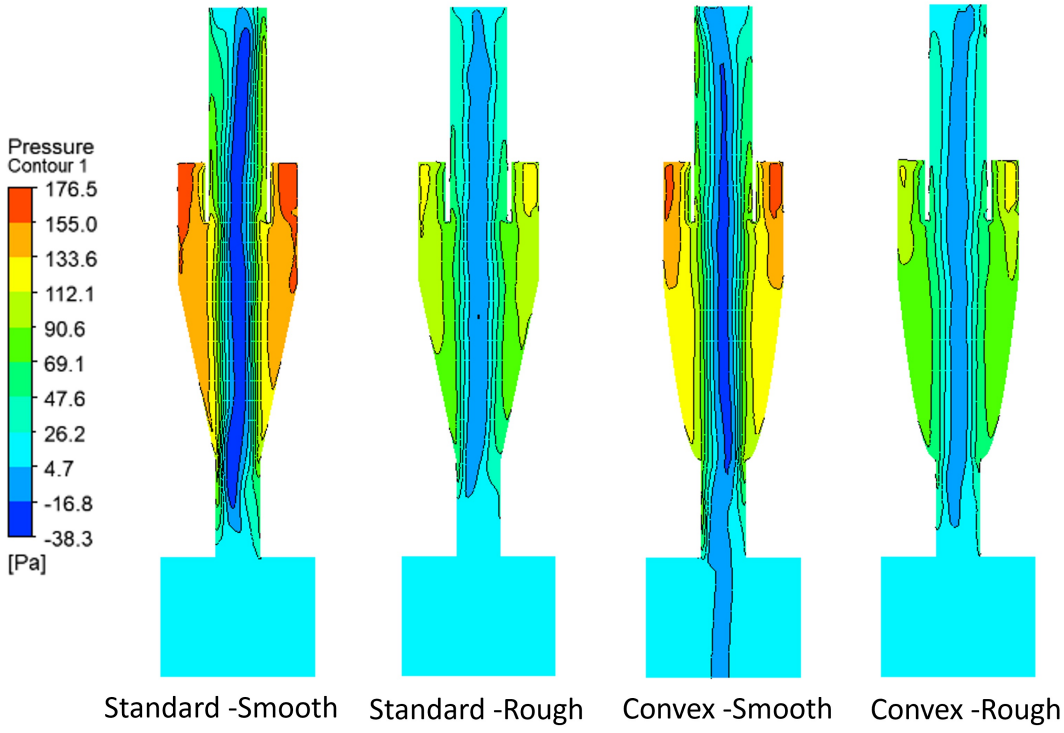


Figure 4.8: Effect of roughness and conic design on Pressure distribution profiles at the center XZ plane (Y=0) for a flowrate 30 lpm

Figure 4.8 illustrates the contour plots of static pressure distribution within the cyclone designs under investigation. It is observed that the static pressure reaches its minimum value in the vortex core region, and increases towards the periphery, where it reaches the maximum. The pressure gradient is most pronounced in the radial direction, while the gradient in the axial direction is less significant. For smooth-surface standard and convex design cyclones, a negative pressure zone is present in the forced vortex region (central

region) due to the intense swirling motion. In contrast, for rough-surface cyclones, the reduction in pressure within the vortex core is less intense compared to their smooth-surface counterparts.

The natural vortex length is defined as the axial distance between the entrance of the outlet tube (vortex finder) and the point where the outer vortex flow weakens and changes its direction. The outer vortex ends where the static pressure reaches its minimum value. As seen from Figure 4.8, for the smooth-surface standard design cyclone, forms an eccentric vortex core, the main vortex terminates near the middle of the dip leg region, where the static pressure is at its lowest. In contrast, for the convex design cyclone, the vortex penetrates deeper into the dust hopper, ending at the bottom wall with the center of the vortex coinciding with the geometric center of the design. The longer vortex length in the convex design facilitates a symmetry of the flow domain in the cyclone. Although the convex cyclone exhibits lower centrifugal forces due to lower tangential velocities, the extended separation zone allows for better classification of finer particles, ensuring that more fine particles exit through the dust bin thereby reducing fines bypass. For the rough-surface configurations, it is observed that the natural vortex length is reduced, which corroborates previous observations [126]. Furthermore, in the rough-surface simulations, the reduction in natural vortex length is more pronounced in the convex design cyclone compared to the rough-surface standard design cyclone.

4.4.3 Cyclone Performance Analysis

Cyclone performance is characterized by pressure drop and collection efficiency. In Figure 4.9, we compare the experimental static pressure differential values measured between taps with CFD model predictions, using the $k-\omega$ SSTCC and RSM turbulent models on the smooth designs of standard and convex gas cyclones, as a function of flow rate. Across all conditions studied, the $k-\omega$ SSTCC model predictions are consistently closer to the experimental values than those of the RSM model, which tends to overestimate the pressure differential. Therefore, the choice of the $k-\omega$ SSTCC turbulence model over RSM is validated in this study. We observe that as the flow rate increases, the measured pressure differential values rise for both cyclone designs. Additionally, at all flow rates studied, the convex design shows lower pressure differential values than the standard design, a trend also captured in the CFD predictions. For the rough-design configurations, the measured pressure differential values are lower than those of the smooth designs. These rough configurations follow similar trends as the smooth designs, with pressure differential increasing with flow rate and the convex design consistently yielding lower values than the standard cyclone design. These values are summarized in Table 4.2.

Figure 4.10 presents the experimental separation efficiency curves for standard and convex gas cyclone designs with rough wall configurations at flow rates of 18 and 30 lpm,

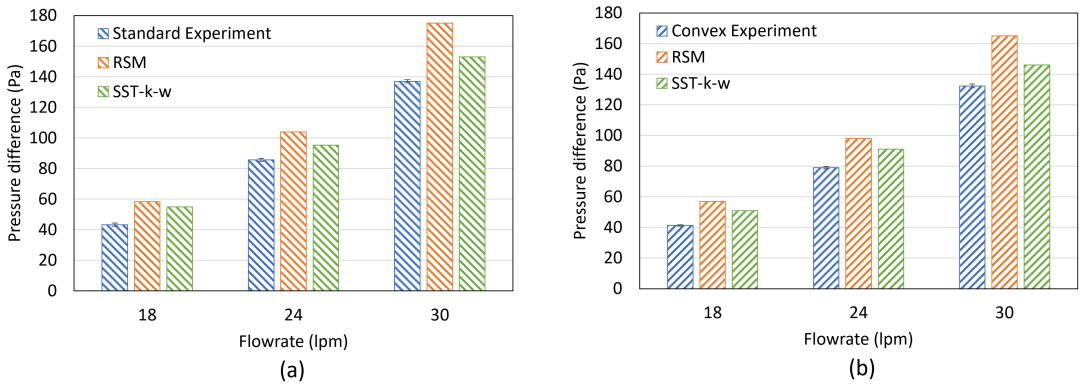


Figure 4.9: Comparion of experimental pressure differential between the taps with the computational measured values as a function of flowrate and turbulence modelling technique. (a) Standard Design (b) Convex Design

Table 4.2: Comparative analysis of performance metrics as a function of rough cyclone designs

Flowrate (lpm)	Pressure (Pa) - Experiment		Pressure (Pa) - CFD Model (k-$\omega SSTCC$)		Solids Recovery (%)		Bypass		Cut-size (microns)	
	Standard	Convex	Standard	Convex	Standard	Convex	Standard	Convex	Standard	Convex
18	40	38	46	42	82.20	75.90	0.505	0.444	3.52	4.48
30	126	122	131	127	90.68	88.04	0.696	0.631	3.31	3.51

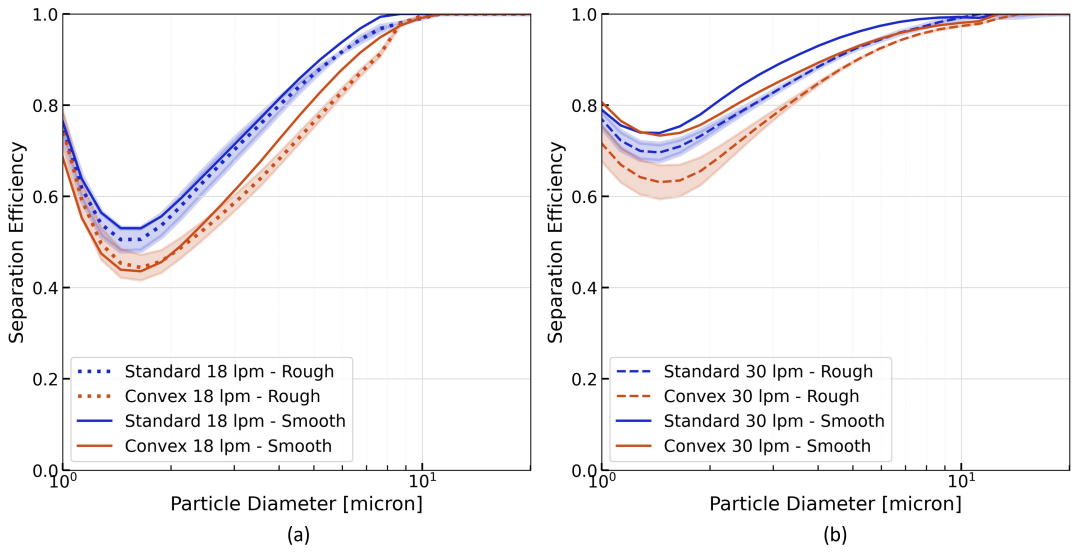


Figure 4.10: Comparison of separation efficiency curves for rough gas cyclone designs across varying flow rates, with results for smooth designs overlaid for reference.

with trends for the corresponding smooth designs included to facilitate comparison and interpretation of results. As observed in Figure 4.10a at 18 lpm, no significant change in bypass is observed between rough and smooth conic configurations. However, at 30 lpm (Figure 4.10b), rough configurations of both standard and convex designs show a reduction in bypass compared to their smooth counterparts. This effect can be explained by the CFD analysis discussed earlier. Although the percentage reduction in downward axial velocities due to surface-wall roughness near the dip-leg region is similar for both low and high flow rates, this reduction at high flow rates has a greater impact on particle trajectories. Specifically, at higher flow rates, particles are more likely to escape through the secondary vortex through the dust outlet rather than being separated through the dip leg into the collection bin. This results in a decrease in particle removal efficiency, allowing particles more opportunities to participate in classification.

Additionally, the separation efficiency curves for rough configurations tend to lie below those of the smoother counterparts. The CFD analysis shows that surface-wall roughness reduces tangential velocities within the flow domain (both cylindrical and conical sections), leading to lower centrifugal forces acting on particles. Consequently, particle separation efficiencies appear lower in rough configurations compared to smooth configurations corroborating the findings of previous studies reported by Foroozesh *et al.* [125]. Further, the trends of convex design gas cyclones yield lower bypass and coarser cut-sizes still hold for rougher configurations as observed for smooth designs. Interestingly, surface roughness reduces the collection efficiency of smooth gas cyclones. However, our findings indicate that, if the goal is to optimize the design of gas cyclone as a classifier, surface roughness could be considered a significant design variable in future research.

4.5 Summary

This chapter demonstrates the impact of conic curvature and surface-wall roughness on gas cyclone performance through a combination of CFD simulations and experimental investigations.

The comparative analysis of standard and convex cyclone designs, along with the effect of surface-wall roughness, has yielded valuable insights for classification applications. Experimental results show that smooth convex designs consistently achieve lower solids recovery to the collection bin and reduced bypass across all flow rates, favoring coarser particle separation. For instance, at a flow rate of 18 lpm, the standard cyclone design exhibited a solids recovery of 86.4% with a cut-size of 3.48 μm, increasing to 93.4% recovery and a cut-size of 2.8 μm at 30 lpm. Whereas, the convex cyclone reported solids recoveries of 79% and 89% with cut-sizes of 3.93 μm and 3.44 μm for the same respective flow rates. Further, the presence of surface-wall roughness reduces tangential velocities

in both designs, leading to lower collection efficiencies and coarser cut-sizes. This effect was more pronounced in convex designs, where roughness contributed to a shift toward coarser particle classification.

CFD simulations aid in explaining the behavior of experimental observations, particularly in the effects of roughness on axial and tangential velocities as well as pressure difference measurements. Despite reducing the overall collection efficiency, roughness introduced a variable that could be leveraged in future cyclone designs for targeted classification applications. Specifically, lower tangential velocities and increased upward axial velocities near the dip leg in rough-surface convex cyclones suggest that roughness-conic interaction may enhance the classification effect.

Chapter 5

Influence of Conic Shape on Bypass and cut size in Hydrocyclones

5.1 Background 92
5.2 CFD Modelling Methodology and Experimental Methods 94
5.2.1 Capturing the Turbulence 94
5.2.2 Air-Core Formation: Volume of Fluid (VOF) Theory 95
5.2.3 Discrete Phase Particle Motion 96
5.2.4 Simulation Details 97
5.2.4.1 Geometry and Boundary conditions 97
5.2.4.2 Meshing and Grid Independency 99
5.2.5 Model Validation 101
5.2.6 Experimental setup and Methods 103
5.3 Results and Discussion 105
5.3.1 CFD Analysis: Understanding the flow-field 105
5.3.1.1 Axial Velocity 106
5.3.1.2 Tangential Velocity 107
5.3.1.3 Radial Velocity 107
5.3.1.4 Static Pressure 109
5.3.1.5 Air-Core formation 109
5.3.2 CFD Analysis: Particle separation characteristics 109
5.3.3 Experimental Analysis: Water-only 112
5.3.4 Experimental Analysis: Particle Separation 113
5.3.4.1 Industrial case study 117
5.4 Summary 118

Chapter Introduction

The preceding chapter (4) found that convex gas cyclones experimentally exhibit coarser cut sizes with lower fines bypass compared to the standard design cyclones across all flowrates. Building on these insights, this chapter shifts its focus to hydrocyclones, investigating the impact of conic shape on bypass and cut size performance.

The chapter begins by emphasizing the need for innovative hydrocyclone designs to minimize bypass while achieving coarser cut sizes (Section 5.1). The subsequent sections detail the combined CFD modeling and experimental methodology (Section 5.2). Key aspects include accurately capturing turbulence (Section 5.2.1), modeling air-core formation using Volume of Fluid (VOF) theory (Section 5.2.2), and simulating discrete particle motion to analyze particle behavior within the flow domain (Section 5.2.3). The Section 5.2.4 encompasses simulation details, including geometry, boundary conditions, meshing, and grid independency. Section 5.2.5 presents the validation of the CFD model against experimental results reported in the literature. The experimental setup and methods, including water-only and particle separation tests, are described in Section 5.2.6.

Section 5.3 discusses the results, comparing the standard and convex hydrocyclone designs using both CFD and experimental analyses. Sections 5.3.1 and 5.3.2 examine the flow field and particle separation characteristics, highlighting how conic shape influences classification efficiency. Experimental analyses validate the CFD findings, with water-only tests (Section 5.3.3) and particle separation tests conducted with 5% solids (Section 5.3.4). Additionally, an industrial case study (Section 5.3.4.1) highlights the practical application of the findings.

Section 5.4 concludes the chapter with a summary of the key findings. These results enhance the understanding of the complex interplay between hydrocyclone geometry, fluid dynamics, and particle separation performance, offering valuable guidance for optimizing hydrocyclone design in industrial applications.

The content of this chapter is published in Separation and Purification Journal: A. K. Pukkella, D. Vega-Garcia, K. Hadler and J. Cilliers, 'Influence of conic shape on bypass and cut-size in hydrocyclones,' *Separation and Purification Technology*, vol. 361, p. 131 224, 2025. Minor modifications have been made to the original text to improve the clarity and readability of the thesis.

5.1 Background

Figure 5.1 depicts the typical Mill-Classifiers circuit. The process begins with crushed ore being introduced into a ball mill for grinding. The ground slurry is directed to either hydrocyclone or Derrick screens for classification by the slurry pump, and the overflow

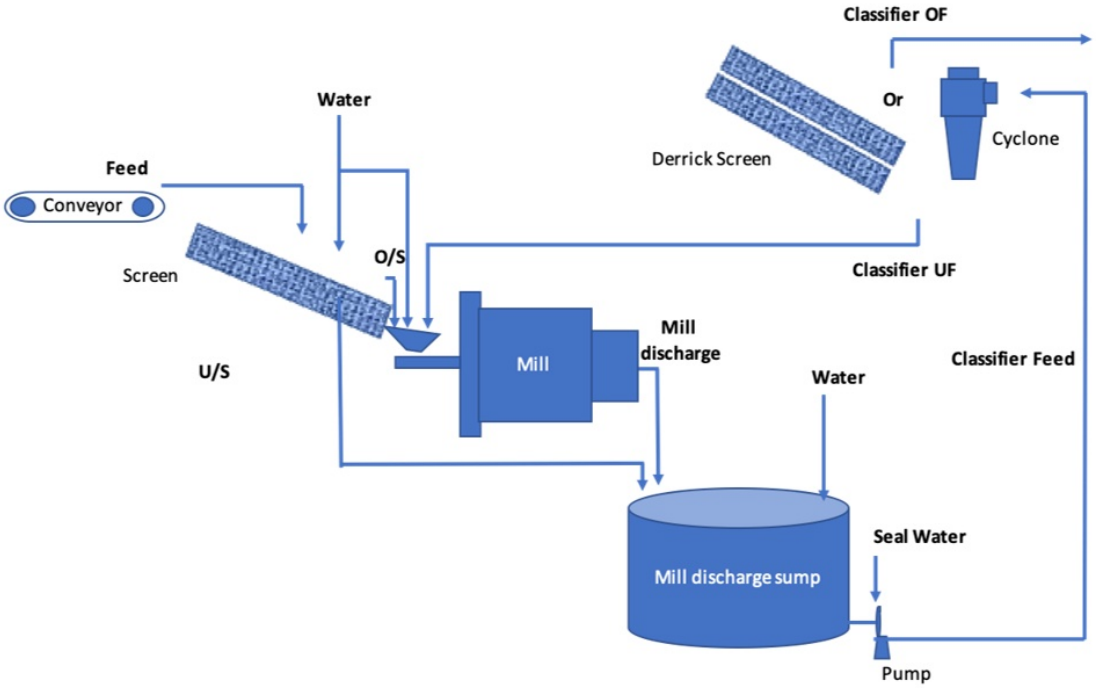


Figure 5.1: Ballmill classifier circuit with recycle, the classifier can be either Derrick screens or Hydrocyclone

concentrate containing fine particles proceeds to the flotation process to form the concentrate. Whereas the coarser particles are recycled to the mill.

Although hydrocyclones are widely used in these circuits, they often suffer from high bypass, which reduces their particle separation efficiency. Several plant case studies have reported analyses comparing the performance of hydrocyclones and Derrick screens [36, 37]. The findings indicate that screens enhance mill capacity and reduce over-grinding, primarily due to their lower bypass rates. However, incorporating screens into circuits designed for hydrocyclones entails significant costs related to plant modifications. A more cost-effective solution is to optimize the design of hydrocyclones to reduce bypass while achieving coarser cut sizes. This approach would enhance circuit performance without requiring extensive plant changes, as the system is already configured for hydrocyclones.

The literature further suggests that conic curvature significantly influences particle misplacement, particularly the bypass phenomenon. While previous studies have primarily focused on understanding this behavior through CFD simulations, there remains a gap in research that combines CFD with experimental validation, especially in the context of feed flowrate and classification performance. This study bridges that gap by not only investigating the influence of inlet velocity on bypass and cut size parameters through CFD but also validating the findings with lab-scale experiments using 3D-printed hydrocyclone designs.

5.2 CFD Modelling Methodology and Experimental Methods

5.2.1 Capturing the Turbulence

The momentum equation for an incompressible fluid is

$$\frac{\partial}{\partial t}\left(\rho u_i\right) + \frac{\partial}{\partial x_j}\left(\rho u_i u_j\right) = -\frac{\partial p}{\partial x_i} + \mu\frac{\partial^2 u_i}{\partial x_j^2} + \rho g_i \tag{5.1}$$

Expressing the instantaneous velocity (u_i) into sum of averaged velocity $(\bar{u}_i)$ and fluctuating velocity (u_i') and time averaging the momentum equation gives

$$\frac{\partial}{\partial t}\left(\rho \bar{u}_i\right) + \frac{\partial}{\partial x_j}\left(\rho \bar{u}_i \bar{u}_j\right) = -\frac{\partial \bar{p}}{\partial x_i} + \mu\frac{\partial^2 \bar{u}_i}{\partial x_j^2} + \rho g_i - \frac{\partial}{\partial x_j}\left(\rho\overline{u_i' u_j'}\right) \tag{5.2}$$

The term $\rho\overline{u_i' u_j'}$ is known as the Reynolds stress and requires a closure model to solve the equation. A common method is to approximately model the Reynolds stress to the mean velocity gradients using the Boussinesq hypothesis by using the turbulent viscosity μ_t as an isotropic scalar quantity. This methodology is employed in traditional $k-\epsilon$ and $k-\omega$ turbulence models.

However, the anisotropic nature of the Reynolds stresses is an important factor to consider in cyclone flows, highly swirling flows in combustors, rotating flow passages, and the stress-induced secondary flows. In these scenarios, the Reynolds Stress Model (RSM) is used to close the Reynolds-averaged Navier Stokes equations by solving transport equations for Reynolds stresses along with dissipation rate (ϵ). This means that seven additional transport equations must be solved in 3D.

The exact transport equations for the transport of the Reynolds stresses may be written as follows:

$$\begin{aligned}
&\underbrace{\frac{\partial}{\partial t}\left(\rho\overline{u_i' u_j'}\right)}_{\text{Local Time Derivative}} + \underbrace{\frac{\partial}{\partial x_k}\left(\rho u_k \overline{u_i' u_j'}\right)}_{C_{ij}\equiv\text{Convection}} \\
&= \underbrace{-\frac{\partial}{\partial x_k}\left[\rho\overline{u_i' u_j' u_k'} + \overline{p\left(\delta_{kj}u_i' + \delta_{ik}u_j'\right)}\right]}_{D_{T,ij}\equiv\text{Turbulent Diffusion}} \\
&\quad + \underbrace{\frac{\partial}{\partial x_k}\left[\mu\frac{\partial}{\partial x_k}\left(\overline{u_i' u_j'}\right)\right]}_{D_{L,ij}\equiv\text{Molecular Diffusion}} \underbrace{-\rho\left(\overline{u_i' u_k'}\frac{\partial u_j}{\partial x_k} + \overline{u_j' u_k'}\frac{\partial u_i}{\partial x_k}\right)}_{P_{ij}\equiv\text{Stress Production}} \\
&\quad \underbrace{-\rho\beta\left(g_i\overline{u_j'\theta} + g_j\overline{u_i'\theta}\right)}_{G_{ij}\equiv\text{Buoyancy Production}} + \underbrace{\overline{p\left(\frac{\partial u_i'}{\partial x_j} + \frac{\partial u_j'}{\partial x_i}\right)}}_{\phi_{ij}\equiv\text{Pressure Strain}} \\
&\quad \underbrace{-2\mu\overline{\frac{\partial u_i'}{\partial x_k}\frac{\partial u_j'}{\partial x_k}}}_{\epsilon_{ij}\equiv\text{Dissipation}} \underbrace{-2\rho\Omega_k\left(\overline{u_j' u_m'}\epsilon_{ikm} + \overline{u_i' u_m'}\epsilon_{jkm}\right)}_{F_{ij}\equiv\text{Production by System Rotation}}
\end{aligned} \tag{5.3}$$

Of the various terms in these equations, C_{ij}, $D_{L,ij}$, P_{ij} and F_{ij} do not require any

approximate models, however, the terms $D_{T,ij}$, G_{ij}, ϕ_{ij}, and ϵ_{ij} requires assumptions to model.

Closure of the RSM Model The quadratic pressure strain model proposed by Speziale *et al.* [165] is considered for the current modeling due to its superior performance for rotating shear flows.

$$\begin{aligned}\phi_{ij} = &-\left(C_1\rho\varepsilon + C_1 p\right) b_{ij} + C_2\rho\varepsilon\left(b_{ik}b_{kj} - \frac{1}{3}b_{mn}b_{mn}\delta_{ij}\right)\\ &+\left(C_3 - C_3\sqrt{b_{ij}b_{ij}}\right)\rho k S_{ij}\\ &+C_4\rho k\left(b_{ik}S_{jk} + b_{jk}S_{ik} - \frac{2}{3}b_{mn}S_{mn}\delta_{ij}\right)\\ &+C_5\rho k\left(b_{ik}\Omega_{jk} + b_{jk}\Omega_{ik}\right)\end{aligned}$$

$$D_{T,ij} = \frac{\partial}{\partial x_k}\left(\frac{\mu_t}{\sigma_k}\frac{\partial\overline{u_i u_j'}}{\partial x_k}\right), \epsilon_{ij} = \frac{2}{3}\delta_{ij}\rho\varepsilon\left(1 + \frac{2k}{a^2}\right) \tag{5.4}$$

The effects of buoyancy on turbulence G_{ij} in the current model are neglected as the fluid under consideration is at a constant temperature.

The term 'b_{ij}' is the Reynolds stress anisotropy tensor; 'Ω_{ij}' is the mean vorticity tensor; 'S_{ij}' is the mean strain rate; 'μ_t' is the turbulent viscosity, given by equation $\mu_t = C_\mu\rho\frac{k^2}{\epsilon}$; 'k' is the turbulent kinetic energy; and, 'a' is the speed of sound. Lien and Leschziner [166] derived the value of $\sigma_k = 0.82$ by applying gradient-diffusion model. Constants used in the quadratic pressure strain are $C_1 = 3.4, C_1^* = 1.8, C_2 = 4.2, C_3 = 0.8$, $C_3^* = 1.3, C_4 = 1.25, C_5 = 0.4$, and $C_\mu = 0.09$.

5.2.2 Air-Core Formation: Volume of Fluid (VOF) Theory

The formation of the air core is modeled using the transient Volume of Fluid (VOF) method, which assumes the non-interpenetration of two phases, *i.e.*, air and water [159]. A single set of momentum equations is solved throughout the computational domain and is shared among the phases. This approach is based on the concept of the volume fraction of a fluid. An additional variable, the volume fraction of a phase, is introduced in the model. For each control volume, the volume fractions of all phases sum to unity. At any given location (cell), the model computes aggregate properties (such as ρ and μ) shared by the phases, representing volume-averaged values. Thus, the variables and properties in any given cell can indicate either one of the phases exclusively or a mixture of the phases based on their volume fraction values. In other words, if the volume fraction of the q^{th} fluid in the cell is represented as α_q, three possible conditions can be defined as follows:

$\alpha_q = 0$: The cell is devoid of the fluid. $\alpha_q = 1$: The cell is completely occupied by the fluid. $0 < \alpha_q < 1$: The cell contains the interface between the q^{th} fluid and one or more other fluids.

The interface(s) between the phases can be tracked by the solution of a continuity equation for the volume fraction of one (or more) of the phases. For the q^{th} phase, this equation is represented as:

$$\frac{1}{\rho_q}\Big(\frac{\partial(\alpha_q\rho_q)}{\partial t} + \nabla\cdot\big(\alpha_q\rho_q\vec{v_q}\big) = \ S + \sum_{p=1}^{n}(\dot{m_{pq}} - \dot{m_{qp}})\Big) \tag{5.5}$$

Where m_{pq} is the mass transfer from phase q to phase p and m_{qp} is the mass transfer from phase p to phase q and S, represents the source term. The primary-phase volume fraction will be solved based on the following condition rather than the volume fraction equation:

$$\sum_{q=1}^{n}\alpha_q = 1 \tag{5.6}$$

A single momentum equation is solved across the entire domain, and the resulting velocity field is shared among the phases. The dependence of this momentum equation on the volume fraction of all phases is manifested through the properties of ρ and μ.

5.2.3 Discrete Phase Particle Motion

The motion of discrete particles in this study is predicted using Lagrangian particle tracking (LPT), which evaluates forces acting on individual particles. This approach is typically applied in systems with dispersed phase volume fractions of less than 10% (dilute phase assumption) [167]. For this study, the dilute phase assumption is applied throughout the computational domain. The trajectory of particles in the Eulerian continuous phase is modeled by:

$$\frac{du_p}{dt} = F_D(u - u_p) + g\frac{\rho_p - \rho}{\rho_p} + F_x \tag{5.7}$$

where u_p is particle velocity, u is fluid velocity, ρ_p is particle density, and d_p is particle diameter. The forces acting on the particle include drag, buoyancy, and other additional forces F_x. The drag force F_D is defined as:

$$F_D = \frac{18\mu}{d_p^2\rho_p}\frac{C_D}{Re_p} \tag{5.8}$$

where C_D is the drag coefficient, and Re_p is the particle Reynolds number:

$$Re_p = \frac{\rho d_p |u_p - u|}{\mu} \tag{5.9}$$

In this study, the Schiller-Naumann drag model for liquid-solid particle systems is used to calculate the drag coefficient C_D, which is given as:

$$C_D = \begin{cases} 24\left(1 + 0.15\mathrm{Re_p}^{0.687}\right)/\mathrm{Re_p} & \mathrm{Re_p} \leqslant 1000 \\ 0.44 & \mathrm{Re_p} \geqslant 1000 \end{cases} \tag{5.10}$$

Turbulent dispersion is modeled using a stochastic approach with the Discrete Random Walk (DRW) model, which incorporates instantaneous fluid velocity fluctuations for individual particle trajectories.

$$u_i' = \xi\sqrt{2k/3}$$

Here, ξ is a normally distributed random number, and k is the turbulent kinetic energy.

5.2.4 Simulation Details

5.2.4.1 Geometry and Boundary conditions

In this study, our primary objective is to investigate the effect of conic curvature on the hydrocyclone performance with a diameter of 75 mm. The geometric details and dimensions are provided in Figure 5.2a. The hydrocyclone features a square tangential inlet with a side length of 20 mm. The overflow and underflow diameters are 25 mm and 12.5 mm, respectively. Both the cylinder barrel length and the vortex finder length are equal to the diameter, 75 mm. The cone extends at an angle of 16.4^o at the apex (*i.e.*, underflow). The curvature of the conical section is designed to be parabolic-convex shape, represented by the parameter n=2. Considering the orientation of axis, the design equations to construct the curved conic surface is given by $(x-h)^2 = (y-k)$, where (h, k) = ($\frac{Du}{2}$, 0) represents the curved conic starting point and (x,y) denotes the spatial co-ordinates, here Du is the underflow diameter.

Water is considered the primary phase, with air as the secondary phase in the simulations. For modeling purposes, we define the density and viscosity of water as 1000 kg/m^3 and 1 $kg/(ms)$, respectively. Specifically, we aim to assess the impact of inlet flow rates of 1000, 1250, and 1500 mL/s, to match the lab-scale experiments. For these conditions, the inlet velocities correspond to 2.5, 3.125, and 3.75 m/s, respectively.

Both overflow and underflow outlets are configured as pressure outlets open to the atmosphere, maintaining zero gauge pressure with a backflow volume fraction of air set to 1. This boundary condition facilitates the return of air into the hydrocyclone to form

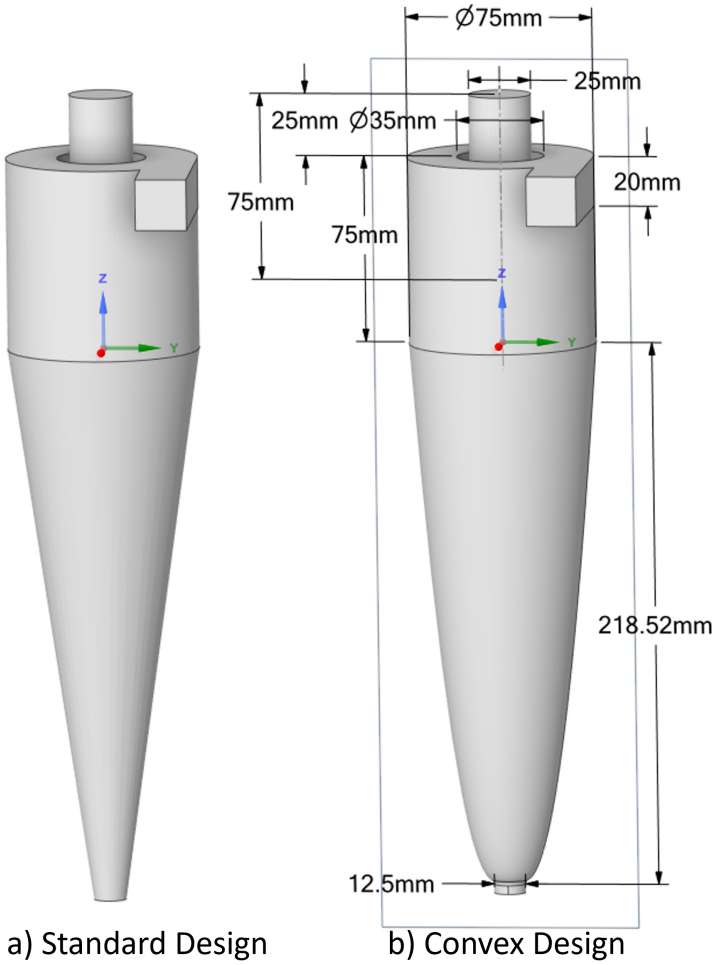


Figure 5.2: Geometrical design of hydrocyclones under study. a) The standard design b) The novel convex bottom design

an air-core, as they are open to the atmosphere in experiments. The remaining walls are treated as no-slip boundaries with scalable wall functions. Initially, the hydrocyclone is entirely filled with air at atmospheric pressure. Subsequently, water enters through the tangential inlet, swiftly swirling and occupying the wall region, generating a zone of negative pressure at the center of the hydrocyclone. This lowered pressure induces the inflow of air from the surroundings, resulting in the formation of the air-core.

Since the particle separation experiments were conducted at a solids concentration of approximately 5% by mass, we employed a Discrete Phase Model (DPM) to capture particle behavior from a Lagrangian perspective. To analyze particle separation characteristics, we applied transient Lagrangian Particle Tracking (LPT) with an assumption of spherical particles having a density of 2650 kg/m^3. Particle sizes ranging from 5 to 150 μm are considered within the LPT framework. These particle injections are individually created based on their size and released from the inlet, with 1000 particles in each injection. The underflow is modelled as a trap for particles and the overflow is modelled with escape boundary conditions for particles. Particle tracking is performed with a fluid time-step of 10^{-5} s.

For solving the governing mass and momentum transport equations, the pressure-based solver in ANSYS FLUENT is employed. The Coupled Scheme algorithm is utilized for pressure-velocity coupling, and pressure interpolation is conducted using the PREssure STaggering Option (PRESTO scheme). The momentum equations are discretized using the higher-order Quadratic Upstream Interpolation for Convective Kinematics (QUICK) scheme. The volume fraction is discretized using the modified High-Resolution Interface Capturing (HRIC) method, and first-order upwind discretization is selected for the turbulence equations and Reynolds stress. In our simulations, the convergence criterion is defined based on residual errors, set at 10^{-5} for all continuity and velocity and turbulence parameters. Each simulation is run for a minimum of 5-6 times their corresponding residence time, equivalent to 10 seconds of physical time. Following convergence, a time-averaging procedure is implemented over several thousand iterations, approximately equivalent to their residence times of $\approx$ 2 seconds of physical time.

5.2.4.2 Meshing and Grid Independency

Figure 5.3 depicts the unstructured hexahedral mesh created in ANSYS ICEM CFD using the blocking technique. In the current work, the viscosity-affected inner region is modeled using a scalable wall function, which is effective for meshes with y^+ values as low as 1. This approach overcomes the limitations of standard wall functions by ensuring that the solver's y^*(used internally by Fluent) remains above 11.225, the intersection point of the linear and logarithmic law profiles. The scalable wall function algorithm selects the higher value between 11.225 and y^*, maintaining boundary layer accuracy across different mesh

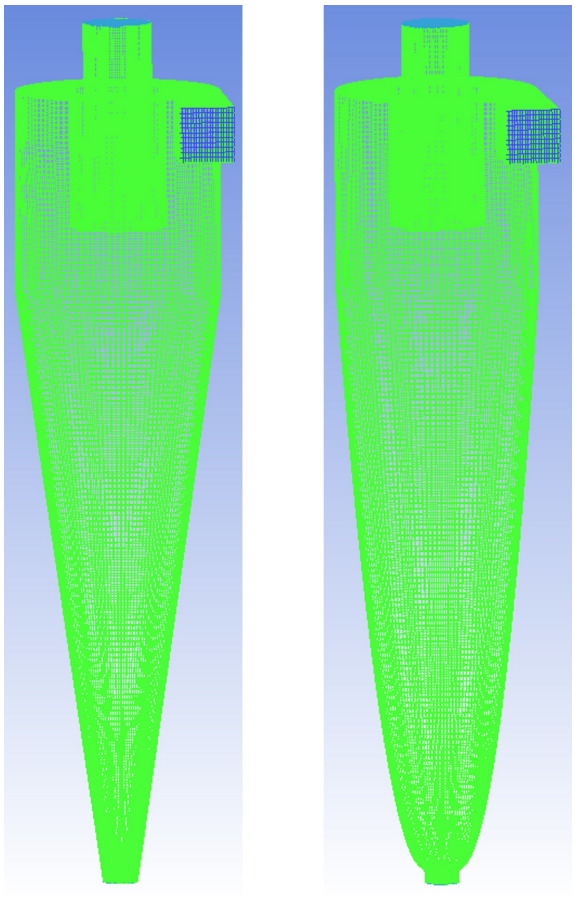


Figure 5.3: Unstructured hexahedral mesh for both standard and convex hydrocyclone designs.

Table 5.1: Details of grid convergence study calculations using GCI method

	Mesh Name	Number of Cells	f_i	$r_{i,i+1}$	$e_{i,i+1}$	$\epsilon_{i,i+1}$	GCI %	R	α
Pressure drop [Pa]	Exact Solution		70796.17						
	M1	681656	70894	1.09057	-355.6	0.00501	0.17319		
	M2	525534	71250	1.10454	-2171	0.03047	0.79616	0.16461	1.00508
	M3	289989	73421						
Turbulent Dissipation Rate [$m^2/s^3/m^3$]	Exact Solution		0.07757						
	M1	681656	0.07954	1.0905	-0.0062	0.07885	3.10085	0.19753	1.07889
	M2	525534	0.08581	1.1045	-0.0342	0.3991	12.0097		
	M3	389989	0.12007						

densities.

Higher mesh density enhances accuracy but increases computational cost. To ensure grid independence, we tested three meshes: M1 (fine), M2 (medium), and M3 (coarse) details are given in Table 5.1, for an inlet flowrate of 1500 mL/s. We measured the overall pressure drop and turbulent dissipation rate per hydrocyclone volume (Table 5.1), along with radial profiles of tangential velocities at Z = 217 mm, scaled to the inlet velocity of 3.75 m/s (Figure 5.4b). Based on the data in Table 5.1 and Figure 5.4, mesh M2 was found to capture the swirling flows inside the hydrocyclone with sufficient accuracy, achieving grid-independent results.

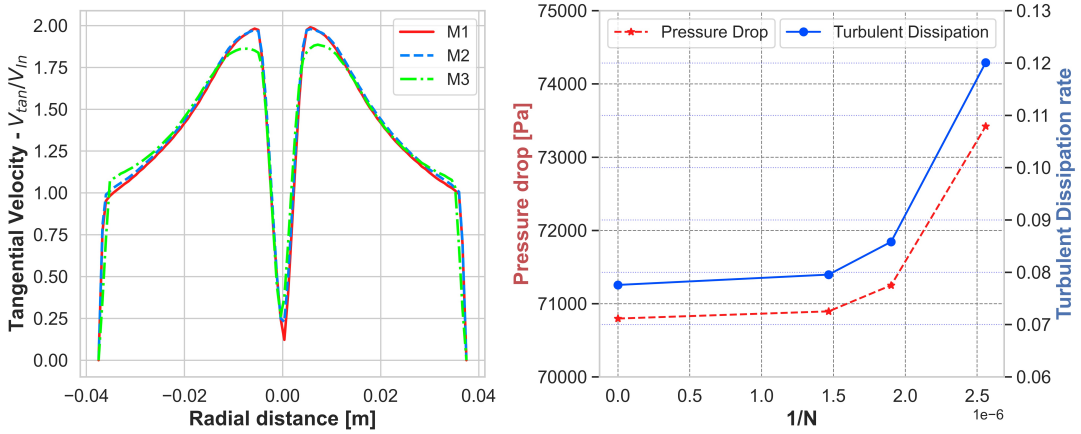


Figure 5.4: Variation of measured quantities on a center-line for an inlet flowrate of 200 kg/s (Height Z = 140 cm, measured from the bottom). a) Pressure drop b) Tangential Velocity scaled with the inlet velocity.

To further confirm mesh independence, we conducted a Grid Convergence Index (GCI) study following the method outlined by Roache [168]. The GCI measures the deviation of the computed value from the asymptotic solution, using three grids: M1, M2, and M3, with N_1, N_2, and N_3 cells, respectively. The relative error ε_{12} and ε_{23}, grid refinement ratio (r_{12}, r_{23}), and the convergence order p were calculated iteratively to determine the GCI values. Table 5.1 shows that the GCI decreased with grid refinement, indicating reduced dependence on cell size. The pressure drop and turbulent dissipation rate α values approached unity, indicating solutions within the asymptotic range. Figure 5.4, qualitatively supports these results, confirming grid independence. Mesh M2 was therefore selected for all simulations.

5.2.5 Model Validation

The CFD model was validated through two test cases. In the first case of water only experiment, we compare the flow profiles of axial velocity, tangential velocity, and total pressure drop with the experimentally reported values by Hsieh [12]. In the second case, we assess the particle separation characteristics of a dilute suspension of limestone with

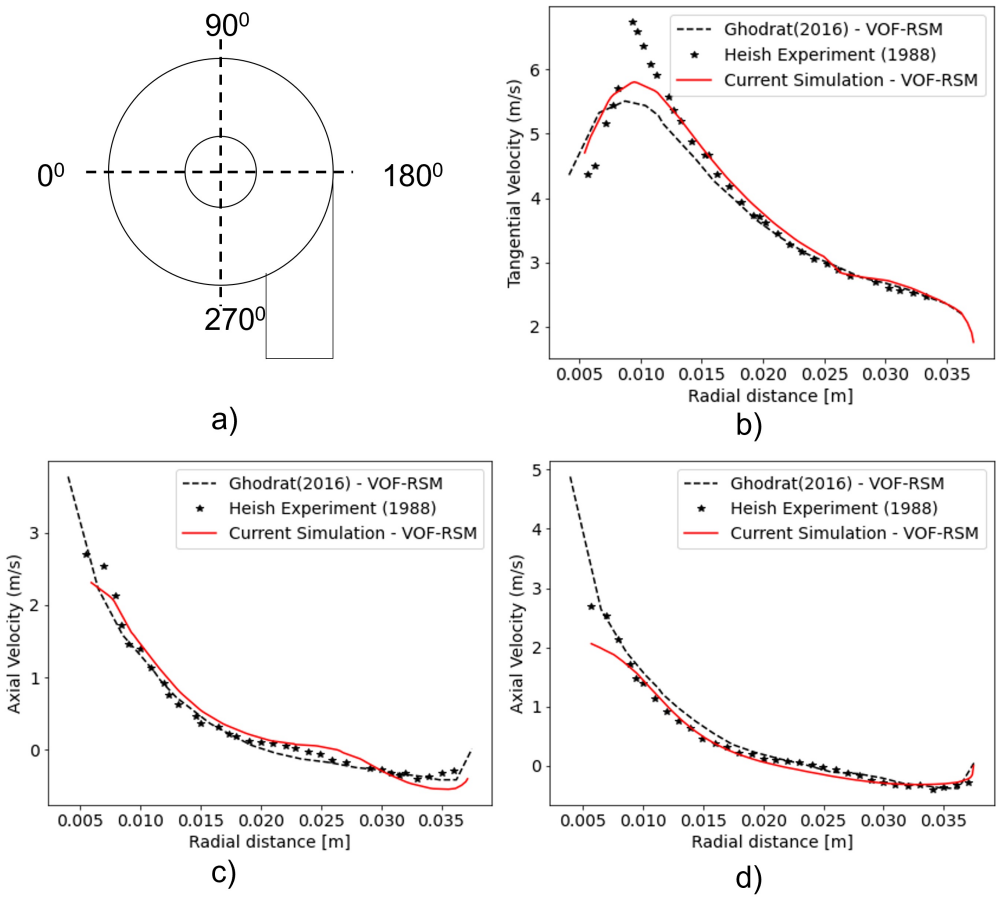


Figure 5.5: Comparison of the experimental LDA measurements of tangential and axial velocities reported by Hsieh [12] and Ghodrat *et al.* [13], with the CFD predictions of RSM - VOF model.

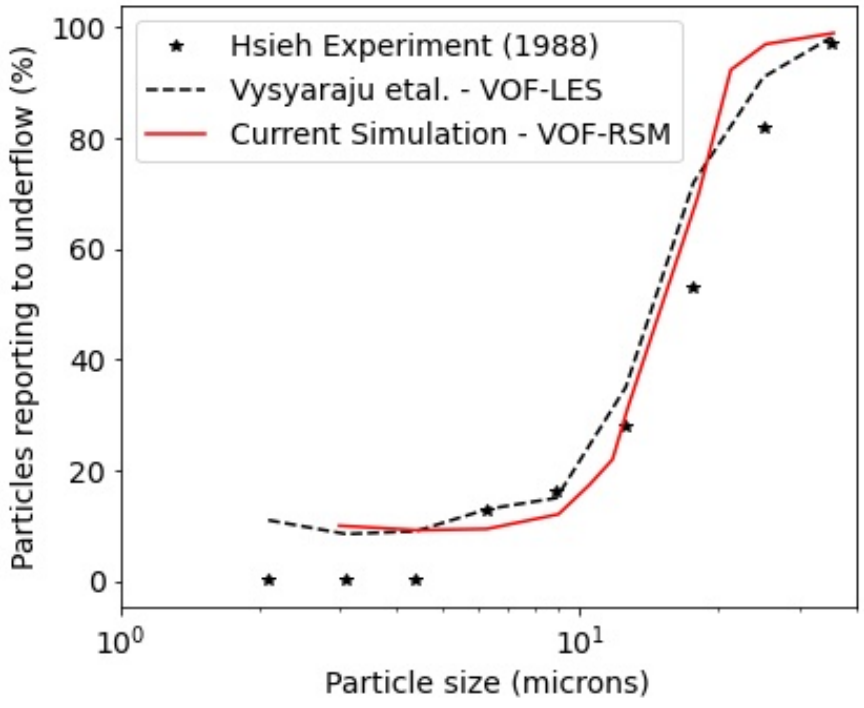


Figure 5.6: Validation of separation efficiency curve for the classification of limestone at feed solids concentration 4.88% (by volume) reported by Hsieh [12], with the CFD predictions by Vysyaraju *et al.* [14] model (LES - VOF) and the current simulation (RSM - VOF).

Table 5.2: Quantitative comparison of flow parameters between the experiments and predicted results

	Pressure Drop (Pa)	Water Split (%)
Hsieh [12](Experiments)	46.7	4.9
Current Method (RSM-VOF)	42.35	5.22
Ghodrat *et al.* [13] (RSM-VOF)	43.3	4.48

a solids loading of 4.88% (by weight), as reported by Hsieh [12]. Since the experiments were conducted for different objectives, the chosen inlet velocities for CFD simulations are 2.28 m/s and 2.5 m/s, respectively, to match the experimental conditions. The pressure at both the outlets (vortex finder and spigot) is set to 1 atm. We use the RSM model to capture turbulence and the VOF method to resolve the multiphase flow phenomenon. Given that the solids concentration is less than 10% (by volume), we employ LPT to study the particle separation characteristics.

Figure 5.5 compares the predicted flow profiles with experimentally reported values of tangential and axial velocities along horizontal lines spanning 0° to 180° and 90° to 270° at a location 60 mm from the cylinder wall. As shown in Figure 5.5, our current simulation method yields tangential and axial velocity predictions that closely align with both the experimental results of Hsieh [12] and the findings from previous modeling studies [13]. Figure 5.6 shows the separation efficiency curve calculated by the LPT model for the classification of limestone. For comparison, we also include LPT results obtained using the VOF-LES method as reported by Vysyaraju *et al.*[14]. As shown in Figure 5.6, the particle separation efficiency results from both the VOF-RSM and VOF-LES models are comparable with the experimental results.

Further comparisons are provided in Table 5.2, which summarizes key parameters. The model successfully reproduces the inlet pressure drop and underflow water split, with predictions closely matching experimental values, and a maximum prediction error of less than 10%. Therefore, we have extended the developed model to analyze and compare the performance of smooth and rough hydrocyclone in the following sections.

5.2.6 Experimental setup and Methods

We utilized rapid prototyping to 3D print the hydrocyclones. The hydrocyclone was fabricated using high-resolution Stereolithography (SLA) technology with a FormLabs (Form-3) printer, achieving a fine surface resolution of less than 25 μm, as shown in Figure 5.7a. The 3D-printed hydrocyclone was installed within a casing and sealed with rubber gaskets, as illustrated in Figure 5.7b. Figure 5.7c shows the flow domain, where the fluid enters the hydrocyclone inlet under pressure.

Figure 5.8b provides a schematic of the experimental setup, which includes a variable-

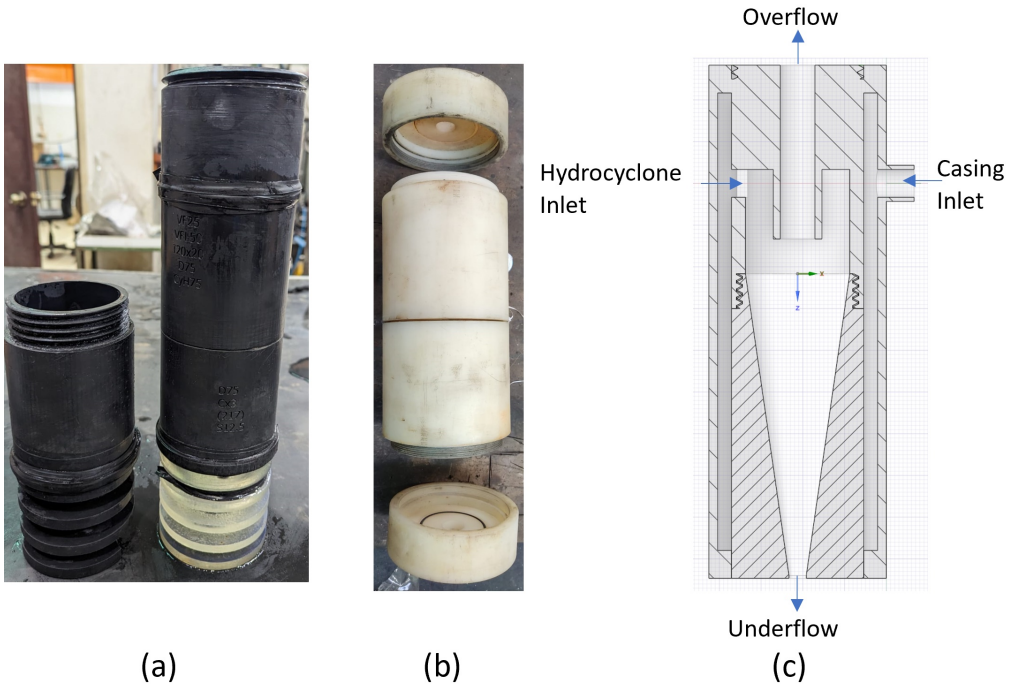


Figure 5.7: (a) 3D printed hydrocyclones, (b) Casing, and (c) Schematic of flow domain.

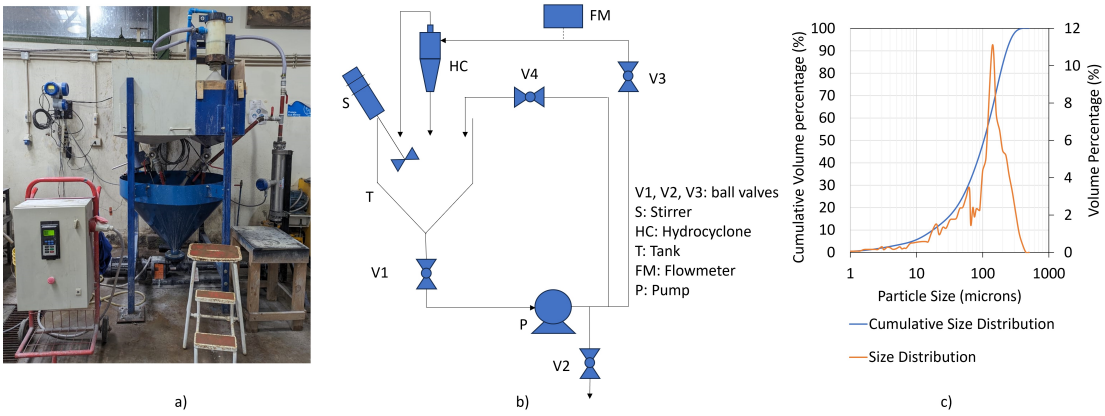


Figure 5.8: (a) Laboratory experimental rig, (b) Schematic of experimental setup, and (c) Feed particle size distribution.

speed centrifugal pump, a conical mixing tank designed to prevent particle settling, digital flowmeters, and bypass valves for regulating flow into the hydrocyclone. For feed sample preparation, silica pebbles having a density of 2650 kg/m^3 were ground in a ball mill to achieve a particle size distribution with a P_{50} of 100 μm, a P_{90} of 220 μm, and a maximum particle size under 450 μm. The particle size distribution of the feed is shown in Figure 5.8c. All experiments were conducted under identical operating conditions, with a solids concentration of 50 g/L in water at 15°C. The stirrer was activated before introducing solids into the sump tank to ensure uniform mixing and prevent particle aggregation. Once the suspension was well-mixed, the pump was activated, and the valves were adjusted to maintain the desired flow rates of 1000 mL/s (V1), 1250 mL/s (V2), and 1500 mL/s (V3). After reaching the target flow rate, the system was run for 10 minutes to achieve a steady state.

Timed samples were collected from both the underflow and overflow streams to determine flow rates. These samples, along with those from the feed, were dried in a furnace to measure solids concentration. Wet samples were analyzed for particle size distribution (PSD) using a Malvern Mastersizer 3000. To ensure accuracy, flow rate determinations, solids concentration measurements, and PSD analyses were performed in triplicate for selected experiments, with a standard deviation error of less than 5% observed.

The experimental conditions in this study were deliberately chosen to provide controlled and stable flow conditions. Operating at a solids concentration of approximately 5 wt% and fixed underflow diameter ensures that the effects of solids loading and geometry (ie., underflow diameter) on bypass and classification performance can be isolated. Previous studies (e.g., Ghodrat *et al.* [169]) have shown that bypass is primarily influenced by the underflow diameter and is less sensitive to solids loading in the range of 4.1% to 30%, supporting the validity of the dilute concentrations. While industrial applications typically involve higher solids concentrations and larger hydrocyclone diameters, the findings of this study are expected to remain relevant, although with an expectation of higher cut sizes.

5.3 Results and Discussion

5.3.1 CFD Analysis: Understanding the flow-field

In this section, we present CFD results comparing key flow properties, including axial, tangential, and radial velocity, pressure distribution profiles, and air-core formation, in standard and convex design hydrocyclones. We observed that, when scaled with the inlet velocity, the flow velocities (tangential and axial) exhibit similar trends. Therefore, for the sake of brevity and clarity, we exclusively present results for the flow rate of 1500 mL/s. Table 5.3 reports the flow and particle separation performance metrics for both the hydro-

Table 5.3: CFD model comparative analysis of performance metrics as a function of hydrocyclone design

Inlet flowrate-(mL/s) Velocity-[m/s]	Underflow recovery (%)		Pressure (Pa)		cut size (microns)		Bypass (%)		Sharpness		Imperfection Index	
Case	Standard	Convex	Standard	Convex	Standard	Convex	Standard	Convex	Standard	Convex	Standard	Convex
1000 [1]	9.26	6.06	30569	27329	24.64	28.25	27.5	21.0	0.36	0.45	0.55	0.40
1250 [1.25]	8.53	5.33	48356	43768	23.53	27.05	30.21	23.4	0.42	0.48	0.50	0.35
1500 [1.5]	7.62	4.65	71811	65064	22.66	26.24	31.31	26.2	0.44	0.49	0.47	0.34

cyclone as a function of inlet flowrate. It is evident from these values that underflow water recoveries decrease with an increase in flow rate for both designs, corroborating previous observations made by Vakamalla *et al.* [170]. However, the convex design hydrocyclone consistently yields lower underflow water recoveries across the range of flow rates tested.

5.3.1.1 Axial Velocity

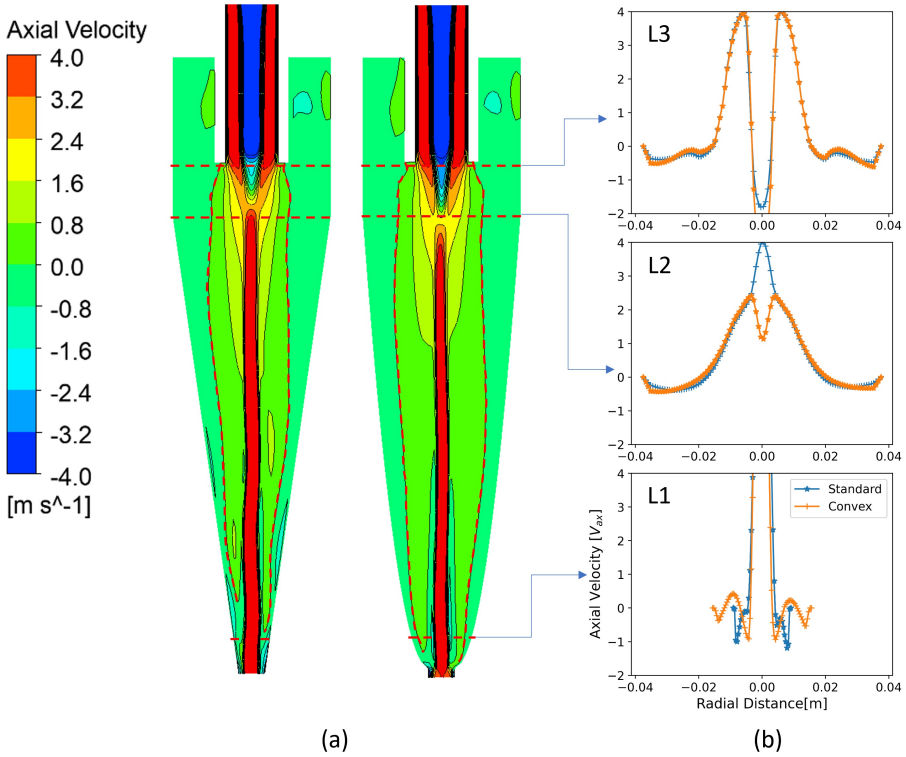


Figure 5.9: Effect of conic design on axial velocity profiles inside hydrocyclones at 1500 mL/s flowrate: a) Contour plots b) radial profiles at three axial locations (L1, L2, and L3)

Figure 5.9 shows the axial velocity distribution contours and their radial profiles at the selected locations comparing the standard and convex designs. Axial velocity distribution is characterized by downward spiral motion near the wall (negative velocities) and upward vortex flow near the air-core (positive velocities). In Figure 5.9a, the red dotted line indicates the Locus of Zero Vertical Velocity (LZVV), which separates the upward and downward flow regions. Figure 5.9b demonstrates how the liquid axial velocity is zero at the wall, initially declines due to the downward vortex flow, and then gradually increases towards the air-core water interface. Further, these profiles in the air domain either con-

tinue with a positive slope or negative depending upon the proximity to underflow and overflow, respectively. In the air-core region, it is observed that positive axial velocities are observed for both standard and convex designs in the vicinity close to the underflow, indicating that air is being entered from the underflow. Similarly, air also enters into the hydrocyclone from the overflow yielding downward axial velocity profiles. Because of the collision of upward air-flow from underflow and downward air-flow from overflow, the liquid is squeezed to vortex finder walls and quickly exits along the wall through the overflow. This behavior is identified by the regions of higher axial velocities near the internal walls of the vortex finder.

In the vicinity of the apex region, as illustrated from Figure 5.9b L1, it is observed that the downward velocities near the wall for standard design are more pronounced than compared to the convex design hydrocyclone which may negatively affect the classification process by yielding higher bypass in standard design. From Figure 5.9b L2 and L3, it is observed that the standard design has comparable axial velocity profiles to the convex design in the cylinder and conic sections. The positive and relatively low axial velocities observed near the apex in the convex design suggest that particles would experience greater residence time before exiting the system compared to the standard design. This extended residence time allows the finer particles that are typically bypassed through in standard design to participate more in classification.

5.3.1.2 Tangential Velocity

The tangential velocity is one of the key parameters that determine the particle separation efficiency as it directly impacts the centrifugal force inside the hydrocyclone. Figure 5.10a depicts the contour plots of tangential velocity profiles comparing the standard and convex design hydrocyclones. The standard design shows consistently higher tangential velocities, particularly in the cylindrical and conical sections, which results in stronger centrifugal forces acting on the particles. This higher tangential velocity contributes to the smaller cut sizes observed in the standard hydrocyclone. By contrast, the convex design exhibits lower tangential velocities, leading to weaker centrifugal forces and consequently larger cut sizes.

5.3.1.3 Radial Velocity

Figure 5.10b displays the radial velocity contour plots comparing standard and convex hydrocyclones. It is observed that near the center core, the radial velocity is positive (outward) on one side and negative on the other. These radial velocities at the center of the hydrocyclone help transport particles from the center to the walls [171]. In the standard design, higher radial velocities are observed near the center, where particles are transported outward more aggressively. This contributes to quicker separation but

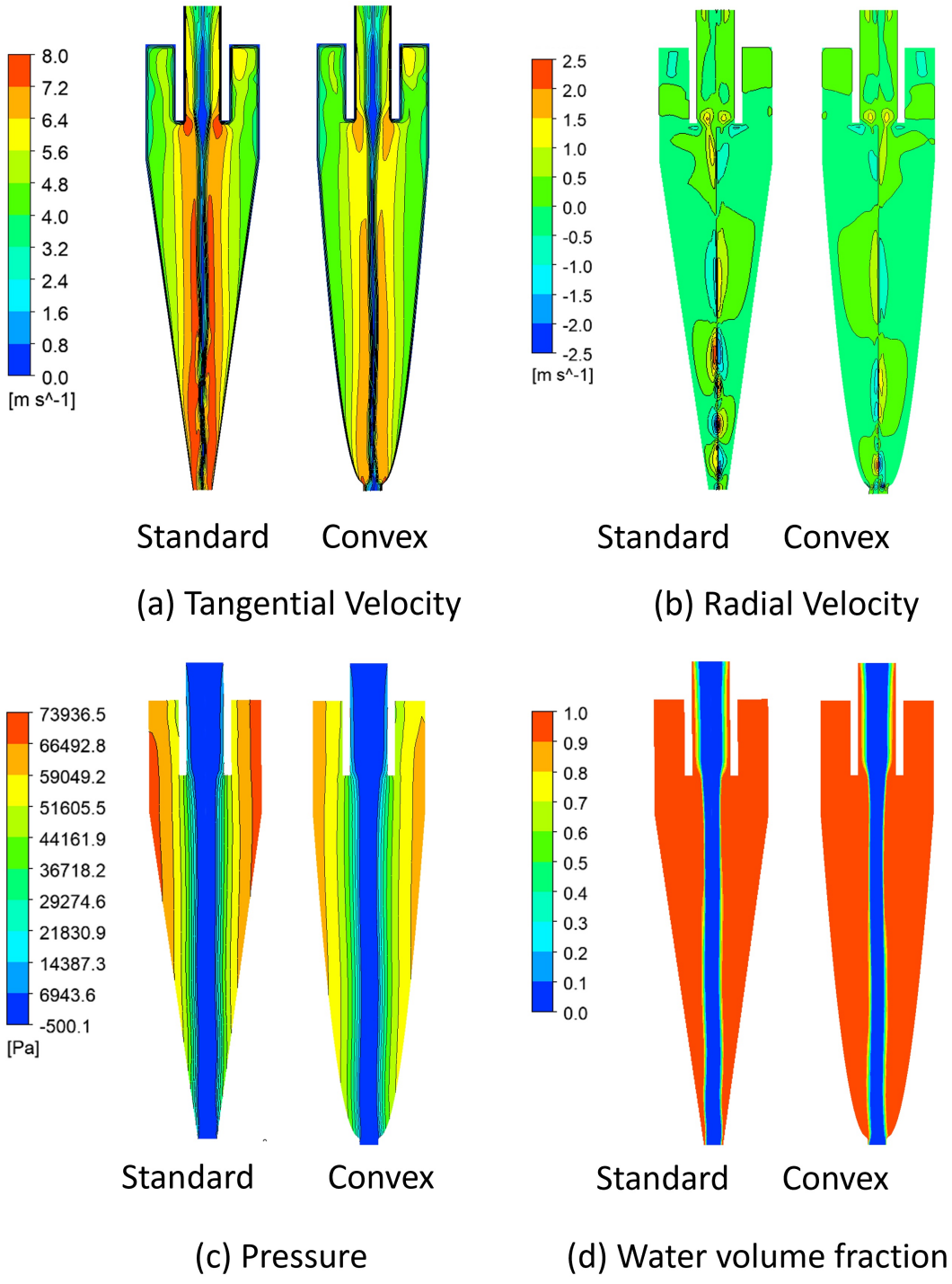


Figure 5.10: Effect of hydrocyclone design on the flow quantities for a flowrate of 1500 mL/s: a) Tangential velocity, b) Radial velocity, c) Pressure distribution, and d) Water volume fraction.

also a higher chance of bypassing finer particles through the underflow. In the convex design, lower radial velocities are seen throughout the hydrocyclone. This, coupled with the lower downward axial velocities, suggests that particles, particularly finer ones, have more time to remain in the liquid domain and participate in the classification process, reducing bypass.

5.3.1.4 Static Pressure

Static pressure represents a crucial parameter for assessing energy loss and flow behavior within the hydrocyclone. Figure 5.10c illustrates the contour plots of static pressure distribution within the hydrocyclone designs under examination. It is noteworthy that, for both designs, static pressure radially increases from the center towards the wall, resulting in a low-pressure area at the core's center. This low-pressure zone is responsible for drawing external air into the domain, forming an air-core. The contour plot demonstrates that axial variations in the pressure distribution profile are minimal in both designs when compared to radial variations. The overall pressure drop across the hydrocyclone is calculated by determining the difference in static pressure between the inlet and overflow and underflow. The overall pressure drop measured for both designs at all the flow rates under study is reported in table 5.3. It is observed that as the inlet velocities increase the overall pressure drop increases. It is interesting to observe that the overall pressure drop measured for the convex design at all the flow rates is lower than the standard design.

5.3.1.5 Air-Core formation

Figure 5.10d depicts the stable and complete air-core formation of both standard and convex-design hydrocyclones. It is observed that the convex design air-core thickness is slightly reduced near the cylinder-conical section intersection in comparison to the standard one. Thus, the convex hydrocyclone offers a slightly higher available separation space (i.e., liquid domain) when compared to the standard design.

5.3.2 CFD Analysis: Particle separation characteristics

Particles of various sizes (5, 10, 22, 35, 60, 105, and 150 μm) were injected through the inlet. Depending on their size, these particles would either report to the underflow or the overflow. Separation efficiency equivalent to partition number is defined as the ratio of the number of particles that are collected at the underflow to the number of particles that are released through the inlet. The separation efficiency curve is constructed by plotting the separation efficiencies as a function of particle size. The primary descriptor is the cut size (D_{50}); particles larger than the cut size have a greater probability of reporting to the underflow. Another measure, the sharpness index is defined as the ratio of D_{25} (the size

at which 25% of particles go to the underflow) to D_{75} (the size at which 75% of particles go to the underflow) a value of 1 indicates a perfect separation. The imperfection index, denoted as $I = \frac{D_{75}-D_{25}}{2D_{50}}$ is another commonly used metric, where smaller values of 'I' suggest better separation. Usually, the value of 'I' ranges from 0.2 to 0.6, and effective classification is achieved when the average value falls between 0.2 and 0.3 [14].

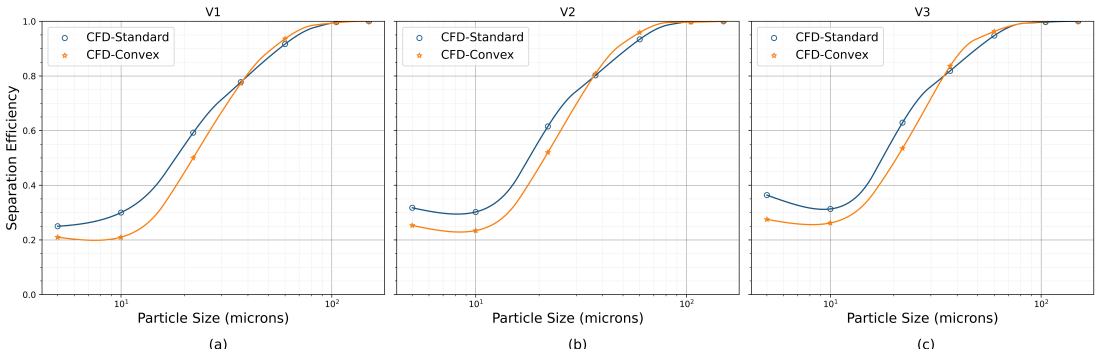


Figure 5.11: Comparison of CFD predictions for particle separation characteristics in standard and convex hydrocyclone designs as a function of inlet flowrate.

Figure 5.11 compiles particle separation efficiencies for both standard and convex design hydrocyclones across various inlet velocities. For a given flow rate, we notice that as particle size increases, the likelihood of particles ending up in the underflow also increases, thus increasing separation efficiency values. In Figure 5.11, it's evident that the separation efficiency of the convex hydrocyclone is consistently lower than that of the standard design, indicating coarser cut sizes. This trend persists across all examined flow rates. As the inlet flow rate increases, the separation efficiency curves shift leftward, signifying smaller cut sizes. This phenomenon is observed in both standard and convex-design hydrocyclones. The separation efficiency values corresponding to smaller particle sizes quantitatively represent the fines bypass fraction. This bypass fraction strongly correlates with the underflow split. Notably, the fines bypass fraction of the convex design is consistently lower than that of the standard design. Additionally, we have corrected the separation efficiency curves with the corresponding bypass fractions. These curves allowed us to extract the parameters of D_{25}, D_{50} and D_{75} from Figure 5.11, enabling the calculation of the cut size (corrected), sharpness and imperfection index and tabulated in the Table 5.3. These indices help us quantify the quality of classification [21].

It is observed from Table 5.3 that as the flowrate increases, the bypass increases for both designs. Notably, at any given flow rate under study, the convex design hydrocyclone consistently produces a lower fraction of fines bypassed to the underflow, along with a coarser cut size, in comparison to the standard design. It is observed that the sharpness of separation increases with an increase in flowrate for both the designs, however, the convex design exhibited a higher sharpness of classification than compared to the standard design for all the flowrates studied. Similarly, the imperfection index for the convex design is low compared to the standard design at all the flow rates studied; the lowest value reported

is for the highest flow rate. Based on the observations reported in Table 5.3 it can be safely assumed that the convex design hydrocyclone offers a superior quality of separation compared to the standard design hydrocyclone.

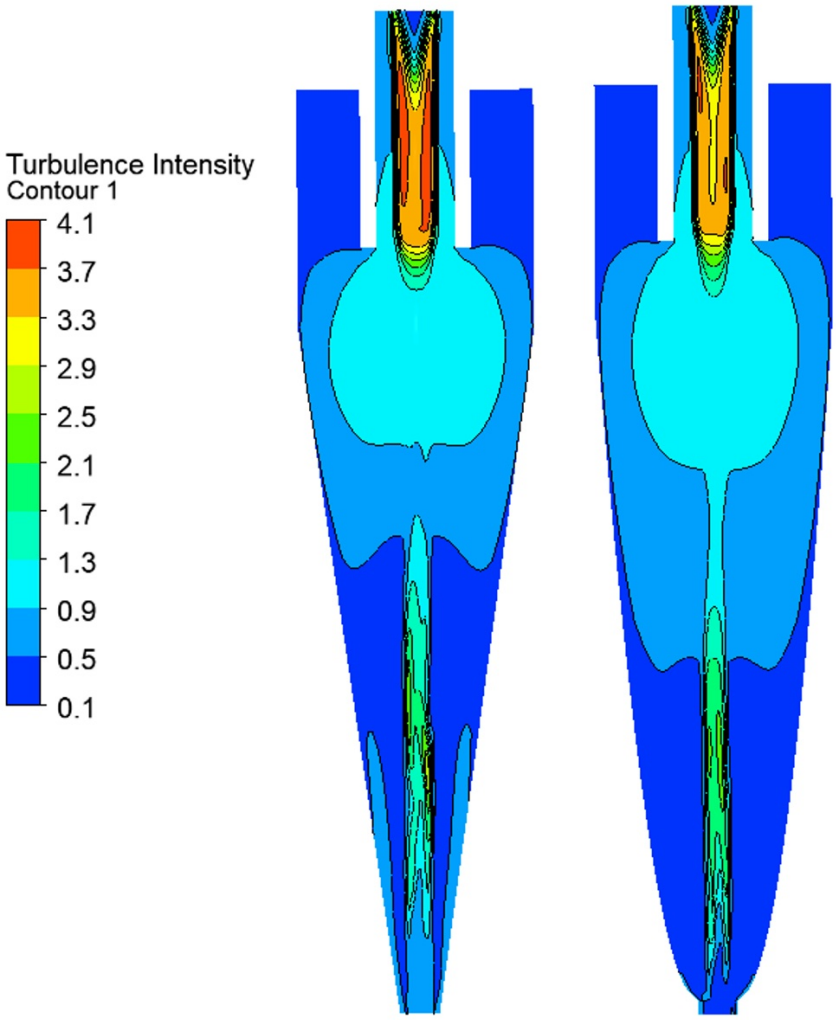


Figure 5.12: Effect of conic design on turbulent intensity profiles inside hydrocyclones at 1500 mL/s flowrate

To gain valuable insights into the coarser cut size behavior of convex design hydrocyclone, we examined the distribution of turbulent intensity profiles. Turbulence Intensity ($TI = \frac{\sqrt{\overline{u'^2}}}{\overline{U}}$) is defined as the ratio of root mean square velocity of fluctuations due to turbulence to mean velocity. In hydrocyclones, turbulent fluctuations result from extensive mixing at the inlet region, flow reversal near the spigot zone, and the presence of large velocity gradients within the domain as reported by Vakamalla and Mangadoddy [172]. Previous studies have discussed the role of turbulence on particle preferential migration due to turbophoerosis [158, 159]. Figure 5.12 illustrates the contour plots of turbulent intensities for both designs at the maximum inlet flow rate under the current study.

As depicted in Figure 5.12, the convex design exhibits higher turbulent intensities inside the entire liquid domain compared to the standard design. Because of the increased

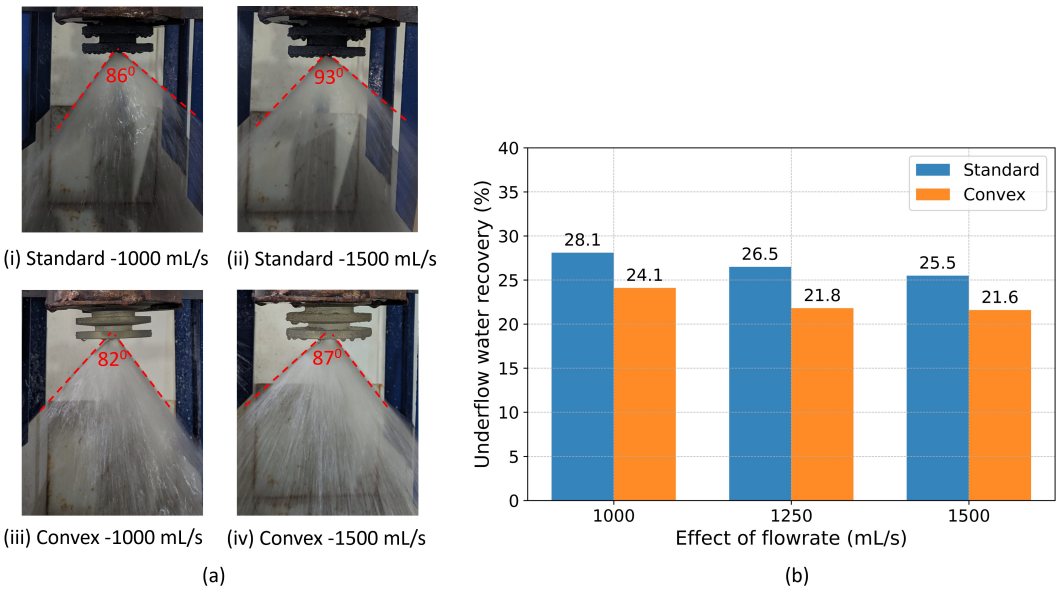


Figure 5.13: (a) Underflow spray profiles as a function of design and flowrate (b) Effect of flowrate on underflow water recoveries as a function hydrocyclone design

turbulent intensities in most of the liquid domain, enhances the chance of particles participating in classification, causing finer particles to be entrained by the upward-rising flow. This increased turbulent intensity combined with the increased tangential velocities and pressure near the spigot region increases the chances of finer particles getting dislodged between the coarser particles. Consequently, finer particles have a greater probability of being entrained by the secondary upward flow, resulting in a reduction in bypass.

5.3.3 Experimental Analysis: Water-only

This section investigates the impact of conic curvature design on the performance of hydrocyclones using both water-only and 5% solids experiments. The underflow water split (R_f), defined as the ratio of water recovered in the underflow to the total water in the feed, serves as a key metric for evaluating hydrocyclone performance. In practice, the separation of solids and liquids in a hydrocyclone is often imperfect. Some solids may exit through the overflow, while a portion of the feed water may report to the underflow. To quantify the separation efficiency, solids recovery (R_s) is employed.

Previous studies have investigated underflow spray profiles as performance indicators for hydrocyclones [173–175]. Figure 5.13a illustrates the underflow exiting the hydrocyclone, which is open to the atmosphere and forms a spray-type discharge. The discharge angles vary depending on process and design variables. It is observed that as the flow rate increases from 1000 mL/s to 1500 mL/s, the underflow spray discharge increases for both designs. However, the convex-design hydrocyclone consistently exhibits lower discharge angles compared to the standard design at corresponding flow rates. Van Deventer *et al.* [176] developed and experimentally validated a theoretical model to predict

the relationship between spray profiles, underflow behavior, and velocity components. It is reported that lower flow rates result in lower spray angles, which are associated with reduced tangential and axial velocities [176]. In our CFD analysis presented in the previous section, the convex-design hydrocyclone consistently demonstrated lower tangential velocities and reduced downward axial velocities at the underflow. These observations align with the findings of Van Deventer *et al.*, corroborating that the lower velocity profiles in the convex hydrocyclone contribute to the observed reduction in discharge spray angles compared to the standard hydrocyclone.

Figure 5.13b illustrates the trends in underflow water recovery (R_f) as a function of flow rate and hydrocyclone design. The results show that for both designs, underflow water recovery decreases slightly with increasing flow rate, reflecting similar trends observed in the CFD simulations. Additionally, across all flow rates studied, the convex design hydrocyclone consistently exhibits lower underflow water recoveries compared to the standard design. Although the experimental and CFD studies share identical hydrocyclone design configurations, notable differences exist in their predictions. These discrepancies are likely due to variations in the flow domain geometries. In the experimental setup, the hydrocyclones are housed within a casing, with the fluid entering the hydrocyclone after swirling through the annular gap between the hydrocyclone body and the casing. This geometric difference may account for the observed variations in performance between the experimental and CFD results.

5.3.4 Experimental Analysis: Particle Separation

Table 5.4: Experimental observations of underflow recoveries for different flow conditions as a function of hydrocyclone design. Water-only data is explicitly labeled; all other data corresponds to 5% solids experiments.

	Flow Split (Rv) - Water Only		Flow Split (Rv)		Water Splits (Rw)		Solids Splits (Rs)	
Flowrate (mL/s)	Standard	Convex	Standard	Convex	Standard	Convex	Standard	Convex
1000	28.1	24.1	31.8	23.6	54.0	56.0	46.0	44.0
1250	26.5	21.8	29.2	22.9	49.9	51.0	50.1	49.0
1500	25.5	21.6	27.9	24.4	46.0	50.0	54.0	50.0

Table 5.4 summarizes the experimental observations of underflow splits, including flow splits for both water-only and 5% solids experiments, as well as water splits and solids recovery for the 5% solids experiments, comparing the standard and convex hydrocyclone designs. Figure 5.14 illustrates the effect of flow rate on underflow solids recovery for each hydrocyclone design. The results show that solids recovery increases with flow rate for both designs, aligning with the trends reported by Cilliers and Harrison [177]. However, solids recovery is consistently lower in convex hydrocyclones compared to the standard

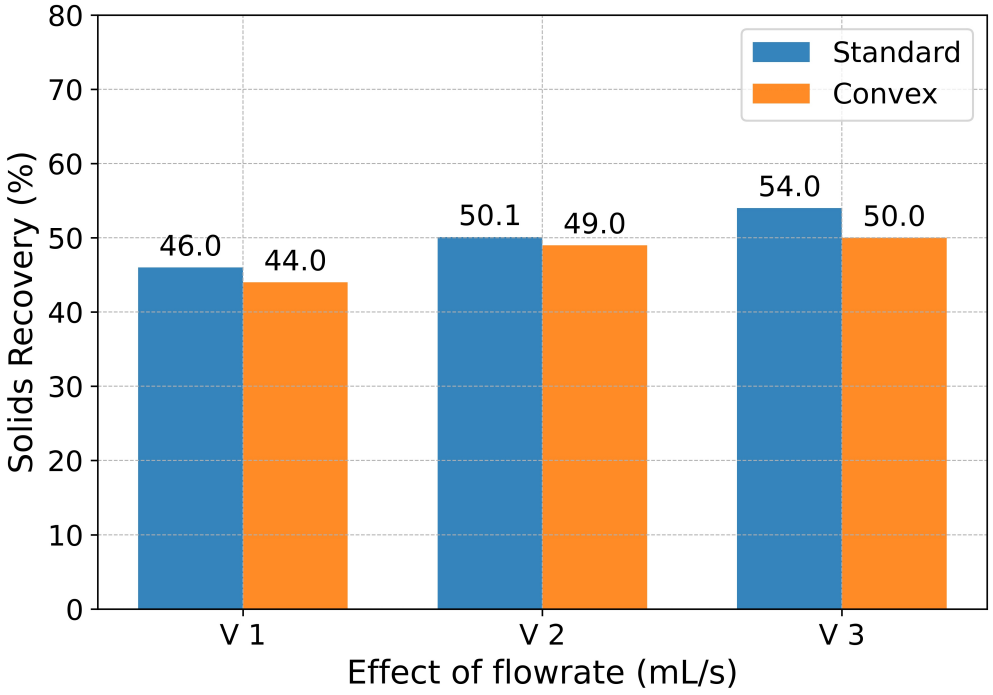


Figure 5.14: Underflow solids recovery as a function of flowrate and design.

Table 5.5: Key metrics of particle separation characteristics from experiments

	Bypass (%)		Cut size (D_{50}) - μm		Sharpness (m)	
Flowrate (mL/s)	Standard	Convex	Standard	Convex	Standard	Convex
1000	24.6	18.6	77.95	94.14	1.43	1.36
1250	32.0	23.4	60.22	73.52	1.18	1.50
1500	35.4	28.0	41.64	62.44	1.02	1.19

design. For instance, at a flow rate of 1000 mL/s, solids recovery for the standard design is 46.0%, whereas it is 44.0% for the convex hydrocyclone. This trend persists across all tested conditions, with the standard hydrocyclone achieving a solids recovery of 54% at a flow rate of 1500 mL/s, compared to 50% for the convex design.

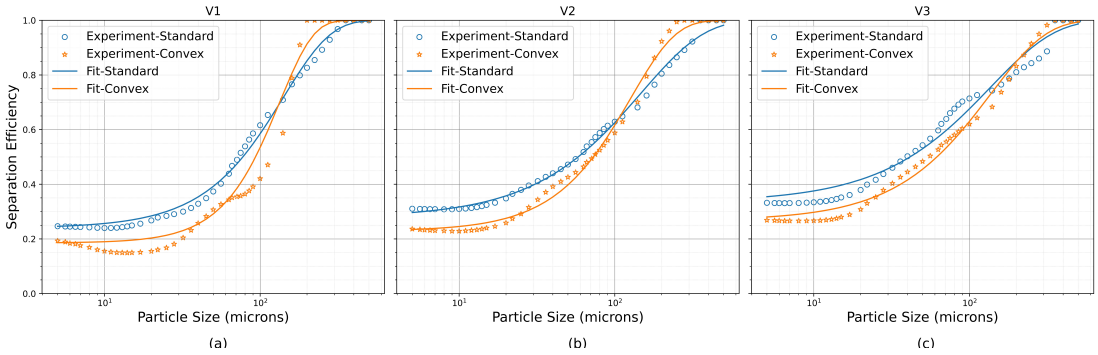
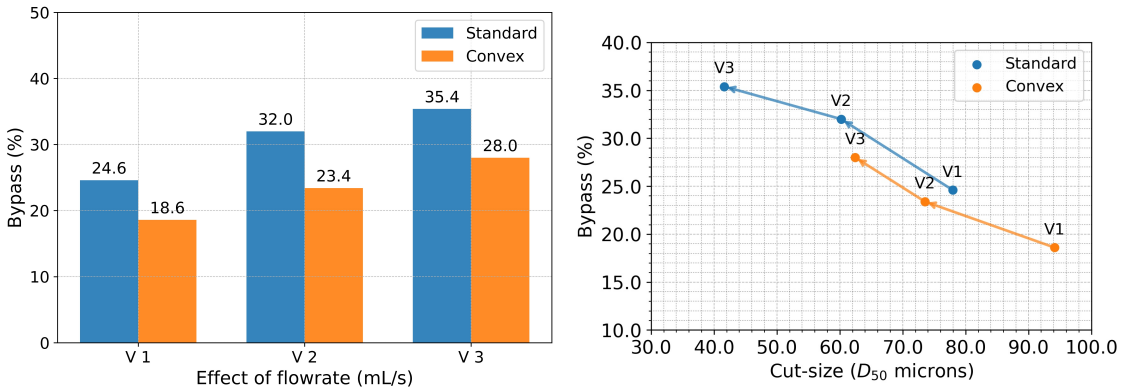


Figure 5.15: Comparison of Separation Efficiency curves for Standard (S) and Convex (C) Hydrocyclone Designs across different Flowrates.

For the 5% solids experiments, particle size assays were measured using the particle size analyzer for the samples collected from the overflow and underflow streams. Figure 5.15 illustrates the separation efficiency as a function of particle size for both hydrocyclone designs at three different flow rates. Separation efficiency values are calculated based on the solids recovery and particle size assays. In the plot, the standard design is color-coded in blue, while the convex design is represented in orange. Experimental partition curves are shown as discrete points, and the fitted curves are modeled using sigmoidal functional forms, such as the Rosin-Rammler distribution [108]:

$$C(d) = 1 - \exp\left(-0.693\left(\frac{d}{D_{50}}\right)^{m}\right) \tag{5.11}$$

Here, C(d) is the corrected partition number, d is the particle size, D_{50} is the classification cut size, and m denotes the sharpness of the classification. The experimental partition



(a) Bypass **(b)** Bypass versus cut size

Figure 5.16: Understanding the effect of flowrate as a function of hydrocyclone design on bypass and cut size (D_{50}).

curve P(d) is derived by using the following relationship:

$$P(d) = B_p + C(d)(1 - B_p) \tag{5.12}$$

Where B_p is the fines bypass, and the parameters D_{50}, and m are determined by minimizing an inverse particle size-weighted least square error. This method ensures a close match between the fitted curves and the experimental data, as depicted in Figure 5.15. It is observed that experimental separation efficiencies for both standard and convex design hydrocyclones increase with particle size. It is observed that the separation efficiency curves moves to the left with increasing flow rate, thereby decreasing the cut size. This shift is attributed to the intensified centrifugal activity within the hydrocyclone, which enhances particle separation. It is observed that the convex design has a lower bypass than compared to the standard design hydrocyclone at all the flowrates under study. Further, lower separation efficiency values are reported for smaller sizes for convex design hydrocyclones compared to the standard design hydrocyclone. However, for the particle sizes greater than 100 μm the convex design hydrocyclones exhibits higher separation efficiency values, indicating the sharper classification of coarser-cutsizes.

Table 5.5 presents key experimental particle separation characteristics, comparing the performance of standard and convex hydrocyclone designs as a function of flow rate. The fines bypass (B_p), often referred to as the partition number for fine particles, asymptotes at a particular value, as discussed by Frachon and Cilliers [108]. Figure 5.16a illustrates the trends in fines bypass for both hydrocyclone designs across different flow rates. It is evident that fines bypass increases with increasing flow rate for both designs. For the standard design, B_p values rise from 24.6% at 1000 mL/s, to 32.1% at 1250 mL/s, and 35.4% at 1500 mL/s. In contrast, the convex design consistently exhibits lower B_p values, with 18.6% at 1000 mL/s, 23.4% at 1250 mL/s, and 28.0% at 1500 mL/s. The lower fines bypass observed in the convex design suggests that this design is more efficient at directing fine particles to the overflow, compared to the standard design, across all flow rates. This difference in performance may be attributed to variations in the internal flow dynamics between the two designs, which could affect the separation of finer particles.

Figure 5.16b shows the relationship between fines bypass and cut size for both designs as a function of flow rate. The convex design demonstrates a clear trend of producing coarser cut sizes with lower fines bypass compared to the standard design at any given flow rate. For example, at a flow rate of 1000 mL/s (V1), the cut size for the convex design is approximately 94 μm, compared to 78 μm for the standard design. As flow rate increases, the cut size decreases while fines bypass increases for both designs, with their trendlines following a similar slope. At the highest flow rate tested (1500 mL/s, V3), the convex design produces a significantly coarser cut size of 62 μm, compared to 41.64 μm

for the standard design.

This finding indicates a trade-off between fines bypass and cut size, as the convex design is better suited for yielding coarser cut sizes while achieving lower fines bypass. Moreover, the consistent trends across all flow rates suggest a stable performance of both hydrocyclone designs, with the convex design offering a distinct advantage in applications requiring lower fines bypass. While reducing the underflow outlet diameter is a recognized strategy to minimize bypass, it also affects solids yield and cut sizes. In this study, the underflow outlet size was intentionally kept constant to focus on the impact of conic curvature, specifically the convex design. We acknowledge that further investigations are required to evaluate the performance of convex hydrocyclone designs, including higher solids concentrations and variable underflow outlet sizes.

5.3.4.1 Industrial case study

The ball-mill-classifier circuit in this case study incorporates two 650 mm diameter hydrocyclones—one with a standard design and the other with a convex design. Due to client confidentiality, specific design details are not disclosed. The slurry used in the circuit consists of clay material with a density of 3013 kg/m^3 and a solids concentration of up to 55% (by weight). The slurry is directed through the hydrocyclones under controlled inlet pressure conditions, with pressures varying between 80 kPa and 100 kPa, to achieve the desired flow rates. A bypass arrangement, regulated by a control valve on the pipeline, is employed to maintain the necessary pressure drop across the hydrocyclones. Samples of both the overflow and underflow products are collected simultaneously and measured for flow rates over a specific period. These samples are then filtered, dried, sieved, and weighed to determine the mass distribution. The particle size distribution of representative dried samples is analyzed by determining the weight fractions for individual sieve size classes. Additionally, the partition number, which indicates the separation efficiency for each size class, is calculated.

Figure 5.17 illustrates the relationship between bypass and cut size for both hydrocyclone designs across the tested operational conditions. The discrete data points represent experimental results, overlaid on a dataset (in a transparent colors) generated from Monte Carlo simulations, with 50,000 data points for each hydrocyclone design. The Monte Carlo simulations allow for continuous exploration of the design space across a range of process and operational conditions, within the limits of the experimental data. This enables a more comprehensive understanding of system behavior and performance across various conditions, helping to identify optimal operating points for both hydrocyclone designs. The models used in the Monte Carlo simulations were built using industrial experimental data, which can be found in the Appendix C.

The industrial data confirms the earlier findings: the standard design hydrocyclone results in a higher bypass with finer cut sizes, while the convex design hydrocyclone achieves lower bypass with coarser cut sizes. This performance advantage makes the convex design hydrocyclone a more suitable alternative to Derrick screens in ball-mill classifier circuits. Recently, a novel convex-bottom hydrocyclone design, supported by our analysis, has been successfully installed by Metso. In their press release, Metso stated, "Imperial College has also provided support in bringing this concept to light and in confirming the validity of this new technology as a third party."[178]

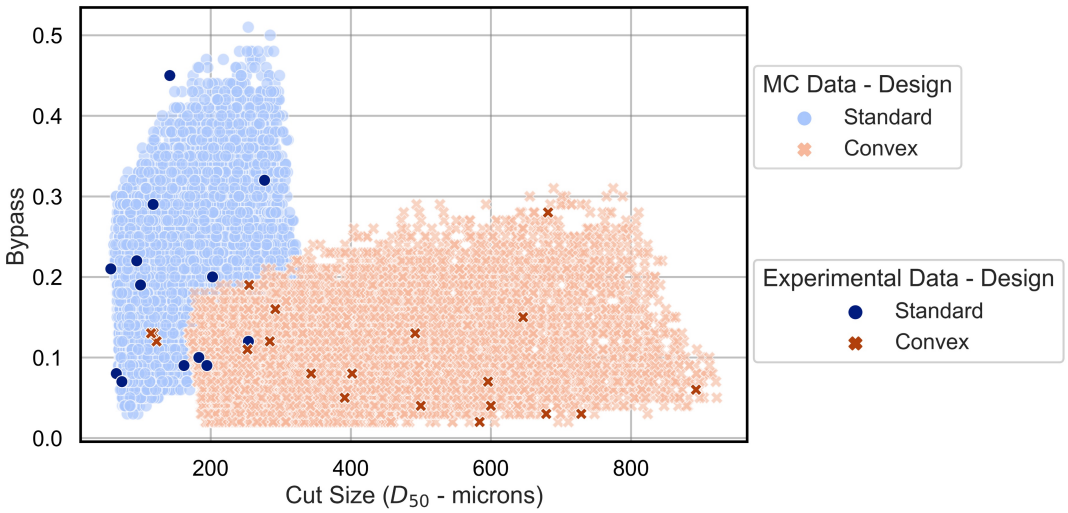


Figure 5.17: Industrial scale hydrocyclone data: Influence of hydrocyclone design and inlet flowrate on bypass and cut size relationship

5.4 Summary

This study elucidates the impact of conic curvature on hydrocyclone performance through a combination of CFD simulations and experimental investigations, revealing several critical insights.

In the CFD analysis, the convex hydrocyclone demonstrated distinct flow characteristics compared to the standard design. Notably, the convex design consistently exhibited lower underflow recoveries across the range of flow rates studied. The flow patterns in the convex hydrocyclone showed more pronounced axial velocities near the apex region and reduced radial velocities at the center. These flow characteristics create a favorable environment for particle classification by allowing particles more opportunities to remain in the classification zone and thus participate in separation more effectively, thereby reducing the fines bypass to underflow.

Experimental results confirm the trends observed in CFD simulations, consistently showing that convex hydrocyclones achieve significantly lower underflow recoveries. As the flow rate increases, underflow water recoveries decrease for both designs. Addition-

ally, for any given flow rate, the convex design results in lower underflow solids recovery and bypass, along with coarser cut sizes, compared to the standard design across all tested flow rates. For example, at a flow rate of 1000 mL/s, the fines bypass for the standard hydrocyclone is 24.6%, whereas it is reduced to 18.6% for the convex design. Similarly, the cut size for the standard design is 78 μm, compared to 94 μm for the convex design. As the flow rate increases from 1000 mL/s to 1500 mL/s, both designs show increased fines bypass and reduced cut sizes. However, the convex design achieves a fines bypass of 28% with a cut size of 62 μm, compared to 35% bypass and a cut size of 41 μm for the standard design.

These findings highlight the potential advantages of the convex conic-curvature design in achieving lower fines bypass and coarser cut sizes, making it a favorable option for particle classification in hydrocyclones, particularly in ball-mill classifier circuits.

Chapter 6

The Influence of Surface-Wall Roughness on Hydrocyclone Performance

6.1 Background . . . 121
6.2 CFD Modelling Methodology and Experimental Methods . . . 122
6.2.1 CFD Modelling theory . . . 122
6.2.1.1 Capturing the Turbulence . . . 122
6.2.1.2 Modelling air-core formation: Volume of Fluid (VOF) Theory 123
6.2.1.3 Modelling of discrete phase particle motion . . . 124
6.2.2 Simulation Set-up . . . 125
6.2.2.1 Geometry and Boundary conditions . . . 125
6.2.3 Meshing and grid independecy . . . 127
6.2.4 Experimental setup and Methods . . . 130
6.3 CFD Results and Analysis . . . 132
6.3.1 Effect of surface-wall roughness . . . 132
6.3.2 Flow-field Analysis . . . 133
6.3.2.1 Axial Velocity . . . 134
6.3.2.2 Tangential Velocity . . . 135
6.3.2.3 Radial Velocity . . . 136
6.3.2.4 Pressure . . . 137
6.3.3 CFD particle separation characteristics . . . 138
6.4 Experimental results . . . 139
6.4.1 Water-only flow splits . . . 139
6.4.2 Experimental particle separation analysis . . . 141
6.5 Conclusions . . . 147

Chapter Introduction

In the preceding chapter, the impact of convex curvature on hydrocyclone performance was studied, with a focus on conic shape and its effects on bypass and cut size. However, hydrocyclones tend to develop surface roughness over time due to hydroabrasion caused by particle-wall interactions, which can be detrimental to their performance. This chapter investigates the role of surface-wall roughness and conic curvature on hydrocyclone performance using CFD simulations and laboratory experiments.

This chapter begins by presenting the background of investigating the effect of surface wall roughness by leveraging 3D printing to create the effect of roughness in the flow domain (Section 6.1). The subsequent Section 6.2 outlines the CFD modeling methodology and experimental methods used to investigate the roughness effect. Section 6.2.2 discusses the simulation set-up, including geometry, boundary conditions, and meshing techniques to capture the effect of wall roughness. Section 6.2.4 outlines the prototyping of geometries to account for roughness using 3D printing, as well as the experimental setup and methodology for both water-only and particle separation tests.

In Section 6.3, the CFD results and analysis are presented, analyzing the effect of surface-wall roughness on hydrocyclone flow dynamics and the trends of particle separation efficiency. Further, experimental results, including water-only flow splits and particle separation tests, are discussed to validate the CFD findings in Sections 6.4.1 and 6.4.2.

The chapter concludes in Section 6.5 with a summary of the key findings, which contribute to a deeper understanding of the complex interactions between surface-wall roughness, fluid dynamics, and particle separation performance in hydrocyclones. The part of this chapter focusing on roughness in standard hydrocyclones has been published in: A. K. Pukkella, D. Vega-Garcia, K. Hadler and J. Cilliers, 'The influence of surface-wall roughness on hydrocyclone performance,' *Separation and Purification Technology*, vol. 360, p. 131 109, 2025. Modifications have been made to the original text, and additional discussions on roughness in convex hydrocyclone have been included in this chapter.

6.1 Background

In recent years, rapid prototyping, especially through 3D printing, has significantly advanced lab-scale experiments in fluid dynamics and separation processes [33, 159, 179]. However, there are often substantial differences in the surface roughness of 3D printed parts, depending on the printing method (FDM, SLS, SLA, etc.), equipment manufacturer, and material. This introduces a source of error into CFD studies aimed at validating certain experimental conditions, as they often assume smooth walls and neglect the impact of wall surface roughness parameters [159, 180, 181]. Recently, Mitchell *et al.* [182] demon-

strated the prototype device of conic centrifuge system by utilizing 3D printing to create an artificial surface roughness to evaluate the quality of separation to benefitiate mineral samples for lunar applications. In this study, we investigate the effect of surface-wall roughness on the bypass of hydrocyclones as a function of flow rate. To accomplish this, we leverage the inherent and controllable roughness introduced by 3D printing to produce hydrocyclones with known roughness profiles. These hydrocyclones enable the study of the impact of roughness on overall performance, specifically in determining whether certain designs function more effectively for classification or separation at different flow rates. This aspect of hydrocyclone behavior has not been previously explored. This study also highlights the importance of considering surface-wall roughness during CFD studies.

6.2 CFD Modelling Methodology and Experimental Methods

6.2.1 CFD Modelling theory

6.2.1.1 Capturing the Turbulence

The momentum equation for an incompressible fluid is:

$$\frac{\partial}{\partial t}\left(\rho u_i\right) + \frac{\partial}{\partial x_j}\left(\rho u_i u_j\right) = -\frac{\partial p}{\partial x_i} + \mu\frac{\partial^2 u_i}{\partial x_j^2} + \rho g$$

By separating the velocity into mean and fluctuating components, and applying time-averaging, we obtain the Reynolds-averaged Navier-Stokes (RANS) equations, introducing the Reynolds stress term, $\rho\overline{u_i' u_j'}$. This term requires modeling through turbulence closures like the Boussinesq hypothesis (for k-ϵ and k-ω models) or the Reynolds Stress Model (RSM), which accounts for anisotropy in flows with swirl or rotation by solving transport equations for the Reynolds stresses.

The simplified transport equation for Reynolds stresses in RSM can be written as:

$$\frac{\partial}{\partial t}\left(\rho\overline{u_i' u_j'}\right) + \frac{\partial}{\partial x_k}\left(\rho u_k\overline{u_i' u_j'}\right) = D_{ij} + P_{ij} - G_{ij} - \epsilon_{ij} + \phi_{ij}$$

The parameters, - D_{ij} represents diffusion of Reynolds stress (turbulent and molecular), - P_{ij} is the production of Reynolds stress, - G_{ij} is the Buoyancy production, - ϵ_{ij} is the dissipation, - ϕ_{ij} is the pressure-strain correlation. The quadratic pressure strain model is used to model ϕ_{ij}, providing accuracy in rotating and shear flows.

The interaction between turbulent flow and surface roughness in hydrocyclones introduces additional flow resistance. This resistance, often described through modified wall functions, affects velocity profiles and, consequently, particle separation efficiency. Hence the law of wall is modified with constant ΔB to take account of roughness.

The sand-grain roughness model, introduced by Nikuradse [164], has been widely adopted for modeling surface roughness in hydrocyclones [114, 132]. In this model, the wall is assumed to be covered by a layer of mono-dispersed sand-grain spheres that represent roughness elements, resembling sandpaper. The height of these spheres corresponds to the equivalent roughness height (k_s), and the roughness effect is captured through a dimensionless roughness parameter $k_s^+ = k_s u^*/v$. The modified law of wall due to surface roughness is given by the following equation.

$$\frac{u}{u^*} = \left(\frac{1}{\kappa}\right) \ln\left(\frac{yu^*}{v}\right) + \mathrm{B} - \Delta B \tag{6.1}$$

where friction velocity is defined as $u^* = (\tau_w/\rho)^{0.5}$, where τ_w is the wall shear stress, and ρ is the fluid density. Where $\kappa = 0.41$ is the von Karman constant, and B is a constant for smooth wall (*i.e.*, 5.56).

The roughness function, ΔB, depends on roughness shape (*i.e.*, degree of homogeneity) (C_s) and roughness size (k_s). Based on the experimental observations of Nikuradse [164], the roughness function (ΔB) is expressed in a piecewise function of ${k_s}^+$, capturing the transition from hydrodynamically smooth to hydrodynamically rough regimes:

$$\Delta B = \begin{cases} 0, & k_s^+ \leqslant 2.25 \\ \frac{1}{\kappa} \ln\left(\frac{k_s^+ - 2.25}{87.75} + C_s k_s^+\right) & \\ * \sin\left[0.4258\left(\ln k_s^+ - 0.811\right)\right], & 2.25 < k_s^+ < 90 \\ \frac{1}{\kappa} \ln\left(1 + C_s k_s^+\right), & k_s^+ > 90 \end{cases} \tag{6.2}$$

The value of the roughness constant C_s is considered as 0.5 assuming uniform distribution of sand grains. From the above equation it is understood that for a hydrodynamically smooth pipe (*i.e.*, ${k_s}^+ <$2.25) the roughness has an insignificant contribution. Whereas, its influence increases for transitional (*i.e.*, $2.25 < k_s^+ < 90$) and hydrodynamically rough regimes (*i.e.*, $k_s^+ > 90$).

6.2.1.2 Modelling air-core formation: Volume of Fluid (VOF) Theory

The VOF method is employed to simulate air-core formation, using a single set of momentum equations shared by the phases (air and water). Phase interaction is tracked using volume fractions, with α_q denoting the fraction of the q^{th} phase in each cell. The VOF approach tracks the interface between phases by solving a continuity equation for the volume fraction:

$$\frac{1}{\rho_q}\left(\frac{\partial(\alpha_q \rho_q)}{\partial t} + \nabla \cdot (\alpha_q \rho_q \vec{v_q}) = S + \sum_{p=1}^{n} (\dot{m_{pq}} - \dot{m_{qp}})\right)$$

The parameter α_q represents the phase's volume fraction, and mass transfer terms between phases are considered. The momentum equation is solved over the entire domain, with volume fraction-dependent properties (ρ, μ).

6.2.1.3 Modelling of discrete phase particle motion

The trajectories of individual particles in the discrete phase are determined using Lagrangian particle tracking (LPT). The momentum balance equation for a particle subject to external forces can be formulated as follows:

$$\frac{du_p}{dt} = F_D(\vec{u} - \vec{u_p}) + \frac{g(\rho_p - \rho)}{\rho_p}) + \vec{F_a} \tag{6.3}$$

In this equation, the left-hand side represents the inertial forces per unit mass (ms^{-2}), where $\vec{u_p}$ denotes the particle velocity. The first term on the right-hand side accounts for the drag force which is computed using a Reynolds number-dependent drag coefficient correlation. Here, F_D represents the inverse of relaxation time (s^{-1}). The second term characterizes buoyancy due to gravity, with ρ and ρ_p representing the fluid density and particle density, respectively. The term $\vec{F_a}$ encompasses any additional forces per unit mass that may be significant, including added mass forces arising from the relative acceleration of the particulate phase, viscous drag forces from the fluid, and other forces such as Brownian motion, thermophoretic forces, and shear-induced lift (Saffman's lift) forces, among others.

In turbulent flow conditions, particle motion is substantially influenced by the fluctuating instantaneous velocities. The dispersion of particles due to turbulence in the fluid phase is tracked using a stochastic approach known as the Random Walk method. This method assumes that each particle encounters a sequence of eddies with random sizes, strengths, and directions as it traverses the flow domain. The DRW (Discrete Random Walk) model postulates that fluctuating velocities follow a Gaussian probability distribution, with the characteristic fluctuating velocity defined as:

$$u_i' = \xi\sqrt{2k/3} \tag{6.4}$$

Where ξ is the normally distributed random number, k signifies the turbulent kinetic energy, and the value of u_i' remains constant during each time step.

6.2.2 Simulation Set-up

6.2.2.1 Geometry and Boundary conditions

In this study, our primary objective is to investigate how flow rate affects smooth and rough-walled hydrocyclones with a diameter of 75 mm. The geometric details and dimensions are provided in Figure 6.1a. The hydrocyclone features a square tangential inlet with a side length of 20 mm. The overflow and underflow diameters are 25 mm and 12.5 mm, respectively. Both the cylinder barrel length and the vortex finder length are equal to the diameter, 75 mm. The cone extends at an angle of 16.4^o at the apex (*i.e.*, underflow).

Water is considered the primary phase, with air as the secondary phase in the simulations. For modeling purposes, we define the density and viscosity of water as 1000 kg/m^3 and $1 * 10^{-3}$ $kg/(ms)$, respectively. Specifically, we aim to assess the impact of inlet flow rates of 1000, 1250, and 1500 mL/s, to match the lab-scale experiments. For these conditions, the inlet velocities correspond to 2.5, 3.125, and 3.75 m/s, respectively.

Both overflow and underflow outlets are configured as pressure outlets open to the atmosphere, maintaining zero gauge pressure with a backflow volume fraction of air set to 1. This boundary condition facilitates the return of air into the hydrocyclone to form an air-core, as they are open to the atmosphere in experiments. The remaining walls are treated as no-slip boundaries with scalable wall functions. The rough-walled hydrocyclone is modelled using the sand-grain roughness model with roughness heights (k_s) varied between 1 to 700 microns at a fixed roughness constant C_s (0.5). Initially, the hydrocyclone is entirely filled with air at atmospheric pressure. Subsequently, water enters through the tangential inlet, swiftly swirling and occupying the wall region, generating a zone of negative pressure at the center of the hydrocyclone. This lowered pressure induces the inflow of air from the surroundings, resulting in the formation of the air-core.

Since the particle separation characteristic experiments were conducted with a solids concentration of $\approx$ 5% (by mass), we used a discrete phase model to capture the behavior of particles from a Lagrangian perspective. To examine particle separation characteristics, we employ transient Lagrangian Particle Tracking (LPT) with particles having a density of 2650 kg/m^3. Particle sizes ranging from 5 to 150 microns are considered within the LPT framework. These particle injections are individually created based on their size and released from the inlet, with 1000 particles in each injection. The underflow is modelled as a trap for particles and the overflow is modelled with escape boundary conditions for particles. Particle tracking is performed with a fluid time-step of 10^{-5} s.

For solving the governing mass and momentum transport equations, the pressure-based solver in ANSYS FLUENT is employed. The Coupled scheme algorithm is utilized for pressure-velocity coupling, and pressure interpolation is conducted using the PREssure STaggering Option (PRESTO scheme). The momentum equations are discretized using

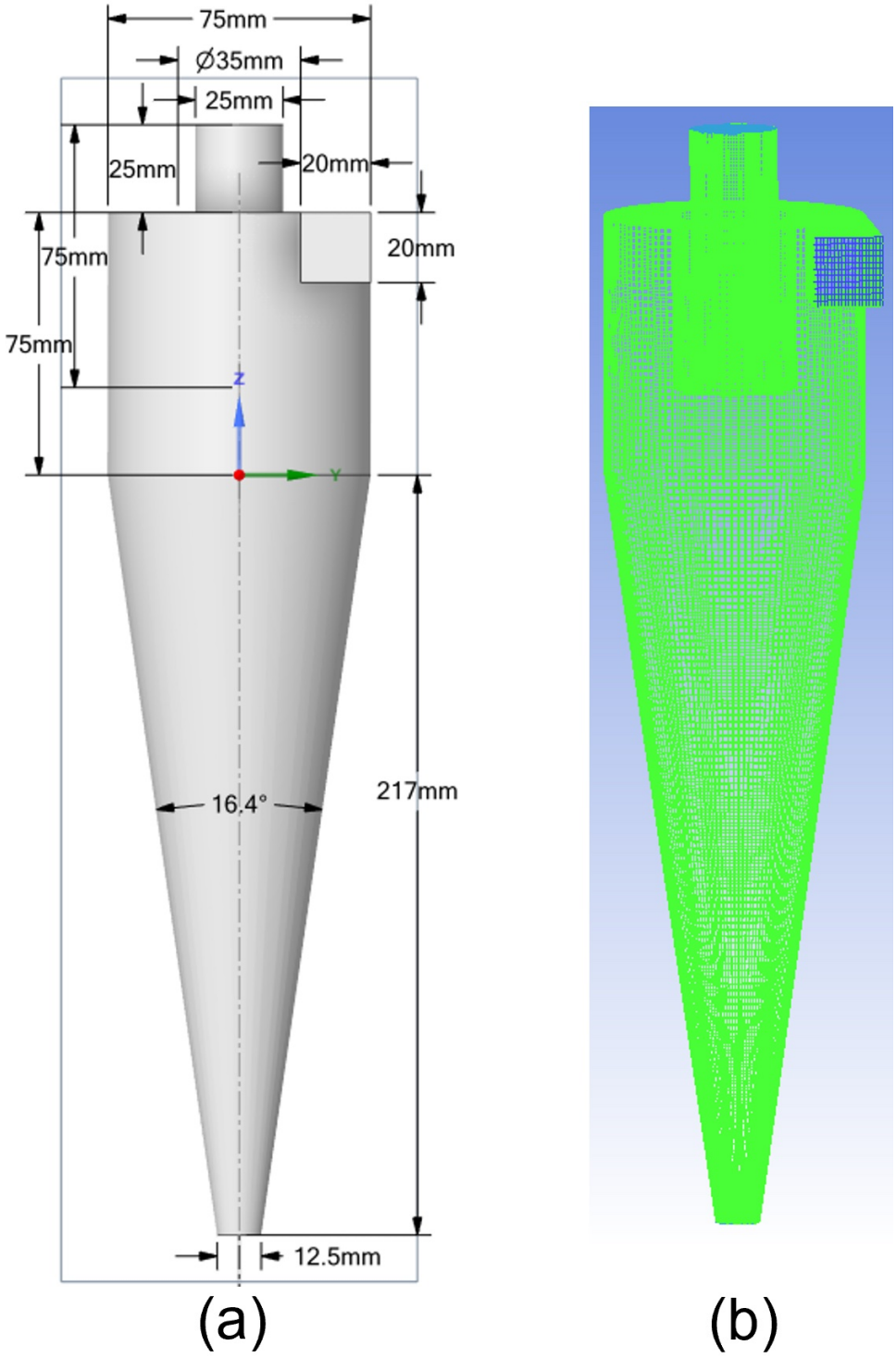


Figure 6.1: (a) Geometrical design of hydrocyclones with dimensions. (b) Unstructured hexahedral mesh

the higher-order Quadratic Upstream Interpolation for Convective Kinematics (QUICK) scheme. The volume fraction is discretized using the modified High-Resolution Interface Capturing (HRIC) method, and first-order upwind discretization is selected for the turbulence equations and Reynolds stress. In our simulations, the convergence criterion is defined based on residual errors, set at 10^{-5} for all continuity and velocity and turbulence parameters. Each simulation is run for a minimum of 5-6 times their corresponding residence time, equivalent to 10 seconds of physical time. Following convergence, a time-averaging procedure is implemented over several thousand iterations, approximately equivalent to their residence times of $\approx$ 2 seconds of physical time.

6.2.3 Meshing and grid independecy

Figure 6.1b depicts the unstructured hexahedral mesh created in ANSYS ICEM CFD using the blocking technique. In the current work, the viscosity-affected inner region is modeled using a scalable wall function, which is effective even for meshes with y^+ values as low as 1. This approach overcomes the limitations of standard wall functions by ensuring that the solver's y^* (used internally by Fluent) always remains above 11.225. The threshold value of 11.225 is derived from the classical boundary layer theory, where the linear velocity profile in the viscous sublayer transitions to the logarithmic profile in the log-law region. The scalable wall function algorithm selects the higher value between 11.225 and y^*, maintaining boundary layer accuracy across different mesh densities. Due to surface roughness, the velocity profiles shift downward, resulting in lower y^+ values. In the transitional roughness regime, the roughness elements are slightly thicker than the viscous sublayer and begin to disturb it. In fully rough flows, the viscous sublayer is destroyed, and viscous effects become negligible. Commercial CFD software, Ansys Fluent addresses this issue by virtually shifting the wall by a distance equal to half the height of the roughness elements (k_s) [183]. This adjustment modifies the original y^+ values as follows: $y_c^+ = y^+ + \frac{k_s}{2}$. This virtual wall-shifting approach effectively mitigates issues related to mesh resolution near the wall, thereby facilitating the use of fine meshes without imposing additional constraints to capture the effects of surface-wall roughness.

It is worth noting that while a higher mesh density (i.e., an increased number of cells) enhances accuracy, it also escalates computational costs. To ascertain the grid independency, we conducted a comprehensive test utilizing three distinct meshes, designated as M1, M2, and M3. The corresponding cell counts are detailed in Table6.1. Our CFD simulations were carried out with an inlet flow rate of 1500 mL/s. The overall pressure drop and turbulent dissipation rate per hydrocyclone volume were measured and recorded in Table 6.1. Additionally, we measured radial profiles of tangential velocities on the central plane, at a height of Z = 217 mm measured from the bottom and scaled with the corresponding inlet velocity (ie., 3.75 m/s) as shown in Figure 6.2b. Based on the observations reported

Table 6.1: Details of grid convergence study calculations using GCI method

	Mesh	Cell count	f_i	$r_{i,i+1}$	$e_{i,i+1}$	$\epsilon_{i,i+1}$	GCI %	R	α
Exact Solution			70796.17						
Pressure drop [pa]	M1	681656	70894	1.09057	-355.6	0.00501	0.17319		
	M2	525534	71250	1.10454	-2171	0.03047	0.79616	0.16461	1.00508
	M3	289989	73421						
Exact Solution			0.07757						
Turbulent	M1	681656	0.07954	1.0905	-0.0062	0.07885	3.10085	0.19753	1.07889
Dissipation Rate	M2	525534	0.08581	1.1045	-0.0342	0.3991	12.0097		
[$m^2/s^3/m^3$]	M3	389989	0.12007						

in Figure 6.2 and Table 6.1, it was concluded that mesh M2 was optimal for capturing the swirling flows inside the hydrocyclone with reasonable accuracy and producing grid-independent results. Because of the large difference in the number of cells between the coarse and fine mesh predictions we further conducted a Grid Convergence Index (GCI) study suggested by Roache which is a quantitative measure of grid convergence [168].

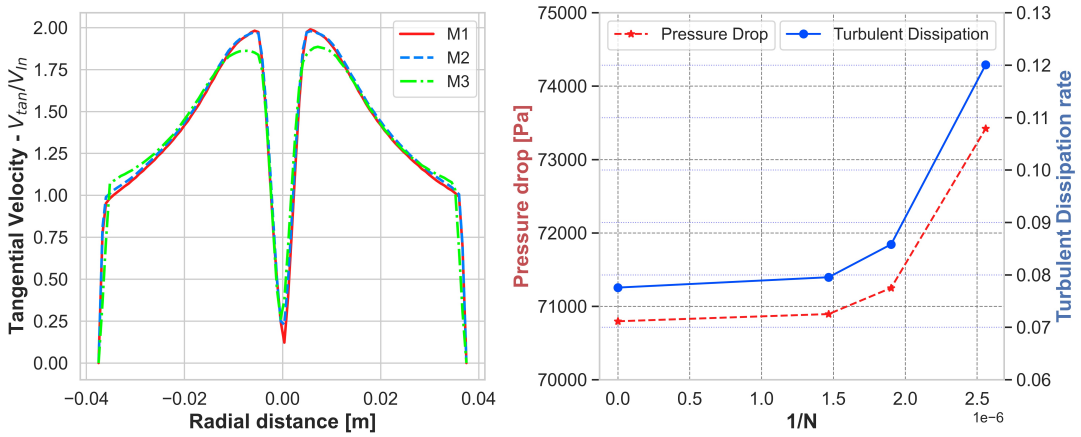


Figure 6.2: Grid independence study: (a) Variation of scaled tangential velocity on a center-line for an inlet flowrate of 1500 mL/s (Height (Z) = 217 mm, measured from the bottom). (b) The measured quantities i.e., pressure drop, and turbulent dissipation rate as a function of the number of cells.

GCI is a measure of how far the computed value is away from the asymptotic value using Richardson extrapolation. For the grid refinement study, three meshes have been used with N_1, N_2, and N_3 cells for the fine (M1), medium (M2), and coarse (M3) three-dimensional meshes, respectively. The difference in the measured variable f between the grids is computed as $e_{i,i+1}$;

$$e_{12} = f_2 - f_1, e_{23} = f_3 - f_2$$

$\varepsilon_{i,i+1}$ is a relative error measure of the measured variable $'f'$ between the grid solutions,

$$\varepsilon_{12} = \frac{f_2 - f_1}{f_1}, \varepsilon_{23} = \frac{f_3 - f_2}{f_2}$$

f_1, f_2, and f_3 are the numerical solutions obtained for fine, medium, and coarse grids with a number of control volume cells N_1, N_2, and N_3 in their respective grids. The grid refinement ratio $(r_{i,i+1})$ is obtained as follows:

$$r_{12} = \left(\frac{N_1}{N_2}\right)^{\frac{1}{3}}, r_{23} = \left(\frac{N_2}{N_3}\right)^{\frac{1}{3}}$$

The grid refinement ratio (r) is further influenced by parameter p which accounts for grid stretching, quality of grid, order of discretization, turbulence modeling, and other factors is obtained by solving by an iterative technique with relaxation factor as described by Roache [168].

$$p = \omega\rho + (1-\omega)\frac{\ln(\frac{(r_{12}^p-1)e_{23}}{(r_{23}^p-1)e_{12}})}{\ln(r_{12})}$$

where, $\omega = 0.5$ and ρ is the previous iteration of p. The author suggest to use $\rho = \ln\left(\frac{e_{23}}{e_{12}}\right)/\ln(r_{12})$ as a first guess. The iteration will stop if $\left|\frac{p-\rho}{p}\right| < 1E-5$. Now one can calculate Grid Convergence Index (GCI) using the below equations,

$$\mathrm{GCI}_{12} = \frac{1.25\,|\varepsilon_{12}|}{(r_{12}^p-1)}, \mathrm{GCI}_{23} = \frac{1.25\,|\varepsilon_{23}|}{(r_{23}^p-1)}$$

GCI_{12} should be smaller than GCI_{23} To check if the solution is in the asymptotic range, $\alpha \approx 1$

$$\alpha = \frac{r_{12}^p \mathrm{GCI}_{12}}{\mathrm{GCI}_{23}}$$

The Richardson extrapolation can be used to obtain the value of f when the grid spacing h vanishes $(h \to 0)$.

$$f_{\text{exact}} = f_1 + (f_1 - f_2)/(r_{12}^p - 1)$$

Table 6.1 displays grid convergence calculations using the GCI method across three grid levels. These results fall within the asymptotic range, with measured variables (Pressure drop and Turbulent dissipation rate) α nearing unity. The ratio R is less than one, signifying monotonic convergence [184]. Notably, there is a reduction in GCI values with successive grid refinements ($\mathrm{GCI}_{12} < \mathrm{GCI}_{23}$) for both variables (Pressure drop and Turbulent dissipation rate). This reduction indicates reduced dependency on cell size, achieving a grid-independent solution. Further grid refinement is unlikely to yield significant changes. The extrapolated value slightly undershoots the finest grid solution for the two variables, confirming effective convergence from the coarser grid to the finer grid. Figure 6.2 provides qualitative evidence supporting results being in the asymptotic range, indicating mesh independence. Consequently, mesh M2 containing around 5.2 lakh cells has been selected for all subsequent simulations to accurately capture the physics.

6.2.4 Experimental setup and Methods

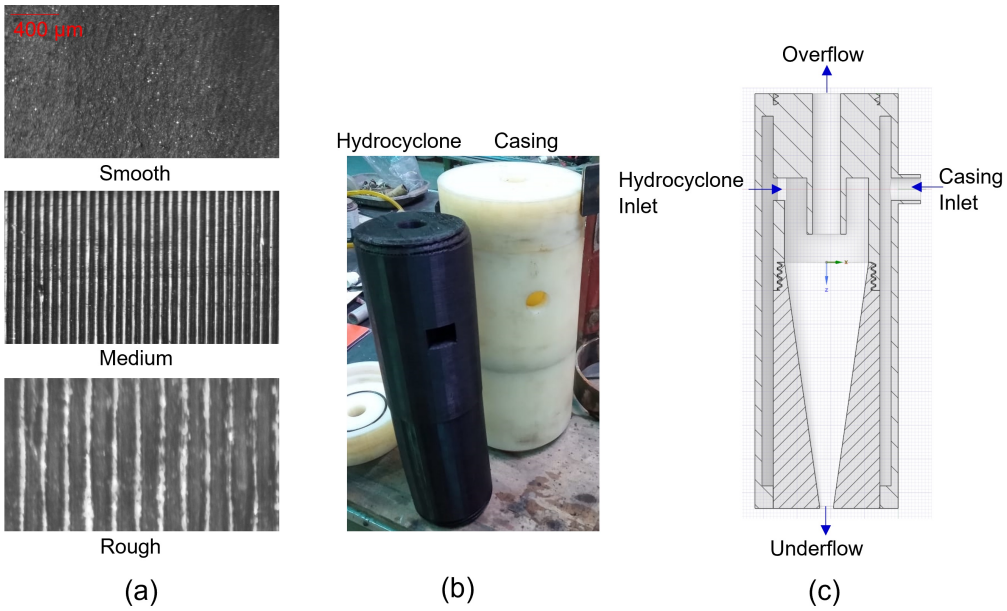


Figure 6.3: (a) Microscopic images of 3-D printed hydrocyclones with three levels of roughness, (b) Hydrocyclone and casing, (c) Schematic of flow domain

We utilize rapid prototyping to 3D print the flow domain with a varied surface texture configuration to simulate the effect of roughness. Figure 6.3a shows the microscopic images of 3D-printed hydrocyclones with varied surface roughness. The smooth-walled hydrocyclone is 3D-printed using a high-resolution Stereolithography (SLA) liquid resin-based FormLabs (Form-3) 3D printer, achieving a fine surface resolution of less than 25 microns. In contrast, the medium and rough hydrocyclones are 3D-printed using the Fused Deposition Modeling (FDM) method with an Ultimaker S5 3D printer, using SLA material with surface resolutions of 150 and 300 microns, respectively. The 3D-printed hydrocyclone is installed in a casing and is sealed with rubber gaskets to prevent leakage (Figure 6.3b). Figure 6.3c depicts the flow domain of the experimental hydrocyclone, where the flow circulates around the annular gap between the casing and the hydrocyclone's exterior wall before entering the cyclone due to pressure.

The silica powder sample was prepared by grinding silica pebbles in a ball mill to achieve a P_{50} of 100 microns, a P_{90} of 220 microns, and an upper size less than 450 microns. The particle size distribution of the feed is shown in Figure 6.4a. Figure 6.4b is a schematic of the experimental setup, which includes a variable-speed centrifugal pump, a conical mixing tank to prevent particle settling, digital flowmeters, and bypass valves to control the flow into the hydrocyclone. All experiments were conducted under consistent operating conditions, with a solids concentration of 50 g/L in water at 15°C. Each slurry batch was prepared by mixing 5 kilograms of silica with 100 liters of water, resulting in an approximate solids concentration of 4.85% by mass. Additionally, the dilute solid concentrations enable us to achieve uniform mixing and stable flow characteristics in analyzing

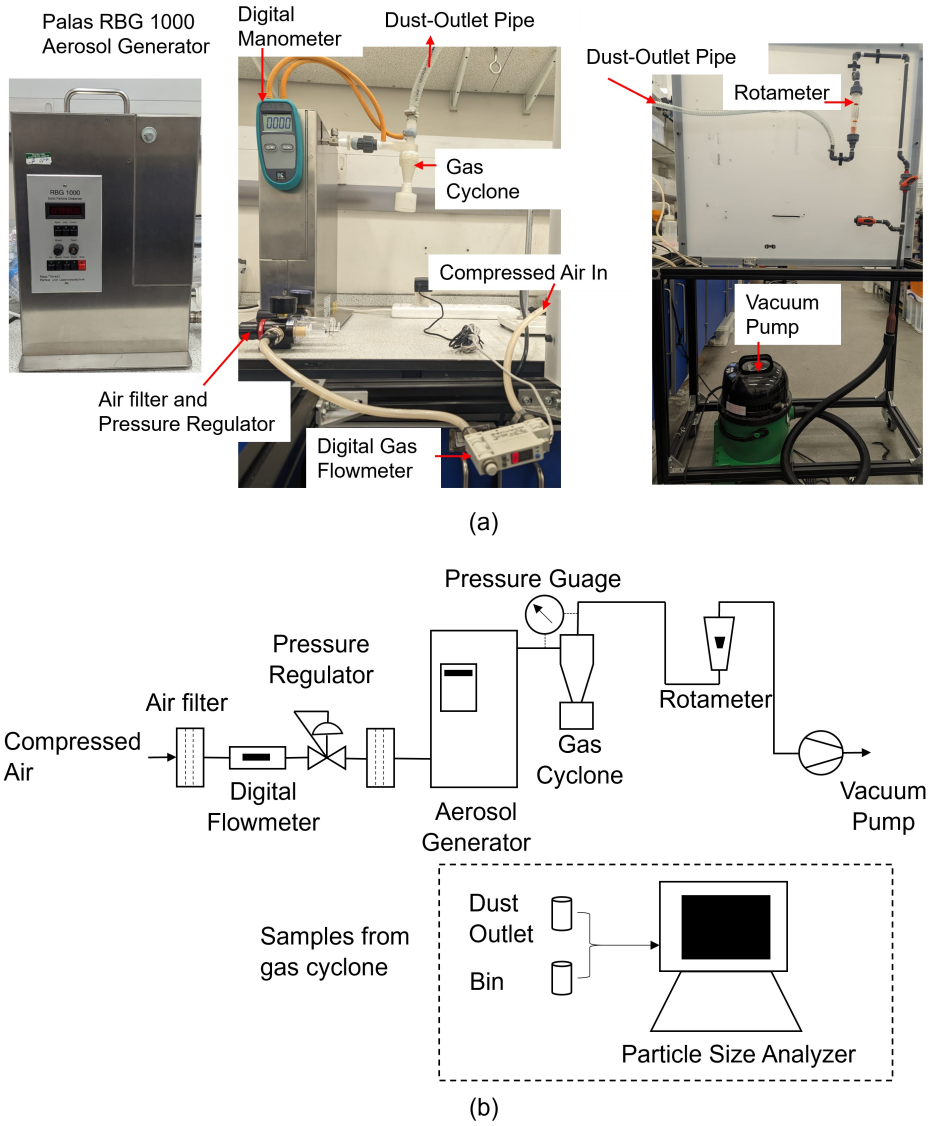


Figure 6.4: (a) Silica feed PSD (b) Schematic of the experimental setup to test the hydrocyclone

hydrocyclones.

Before introducing solids into the sump tank, the stirrer was activated to prevent particle aggregation. Once the suspension was uniformly mixed, the pump was activated, and the valves were adjusted until the flow rate through the hydrocyclone reached the desired values of 1000 mL/s (V1), 1250 mL/s (V2), and 1500 mL/s (V3). Upon reaching the desired flow rate, the system was allowed to operate for 10 minutes to reach a steady state.

To determine the flow rates, timed samples were simultaneously collected from both the underflow and overflow streams. Samples from the feed, underflow, and overflow were then collected and dried in a furnace to calculate the solids concentration. Additionally, the wet samples were directly analyzed for particle size distribution (PSD) using a Malvern Mastersizer 3000. Flow rate measurements, solids concentration determinations, and particle size distribution (PSD) analyses were repeated three times for selected experiments to ensure accuracy. For water-only experiments, triplicate measurements were conducted at all flow rates for the rough configurations under study, with standard deviation errors consistently below 5%. For experiments with 5% solids concentration, measurements focused only on the smooth and rough configurations across different flow rates.

6.3 CFD Results and Analysis

6.3.1 Effect of surface-wall roughness

Initially, we predicted the underflow recovery for a smooth-walled base CFD simulation as 10%. We then systematically explored the effect of surface roughness (k_s) at values of 1, 10, 50, 100, 200, 300, 500, and 700 microns, while maintaining a roughness constant (C_s) of 0.5. Figure 6.5 illustrates a semi-log plot, revealing two distinct regimes: minimal influence of roughness on underflow recovery for ks <30 microns, and a linear variation in underflow recovery as roughness increases logarithmically. This observation may explain why Bradley did not observe any difference between 'machined' and 'highly polished' hydrocyclones [104]. The roughness in the machined hydrocyclone was likely below the threshold value.

The threshold effect in underflow recovery as a function of roughness height can be attributed to the interplay between turbulence and frictional resistance in the hydrocyclone. Below a certain level of surface roughness, the turbulence introduced by the roughness elements is minimal and may be dampened by fluid viscous forces, allowing efficient particle separation to continue largely unaffected. However, beyond this threshold value, the increased surface roughness adds significant frictional resistance which affects both

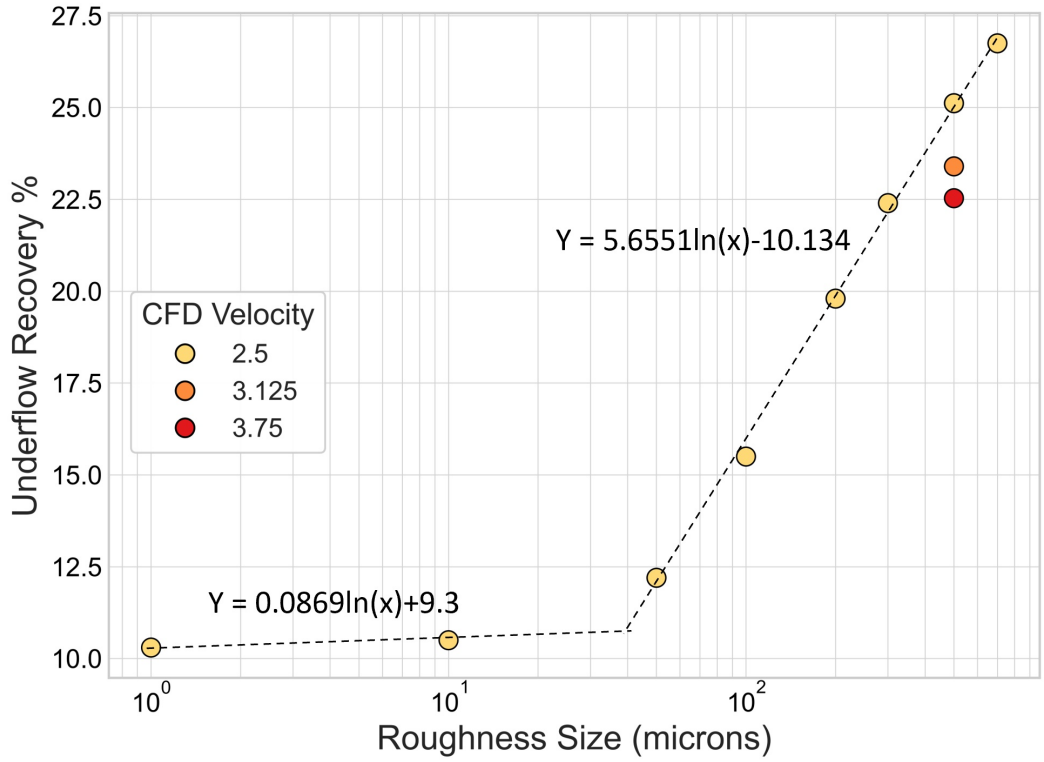


Figure 6.5: Effect of surface wall roughness on the underflow water recovery for a flowrate of 1000 mL/s and roughness constant of 0.5

the velocity distribution and particle separation mechanisms within the hydrocyclone. Understanding how surface roughness affects flow behavior can guide decisions on material selection and the maintenance of hydrocyclone components. This knowledge allows for more informed choices regarding operational conditions and part replacements, and to achieve sustained performance in various industrial applications.

6.3.2 Flow-field Analysis

In this section, we present CFD results comparing key flow properties, including axial, tangential, and radial velocities, pressure distribution profiles, and air-core formation, in standard and rough-design (k_s= 500 microns and C_s = 0.5) hydrocyclones at the three flow rates described previously. We observed that, when scaled with the inlet velocity, the flow quantities exhibit similar trends. Therefore, for brevity and clarity, we exclusively present results for the highest flow rate condition.

Table 6.2 presents the flow and particle separation performance metrics for both hydrocyclone designs as a function of inlet flow rate. For the smooth-design hydrocyclone, the underflow water recoveries decrease with an increase in flow rate, confirming previous observations [170]. Notably, surface-wall roughness significantly increases the underflow recoveries compared to smooth designs, though the recoveries slightly decrease with an increase in flow rate.

Table 6.2: Comparative analysis of CFD model performance metrics as a function of hydrocyclone surface-wall roughness and flowrate.

Inlet flowrate-(mL/s) Velocity-[m/s]	Underflow recovery		Pressure drop (Pa)		Bypass	
Case	**Smooth**	**Rough**	**Smooth**	**Rough**	**Smooth**	**Rough**
1000 [2.5]	9.26	25.14	30569	14040	27.5	29.5
1250 [3.125]	8.53	23.23	48356	22188	30.21	54.5
1500 [3.75]	7.62	22.17	71250	32166	31.31	58.2

6.3.2.1 Axial Velocity

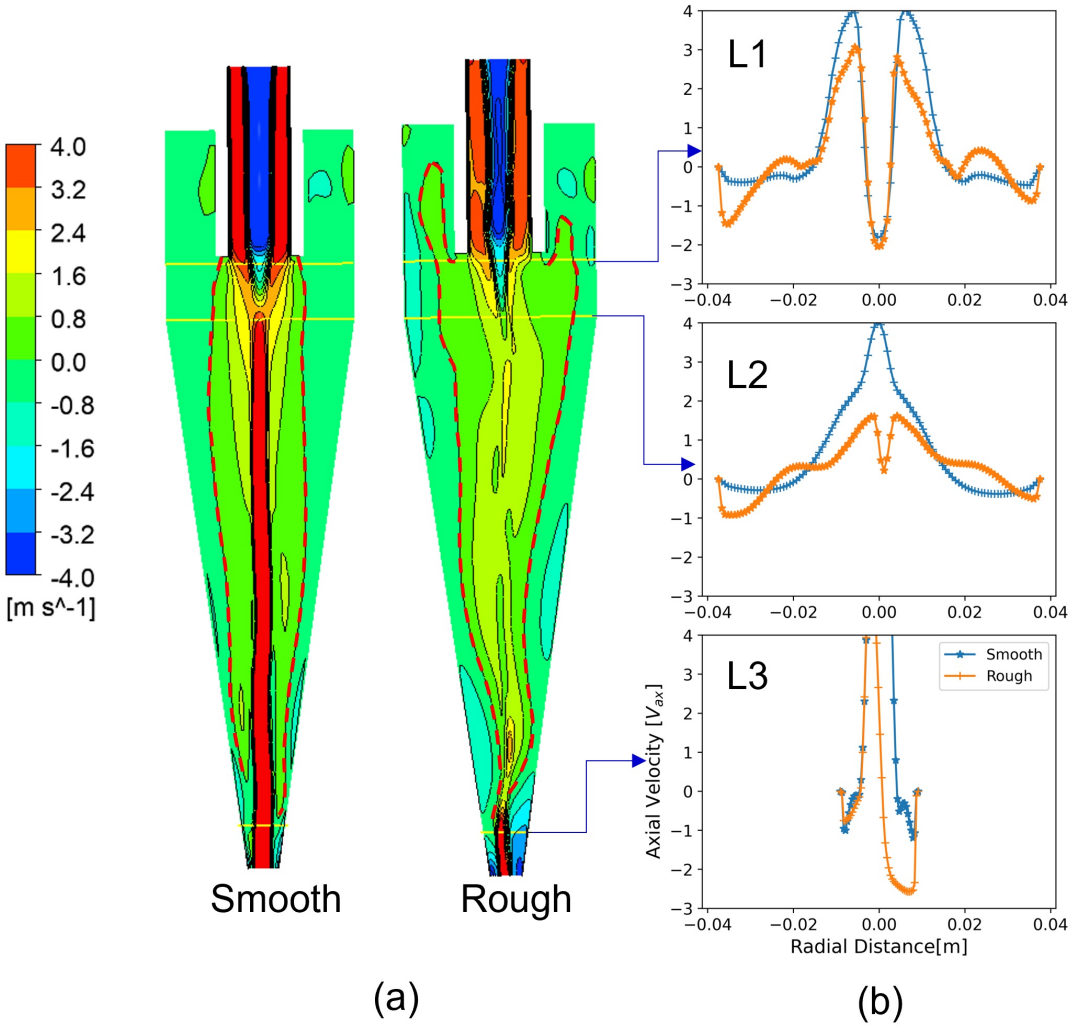


Figure 6.6: Effect of surface-wall roughness on axial velocity profiles inside hydrocyclones at 1500 mL/s flowrate: a) Contour plots at center XZ plane (Y=0) b) radial profiles at three axial locations (L1, L2, and L3)

Figure 6.6 shows the axial velocity distribution contours and their radial profiles at the selected locations comparing the smooth and rough designs.

The axial velocity distribution is characterized by negative velocities adjacent to the wall, inducing a downward spiral motion towards the underflow region, and an upward-

moving vortex flow near the air-core region with positive axial velocities. As shown in Figure 6.6a, the red dotted line, which is known as the Locus of Zero Vertical Velocity (LZVV), divides the upward and downward flow in liquid domain. Figure 6.6b demonstrates the radial profiles measured at lines L1, L2, and L3 as indicated on the contour plot. The axial velocity profiles follows the trend of zero axial velocity at the wall and negative values in the proximity to the wall and gradually increase towards the air-core water interface.

In the air-core region, it is observed that positive axial velocities are more pronounced for smooth design extending from the underflow to cylindrical section. Whereas for the rough design, it is only to the vicinity close to the underflow. These observations indicate that the air is being sucked from the underflow forming a thick and stable core for the smooth design, whereas for the rough design, it is thin and wavy. These observations are also confirmed by the contour plot of water volume fractions as shown in Figure 6.7c.

It is observed that the rough design exhibits lower liquid upward axial velocities in the vortex finder compared to the smooth design. This is indicated by the light red annular passage in the vortex finder of the rough hydrocyclone, in contrast to the bright red color observed in the contour plot of the smooth design. This trend is more clearly depicted by the radial profiles at location L1, near the tip of the vortex finder. Compared to the smooth design, the presence of lower axial velocities near the overflow in the rough design supports the observation of higher underflow recoveries, as reported in table 6.2.

In the vicinity of the apex region (*i.e.*, underflow), as illustrated in Figure 6.6b at L3, it is observed that the downward velocities near the wall are more pronounced in the rough design compared to the smooth design hydrocyclone. This increased downward velocity may negatively affect the classification process by yielding higher bypass. This is also depicted by the intense blue region near the apex of the rough hydrocyclones compared to the smooth design, as shown in Figure 6.6a. In the region close to the wall, it is observed that the rough design exhibits higher negative axial velocities compared to the smooth design. These higher negative velocities, combined with the lower upward axial velocities in the rest of the flow domain, as observed in 6.6b at L1 and L2, cause particles to be conveyed downward and exit through the underflow, potentially leading to higher bypass.

6.3.2.2 Tangential Velocity

The tangential velocity is one of the key parameters that determine the particle separation efficiency as it directly impacts the centrifugal force inside the hydrocyclone. Figure 6.7a depicts the contour plots of tangential velocity profiles comparing the smooth and rough design hydrocyclones. It is observed that tangential velocities of both smooth and rough

hydrocyclones follow a similar trend reported elsewhere in the literature [132]. It is observed from Figure 6.7a, the roughness significantly reduces the tangential flow field when compared to the smooth design. Surface roughness increases frictional resistance, which dampens tangential velocity, reducing the centrifugal forces necessary for effective particle classification. Thereby reducing the centrifugal forces acting on the particles to classify and thereby providing the chances for the particles to escape through the overflow.

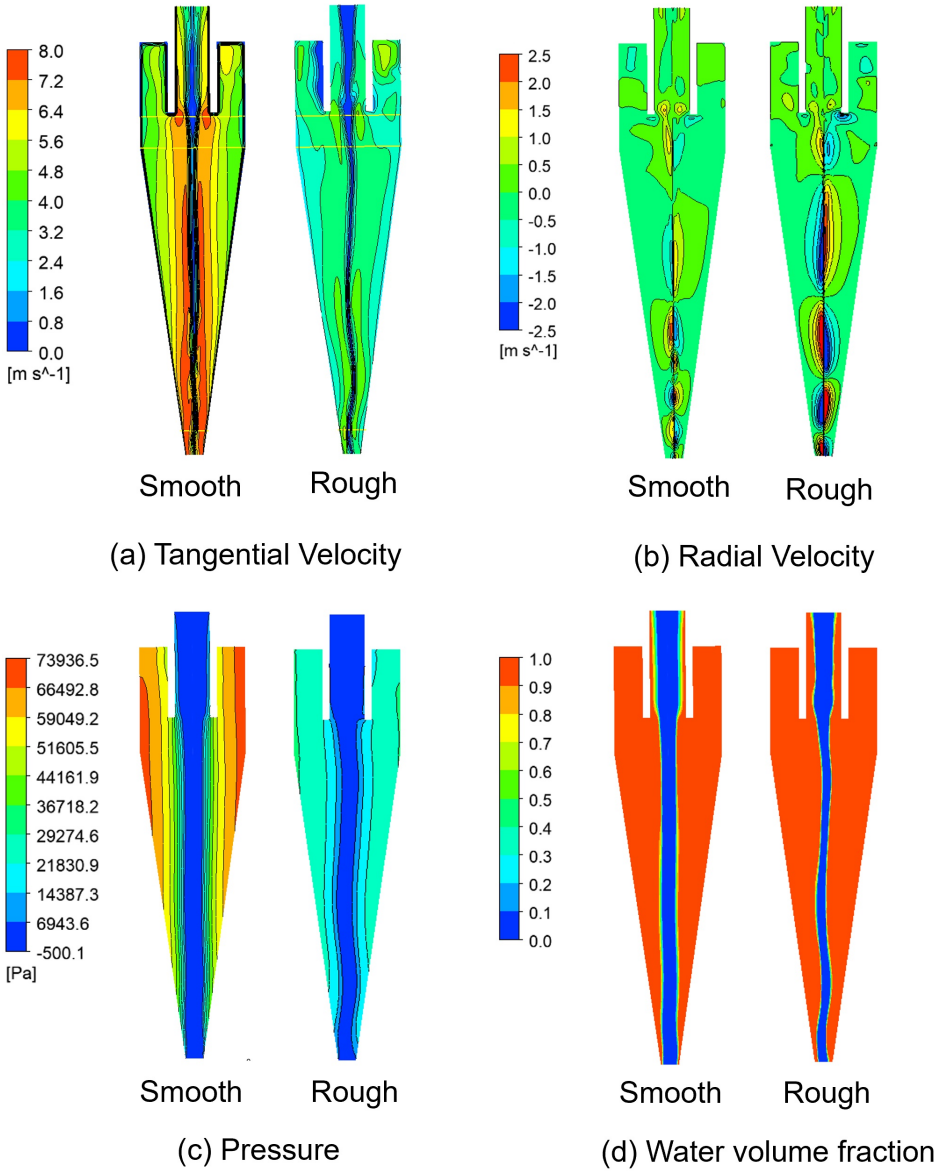


Figure 6.7: Effect of surface-wall roughness on flow quantities at the center XZ plane (Y=0) for a flow rate of 1500 mL/s: (a) Tangential velocity, (b) Radial velocity, (c) Pressure distribution, and (d) Water volume fraction.

6.3.2.3 Radial Velocity

Figure 6.7b shows time-averaged radial velocity contour plots comparing smooth and rough hydrocyclones. The data indicate that the magnitude of radial velocity is smal-

ler compared to axial and tangential velocities. Near the center core, the radial velocity is positive (outward) on one side and negative on the other, creating a flow dipole. This distribution also causes a swirl in the surrounding fluid. The figure reveals that radial velocities are more pronounced in the rough design compared to the smooth design. In the rough hydrocyclone, this increased instability in the flow domain surrounding the air-core region results in a thinner and wavier air-core, as depicted in Figure 6.7d. Additionally, these high radial velocities at the center of the hydrocyclone help transport particles from the center to the walls [171]. The higher downward axial velocities make the flow field inside the rough hydrocyclone more conducive to particle separation rather than classification.

6.3.2.4 Pressure

Pressure distribution is a crucial parameter for assessing hydrocyclone flow behavior as it is responsible for converting potential energy to kinetic energy, which imparts centrifugal force on the particles, leading to separation. As shown in Figure 6.7c, the contour plot of pressure distribution within the hydrocyclones reveals that pressure increases radially from the hydrocyclone's center towards the wall, creating a low-pressure area at the core's center. However, this trend is more pronounced for smooth-surfaced hydrocyclone than compared to rough-surfaced hydrocyclone. This low-pressure region draws external air into the hydrocyclone, forming an air-core.

A key observation is that the pressure distribution in the rough hydrocyclone is significantly lower compared to the smooth design, in agreement with previous findings reported [14, 132]. This difference in pressure distribution is directly linked to the overall pressure drop across the hydrocyclone, which is calculated by determining the difference in pressure between the inlet, overflow, and underflow. As shown in Table 6.2, the overall pressure drop increases with increasing flow rates, for both the hydrocyclone designs. However, it is observed that the pressure drop of rough hydrocyclones is consistently lower compared to those for smooth hydrocyclones across all flow rates studied. At a flowrate of 1000 mL/s, the smooth hydrocyclone exhibits a pressure drop of 30,569 Pa, which increases to 71,250 Pa at 1500 mL/s. In comparison, the rough hydrocyclone shows a pressure drop of 14,040 Pa at 1000 mL/s and 32,166 Pa at 1500 mL/s, indicating significantly lower values than the smooth design.

The interaction between the liquid and the hydrocyclone's internal surfaces plays a crucial role in determining the pressure drop. As the liquid moves from the outer to the inner part of the vortex in the hydrocyclone, it is accelerated due to the conservation of angular momentum, resulting in a decrease in its static pressure. In smooth-walled hydrocyclones, the liquid encounters minimal friction, allowing for an intense swirling motion as it spirals toward the center, thereby exerting higher centrifugal forces on the particles.

This intense swirl converts a significant amount of static pressure into dynamic pressure, resulting in a substantial pressure drop when this energy is dissipated at the vortex finder and underflow. However, when the hydrocyclone walls are rough, the increased friction dampens the swirling motion, reducing the liquid velocity and, consequently, the amount of static pressure converted into dynamic pressure [185]. This results in a lower pressure drop but also diminishes the centrifugal forces that are acting on the particles. This effect is counter-intuitive when compared to general pipe flow, where increased wall roughness typically leads to higher frictional losses and a higher pressure drop. In hydrocyclones, however, the situation is different because the primary source of pressure drop is not just frictional loss but also the conversion of static pressure into dynamic pressure. Thus, the energy "saved" may come at the cost of compromised separation efficiency of hydrocyclone. Therefore, the stability and scalability of rough-walled hydrocyclones cannot be directly compared to those of smooth-walled designs to fully leverage their advantages.

This behavior contrasts with findings in axial flow cyclones, as reported by Jun *et al.* [186]. In axial flow cyclones, wall roughness leads to a higher pressure drop because these systems rely on a primarily axial flow and lack the dominant swirling flows. In such designs, rough walls increase friction along the axial path in the exhaust pipe, directly raising pressure losses, similar to general pipe flow behavior.

6.3.3 CFD particle separation characteristics

Particles of various sizes (5, 10, 22, 35, 60, 105, and 150 microns) were injected through the inlet. Depending on their size, these particles would either report to the underflow or the overflow. Separation efficiency equivalent to partition number is defined as the ratio of the number of particles that are collected at the underflow to the number of particles that are released through the inlet. The separation efficiency curve is constructed by plotting the separation efficiencies as a function of particle size. The primary descriptor is the cut size (D_{50}); particles larger than the cut size have a greater probability of reporting to the underflow.

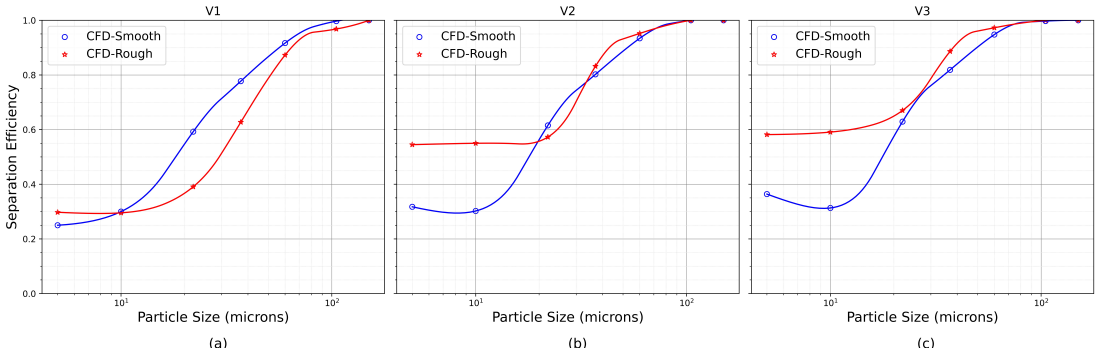


Figure 6.8: Comparison of CFD predicted separation efficiency curves for smooth and rough designs as a function of flowrate. (a) 1000 mL/s, (b) 1250 mL/s, (c) 1500 mL/s

Figure 6.8 presents particle separation efficiencies for smooth and rough-design hydrocyclones across various inlet velocities. For a given flow rate, as particle size increases, the likelihood of particles ending up in the underflow also increases, leading to higher separation efficiency values. In Figure 6.8-a, at a low flow rate (*i.e.*, V1), the rough-surface hydrocyclones exhibit higher fines bypass and lower separation efficiency compared to the smooth design. These trends, producing coarser cut sizes, are consistent with previous findings reported by Zhao *et al.* [132]. However, with increasing velocities (*i.e.*, for flow rates corresponding to V2 and V3), the bypass in rough hydrocyclones becomes more pronounced compared to smooth hydrocyclones. Furthermore, it is observed that with higher flow rates (*i.e.*, from V2 to V3), the separation efficiency values for all particle sizes, including fine sizes, are higher in rough hydrocyclones than in smooth hydrocyclones. This trend intensifies with increasing flow rates. As indicated by the previous CFD analysis, particles carried by higher radial velocities at the center are pushed to the walls and swept along by the increased downward axial velocities in rough hydrocyclones compared to smooth hydrocyclones, resulting in higher underflow solids recoveries.

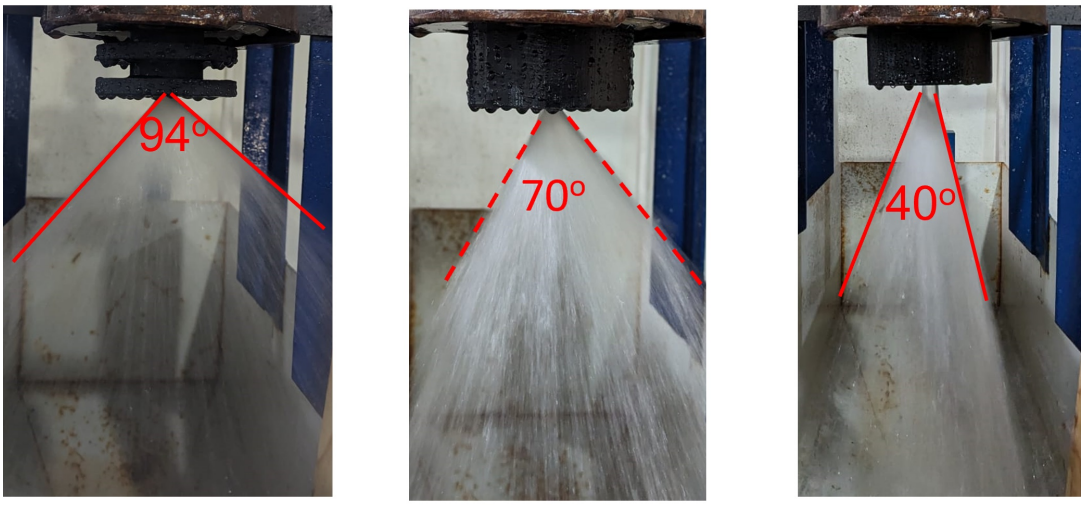
At higher flow rates, smooth-walled hydrocyclones maintain enhanced particle separation due to intensified centrifugal effects, which decrease underflow water recovery, cut sizes and slightly increasing bypass fractions. However, as the flowrate increases in rough-walled designs, frictional losses from the wall roughness dampen fluid momentum, leading to a higher bypass of fine particles and a less effective classification. This indicates that rough-walled hydrocyclones are limited in applications requiring precise particle classification at high flow rates, whereas smooth-walled hydrocyclones are better suited to maintain classification efficiency across a broader range of flow rates.

6.4 Experimental results

We investigate the influence of surface-wall roughness on the performance of hydrocyclones using both water-only and 5% solids experiments.

6.4.1 Water-only flow splits

Underflow water split (R_f), defined as the ratio of underflow to feed water recovery, is a useful metric for evaluating hydrocyclone performance. The separation of solids and liquids in a hydrocyclone is often inefficient. As a result, some solids exit through the overflow instead of the underflow, and a portion of the water in the feed ends up in the underflow. Key metrics such as solids recovery (R_s) and the concentration ratio (C)—the ratio of the concentration in the underflow to that in the feed—are used to quantify the separation efficiency. The concentration ratio is determined by the ratio of solids recovery (R_s) to the volumetric recovery of the suspension (R_v) or the flow ratio.



(a) Smooth (b) Medium (c) Rough

Figure 6.9: Underflow discharge spray profiles for flowrate of 1500 mL/s as function of surface-wall roughness: (a) Smooth, (b) Medium, (c) Rough.

The underflow exiting the hydrocyclone is open to the atmosphere, forming a spray-type discharge with varied angles depending on process and design variables such as flow rate and wall roughness. Considerable research has focused on studying the exit spray profiles of hydrocyclones to use as a performance indicator [173–175]. Earlier studies reported that for a given design, an increase in the underflow spray angle results in an increase in underflow solids recovery (R_s) and a decrease in underflow water and slurry recoveries (R_f and R_v) [174]. Figure 6.9 illustrates the underflow discharge profiles and corresponding spray angles for hydrocyclones as a function of surface-wall roughness for an inlet flowrate of 1500 mL/s (*i.e.*, V3). The spray angles are measured and displayed in red, highlighting the effect of wall roughness on the discharge flow pattern. It observed that from Figures 6.9, smooth-walled hydrocyclone has a pronounced spray angle (94°), which decreases with increasing wall roughness. For the case of medium and rough hydrocyclone designs, the exit spray angles measured were 70 and 40° respectively. The drop in spray angle can be interpreted from the loss of fluid momentum.

In the experimental analysis, the impact of surface roughness on underflow recovery was investigated at three discrete levels: smooth, medium rough, and rough. The roughness levels explored in the experiments are approximated to be 25, 150, and 300 microns. Figure 6.10 compares the trends of CFD and experimental observations of underflow water recovery (R_f) as a function of flowrate and surface-wall roughness in three levels. It is observed that at a given hydrocyclone roughness, the underflow recoveries exhibit a slight decrease as the flowrate increases. This trend is consistent across the experimental results and aligns with the predictions obtained from the CFD simulations. However, a more significant observation is the pronounced influence of surface roughness on underflow recovery. As shown in the combined plot, the experimental results confirm the strong de-

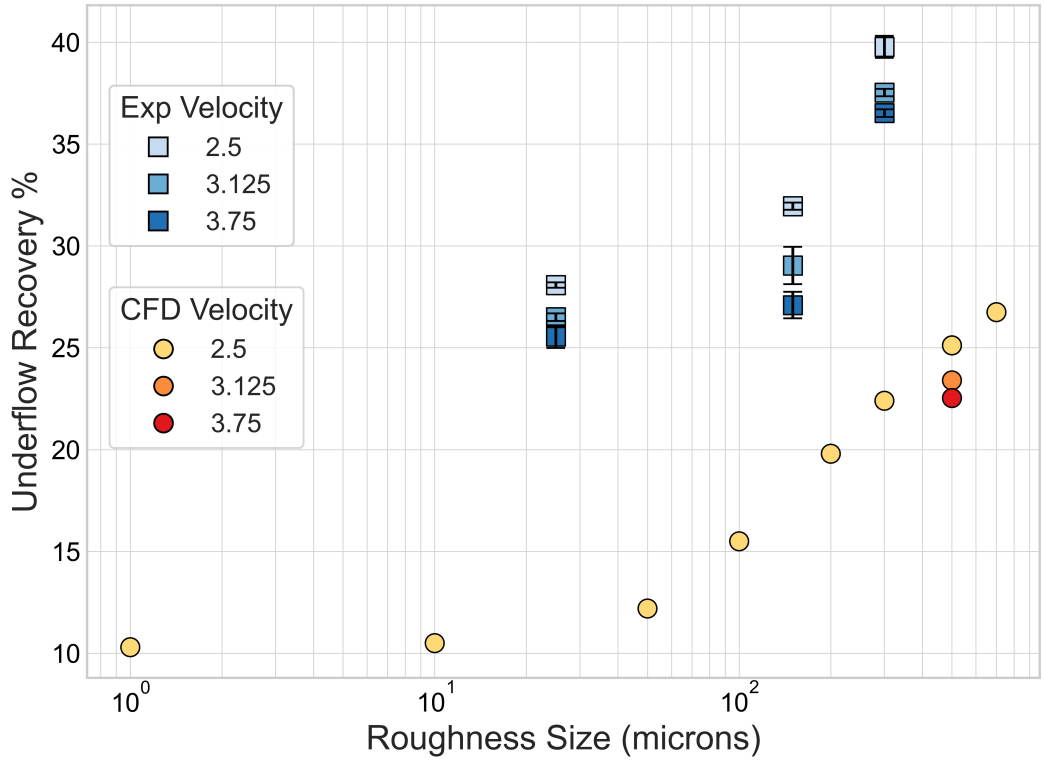


Figure 6.10: Effect of surface roughness on experimental water recoveries as a function of flow rate, with CFD predictions overlaid for trend comparison.

pendency of underflow recovery on roughness, mirroring the trends identified in the CFD simulations. Although the experimental and CFD studies share identical hydrocyclone design configurations, notable differences in predictions are observed. These differences can be primarily attributed to variations in the flow domain geometries. In the experimental setup, the hydrocyclones are enclosed within a casing, causing the fluid to enter the hydrocyclone inlet after swirling through the annular gap between the hydrocyclone and its casing.

6.4.2 Experimental particle separation analysis

Table 6.3 presents experimental observations of underflow slurry splits, water splits, solids recovery, bypass, and concentration ratios for smooth and rough-surfaced configurations of standard hydrocyclones and rough-surfaced convex hydrocyclone.

Table 6.3: Key performance metrics from slurry experimental results comparing rough and smooth-surface hydrocyclones across various flowrates

	Flow Split (Rv)			Water Splits (Rw)			Solids Splits (Rs)			Bypass			Concentration (C)		
Flowrate (mL/s)	Standard-S	Standard-R	Convex-R	Standard-S	Standard-R	Convex-R	Standard-S	Standard-R	Convex-R	Standard-S	Standard-R	Convex-R	Standard-S	Standard-R	Convex-R
1000	31.8	42.4	32.3	54.0	42	35.6	46.0	58.0	64.4	24.6	41.7	37.8	1.44	1.37	1.99
1250	29.2	39.3	28.3	49.9	30.7	24.1	50.1	69.3	75.9	32.0	57.7	41.6	1.71	1.76	2.68
1500	27.9	36.9	26.9	46.0	18.8	16.0	54.0	81.2	84.0	35.4	70.0	61.7	1.93	2.20	3.12

Figure 6.11 illustrates the effect of flow rate on solids recovery and concentration ratio as a function of wall roughness and the interaction of coupled roughness-conic design. It is observed that both metrics increase with flow rates, corroborating the trends reported by Cilliers and Harrison [177]. Notably, from Figure 6.11a, it is observed that solids recovery is significantly higher in hydrocyclones with rough walls compared to those with a standard smooth surface hydrocyclone. For example, at a flow rate of 1000 mL/s, the recovery of solids for the standard rough surface is 58.0% and for the convex rough surface hydrocyclone is 64.4%, compared to 46.0% for the standard smooth surface hydrocyclone. This trend of convex-rough surface hydrocyclones yielding higher solid recovery than that of standard-rough and smooth surface hydrocyclones is consistent across all flow rates tested under study. Interestingly, although the standard rough-surfaced hydrocyclone achieves higher solids recovery at lower flow rates, its concentration ratio is slightly lower than that of the smooth-surfaced standard hydrocyclone. However, with increasing flow rate, the concentration ratio for the standard rough-surfaced hydrocyclone surpasses that of the standard smooth-surfaced hydrocyclone. It is to be noted that the convex-rough hydrocyclone reports significantly higher concentration ratio's compared to its counterparts; indicating the coupled conic-roughness interaction has significant influence.

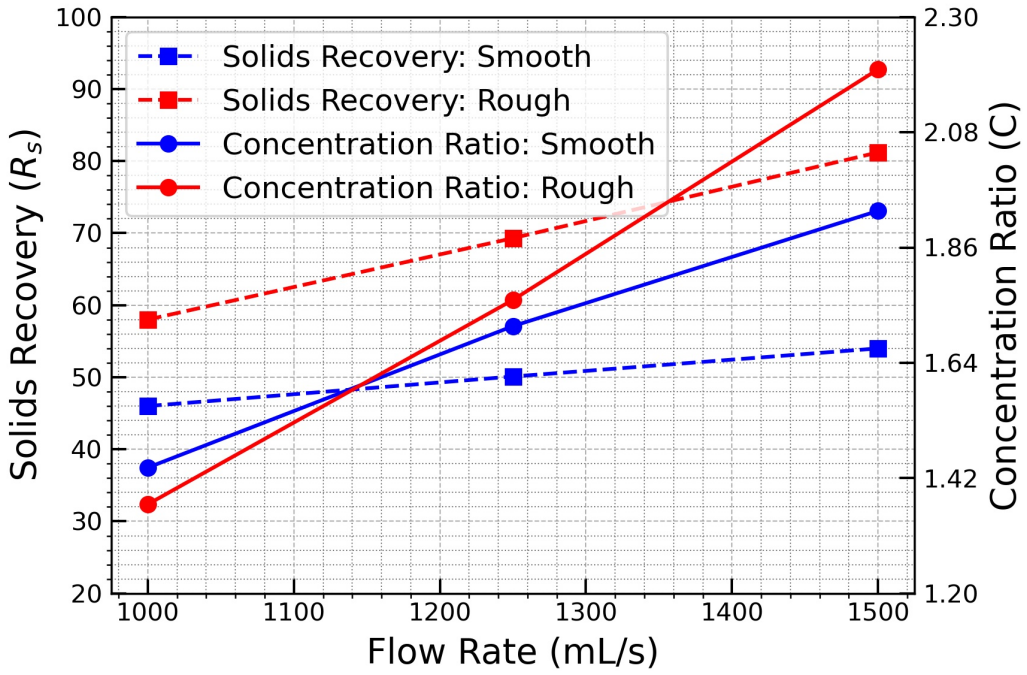


Figure 6.11: Effect of flowrate and wall roughness on the solids recovery and concentration ratio

While increased wall roughness appears to mimic the effect of reduced fluid velocity by lowering underflow water recoveries and spray angles as discussed earlier, this alone does not fully explain the observed increase in solids recovery. Typically, a decrease in velocity would also lead to lower underflow solids recovery as observed by Dubey *et al.* [174]. However, the higher solids recovery with increased roughness suggests that other

mechanisms are at play, such as enhanced particle settling due to increased downward axial velocities and turbulence as observed in CFD simulations within the rough-walled hydrocyclone. These findings highlight the complex interplay between fluid dynamics and particle separation, indicating that wall roughness can effectively enhance solids recovery beyond what would be expected from velocity changes alone.

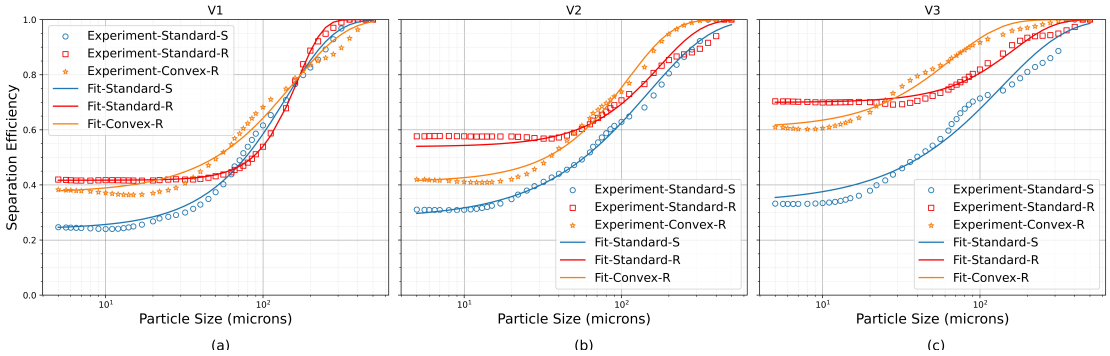


Figure 6.12: Comparison of Separation Efficiency curves for Standard smooth, rough, and Convex rough designs as a function of flowrate. (a) 1000 mL/s, (b) 1250 mL/s, (c) 1500 mL/s

For the 5% solids experiments, size assays were measured using the particle size analyzer for the samples collected from the overflow and underflow streams. Figure 6.12 illustrates the separation efficiency curves as a function of particle size for standard smooth, rough wall surface, and convex rough hydrocyclones at three different flow rates. Partition numbers are calculated on the solids recovery and particle size assays. In the plot, the smooth surface design is color-coded in blue, while the rough surface design is represented in red. Experimental partition curves are shown as discrete points, and the fitted curves are modeled using sigmoidal functional forms, such as the Rosin-Rammler distribution [108]:

$$C(d) = 1 - \exp\left(-0.693\left(\frac{d}{D_{50}}\right)^{m}\right) \tag{6.5}$$

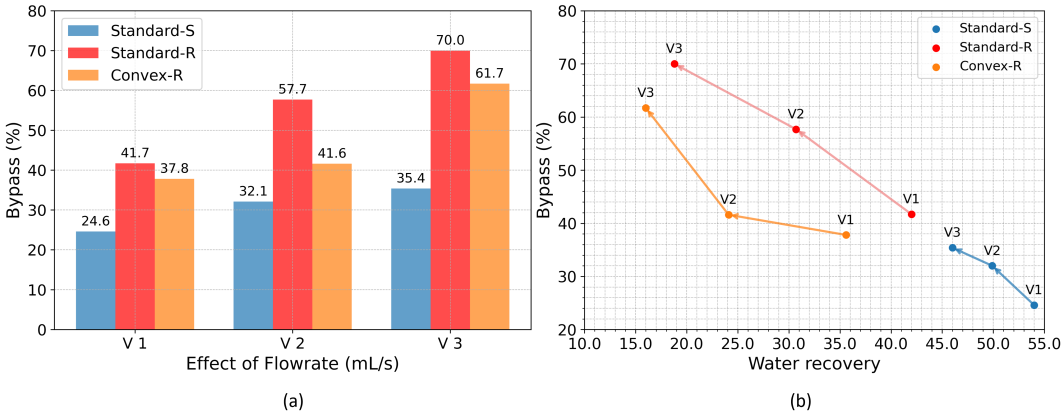


Figure 6.13: Effect of flowrate on surface roughness and the interplay between roughness and conic design in relation to bypass and water recovery.

Further, the experimental partition curve P(d) is derived by using the following relationship:

$$P(d) = B_p + C(d)(1 - B_p) \tag{6.6}$$

Here, C(d) is the corrected partition number, d is the particle size, D_{50c} is the corrected classification cut size, and m denotes the sharpness of the classification. The parameters B_p, D_{50c}, and m in the above equations are determined by minimizing an inverse particle size-weighted least square error. This method ensures a close match between the fitted curves and the experimental separation efficiency results, as illustrated in Figure 6.12. It is observed that experimental separation efficiencies for all the designs increase with particle size. For the standard smooth design, the raw cut size decreases with increasing flow rate. This decrease is attributed to the intensified centrifugal activity within the hydrocyclone, which enhances particle separation. In contrast, in rough designs, the partition curves start high due to high underflow solid recoveries, indicating a significant bypass of fine particles. A notable observation is that the particle separation performance in rough-design hydrocyclones is more sensitive to increases in flow rate compared to the smoother design. These experimental trends are in line with CFD predictions of standard hydrocyclone discussed earlier.

The metric of fines bypass (B_p), is commonly considered the partition number for the fine sizes which asymptotes at a particular value, as discussed by Frachon and Cilliers [108]. This metric has been extracted from Figure 6.12 a, b, and c and presented in Figure 6.13a for clarity. The bar plot clearly shows that fines bypass increases with increasing flow rate for all hydrocyclone designs. For the standard-smooth hydrocyclone, the B_p values are 24.6% at 1000 mL/s, 32.1% at 1250 mL/s, and 35.4% at 1500 mL/s flowrates. In contrast, for standard-rough design exhibits higher B_p values of 41.7% at 1000 mL/s, 57.7% at 1250 mL/s, and 70.0% at 1500 mL/s flowrates. Similarly, convex-rough hydrocyclones report B_p values of 37.8% at 1000 mL/s, 41.6% at 1250 mL/s, and 61.7% at 1500 mL/s flowrates, respectively. Thus, the convex-rough exhibits have a lower bypass than compared to the standard-rough design at all flowrates.

Figure 6.13b, depicts the relation between the bypass and underflow water recovery comparing hydrocyclones as a function of flowrate. Many authors in the literature assumed that bypass is equal to either underflow water or slurry recovery [103, 187, 188]. It is observed that bypass as a function of underflow water recovery exhibits an inverse relationship with increasing flow rate (inlet velocity). This finding aligns with observations by Cilliers *et al.*, who noted a similar inverse relationship between bypass and water recovery with increasing fluid temperature. Previous studies also corroborate these trends, indicating that water recovery decreases while bypass increases with rising inlet pressure [108]. In the current work, it is observed that the slope of the bypass as a function of wa-

ter recovery remains constant for both smooth and rough standard hydrocyclone designs when the flow rate is increased. Whereas, for the convex-rough hydrocyclone slope is higher at higher flowrates. However, the change in bypass and its corresponding water recovery with increasing flow rate is more pronounced for rough designs compared to smooth design.

Comparing standard smooth, rough, and convex-rough hydrocyclone designs reveals distinct flow field characteristics that significantly affect particle separation efficiency. In standard smooth hydrocyclones, higher tangential velocities generate strong centrifugal forces, enabling efficient particle classification. This design features a stable, thicker air core extending from the underflow to the cylindrical section, which supports lower bypass fractions and finer cut sizes while maintaining efficiency across varying flow rates. In contrast, the standard-rough hydrocyclone exhibits reduced tangential velocity, resulting in weaker centrifugal forces but increased radial and axial velocities. These changes direct particles toward the underflow, particularly at higher flow rates, producing coarser cut sizes and greater solids recovery. However, this comes with a thinner, more irregular air core and a higher bypass fraction.

Although CFD analysis for the convex-rough hydrocyclone is not included here, insights can be drawn from the convex-smooth CFD simulations presented in Chapter 5, which suggest that the convex design facilitates a flow field conducive to reduced bypass fractions; this observation is also reflected in the rough designs. Experimental observations of the convex-rough hydrocyclone reveal higher underflow solids recovery with a greater solids concentration ratio and lower water recovery compared to the standard-rough hydrocyclone. This highlights the significant role of the coupled interaction between conic design and surface roughness in enhancing performance for solid removal applications.

One notable difference in the effect of roughness between hydrocyclones and gas cyclones (Refer Chapter 4)is that roughness significantly increases downward axial velocities in hydrocyclones compared to their smoother counterparts, whereas the increase in gas cyclones is more modest. This difference leads to contrasting impacts on their behavior: in hydrocyclones, roughness shifts the performance from classification toward separation, while in gas cyclones, it shifts from separation toward classification.

In industrial applications such as mining, wastewater treatment, and mineral processing, hydrocyclones are extensively used for particle separation due to their efficiency and compact design. Surface roughness on the interior walls of hydrocyclones can have a significant impact on operational efficiency. For precise particle classification, smooth wall surfaces tend to enhance efficiency by reducing bypass fractions, whereas rough wall surfaces may be advantageous in high-solids recovery applications, such as de-watering.

In wastewater treatment, the ability of rough hydrocyclones to separate particles more effectively can improve water quality and reduce the need for secondary filtration steps. Over time, abrasive operations can increase wall roughness through wear, impacting separation efficiency and energy consumption. This study provides insights into how wall roughness influences performance, supporting informed decisions on timely part replacements to maintain optimal efficiency.

6.5 Conclusions

This study elucidates the impact of surface-wall roughness on hydrocyclone performance through both CFD simulations and experimental investigations. Our findings reveal several critical insights.

The rough-surface hydrocyclones exhibit distinct flow characteristics compared to smooth designs. Specifically, the rough surfaces result in more pronounced negative axial velocities near the wall and higher radial velocities at the center, responsible for scavenging more particles through the underflow. Due to the instability in the flow domain, rough-surface hydrocyclones form a thinner and unstable air core.

Experimental and CFD results consistently show that rough-surface hydrocyclones achieve significantly higher underflow recoveries. It is observed that as the flow rate increases, the underflow water recoveries decrease for both smooth and rough surfaces. Furthermore, for a given flow rate, the rough surfaces offer lower underflow water recovery compared to the smoother designs. For instance, at a flow rate of 1000 mL/s, the underflow solids recovery for the standard-rough design is 58%, compared to 46% for the standard-smooth design, while it is 64.4% for the convex-rough hydrocyclone. Similar trends are observed across different flow rates, underscoring the effectiveness of individual surface roughness and roughnes-conic design interplay in enhancing solids recovery.

Moreover, the increase in flow rate results in a more significant increase in the underflow solids concentration ratio for both standard and convex rough-surface hydrocyclones compared to standard smooth-surface hydrocyclones. However, it is pronounced for the convex-rough hydrocyclone. These findings suggest that rough surfaces facilitate better particle separation at higher flowrates.

The study highlights the potential of surface-wall roughness and the interplay of wall roughness and conic design in optimizing hydrocyclone performance. For applications requiring high solids recovery and efficient de-watering, rough-design hydrocyclones offer significant advantages. Conversely, smooth-design hydrocyclones may be preferable for applications focused on precise particle classification due to lower bypass fractions.

Chapter 7

Conclusions and Future Work

7.1 Thesis Summary 149
7.2 Conclusions 151
7.3 Study Limitations & Future Work 152

7.1 Thesis Summary

This thesis investigated the impact of curved conic design modifications and surface wall roughness on the classification performance of gas cyclones and hydrocyclones by utilizing computational fluid dynamics (CFD) simulations and lab-scale experimental validation. The findings closed significant gaps in the understanding of particle classification mechanisms, providing practical insights for optimizing industrial classifiers.

In Chapter 2, a summary of dry classification equipment used for particle size-based classification was presented, with a primary focus on centrifugal, gravity, and inertial forces that drive particle segregation. A thorough review was presented on static and dynamic centrifugal air classifiers because of their adaptability to a wide range of cut sizes and high throughput rates. Importantly, studies on gas cyclones indicate that they were conventionally employed as gas-solid separators with cut sizes (d_{50}) below 3 μm, rather than as particle classifiers. Although some studies aim to use cyclones as classifiers, they achieve this through modifications such as introducing blow-up airflow or constricting the apex outlet to resist gas flow near the apex. However, no prior research has explored inherent design modifications to adapt cyclones specifically for classification purposes.

Several CFD studies on hydrocyclones from the literature reveal that hydrocyclone having a convex conic design have the potential to significantly influence the cut sizes. However, similar investigations on the gas cyclone are very limited. Moreover, as these classifiers are subjected to operational wear and tear, the interaction between convex-conic designs and surface-wall roughness remains unexamined. The overall aim of this thesis was to address these gaps by studying the effects of conic curvature and surface wall roughness on gas cyclones and hydrocyclones using CFD simulations and experimental validation.

To achieve these aims, the objectives of this thesis were:

1. Design of parabolic conic gas cyclones for coarse particle classification using CFD simulations coupled with Response Surface Methodology (RSM);
2. Experimentally evaluate the impact of conic curvature and wall roughness on gas cyclones;
3. Transfer insights on the influence of conic shape from gas cyclones to hydrocyclones through CFD simulations and experimental validation;
4. Investigate the effects of surface wall roughness and conic design on hydrocyclones through CFD simulations and experiments.

In Chapter 3, the impact of curved conical wall shapes, particularly parabolic concave and convex designs, on particle classification in a 31 mm diameter gas cyclone was analyzed using CFD simulations. The model predictions for standard straight conic designs

were validated against experimental data from the literature across various inlet flow rates. The curved conic cyclones demonstrated sharper and coarser cut sizes compared to standard-design gas cyclone. RSM was employed to explore interaction effects between design parameters. Further, Monte Carlo simulations were performed on the RSM models to explore the design space. The two most important findings from Chapter 3 in the context of achieving coarser cut-sizes; the convex design has higher potential in achieving the coarser cut-sizes than compared to the concave and standard conic cyclones. Additionally, maintaining lower flowrates aids in suppressing the centrifugal forces acting on the particles; thereby coarser cut sizes.

The main objective of Chapter 4 was to validate experimentally the CFD findings from Chapter 3 and investigate the effects of surface wall roughness on gas cyclone performance. A CFD model was developed to replicate the experimental conditions and explain the underlying physics by comparing smooth and rough cyclones. Gas cyclones were 3D printed with different surface textures to simulate the effect of surface wall roughness. Developed a novel technique for dust particle collection using expandable chambers. This helps to measure the particle size distribution of the particles at the dust outlet section. Experimental results confirm that convex designs yield consistently coarser cut sizes with lower bypass and solids recovery across all studied flow rates resulting in a classification effect. CFD simulations reveal that surface wall roughness reduces tangential velocities in both designs; this results in lower collection efficiencies and coarser cut sizes as observed in experiments. This effect was more pronounced in convex designs, where roughness contributed to a shift toward coarser particle classification. The key findings of Chapter 4, was convex design flow domain facilitates lower bypass and coarser cut-sizes in gas cyclones. This motivates us to translate these findings to hydrocyclones, which could benefit the ball-mill classifier circuits.

In Chapter 5, the influence of convex conic shape on classification behavior on 75 mm hydrocyclones was investigated through a combination of CFD simulations and laboratory experiments. Experimental studies were conducted under water-only and 5% solids conditions, reveal that convex-conic hydrocyclones consistently achieve coarser cut sizes and lower bypass rates compared to standard hydrocyclones across the flow rates studied. CFD results revealed that convex designs exhibit distinct flow characteristics, such as higher upward axial velocities near the apex with lower tangential and radial velocities creating a favorable environment for particle classification; thereby reducing fines bypass with coarser cut size. These findings prove that convex-conic hydrocyclones offer superior performance, making them a cost-effective alternative to Derrick screens. Subsequently, this analysis has supported the successful development of an industrial-scale convex hydrocyclone, by Metso.

In Chapter 6, the effects of surface wall roughness and conic curvature on hydrocyc-

lone separation performance were examined. Using a similar methodology as in Chapter 5, sand-grain models simulate artificial roughness, and 3D printing introduces varying degrees of surface textures. CFD analyses identify a threshold roughness level above which underflow water recovery significantly increases. Velocity and pressure distributions exhibit distinct trends between smooth and rough hydrocyclones. Experimental results align with CFD predictions, demonstrating that rough-surfaced hydrocyclones achieve higher underflow solids recovery and concentration at increased flow rates compared to smooth designs.

7.2 Conclusions

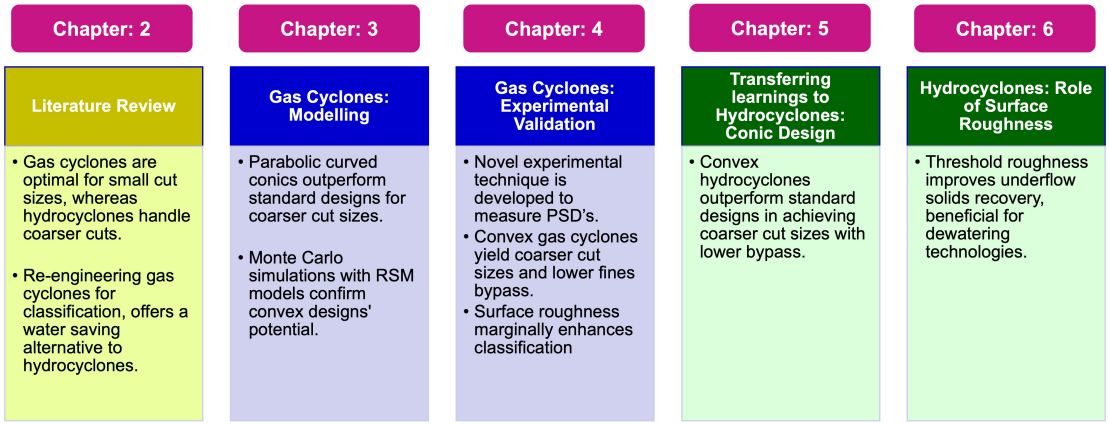


Figure 7.1: Summary of key findings from the thesis

The key findings and conclusions of this thesis are summarised as follows:

1. The literature review on dry particle separation technologies brings together the research that classifies the particles based on size, carried out by different active forces, such as gravity, inertial, centrifugal, and air fludizers. Feed throughput rate versus cut size data were compiled for all the equipment reviewed and a new graphical illustration of throughput rate vs cut size was used to identify the major gaps in dry classification technology and to recommend research directions. It is identified that gas cyclones are predominantly used as the particle separator operating with small cut sizes. Whereas hydrocyclones that operate on a similar operating principle are typically used as classifiers in mineral processing circuits. This observation intrigued me to re-engineer the gas cyclone to function as a classifier rather than a separator. Thereby addressing the pressing need for water usage.

2. CFD simulations show that curved parabolic comics have greater potential in achieving coarser cut sizes compared to standard straight conic gas cyclones. Further, the Response Surface Methodology models built using D-optimal design are used to explore the design space with the help of Monte Carlo simulations. It is observed that

due to lower tangential velocity within the flow domain Convex design has a higher potential to yield coarser cut-sizes compared to the concave and standard design cyclones.

3. Experimentally validated the trends of convex design gas cyclone yields coarser cut sizes across the flowrates studied compared to the standard cyclone. Developed a novel experimental technique using expandable collection chambers to measure particle size distributions. Another interesting observation is that convex designs yield lower bypass for fine sizes compared to the standard design cyclones. Further, the surface wall roughness aids classification with reduced solids recovery to collection; this is due to reduced tangential velocities and with marginal increase in axial velocities that carry more particles into the dust outlet.
4. The insights gained from gas cyclones were applied to hydrocyclones, utilizing both experimental and CFD modeling approaches. Convex hydrocyclone consistently yields lower bypass with coarser cut-sizes for all the flowrates understudy than compared to the standard hydrocyclone.
5. Using CFD simulations, a threshold roughness is identified above which the underflow recoveries start increasing. These trends are further validated with experiments. Roughness consistently increases the underflow solids recoveries with higher solids concentrations compared to the smoother counterparts and this trend is more pronounced at higher flowrates; thus showing potential for dewatering technologies. A physics-based CFD model explanation was provided on the role of surface wall roughness on the decrease in pressure drop which is counter-intuitive.

7.3 Study Limitations & Future Work

The results presented in this work supported and validated the methodologies outlined previously. However, several limitations have been identified in this thesis, as have potential avenues for future studies to address them.

1. In all the CFD models and experimental investigations with gas cyclones, it was assumed that dilute concentrations of particles were maintained. This simplifies the modelling approach to the one-way coupling by removing the effects of particle-particle, frictional forces between the particles and wall surfaces, and particle-wall interactions. However, for industrial applications higher throughput rates are desired, hence future studies should be performed at higher loading conditions to evaluate the particle separation performance.
2. In the study related to gas cyclones, all the simulations and experimental studies are conducted for a fixed cyclone diameter, however Brar *et al.* [189] has com-

putationally reported that cut-sizes increases with an increase in diameter. Thus, future scalability studies investigating convex design cyclones will have great scope in achieving classification objectives in gas cyclones.

3. As the modelling and experimental studies have been only focussed on for a fixed degree of curvature, however the future optimization studies including conic curvature, apex, and dust outlet diameters have greater role in optimizing the cyclone to achieve coarser cut-sizes.

4. Typically, the bypass is controlled in industries by reducing the underflow diameter; which in turn reduce the bypass and increases the cut-size for standard design hydrocyclone. Hence further investigations are required to evaluate the performance of convex hydrocyclone designs, for variable underflow outlet sizes.

5. Optimization studies to find the relationship between the degree of curvature, solids loading and underflow diameters will be of great benefit.

6. As discussed in Chapter 6, surface wall roughness after a threshold value increases the underflow recoveries with high bypass. However, the dependence of process variables such as the fluid density and viscosity of the fluid medium can play a key role in influencing the threshold limit. Thus, future studies to understand the factors that influence the threshold limit can provide valuable insights.

7. Further, as the internal walls acquire roughness due to hydro abrasion and wear and tear, time-dependent models on surface wall roughness impact on the hydrocyclone play a key role in helping industry practitioners make informed decisions on part replacements to achieve sustained performance.

Bibliography

[1] H. Yoshida, 'Effect of apex cone shape and local fluid flow control method on fine particle classification of gas-cyclone,' *Chemical Engineering Science*, vol. 85, pp. 55–61, 2013, 19^{th} Nisshin Engineering Particle Technology International Seminar (NEPTIS), ISSN: 0009-2509.

[2] T. Oshitari, M. Kimura, K. Yamamoto, K. Fukui and H. Yoshida, 'Development and evaluation of a cyclone type classifier for separating coarse particles,' *Journal of the Society of Powder Technology, Japan*, vol. 52, no. 8, pp. 435–444, 2015.

[3] H. Rumpf and K. Leschonski, 'Prinzipien und neuere verfahren der windsichtung,' *Chemie Ingenieur Technik*, vol. 39, no. 21, pp. 1231–1241, 1967.

[4] K. Leschonsi and K. Legenhausen, 'Investigation of the flow field in deflector wheel classifiers,' *Chemical Engineering and Processing: Process Intensification*, vol. 31, no. 2, pp. 131–136, 1992, ISSN: 0255-2701.

[5] K. Leschonski, 'Classification of particles in the submicron range in an impeller wheel air classifier,' *KONA Powder and Particle Journal*, vol. 14, pp. 52–60, 1996.

[6] K. Leschonski, 'Sieve analysis, the cinderella of particle size analysis methods?' *Powder Technology*, vol. 24, no. 2, pp. 115–124, 1979.

[7] J. Galk, W. Peukert and J. Krahnen, 'Industrial classification in a new impeller wheel classifier,' *Powder Technology*, vol. 105, no. 1, pp. 186–189, 1999, ISSN: 0032-5910.

[8] H. Morimoto and T. Shakouchi, 'Classification of ultra fine powder by a new pneumatic type classifier,' *Powder Technology*, vol. 131, pp. 71–79, 1 Mar. 2003, ISSN: 00325910. DOI: 10.1016/S0032-5910(02)00337-6.

[9] Z. Sun, G. Sun, X. Yang, Y. Yuan, Q. Wang and J. Liu, 'Effects of fine particle outlet on performance and flow field of a centrifugal air classifier,' *Chemical Engineering Research and Design*, vol. 117, pp. 139–148, Jan. 2017, ISSN: 02638762. DOI: 10.1016/j.cherd.2016.10.028.

[10] R. A. Worthen, 'Centrifugal air classification of fine particles using rotating disks.,' *Doctoral thesis-University of Florida*, 2002.

[11] R. Xiang, S. Park and K. Lee, 'Effects of cone dimension on cyclone performance,' *Journal of Aerosol Science*, vol. 32, no. 4, pp. 549–561, 2001.

[12] K.-T. Hsieh, *Phenomenological model of the hydrocyclone*. The University of Utah, 1988.

[13] M. Ghodrat, Z. Qi, S. Kuang, L. Ji and A. Yu, 'Computational investigation of the effect of particle density on the multiphase flows and performance of hydrocyclone,' *Minerals Engineering*, vol. 90, pp. 55–69, 2016.

[14] R. Vysyaraju, A. K. Pukkella and S. Subramanian, 'Computational investigation of a novel hydrocyclone for fines bypass reduction,' *Powder Technology*, vol. 395, pp. 501–515, 2022.

[15] Q. Wang, M. C. Melaaen and S. R. De Silva, 'Investigation and simulation of a cross-flow air classifier,' *Powder Technology*, vol. 120, no. 3, pp. 273–280, 2001.

[16] R. Johansson and M. Evertsson, 'Cfd simulation of a gravitational air classifier,' *Minerals Engineering*, vol. 33, pp. 20–26, 2012.

[17] R. Johansson and M. Evertsson, 'Cfd simulation of a centrifugal air classifier used in the aggregate industry,' *Minerals Engineering*, vol. 63, pp. 149–156, 2014, ISSN: 08926875. DOI: 10.1016/j.mineng.2014.03.013.

[18] H. A. Petit and E. F. Irassar, 'The throat classifier: A novel air classifier for the control of dust in manufactured sands,' *Powder Technology*, vol. 390, pp. 417–427, 2021.

[19] S. Liang, D. Hu, C. Zhu and A. Yu, 'Production of fine polymer powder under cryogenic conditions,' *Chemical Engineering & Technology*, vol. 25, no. 4, pp. 401–405, 2002.

[20] M. Yoshihiro *et al.*, 'Fluidized-bed classifier,' *USA patent 5975309*, 1999.

[21] A. K. Pukkella, J. J. Cilliers and K. Hadler, 'A comprehensive review and recent advances in dry mineral classification,' *Minerals Engineering*, vol. 201, p. 108 208, 2023.

[22] T. Oshitari, K. Yamamoto, K. Fukui and H. Yoshida, 'Classification characteristics of a cyclone type classifier with improved collection boxes for separating particles near the wall surface,' *Journal Of Chemical Engineering Of Japan*, vol. 50, no. 7, pp. 492–500, 2017.

[23] F. Gasbarro, F. Rizzi and M. Frey, 'Adaptation measures of energy and utility companies to cope with water scarcity induced by climate change,' *Business Strategy and the Environment*, vol. 25, no. 1, pp. 54–72, 2016.

[24] H. Yoshida, T. Saeki, T. Fujioka, T. Ueda and T. Fuyuki, 'Fine particle separation by revised type air-cyclone classifier,' *Kagaku kōgaku ronbunshū*, vol. 19, no. 3, pp. 476–482, 1993.

[25] H. Yoshida, T. Fujioka, K. Hashimoto and K. Nagahashi, 'Effect of blow-down on fluid flow and particle movement in cyclone classifier,' *Kagaku Kogaku Ronbunshu*, vol. 21, 1995.

[26] H. Yoshida, K. Ono and K. Fukui, 'The effect of a new method of fluid flow control on submicron particle classification in gas-cyclones,' *Powder technology*, vol. 149, no. 2-3, pp. 139–147, 2005.

[27] H. Yoshida, Y. Inada, K. Fukui and T. Yamamoto, 'Improvement of gas-cyclone performance by use of local fluid flow control method,' *Powder Technology*, vol. 193, no. 1, pp. 6–14, 2009.

[28] H. Yoshida, K. Fukui, K. Yoshida and E. Shinoda, 'Particle separation by iinoya's type gas cyclone,' *Powder Technology*, vol. 118, no. 1, pp. 16–23, 2001, In Commemoration of Prof. Koichi Iinoya, edited by C. Kanaoka and H. Masuda, ISSN: 0032-5910.

[29] Y. Wakizono, T. Maeda, K. Fukui and H. Yoshida, 'Effect of ring shape attached on upper outlet pipe on fine particle classification of gas-cyclone,' *Separation and Purification Technology*, vol. 141, pp. 84–93, 2015.

[30] B. Wang, D. Xu, K. Chu and A. Yu, 'Numerical study of gas–solid flow in a cyclone separator,' *Applied Mathematical Modelling*, vol. 30, no. 11, pp. 1326–1342, 2006.

[31] M. Ghodrat, S. Kuang, A. Yu, A. Vince, G. D. Barnett and P. J. Barnett, 'Numerical analysis of hydrocyclones with different conical section designs,' *Minerals Engineering*, vol. 62, pp. 74–84, 2014.

[32] A. Motin and A. Bénard, 'Design of liquid–liquid separation hydrocyclones using parabolic and hyperbolic swirl chambers for efficiency enhancement,' *Chemical Engineering Research and Design*, vol. 122, pp. 184–197, 2017.

[33] D. Vega-Garcia, P. Brito-Parada and J. Cilliers, 'Optimising small hydrocyclone design using 3d printing and cfd simulations,' *Chemical Engineering Journal*, vol. 350, pp. 653–659, 2018.

[34] L. Jiang *et al.*, 'Experimental study of the separation performance of a hydrocyclone with a compound curve cone,' *Powder Technology*, vol. 409, p. 117 829, 2022.

[35] S. Pandey and L. S. Brar, 'On the performance of cyclone separators with different shapes of the conical section using cfd,' *Powder Technology*, vol. 407, p. 117 629, 2022.

[36] L. Albuquerque, J. Wheeler, S. Valine, B. Ganahl and G. Barrios, 'Application of high frequency screens in closing grinding circuits,' in *In International Mineral Processing Seminar–Gecamin*, Citeseer, 2008, pp. 1–9.

[37] S. B. Valine, J. E. Wheeler and L. G. Albuquerque, 'Fine sizing with the derrick stack sizer screen,' *Recent advances in mineral processing plant design*, pp. 433–443, 2009.

[38] A. K. Pukkella, J. Cilliers and K. Hadler, 'Design of parabolic conic gas cyclones for coarse particle classification: A cfd study with response surface methodology,' *Powder Technology*, vol. 433, p. 119 217, 2024.

[39] A. K. Pukkella, D. Vega-Garcia, K. Hadler and J. Cilliers, 'The influence of surface-wall roughness on hydrocyclone performance,' *Separation and Purification Technology*, vol. 360, p. 131 109, 2025.

[40] A. K. Pukkella, D. Vega-Garcia, K. Hadler and J. Cilliers, 'Influence of conic shape on bypass and cut-size in hydrocyclones,' *Separation and Purification Technology*, vol. 361, p. 131 224, 2025.

[41] A. K. Pukkella, J. Rasera, K. Hadler and J. Cilliers, 'Impact of conic curvature and wall roughness on gas cyclones: A computational and experimental study,' *Powder Technology - Under Review*,

[42] T. Napier-Munn and R. Morrison, 'The potential for the dry processing of ores,' 2003.

[43] E. T. Brown, 'Water for a sustainable minerals industry.,' *Report to Sustainable Minerals Institute*, 84pp, 2002.

[44] G. V. Franks, E. Forbes, J. Oshitani and R. J. Batterham, 'Economic, water and energy evaluation of early rejection of gangue from copper ores using a dry sand fluidised bed separator,' *International Journal of Mineral Processing*, vol. 137, pp. 43–51, 2015.

[45] B. A. Wills and T. Napier-Munn, '9 - classification,' in *Wills' Mineral Processing Technology*, B. A. Wills and T. Napier-Munn, Eds., 7^{th}, Oxford: Butterworth-Heinemann, 2005, pp. 203–224, ISBN: 978-0-7506-4450-1.

[46] Cemnet, *The Global Cement Report, 13^{th} edition*, `https://www.cemnet.com/Publications/Item/182291/the-global-cement-report-13th-edition.html`, Accessed: 2022-11-15, 2019.

[47] A. Jankovic, W. Valery and E. Davis, 'Cement grinding optimisation,' *Minerals Engineering*, vol. 17, no. 11, pp. 1075–1081, 2004, Communition, ISSN: 0892-6875.

[48] D.-I. C. Wadenpohl, 'Production of powder coatings with defined particle size distribution by grinding and inline classification,' *International Journal of Mineral Processing*, vol. 74, S155–S164, 2004, Special Issue Supplement Comminution 2002, ISSN: 0301-7516.

[49] M. Farooq, S. Ray, A. Sarkhel and C. Goldsmith, 'Evaluation of lead (pb)-free ceramic ball grid array (cbga): Wettability, microstructure and reliability,' in *2001 Proceedings. 51st Electronic Components and Technology Conference*, IEEE, 2001, pp. 978–986.

[50] N. Denmud, K. Baite, T. Plookphol and S. Janudom, 'Effects of operating parameters on the cut size of turbo air classifier for particle size classification of sac305 lead-free solder powder,' *Processes*, vol. 7, no. 7, p. 427, 2019.

[51] C. R. Jones, P. Halton and D. J. Stevens, 'The separation of flour into fractions of different protein contents by means of air classification,' *Journal of Biochemical and Microbiological Technology and Engineering*, vol. 1, no. 1, pp. 77–98, 1959.

[52] C. Eswaraiah, S. I. Angadi and B. K. Mishra, 'Mechanism of particle separation and analysis of fish-hook phenomenon in a circulating air classifier,' *Powder Technology*, vol. 218, pp. 57–63, Mar. 2012, ISSN: 00325910. DOI: 10.1016/j.powtec.2011.11.036.

[53] M. Frachon and J. Cilliers, 'A general model for hydrocyclone partition curves,' *Chemical Engineering Journal*, vol. 73, no. 1, pp. 53–59, 1999, ISSN: 1385-8947.

[54] A. Hoffmannc, A. Van Santen, R. Allen and R. Clift, 'Effects of geometry and solid loading on the performance of gas cyclones,' *Powder Technology*, vol. 70, no. 1, pp. 83–91, 1992.

[55] N. Yoshioka and Y. Hotta, 'Liquid cyclone as a hydraulic classifier,' *Chemical Engineering*, vol. 19, no. 12, pp. 632–641, 1955. DOI: 10.1252/kakoronbunshu1953.19.632.

[56] B. A. Wills and J. Finch, *Wills' mineral processing technology: An introduction to the practical aspects of ore treatment and mineral recovery*. Butterworth-heinemann, 2015.

[57] H. Rumpf, 'The characteristics of systems and their changes of state,' in *Particle Technology*. Dordrecht: Springer Netherlands, 1975, pp. 8–55.

[58] Y. Yamada, M. Yasuguchi and K. Iinoya, 'Effects of particle dispersion and circulation systems on classification performance,' *Powder Technology*, vol. 50, no. 3, pp. 275–280, 1987.

[59] T. Abbasi and S. Abbasi, 'Dust explosions–cases, causes, consequences, and control,' *Journal of Hazardous Materials*, vol. 140, no. 1-2, pp. 7–44, 2007.

[60] L. Perrin, A. Laurent, V. Falk, O. Dufaud and M. Traoré, 'Dust and electrostatic hazards, could we improve the current standards?' *Journal of Loss Prevention in the Process Industries*, vol. 20, no. 3, pp. 207–217, 2007.

[61] M. Shapiro and V. Galperin, 'Air classification of solid particles: A review,' *Chemical Engineering and Processing: Process Intensification*, vol. 44, no. 2, pp. 279–285, 2005.

[62] O. Altun, A. Toprak, H. Benzer and O. Darilmaz, 'Multi component modelling of an air classifier,' *Minerals Engineering*, vol. 93, pp. 50–56, 2016.

[63] O. Altun and H. Benzer, 'Selection and mathematical modelling of high efficiency air classifiers,' *Powder Technology*, vol. 264, pp. 1–8, 2014.

[64] W. H. Duda, *Cement-data-book*. Bauverlag, 1976, vol. 1.

[65] J. Yardi, 'Separator technology,' *World cement*, vol. 36, no. 10, pp. 87–104, 2005.

[66] K. Iinoya, T. Fuyuki, Y. Yamada, H. Hisakuni and E. Sue, 'Dry submicron classification by a small blow down cyclone,' *Journal of the Society of Powder Technology, Japan*, vol. 29, no. 5, pp. 351–355, 1992.

[67] Y. Hiraiwa, T. Oshitari, K. Fukui, T. Yamamoto and H. Yoshida, 'Effect of free air inflow method on fine particle classification of gas-cyclone,' *Separation and Purification Technology*, vol. 118, pp. 670–679, 2013, ISSN: 1383-5866.

[68] A.-N. Huang *et al.*, 'Influence of a laminarizer at the inlet on the classification performance of a cyclone separator,' *Separation and Purification Technology*, vol. 174, pp. 408–416, 2017, ISSN: 1383-5866.

[69] D. Misiulia, A. G. Andersson and T. S. Lundström, 'Effects of the inlet angle on the flow pattern and pressure drop of a cyclone with helical-roof inlet,' *Chemical Engineering Research and Design*, vol. 102, pp. 307–321, 2015, ISSN: 0263-8762.

[70] D. Misiulia, A. G. Andersson and T. S. Lundström, 'Effects of the inlet angle on the collection efficiency of a cyclone with helical-roof inlet,' *Powder Technology*, vol. 305, pp. 48–55, 2017, ISSN: 0032-5910.

[71] A.-N. Huang, K. Ito, T. Fukasawa, H. Yoshida, H.-P. Kuo and K. Fukui, 'Classification performance analysis of a novel cyclone with a slit on the conical part by cfd simulation,' *Separation and Purification Technology*, vol. 190, pp. 25–32, 2018, ISSN: 1383-5866.

[72] Y. Wakizono, T. Maeda, K. Fukui and H. Yoshida, 'Effect of ring shape attached on upper outlet pipe on fine particle classification of gas-cyclone,' *Separation and Purification Technology*, vol. 141, pp. 84–93, 2015, ISSN: 1383-5866.

[73] A. Bauder, F. Müller and R. Polke, 'Investigations concerning the separation mechanism in deflector wheel classifiers,' *International Journal of Mineral Processing*, vol. 74, S147–S154, 2004, Special Issue Supplement Comminution 2002, ISSN: 0301-7516.

[74] R. Nied, 'Cfs-hd: A new classifier for fine classification with high efficiency,' *International Journal of Mineral Processing*, vol. 44-45, pp. 723–731, 1996, Comminution, ISSN: 0301-7516.

[75] K. William and S. Craig, 'High efficiency separator,' in *Society of Mining Engineers of AIME Annual meeting, New York*, 1985, pp. 1–10.

[76] L. Guo, J. Liu, S. Liu and J. Wang, 'Velocity measurements and flow field characteristic analyses in a turbo air classifier,' *Powder Technology*, vol. 178, no. 1, pp. 10–16, 2007.

[77] Y. Feng, J. Liu and S. Liu, 'Effects of operating parameters on flow field in a turbo air classifier,' *Minerals Engineering*, vol. 21, no. 8, pp. 598–604, 2008.

[78] M. Adamčík, T. Svěrák and P. Peciar, 'Parameters effecting forced vortex formation in blade passageway of dynamic air classifier,' *České vysoké učení technické v Praze*, 2017.

[79] L. Karunakumari, C. Eswaraiah, S. Jayanti and S. Narayanan, 'Experimental and numerical study of a rotating wheel air classifier,' *AIChE Journal*, vol. 51, no. 3, pp. 776–790, 2005.

[80] M. Ito, T. Furukawa, S. Fujii and H. Tanaka, 'Particle comminution in a centrifugal air classifier1,' *Advanced Powder Technology*, vol. 4, no. 1, pp. 9–23, 1993, ISSN: 0921-8831.

[81] B. Furchner and S. Zampini, 'Air classifying,' *Ullmann's Encyclopedia of Industrial Chemistry*, 2000.

[82] J. Muscolino, 'Mechanical centrifugal air classifiers,' *Chemical Engineering*, vol. 117, no. 12, p. 48, 2010.

[83] B. Sagot, A. Forthomme, L. A. A. Yahia and G. De La Bourdonnaye, 'Experimental study of cyclone performance for blow-by gas cleaning applications,' *Journal of Aerosol Science*, vol. 110, pp. 53–69, 2017, ISSN: 0021-8502.

[84] R. Roy, 'Case studies of creativity in innovative product development,' *Design Studies*, vol. 14, no. 4, pp. 423–443, 1993, ISSN: 0142-694X.

[85] A. Prieto Lago, G. López Lorenzo, P. Díaz Fernández, J. M. Díaz Cao, P. Díez Baños and G. Fernández Rodríguez, 'Viral and bacterial environmental detection in livestock farms,' in *Reference Module in Earth Systems and Environmental Sciences*, Elsevier, 2018, ISBN: 978-0-12-409548-9.

[86] Z.-D. Guo *et al.*, 'Aerosol and surface distribution of severe acute respiratory syndrome coronavirus 2 in hospital wards, wuhan, china, 2020,' *Emerging infectious diseases*, vol. 26, no. 7, p. 1586, 2020.

[87] H. S. Adams, L. C. Kenny, M. J. Nieuwenhuijsen, R. N. Colvile and R. A. Gussman, 'Design and validation of a high-flow personal sampler for pm2. 5,' *Journal of Exposure Science & Environmental Epidemiology*, vol. 11, no. 1, pp. 5–11, 2001.

[88] K. Elsayed and C. Lacor, 'The effect of cyclone inlet dimensions on the flow pattern and performance,' *Applied mathematical modelling*, vol. 35, no. 4, pp. 1952–1968, 2011.

[89] B. Zhao, Y. Su and J. Zhang, 'Simulation of gas flow pattern and separation efficiency in cyclone with conventional single and spiral double inlet configuration,' *Chemical Engineering Research and Design*, vol. 84, no. 12, pp. 1158–1165, 2006, ISSN: 0263-8762.

[90] A. Raoufi, M. Shams, M. Farzaneh and R. Ebrahimi, 'Numerical simulation and optimization of fluid flow in cyclone vortex finder,' *Chemical Engineering and Processing: Process Intensification*, vol. 47, no. 1, pp. 128–137, 2008, ISSN: 0255-2701.

[91] A. Khalkhali and H. Safikhani, 'Pareto based multi-objective optimization of a cyclone vortex finder using cfd, gmdh type neural networks and genetic algorithms,' *Engineering Optimization*, vol. 44, no. 1, pp. 105–118, 2012.

[92] H. Safikhani, M. Akhavan-Behabadi, M. Shams and M. Rahimyan, 'Numerical simulation of flow field in three types of standard cyclone separators,' *Advanced Powder Technology*, vol. 21, no. 4, pp. 435–442, 2010, Special Issue Featuring Articles From Chemeca 2009, ISSN: 0921-8831.

[93] M. E. Caliskan, I. Karagoz, A. Avci and A. Surmen, 'An experimental investigation into the particle classification capability of a novel cyclone separator,' *Separation and Purification Technology*, vol. 209, pp. 908–913, 2019.

[94] F. Qian and M. Zhang, 'Study of the natural vortex length of a cyclone with response surface methodology,' *Computers & chemical engineering*, vol. 29, no. 10, pp. 2155–2162, 2005.

[95] H. Safikhani, 'Modeling and multi-objective pareto optimization of new cyclone separators using cfd, anns and nsga ii algorithm,' *Advanced Powder Technology*, vol. 27, no. 5, pp. 2277–2284, 2016.

[96] K. Elsayed and C. Lacor, 'Modeling, analysis and optimization of aircyclones using artificial neural network, response surface methodology and cfd simulation approaches,' *Powder technology*, vol. 212, no. 1, pp. 115–133, 2011.

[97] D. Misiulia, K. Elsayed and A. G. Andersson, 'Geometry optimization of a deswirler for cyclone separator in terms of pressure drop using cfd and artificial neural network,' *Separation and Purification Technology*, vol. 185, pp. 10–23, 2017, ISSN: 1383-5866.

[98] D. Misiulia, V. Kuzmin and V. Markov, 'Ways of decrease in power consumption of cyclone separators,' *ISJAEE*, vol. 96, no. 4, pp. 74–88, 2011.

[99] Q. Li, W. Xu, J. Wang and Y. Jin, 'Performance evaluation of a new cyclone separator – part i experimental results,' *Separation and Purification Technology*, vol. 141, pp. 53–58, 2015, ISSN: 1383-5866.

[100] W. Xu, Q. Li, J. Wang and Y. Jin, 'Performance evaluation of a new cyclone separator – part ii simulation results,' *Separation and Purification Technology*, vol. 160, pp. 112–116, 2016, ISSN: 1383-5866.

[101] M. Guo, D. K. Le, X. Sun and J. Y. Yoon, 'Multi-objective optimization of a novel vortex finder for performance improvement of cyclone separator,' *Powder Technology*, vol. 410, p. 117 856, 2022, ISSN: 0032-5910.

[102] P. Singh, I. Couckuyt, K. Elsayed, D. Deschrijver and T. Dhaene, 'Shape optimization of a cyclone separator using multi-objective surrogate-based optimization,' *Applied Mathematical Modelling*, vol. 40, no. 5, pp. 4248–4259, 2016, ISSN: 0307-904X.

[103] L. Svarovsky and M. Thew, *Hydrocyclones: analysis and applications*. Springer Science & Business Media, 1992, vol. 12.

[104] D. Bradley, *The Hydrocyclone: International Series of Monographs in Chemical Engineering*. Elsevier, 2013, vol. 4.

[105] E. Roldanvillasana, R. A. Williams and T. Dyakowski, 'The origin of the fish-hook effect in hydrocyclone separators,' *Powder Technology*, vol. 77, no. 3, pp. 243–250, 1993.

[106] T. J. Napier-Munn, S. Morrell, R. D. Morrison and T. Kojovic, 'Mineral comminution circuits: Their operation and optimisation,' 1996.

[107] J. Cilliers, L. Diaz-Anadon and F. Wee, 'Temperature, classification and dewatering in 10 mm hydrocyclones,' *Minerals Engineering*, vol. 17, no. 5, pp. 591–597, 2004.

[108] M. Frachon and J. Cilliers, 'A general model for hydrocyclone partition curves,' *Chemical Engineering Journal*, vol. 73, no. 1, pp. 53–59, 1999.

[109] C. Banerjee, R. K. Dubey and A. K. Majumder, 'Phenomenological study on fine particle misplacement behavior in hydrocyclone,' *Transactions of the Indian Institute of Metals*, vol. 70, pp. 313–322, 2017.

[110] S. Fu, Y. Qian, H. Yuan and Y. Fang, 'Effect of cone angles of a hydrocyclone for the separation of waste plastics with low value of density difference,' *Waste Management*, vol. 140, pp. 183–192, 2022.

[111] X. Yang, M. J. Simmons, P. Liu, Y. Zhang and L. Jiang, 'Effect of feed body geometry on separation performance of hydrocyclone,' *Separation Science and Technology*, vol. 54, no. 17, pp. 2959–2970, 2019.

[112] L. Jiang, P. Liu, Y. Zhang, X. Yang, H. Wang and X. Gui, 'Design boundary layer structure for improving the particle separation performance of a hydrocyclone,' *Powder Technology*, vol. 350, pp. 1–14, 2019.

[113] L. Jiang, P. Liu, X. Yang, Y. Zhang and H. Wang, 'Designing w-shaped apex for improving the separation efficiency of a full-column hydrocyclone,' *Separation Science and Technology*, vol. 55, no. 9, pp. 1724–1740, 2020.

[114] D. Hou, Q. Zhao, B. Cui, D. Wei, Z. Song and Y. Feng, 'The effects of solid shear stress and wall roughness on the simulation of cylindrical hydrocyclone classification,' *Powder Technology*, vol. 393, pp. 184–204, 2021.

[115] R. Changirwa, M. Rockwell and D. Mutua, 'Mathematical modelling multiple-cone concurrent three-phase (ctp) hydrocyclone separation,' *Journal of Canadian Petroleum Technology*, vol. 38, no. 13, 1999.

[116] N. Kharoua, L. Khezzar and Z. Nemouchi, 'Hydrocyclones for de-oiling applications—a review,' *Petroleum Science and Technology*, vol. 28, no. 7, pp. 738–755, 2010.

[117] M. Sun, L. Wei and G. Cui, 'Studies of a water-only cyclone with a three-stage cone for fine coal beneficiation,' *International Journal of Coal Preparation and Utilization*, vol. 37, no. 2, pp. 75–86, 2017.

[118] Q. Yang, H.-l. Wang, Y. Liu and Z.-m. Li, 'Solid/liquid separation performance of hydrocyclones with different cone combinations,' *Separation and Purification Technology*, vol. 74, no. 3, pp. 271–279, 2010.

[119] L.-Y. Chu, W.-M. Chen and X.-Z. Lee, 'Effect of structural modification on hydrocyclone performance,' *Separation and purification technology*, vol. 21, no. 1-2, pp. 71–86, 2000.

[120] F. Li *et al.*, 'Purification of granular sediments from wastewater using a novel hydrocyclone,' *Powder Technology*, vol. 393, pp. 751–763, 2021.

[121] W. Barth, 'Berechnung und auslegung von zyklonabscheidern auf grund neuer untersuchungen,' *Brennst.-Warme-Kraft*, vol. 8, pp. 1–9, 1956.

[122] P. Meißner and F. Löffler, 'Zur berechnung des strömungsfeldes im zyklonabschneider,' 1977.

[123] I. K. Fuat Kaya and A. Avci, 'Effects of surface roughness on the performance of tangential inlet cyclone separators,' *Aerosol Science and Technology*, vol. 45, no. 8, pp. 988–995, 2011. DOI: 10.1080/02786826.2011.574174.

[124] H. Ci and G. Sun, 'Effects of wall roughness on the flow field and vortex length of cyclone,' *Procedia engineering*, vol. 102, pp. 1316–1325, 2015.

[125] J. Foroozesh, F. Parvaz, S. Hosseini, G. Ahmadi, K. Elsayed and N. U. Babaoğlu, 'Computational fluid dynamics study of the impact of surface roughness on cyclone performance and erosion,' *Powder Technology*, vol. 389, pp. 339–354, 2021.

[126] F. Zhou, G. Sun, Y. Zhang, H. Ci and Q. Wei, 'Experimental and cfd study on the effects of surface roughness on cyclone performance,' *Separation and Purification Technology*, vol. 193, pp. 175–183, 2018.

[127] L. Zhou, X. Zhang and Y. Yu, 'Experimental and numerical studies on the wall-roughness effect to particle dynamics in various gas-particle flows,' *Experimental and Computational Multiphase Flow*, pp. 1–8, 2024.

[128] F. Zhou, Y. Guo, H. Qian, S. Fu and H. Yuan, 'Effect of wall roughness on particle deposition on the outer wall of the vortex finder in a cyclone separator,' *Advanced Powder Technology*, vol. 35, no. 5, p. 104 428, 2024.

[129] E. Dehdarinejad, M. Bayareh and M. Ashrafizaadeh, 'Impact of cone wall roughness on turbulence swirling flow in a cyclone separator,' *Chemical Papers*, vol. 76, no. 9, pp. 5579–5599, 2022.

[130] E. Dehdarinejad and M. Bayareh, 'Impact of non-uniform surface roughness on the erosion rate and performance of a cyclone separator,' *Chemical Engineering Science*, vol. 249, p. 117 351, 2022.

[131] F. Fontein, J. Van Kooy and H. Leniger, 'The influence of some variables upon hydrocyclone performance,' *British Chemical Engineering*, vol. 7, no. 1, pp. 410–420, 1962.

[132] Q. Zhao, B. Cui, D. Hou, D. Wei, T. Song and Y. Feng, 'Effects of wall roughness on the separation performance of hydrocyclones under different inlet conditions,' *Industrial & Engineering Chemistry Research*, vol. 60, no. 30, pp. 11 251–11 266, 2021.

[133] L. Jiang *et al.*, 'Experimental study of the separation performance of a hydrocyclone with a compound curve cone,' *Powder Technology*, vol. 409, p. 117 829, 2022, ISSN: 0032-5910.

[134] M. Azadi, M. Azadi and A. Mohebbi, 'A cfd study of the effect of cyclone size on its performance parameters,' *Journal of hazardous materials*, vol. 182, no. 1-3, pp. 835–841, 2010.

[135] M. Slack, R. Prasad, A. Bakker and F. Boysan, 'Advances in cyclone modelling using unstructured grids,' *Chemical Engineering Research and Design*, vol. 8, no. 78, pp. 1098–1104, 2000.

[136] G. Gronald and J. Derksen, 'Simulating turbulent swirling flow in a gas cyclone: A comparison of various modeling approaches,' *Powder technology*, vol. 205, no. 1-3, pp. 160–171, 2011.

[137] K. Elsayed and C. Lacor, 'Analysis and optimisation of cyclone separators geometry using rans and les methodologies,' in *Turbulence and Interactions*, Springer, 2014, pp. 65–74.

[138] A. Hoekstra, J. Derksen and H. Van Den Akker, 'An experimental and numerical study of turbulent swirling flow in gas cyclones,' *Chemical engineering science*, vol. 54, no. 13-14, pp. 2055–2065, 1999.

[139] T. P. Dhakal, D. K. Walters and W. Strasser, 'Numerical study of gas-cyclone airflow: An investigation of turbulence modelling approaches,' *International Journal of Computational Fluid Dynamics*, vol. 28, no. 1-2, pp. 1–15, 2014.

[140] P. Spalart and M. Shur, 'On the sensitization of turbulence models to rotation and curvature,' *Aerospace Science and Technology*, vol. 1, no. 5, pp. 297–302, 1997.

[141] Y. H. Alahmadi and A. F. Nowakowski, 'Modified shear stress transport model with curvature correction for the prediction of swirling flow in a cyclone separator,' *Chemical Engineering Science*, vol. 147, pp. 150–165, 2016.

[142] L. Queiroz, F. Santos, J. Oliveira and M. Souza Jr, 'Physics-informed deep learning to predict flow fields in cyclone separators,' *Digital Chemical Engineering*, vol. 1, p. 100 002, 2021.

[143] Y. You, F. Seibold, S. Wang, B. Weigand and U. Gross, 'Urans of turbulent flow and heat transfer in divergent swirl tubes using the k-ω sst turbulence model with

curvature correction,' *International Journal of Heat and Mass Transfer*, vol. 159, p. 120 088, 2020.

[144] C. Song, B. Pei, M. Jiang, B. Wang, D. Xu and Y. Chen, 'Numerical analysis of forces exerted on particles in cyclone separators,' *Powder Technology*, vol. 294, pp. 437–448, 2016.

[145] S. Morsi and A. Alexander, 'An investigation of particle trajectories in two-phase flow systems,' *Journal of Fluid mechanics*, vol. 55, no. 2, pp. 193–208, 1972.

[146] A. J. Hoekstra, 'Gas flow field and collection efficiency of cyclone separators,' *TU Delft, Ph. D. Thesis, Delft University of Technology*, 2000.

[147] R. A. Fisher, 'Design of experiments,' *British Medical Journal*, vol. 1, no. 3923, p. 554, 1936.

[148] J. L. Goupy, *Methods for experimental design: principles and applications for physicists and chemists*. Elsevier, 1993.

[149] A. C. Atkinson and A. N. Donev, *Optimum experimental designs*. Clarendon Press, 1992, vol. 5.

[150] E. Kuram, B. Ozcelik, M. Bayramoglu, E. Demirbas and B. T. Simsek, 'Optimization of cutting fluids and cutting parameters during end milling by using d-optimal design of experiments,' *Journal of Cleaner Production*, vol. 42, pp. 159–166, 2013.

[151] R. Mathieu, I. Baghdadi, O. Briat, P. Gyan and J.-M. Vinassa, 'D-optimal design of experiments applied to lithium battery for ageing model calibration,' *Energy*, vol. 141, pp. 2108–2119, 2017.

[152] A. K. Pukkella, J. J. Cilliers and K. Hadler, 'A comprehensive review and recent advances in dry mineral classification,' *Minerals Engineering*, vol. 201, p. 108 208, 2023, ISSN: 0892-6875.

[153] H. I. Erol, O. Turgut and R. Unal, 'Experimental and numerical study of stairmand cyclone separators: A comparison of the results of small-scale and large-scale cyclones,' *Heat and Mass Transfer*, vol. 55, no. 8, pp. 2341–2354, 2019.

[154] A. C. Hoffmann, M. D. Groot and A. Hospers, 'The effect of the dust collection system on the flowpattern and separation efficiency of a gas cyclone,' *The Canadian Journal of Chemical Engineering*, vol. 74, no. 4, pp. 464–470, 1996.

[155] W. Peng *et al.*, 'Flow pattern in reverse-flow centrifugal separators,' *Powder Technology*, vol. 127, no. 3, pp. 212–222, 2002.

[156] M. Caporaloni, F. Tampieri, F. Trombetti and O. Vittori, 'Transfer of particles in nonisotropic air turbulence,' *Journal of Atmospheric Sciences*, vol. 32, no. 3, pp. 565–568, 1975.

[157] M. Reeks, 'The transport of discrete particles in inhomogeneous turbulence,' *Journal of Aerosol Science*, vol. 14, no. 6, pp. 729–739, 1983, ISSN: 0021-8502.

[158] A. Noorani, G. Sardina, L. Brandt and P. Schlatter, 'Particle transport in turbulent curved pipe flow,' *Journal of Fluid Mechanics*, vol. 793, pp. 248–279, 2016.

[159] A. K. Pukkella, R. Vysyaraju and S. Subramanian, 'Enhanced gravity particle classifier: Experiments with 3d printed device and computational fluid dynamics simulations,' *AIChE Journal*, vol. 65, no. 9, e16669, 2019.

[160] G. James, D. Witten, T. Hastie and R. Tibshirani, *An introduction to statistical learning*. Springer, 2013, vol. 112.

[161] P. Supachart, T. Swasdisevi, P. Wongsarivej, M. Amornkitbamrung and N. Pratinthong, 'Development of separation sharpness model for hydrocyclone,' *Chinese Journal of Chemical Engineering*, vol. 28, no. 3, pp. 785–792, 2020.

[162] S. Rahimi, M. Ataee-pour, H. Madani and S. M. Aminossadati, 'Investigating the impact of gas emission uncertainty on airflow distribution in an auxiliary ventilation system using cfd and monte-carlo simulation,' *Building and Environment*, vol. 204, p. 108 165, 2021.

[163] J. Cilliers, J. Rasera and K. Hadler, 'Estimating the scale of space resource utilisation (sru) operations to satisfy lunar oxygen demand,' *Planetary and Space Science*, vol. 180, p. 104 749, 2020.

[164] J. Nikuradse, 'Stromungsgesetze in rauhen rohren,' *vdi-forschungsheft*, vol. 361, p. 1, 1933.

[165] C. G. Speziale, S. Sarkar and T. B. Gatski, 'Modelling the pressure–strain correlation of turbulence: An invariant dynamical systems approach,' *Journal of fluid mechanics*, vol. 227, pp. 245–272, 1991.

[166] F.-S. Lien and M. Leschziner, 'Assessment of turbulence-transport models including non-linear rng eddy-viscosity formulation and second-moment closure for flow over a backward-facing step,' *Computers & Fluids*, vol. 23, no. 8, pp. 983–1004, 1994.

[167] B. Wang, K. Chu, A. Yu and A. Vince, 'Modeling the multiphase flow in a dense medium cyclone,' *Industrial & Engineering Chemistry Research*, vol. 48, no. 7, pp. 3628–3639, 2009.

[168] P. J. Roache, 'Perspective: A method for uniform reporting of grid refinement studies,' *Journal of Fluids Engineering*, vol. 116, no. 3, pp. 405–413, 1994.

[169] M. Ghodrat, S. Kuang, A. Yu, A. Vince, G. D. Barnett and P. J. Barnett, 'Computational study of the multiphase flow and performance of hydrocyclones: Effects of cyclone size and spigot diameter,' *Industrial & Engineering Chemistry Research*, vol. 52, no. 45, pp. 16 019–16 031, 2013.

[170] T. R. Vakamalla, K. S. Kumbhar, R. Gujjula and N. Mangadoddy, 'Computational and experimental study of the effect of inclination on hydrocyclone performance,' *Separation and purification technology*, vol. 138, pp. 104–117, 2014.

[171] T. Bu, D. Mesa, A. K. Pukkella and P. R. Brito-Parada, 'Optimising miniaturised hydrocyclones for enhanced separation of microplastics,' *Chemical Engineering Journal*, p. 153 718, 2024.

[172] T. R. Vakamalla and N. Mangadoddy, 'Numerical simulation of industrial hydrocyclones performance: Role of turbulence modelling,' *Separation and Purification Technology*, vol. 176, pp. 23–39, 2017.

[173] A. Mazumdar, R. Dubey, C. Banerjee, K. Sengupta and A. Majumder, 'A study on the characteristics of spray angle formation in a 2 inch hydrocyclone using water only,' *International Journal of Mineral Processing*, vol. 126, pp. 141–145, 2014.

[174] R. Dubey, E. Climent, C. Banerjee and A. K. Majumder, 'Performance monitoring of a hydrocyclone based on underflow discharge angle,' *International Journal of Mineral Processing*, vol. 154, pp. 41–52, 2016.

[175] D. Pérez, P. Cornejo, C. Rodríguez and F. Concha, 'Transition from spray to roping in hydrocyclones,' *Minerals Engineering*, vol. 123, pp. 71–84, 2018.

[176] J. Van Deventer, D. Feng, K. Petersen and C. Aldrich, 'Modelling of hydrocyclone performance based on spray profile analysis,' *International journal of mineral processing*, vol. 70, no. 1-4, pp. 183–203, 2003.

[177] J. Cilliers and S. Harrison, 'The application of mini-hydrocyclones in the concentration of yeast suspensions,' *The Chemical Engineering Journal and the Biochemical Engineering Journal*, vol. 65, no. 1, pp. 21–26, 1997.

[178] B. Klein. 'Metso launches breakthrough hydrocyclone technology, the mhc hydrocyclone curved bottom, to enhance efficiency and maximize capacity in the classification process.' Accessed: 2024-09-27. (Sep. 2024), [Online]. Available: `https://shorturl.at/cYOfH`.

[179] A. Gomez-Flores, G. W. Heyes, S. Ilyas and H. Kim, 'Effects of artificial impeller blade wear on bubble–particle interactions using cfd (k–ε and les), piv, and 3d printing,' *Minerals Engineering*, vol. 186, p. 107 766, 2022.

[180] L. He *et al.*, 'Experimental and numerical analysis of chinese hamster ovary cell viability loss in mini-hydrocyclones,' *Separation and Purification Technology*, vol. 295, p. 121 203, 2022.

[181] P. Yuan *et al.*, 'Comprehensive analysis of chinese hamster ovary cell viability loss in mini-hydrocyclones,' *Powder Technology*, vol. 438, p. 119 603, 2024.

[182] K. Mitchell, S. Urade, A. Kershaw, P. Chu and Y. Jin, '3d printing of conical centrifuge system for mineral particle separation,' *Separation and Purification Technology*, vol. 306, p. 122 567, 2023.

[183] Fluent, 'Chapter 4: Turbulence, 4.18. near-wall treatments for wall-bounded turbulent flows.,' in *Theory Guide*, Ansys, 2023.

[184] M. S. M. Ali, C. J. Doolan and V. Wheatley, 'Grid convergence study for a two-dimensional simulation of flow around a square cylinder at a low reynolds number,' in *Seventh International Conference on CFD in The Minerals and Process Industries (ed. PJ Witt & MP Schwarz)*, 2009, pp. 1–6.

[185] A. C. Hoffmann and L. E. Stein, 'Cyclone flow pattern and pressure drop,' in *Gas Cyclones and Swirl Tubes: Principles, Design and Operation*. Berlin, Heidelberg: Springer Berlin Heidelberg, 2002, pp. 49–76, ISBN: 978-3-662-07377-3. DOI: 10.1007/978-3-662-07377-3_4.

[186] L. Jun, C. Ma, W. Tao, J. Chang and X. Zhao, 'Effects of roughness on the performance of axial flow cyclone separators using numerical simulation method,' *Proceedings of the Institution of Mechanical Engineers, Part A: Journal of Power and Energy*, vol. 233, no. 7, pp. 914–927, 2019.

[187] T. Braun and M. Bohnet, 'Influence of feed solids concentration on the performance of hydrocyclones,' *Chemical engineering & technology*, vol. 13, no. 1, pp. 15–20, 1990.

[188] K. Heiskanen, 'Particle classification. chapman and hall, london-glasgow,' 1993.

[189] L. S. Brar, R. Sharma and K. Elsayed, 'The effect of the cyclone length on the performance of stairmand high-efficiency cyclone,' *Powder Technology*, vol. 286, pp. 668–677, 2015.

[190] W.-H. Lai, W.-F. Lu and M.-C. Chou, 'Sorting of fine powder by gravitational classification chambers,' *Advanced Powder Technology*, vol. 20, no. 2, pp. 177–184, 2009.

[191] Y. Li, X. Zhang, X. Shen, H. Li and K. Gao, 'Experiment and simulation study on optimized structure of a gravitational air classifier,' *International Journal of Mineral Processing*, vol. 141, pp. 44–50, 2015.

[192] H. Petit, E. F. Irassar and M. R. Barbosa, 'Evaluation of the performance of the cross-flow air classifier in manufactured sand processing via cfd–dem simulations,' *Computational Particle Mechanics*, vol. 5, no. 1, pp. 87–102, 2018.

[193] V. Banjac *et al.*, 'Optimization of the classification process in the zigzag air classifier for obtaining a high protein sunflower meal–chemometric and cfd approach,' *Advanced Powder Technology*, vol. 28, no. 3, pp. 1069–1078, 2017.

[194] Y. Zhou and W. Shen, 'Numerical simulation of particle classification in new multi-product classifier,' *Chemical Engineering Research and Design*, vol. 177, pp. 484–492, 2022.

[195] D. Schwechten and K. Straetmans, 'A new type of zig-zag cassifier for dedusting separation and sorting in the fines range,' *Aufbereitungstechnik*, vol. 44, no. 10, pp. 43–46, 2003.

[196] M. W. Biddulph, 'Design of vertical air classifiers for municipal solid waste,' *The Canadian Journal of Chemical Engineering*, vol. 65, no. 4, pp. 571–580, 1987.

[197] T. Hagemeier, H. Glöckner, C. Roloff, D. Thévenin and J. Tomas, 'Simulation of multi-stage particle classification in a zigzag apparatus,' *Chemical Engineering & Technology*, vol. 37, no. 5, pp. 879–887, 2014.

[198] A. Kaas, T. Mütze and U. A. Peuker, 'Review on zigzag air classifier,' *Processes*, vol. 10, no. 4, p. 764, 2022.

[199] J. Vandenhoeck, 'Classifier with gas flow distributor,' *USA Patent*, vol. 3006470, 1961.

[200] J. Franken, 'Apparatus for classifying particulate material,' *USA Patent*, vol. 3006470, 1961.

[201] T. Kaya, M. Hashimoto and H. Pettingell, 'The development of sand manufacture from crushed rock in japan, using advanced vsi technology,' in *Proceedings of the International Center for Aggregates Research Symposium, Austin, TX, USA (2009)*, 2009, pp. 4–5.

[202] I. Sims and B. Brown, 'Concrete aggregates,' in *Lea's chemistry of cement and concrete*, Butterworth-Heinemann, 1998, pp. 907–1015.

[203] R. Johansson and M. Evertsson, 'An empirical study of a gravitational air classifier,' *Minerals Engineering*, vol. 31, pp. 10–16, 2012.

[204] Z. Sun, L. Liang, C. Liu and G. Yang, 'Structural optimization of vortex finder for a centrifugal air classifier,' *Chemical Engineering Research and Design*, vol. 166, pp. 220–226, Feb. 2021, ISSN: 02638762. DOI: 10.1016/j.cherd.2020.12.008.

[205] S. Okuda, 'New submicron air classification-classification by coanda effect,' *Powder Technology*, vol. 24, no. 5, pp. 35–41, 1992.

[206] S. Liang, 'Numerical study of classification of ultrafine particles in a gas-solid field of elbow-jet classifier,' *Chemical Engineering Communications*, vol. 197, no. 7, pp. 1016–1032, 2010.

[207] P. Systems. 'Elbow classifier.' (2023), [Online]. Available: https://www.powder.co.jp/EN/products/01/.

[208] R. Akatsuka *et al.*, 'Characteristics of hydroxyapatite film formed on human enamel with the powder jet deposition technique,' *Journal of Biomedical Materials Research Part B: Applied Biomaterials*, vol. 98, no. 2, pp. 210–216, 2011.

[209] Y. Zhang, H. Wang, L. Chen and C. Lu, 'Systematic investigation of particle segregation in binary fluidized beds with and without multilayer horizontal baffles,' *Industrial & Engineering Chemistry Research*, vol. 51, no. 13, pp. 5022–5036, 2012.

[210] I. V. Klumpar, F. N. Currier and T. A. Ring, 'Air classifiers,' *Chemical Engineering (New York, NY)*, vol. 93, no. 5, pp. 77–92, 1986.

[211] N. Gelperin, V. Ainshtein, V. Kvasha, A. Kogan and S. Vil'nits, 'Apparatus for classification of free-flowing materials in a fluidized bed,' *Int. Chem. Eng*, vol. 4, pp. 198–203, 1964.

[212] G. Hartholt, R. La Riviere, A. Hoffmann and L. Janssen, 'The influence of perforated baffles on the mixing and segregation of a binary group b mixture in a gas–solid fluidized bed,' *Powder Technology*, vol. 93, no. 2, pp. 185–188, 1997.

[213] J. Bosma and A. Hoffmann, 'On the capacity of continuous powder classification in a gas-fluidized bed with horizontal sieve-like baffles,' *Powder Technology*, vol. 134, no. 1-2, pp. 1–15, 2003.

[214] P. Rowe, 'The mechanisms by which particles segregate in gas fluidised beds-binary system of near spherical particles,' *Trans. Inst. Chem. Engng*, vol. 50, pp. 310–323, 1972.

[215] L. Gibilaro and P. Rowe, 'A model for a segregating gas fluidised bed,' *Chemical Engineering Science*, vol. 29, no. 6, pp. 1403–1412, 1974, ISSN: 0009-2509.

[216] A. Hoffmann and E. Romp, 'Segregation in a fluidised powder of a continuous size distribution,' *Powder Technology*, vol. 66, no. 2, pp. 119–126, 1991, ISSN: 0032-5910.

[217] X. Wang and M. Rhodes, 'Using pulsed flow to overcome defluidization,' *Chemical Engineering Science*, vol. 60, no. 18, pp. 5177–5181, 2005, ISSN: 0009-2509.

[218] H. Khosravi Bizhaem and H. Basirat Tabrizi, 'Experimental study on hydrodynamic characteristics of gas–solid pulsed fluidized bed,' *Powder Technology*, vol. 237, pp. 14–23, 2013, ISSN: 0032-5910.

[219] M. Saidi, H. B. Tabrizi, S. Chaichi and M. Dehghani, 'The effect of non-continuous inlet air on increasing the segregation of binary particles in a fluidized bed,' ASME International Mechanical Engineering Congress and Exposition, vol. Volume 7: Fluids Engineering Systems and Technologies, Nov. 2014, V007T09A005.

[220] C. K. Jayarathna, J. Chladek, M. Balfe, B. M. Moldestad and L.-A. Tokheim, 'Impact of solids loading and mixture composition on the classification efficiency of a novel cross-flow fluidized bed classifier,' *Powder Technology*, vol. 336, pp. 30–44, 2018.

[221] J. Chladek, C. K. Jayarathna, B. M. Moldestad and L.-A. Tokheim, 'Fluidized bed classification of particles of different size and density,' *Chemical Engineering Science*, vol. 177, pp. 151–162, 2018.

[222] C. K. Jayarathna, M. Balfe, B. M. Moldestad and L.-A. Tokheim, 'Improved multi-stage cross-flow fluidized bed classifier,' *Powder Technology*, vol. 342, pp. 621–629, 2019.

[223] G. Nguyentranlam and K. Galvin, 'Particle classification in the reflux classifier,' *Minerals Engineering*, vol. 14, no. 9, pp. 1081–1091, 2001, ISSN: 0892-6875.

[224] G. J. Sanders, *The principles of coal preparation*. Australian Coal Preparation Society Newcastle, 2007, vol. 130.

[225] A. Callen, B. Moghtaderi and K. Galvin, 'Use of parallel inclined plates to control elutriation from a gas fluidized bed,' *Chemical Engineering Science*, vol. 62, no. 1-2, pp. 356–370, 2007.

[226] N. Shilton and K. Niranjan, 'Fluidization and its applications to food processing,' *Food structure*, vol. 12, no. 2, p. 8, 1993.

[227] V. Singh and S. M. Rao, 'Selective classification of mineral sand slimes in an air fluidized bed,' *Mineral Processing & Extractive Metallurgy Review*, vol. 31, no. 2, pp. 59–72, 2010.

[228] G. Brown, D. Farkas and E. De Marchena, 'Centrifugal fluidized bed, blanches, dries, and puffs piece-form foods,' *Food technology*, 1972.

[229] A. L. Peraza, J. G. Penã, J. S. Segurajauregui and M. Vizcarra, 'Dehydration and separation of grape pomace in a fluidized bed system,' *Journal of Food Science*, vol. 51, no. 1, pp. 206–210, 1986.

[230] R. Cocco, S. R. Karri, T. Knowlton *et al.*, 'Introduction to fluidization,' *Chem. Eng. Prog*, vol. 110, no. 11, pp. 21–29, 2014.

[231] V. Galperin and M. Shapiro, 'Separation of solid particles in a fluidized bed air classifier,' *Powder Handling and Processing*, vol. 11, no. 2, pp. 185–188, 1999.

[232] L. Plitt, 'A mathematical model of the hydrocyclone classifier.,' 1976.

[233] K. Nageswararao, D. Wiseman and T. Napier-Munn, 'Two empirical hydrocyclone models revisited,' *Minerals Engineering*, vol. 17, no. 5, pp. 671–687, 2004.

Appendices

Appendix A

Literature Review

A.1 Gravitational and Inertial Air Classifiers

A.1.1 Gravitational Classifiers

In a gravitational classifier, the particle equilibrium position depends on the force balance between the gravitational force (F_m) due to the mass of the particle and the drag force (F_D). The settling velocity of a particle at equilibrium corresponds to the velocity of the ascending air. All the finer particles with lower settling velocities rise upwards and exit through an outlet vent. Coarser particles with higher settling velocities settle down into the classifier. The gravitational force acting on a spherical particle is given by the following equation.

$$F_m = m_p g \tag{A.1}$$

Where 'g' is the acceleration due to gravity and m_p is the mass of the particle which can be calculated as the product of the density and volume of the particle. The above equation can be written as follows:

$$F_m = \rho_p \frac{\pi}{6} D_p^3 g \tag{A.2}$$

The general form of drag force is given by the expression:

$$F_D = C_D \frac{\pi D_p^2}{4} \frac{\rho_g V_s^2}{2} \tag{A.3}$$

Where C_D is the drag co-efficient which is strongly correlated with the Reynolds number (Re) flow regime, ρ_g is the density of the gas and V_s is the settling velocity. The equation of motion of the particle inside the gravitational classifier is given by equation A.4.

The content within this appendix have been published in **Rasera2020** (see Appendix D)

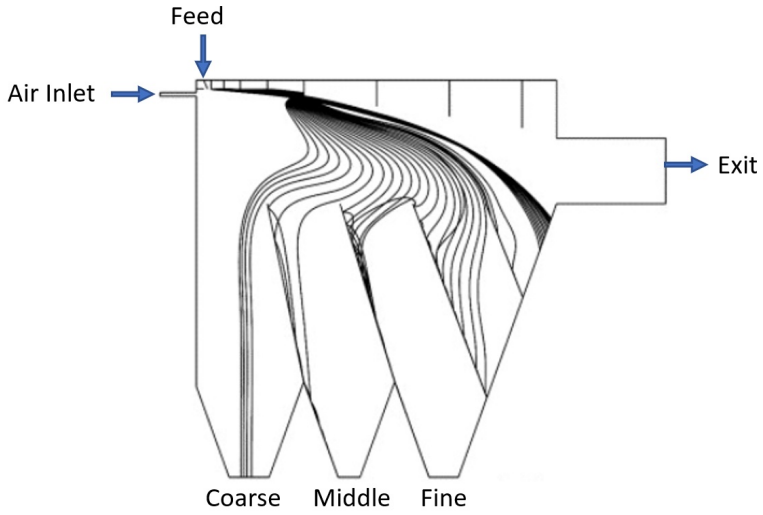


Figure A.1: Horizontal Cross-flow classifier: Particle tracks as a function of particle size (Image Source: Wang *et al.* [15])

$$m_p \frac{dV_p}{dt} = F_m - F_D \tag{A.4}$$

By substituting the expressions for mass and drag force in the above equation to get the final form as:

$$m_p \frac{dV_p}{dt} = \frac{\pi}{6} d_p^3 \rho_p g - C_D \frac{\pi D_p^2}{4} \frac{\rho_g V_s^2}{2} \tag{A.5}$$

The settling velocity (V_s) at equilibrium for any diameter of the particle is obtained by solving equation A.5

$$V_s = 1.15 \sqrt{\frac{\rho_p D_p}{\rho_g C_D}} \tag{A.6}$$

Cross-flow air classifiers, also known as *winnowing machines*, achieve a separation of particles from the difference in trajectories of coarse and fine particles. It has the advantage of rapidly producing multiple product-size fractions from a mixed feed. Wang *et al.* [15] performed extensive experiments and CFD analysis to optimize the geometry and process conditions. The sharpness and cut-size are influenced by the particle loading and turbulence inside the classification chamber [15, 190]. It was observed that inlet velocity has more influence on fine particles than coarser particles. At higher velocities fewer fine particles report to coarser streams, however, coarser particles are carried into fines stream [190]. By reducing the turbulence the fine particles are effectively carried by the drag, hence sharper classification [15]. In this study, a large vortex was observed downstream of the feed nozzle which caused the fine particles to report to coarser products. This can be minimized by maintaining a negative pressure in a small region below the nozzle. Further, the performance can be improved by modifying the hopper structure, ensuring uniform inlet particle velocities [15]. Li *et al.* [191] have performed both experiments and CFD simulations to optimize the design of the gravitational classifier by placing dispersion

structures inside the classification chamber. It was found that the separation efficiency decreases with an increase in the feed rate which agrees with the previous observation made by Wang *et al.* [15] and Lai *et al.* [190]. Li *et al.* [191] observed that particle packing is predominant as particle loading increases. Particle packing causes an increase in pseudo-gravitational forces experienced by the fine particles. The particles then resist the drag force and report to the coarse stream, resulting in increase of bypass and decrease in sharpness of separation.

Manufactured sand, the by-product of rock crushing, has been proposed as an alternative to fine aggregate in concrete because of a shortage of natural sand. Manufactured sand has particles of sizes ranging from 6 mm to as fine as $\leqslant 75\ \mu m$. The fine dust must be removed for it to be used as a natural sand replacement. Traditionally, manufactured sand is water washed, which requires subsequent de-watering and disposal, causes contamination, and has a significant cost. Petit *et al.* [192] simulated cross-flow air classification for dust removal from manufactured sands using CFD-DEM. A cross-flow air classifier with a 5 m/s inlet velocity produced the required product stream quality. Higher inlet velocities increased re-circulation zones detrimental to classification but re-engineering such a classifier to operate at low flowrates may improve its performance.

Gravitational classifiers are in general used to classify the powders larger than 200 μm [190]. However, Lai *et al.* [190] performed controlled experiments in a closed loop wind tunnel to improve their performance for fine particles. This is achieved by damping the particle-wall interaction with lower turbulence inside the chamber. Experiments were performed with Lead-Tin (Pb-Sn) alloy powder ($< 200\ \mu m$). They achieved finer cut-sizes of 15 μm with particle flow rates up to 140 kg/h. It was reported that by having several passes through the classifiers, the fine particle bypass can be reduced significantly. Though this study has shown the promise of using gravitational classification for fine particles, the challenge of throughput rates remains unaddressed. As particle flowrate increases, the particle-particle interactions increase which results in lower sharpness and separation efficiency [190]. In recent studies, CFD simulations were performed to understand the flow structure and particle trajectories inside the gravitational air classifiers; which were helpful in optimizing the design for improved classification [193, 194]. Banjac *et al.* [193] optimized the flow conditions of Zig-Zag air classifiers to maximize the protein enrichment in sunflower meals. Zhou and Shen [194] studied the effect of feed particles inlet velocity on the inclined gravitational classifier in achieving multi-product classification.

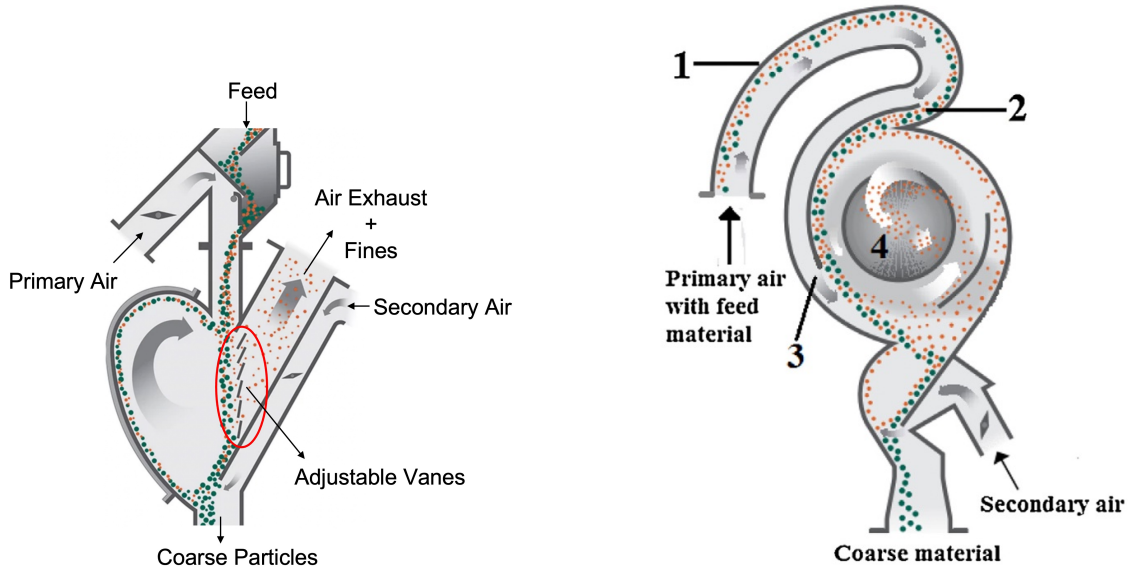
As seen in Figure 2.2 the cut size (d_{50}) range obtained by gravitational classifiers is within the limits of aperture based method i.e., traditional sieving. Sieving is a low-cost operation compared to gravitational classification. Hence, gravitational classifiers are sparsely employed in industries for particle size-based operations and are usually employed for density-based classification operations.

Gravitational classifiers have several advantages and disadvantages [195]. They are simple devices with low capital and operating costs. Although they have a large footprint, they can be designed and adapted to suit the particular operational and material requirements and can be used in multi-stage operations. However, they present significant challenges, particularly for classifying finely dispersed particles. High air velocities are required to treat particles with high terminal velocities, which increase turbulence and decrease performance [196]. Segregation in the feed hopper affects separation efficiency [197, 198]. Despite these drawbacks, gravitational classifiers find wide applications and are used for the recycling of solid waste materials including compostable materials, building materials, and electronic scrap. They are also used for the separation of vegetables, grains, husks, shells, stones, spices, herbs, fibers, and finished textiles. Zig-zag classifiers are used in car recycling to produce "shredder light fraction," which is a mixture of chopped light polymeric materials [198].

A.1.2 Inertial Air Classifiers

In gravitational classifiers, particles of certain sizes are removed through intermediate cuts. These particles are removed along with the conveying gas through the exhaust duct. The force acting on the particles is proportional to the amount of conveying gas available. Hence, the total force acting on particles in the gravitational classifier gradually diminishes with intermediate product removals. This causes a braking effect on the particles and hampers the separation performance [199]. To circumvent this challenge *inertial classifiers* was developed with the objective of maintaining the constant net resultant forces acting on the particles. This is achieved by gradually varying inertial forces in proportion to the reduced force because of the intermediate exhaust streams [199]. In gravitational classifiers, the fine particles are carried by the drag force which is a linear function of particle diameter. However, in inertial classifiers, the fine particles are acted on by the gravitational or inertial forces which are a function of the mass of the particle and hence proportional to the cube of the particle diameter [200]. Classification effects produced by inertial forces are greater than the effect produced by gravitational force which results in sharper separation with smaller cut-sizes.

When a particle-laden flow encounters a sharp change in direction in an inertial-air classifier, the fine particles are carried by the gas, while coarse particles continue on their original path due to their inertia. Inertial classifiers are divided into gravitational-inertial and centrifugal-inertial classifiers. In centrifugal-inertial classifiers, the inertial forces acting on the particles are further intensified because of the curved design of the classification chamber. A simple schematic depicting the operation of Gravitational-Inertial and Centrifugal-Inertial classifiers are shown in Figure A.2. Gravitational-inertial classifiers contain adjustable vanes and the annular gap between them varies according to their angle



(a) Gravitational Inertial Classifier **(b)** Centrifugal Inertial Classifier

Figure A.2: Inertial Air-Classifiers. Image Source: Johansson and Evertsson [16, 17]

of orientation. As shown in Figure A.2, the air containing the particles enters through the inlet, after reaching the separation chamber the air takes a sharp turn and passes through the vanes carrying the fines along it. The unseparated fines which are blocked in between the coarser particles are further classified as they intersect with secondary airflow in their descent.

In many countries depleting resources of natural sand creates a huge demand for manufactured sand in concrete and asphalt industries [201]. The objective of air classification in the manufactured sand process is to produce three product fractions from a crushed rock feed (Size $<$2 mm): a coarse product (0.5–2 mm), an intermediate fraction (63 μm–0.5 mm) and fines ($<$63 μm), where the size fraction $<$63 μm is undesirable in the concrete industry [202]. Inertial air classifiers i.e., Gravitational-Inertial classifiers are used to separate the particles around 150 μm as the first stage, with a capacity of up to 200 tph. In the second stage, the Centrifugal-Inertial air classifier is used to separate particles smaller than 100 μm [203]. Johansson and Evertsson [16] developed a CFD model to understand the influence of the geometry of a gravitational-inertial classifier on the flow field and classification efficiency. It was observed that turbulence and particle crowding can influence the flow path resulting in bypass. Secondary air inlet angle and re-circulation chamber design configurations may improve classification efficiency. Further, Johansson and Evertsson [17] extended their CFD analysis to centrifugal-inertial classifier design and found that secondary air moves particles from the intermediate stream to the separation chamber. Though the strength of re-circulation flow is low, it is sufficient to carry the fine particles along the flow stream [15, 17, 159]. Similar to cyclone separators, in centrifugal-inertial classifier Sun *et al.* [9] found that extending the fine particle exit

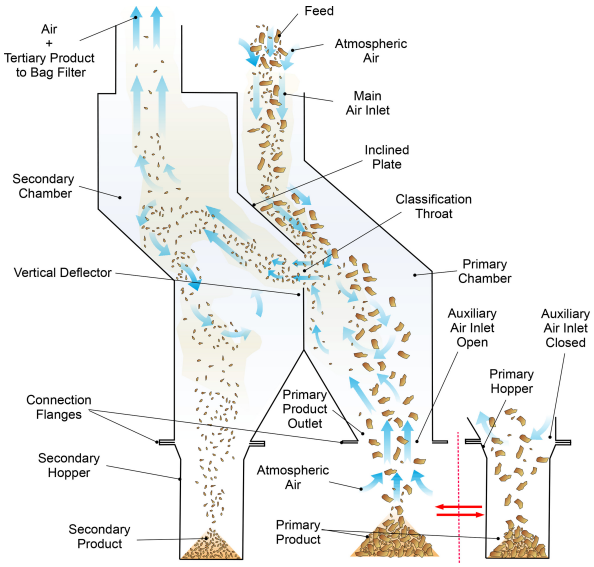


Figure A.3: A schematic of Throat Classifier (Image Source: Petit and Irassar [18])

pipe (i.e., vortex finder) into the classification chamber reduces secondary re-circulation zones and increases classification efficiency [9, 204]

Petit and Irassar [18] developed a novel Throat classifier that is employed to prepare manufactured sands. As shown in Figure A.3 the classifiers consist of two parallel chambers separated by an inclined plane and vertical deflector plate. The airflow at the throat of the classifier i.e., the narrow gap between the inclined plane and deflector plate brings the classification effect which is a combination of gravity and drag forces. The feed is discharged from the top section of the primary chamber, where it impacts the inclined plane. The coarser particles bounce off the plate and fall into primary product discharge. The fines and intermediates are carried by the airflow at the throat region into the secondary chamber, producing the classification effect. Some of the particles in the secondary chamber settle to the bottom and are removed as a secondary product, whereas the fines follow the air exit at the top. It is reported that the primary product cut-sizes vary between 50-400 μm, whereas the secondary product cut-size is in the range of 30-100 μm. This novel throat classifier operates at lower velocities and pressure losses when compared with Gravitational-inertial and Centrifugal-inertial classifiers developed by Johansson and Evertsson [16].

The elbow jet classifier is a static sub-micron cross-flow inertial air classifier, producing multiple cut sizes of particles based on the Coanda effect. The typical design of the elbow-jet classifier is illustrated in Figure A.4. A Coanda jet is created by ejecting a high-pressure gas containing the particles over a curved surface (Known as a Coanda block). Because of the pressure differences, the gas-solid jet stream deflects and adheres to the curved surface. The trajectories of the particles inside the classifier depend upon the drag force and inertia acting on them. Owing to their low inertia, the finer particles get carried away by the deflected low-pressure gas stream along the curved surface. The coarse particles

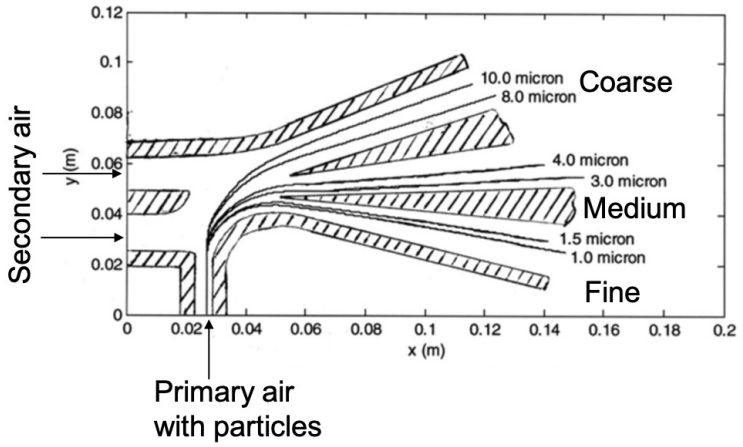


Figure A.4: Elbow jet classifier: Particle tracks as a function of particle size (Image Source: Liang *et al.* [19])

will separate from the mainstream because of their higher inertia. The magnitude of deviation from the mainstream depends upon the particle diameter allowing for multiple classifications [19, 205]. Liang [206] performed experiments using Talc powder (Density - 2860 kg/m^3) with a feed rate of 3.5 kg/h having solids loading of 10 mass percent (in the air) in an elbow classifier under the pressure of 0.4 MPa (abs). They also construct a 2D-CFD model to capture the cross-flow field inside the chamber using a standard k-ϵ turbulence model. The trajectories of particles of various diameters were tracked through Lagrangian Particle Tracking (LPT). The CFD model predicted cut sizes (d_{50}) of the coarse, medium, and fine fractions were in agreement with the experimental values of 1.9, 7.0 and 13.5 μm respectively.

Inertial air classifiers were first developed to prepare manufactured sands. However, gravitational-inertial and centrifugal classifiers require high air velocities and, hence ceramic protection against erosion from particle-wall impacts [203] and produce significant pressure losses. In contrast, throat classifiers have fewer particle-wall impacts and hence lower operating and maintenance costs. Primary throat classifier chamber cut sizes are comparable to gravitational-inertial air classifiers, while secondary chamber cut sizes are similar to centrifugal classifiers [18]. Inertial air classifiers tend to have a larger industrial footprint due to their open aerodynamic cycle, and an external filter system is required to prevent fines from entering fans or creating dust, further increasing the overall installed size. Elbow-jet classifiers can produce multiple product fractions, and the robust design and scalability make it a popular choice for commercial applications [207], however, high-pressure gas flow increases both CAPEX and OPEX. Elbow classifiers have been used at extreme temperatures, such as for fine polymeric particles under cryogenic conditions [19], and hydroxyapatite at calcination temperatures of around $1200°C$ [208]. To summarize, it is observed from Figure A.7a that gravitational classifiers operate with coarser cut-sizes i.e., $100 \geqslant d_{50}$ with higher throughput values ranging from

50-10,000 kg/h. Zig-Zag Classifiers (ZZC) offer the highest adaptability to scale for classifying particles having coarser cut-sizes i.e., $100 \leqslant d_{50} \leqslant 1000\ \mu m$. Counter-flow vertical raise air classifier (CFVAC) separates particles within a narrow range of cut-sizes ie., $100 \leqslant d_{50} \leqslant 200\ \mu m$. Cross-flow horizontal air stream classifier (CFH1 $\&$ CFH2) can vary the cut sizes from 200 μm to 900 μm by increasing the incoming air flow rate.

Figure A.7b captures the operational characteristics of dry classifiers based on inertial forces. As observed from Figure A.7b the Elbow-Jet classifier shows remarkable performance in terms of adaptability for higher throughput rates while yielding the cut-sizes $\leqslant 10$. Because of the compounding effect of inertial forces, the average cut-point diameter in a Gravitational-Inertial classifier (GIC) is brought down while processing at similar throughput rates, whereas Centrifugal-Inertial Classifiers (CIC) are able to effectively classify with cut-sizes ranging from 20 to 100 μm, respectively. The novel throat classifier has a similar range of cut-sizes as compared to Gravitational, Centrifugal-Inertial classifiers. As observed from Figure A.7b throat classifiers have lower throughput rates in their pilot plant studies when compared with GIC and CIC equipment. But it is to be noted that throat classifiers operate under lower air velocities and pressure losses when compared with the GIC and CIC [18].

A.2 Fluidizers

Fluidization is widely used in chemical (fluidized catalytic cracking) and mineral processing industries (drying, calcining, and sulphide roasting), etc. Fluidization generates intense mixing between solid particles which is exploited to enhance heat transfer to achieve uniform temperatures across the bed. Depending upon the process and operating conditions fluidized beds exhibit distinctly different behaviors of segregation and mixing. Segregation is an unwanted phenomenon as it results in poor mixing of particles which promotes undesired properties like uneven temperature distribution in the bed, catalyst agglomeration, etc. However, segregation has applications in particle classification, cleaning of agglomerated ash from gas fluidizers [209].

The fluidized bed air classifier is a gravitational counter-current flow classifier. The material on the supporting grid is scavenged by the raising current of air thus creating a fluidized bed. Hence a fluidized bed classifier is able to segregate particles based on dissimilar drag forces. The particle position inside the separation chamber is determined by the force balance between drag and gravity acting on the particles. The drag force dominates for fines thus they get carried away by the exiting airflow. Whereas, the gravitational force dominates drag for coarser particles which makes them fall down and move from the discharge outlet. The presence of collision surfaces inside the fluidiziers further enhances the sharpness of classification [210]. Baffles in the fluidized beds enhance the particle

segregation by suppressing the circulation, and particle axial mixing, and breaking the bubbles in the fluidized bed [209, 211–213].

Rowe and Nienow and their co-workers made early contributions to fluidized-bed segregation studies [214, 215]. They were the first to use the terms *Jetsam* and *Flotsam* which are widely used in binary fluidized beds [209]. The solids fraction which floats towards the top of the bed is called *Flotsam* and the fraction which sinks to the bottom of the fluidized bed is termed *Jetsam*. Gibilaro and Rowe [215] defined a correlation for the extent of segregation of particles in binary mixtures using Mixing Index (M), which is dependent upon factors such as density, size, and superficial gas velocity (u_0) as given by equation A.7. The mixing Index is determined by the jetsam fraction in the top bed $x_{j,t}$ to the jetsam fraction when completely mixed $x_{j,0}$. It is observed from the correlation that the density difference between the particles has more influence on segregation than the size difference.

$$M = \frac{x_{j,t}}{x_{j,0}} = f(u_0) \left(\frac{\rho_j}{\rho_f}\right)^{2.5} \left(\frac{d_j}{d_f}\right)^{0.2} \tag{A.7}$$

Hoffmann and Romp[216] studied the effect of fluidization velocities on wide and continuous size distributions of sand particles.[216] The mode of incoming inlet air flowrate has a strong influence on segregation efficiency. It was observed that by changing the inlet air from continuous to pulsating (Pulsating frequency 1-10 Hz) there is significant improvement in segregation efficiency. Studies reveal that the pulsation helps in mitigating the channel/slug flows in the bed thereby reducing the gas bypassing and also helps in improving the gas-particle contact inside the fluidized bed.[217–219] Figure A.5 depicts the before and after segregation of particles in a cylindrical fluidized bed for a pulsed air inlet with a frequency of 1 Hz. It was observed that segregation efficiency had increased because the pulsating flowrates reduces static channelling structures in the bed.[219]

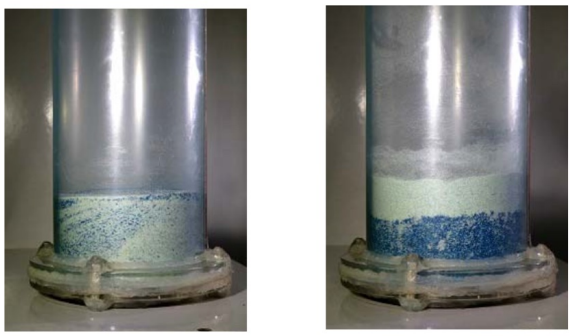


Figure A.5: Saidi *et al.* depicted the segregation of particles based on the size (Blue - 920 μm, white - 330 μm) from the mixed feed Saidi *et al.* [219]

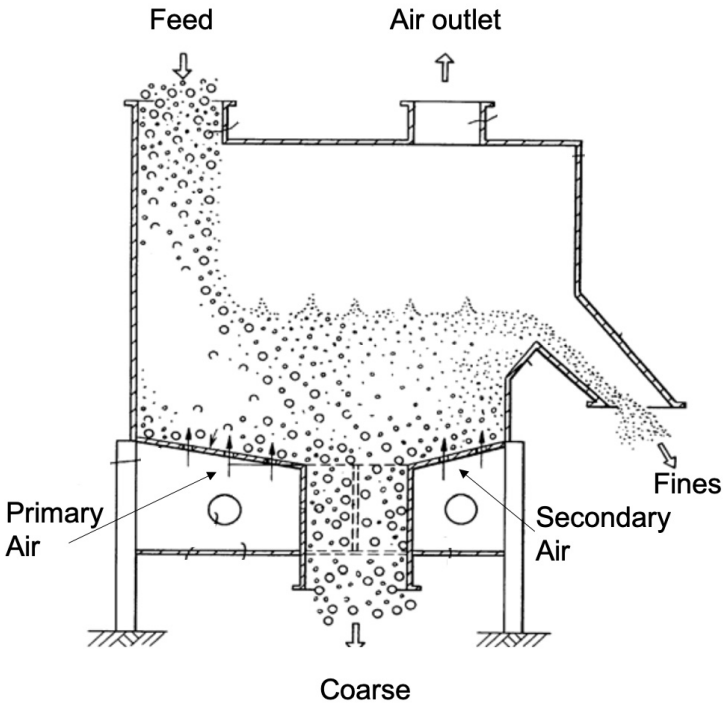
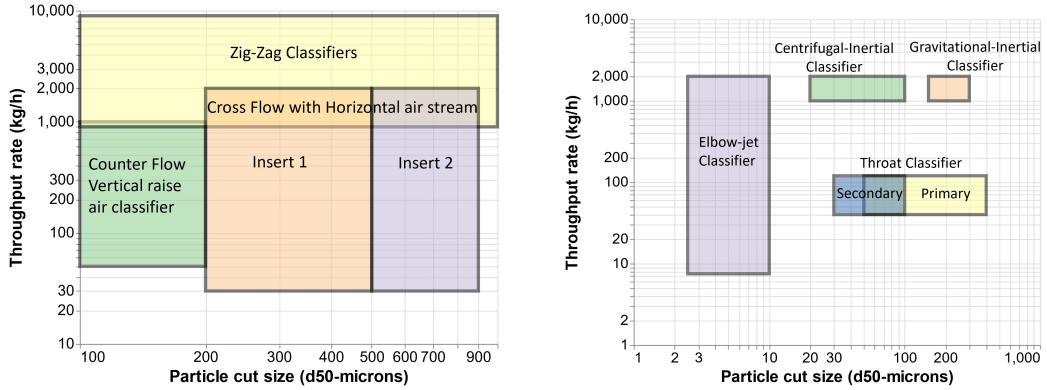


Figure A.6: Continuous Fluidized bed particle classifier Yoshihiro *et al.* [20]

Yoshihiro *et al.* [20] designed a continuous fluidized bed classifier as shown in Figure A.6. The total air required to classify the material through fluidization is divided and blown through the first gas chamber (Primary air) and second gas chamber (Secondary air). The primary air flow rate is greater than the secondary air flow rate, so the coarse particles are fluidized in the first gas chamber. The lower gas velocities in the secondary chamber prevent the coarse particles from being fluidized and mixed with the fine particles. The fine particles are removed through the side outlet whereas the coarse particles exit through the bottom outlet [20]. Recently Jayarathna *et al.* explored the applicability of fluidized bed classification for high-temperature, fully integrated calcium looping (FICaL) in a CO_2 capture plant by conducting cold-flow experiments on Zirconia (Sorbent) – 69 μm and Steel (Heat Transfer-HT solids) -290 μm [220–222]. A novel multi-stage cross-flow fluidized bed attained recoveries of 90% and 99% for lighter (Sorbent) and heavier (HT-Particles) components [220]. By improving the design of the classifier shape with the help of CFD simulations, the recoveries were further improved to 97% and 98% for lighter and heavier particles, respectively [222].

Nguyentranlam and Galvin [223] developed a reflux classifier; by stacking inclined channels above conventional fluidized bed. The particle segregation happens near the upward-facing inclined channels. The heavier particles slide along the inclined surface and then fall into the fluidization zone, which provides a chance for particles to re-participate in the classification process [223]. Water-based fluidized reflux classifier has been successfully deployed in industries for various applications [224]. Further, Callen *et al.* [225]



(a) Gravitational-Air classifiers **(b)** Inertial-Air Classifiers

Figure A.7: Charts depicting the operational characteristics for Gravitational and Inertial air classifiers

explored the possibility of using a reflux classifier for gas-solid particle classification based on size. It was reported that the cut-size is increased with an increase in superficial gas velocity and decreases with an increase in the number of inclined parallel channels [225].

Rapid mixing in fluidized beds offers effective heat and mass transfer, allowing rapid heating and cooling [226]. Further, the absence of moving parts results in low maintenance costs. Fluidisation can be used for pre-concentration of mineral sands [227], classification [228], or combined with drying [229]. Operating drawbacks include slug formation, and attrition and erosion cause particle fragmentation or abrasion [230], often limiting fluidization to hard materials. Contamination of products with traces of bed particles may require downstream treatment, increasing costs [226].

Galperin and Shapiro [231] demonstrated that in air-fluidizers the cut size can be varied in a wide range (52 μm – 420 μm) by varying the air flow rate (1 - 6.7 m^3/min). The efficiency in terms of effective classification is increased by 15-20$\%$ compared with conventional gravitational separators. Further, the efficiency is not compromised with the increase in loading which indicates the robustness of fluidization as a particle classification technique [231].

Appendix B

Supplemental Data for Chapter 4: “Impact of Conic Curvature and Wall Roughness on Gas Cyclones: A Computational and Experimental Study”

B.1

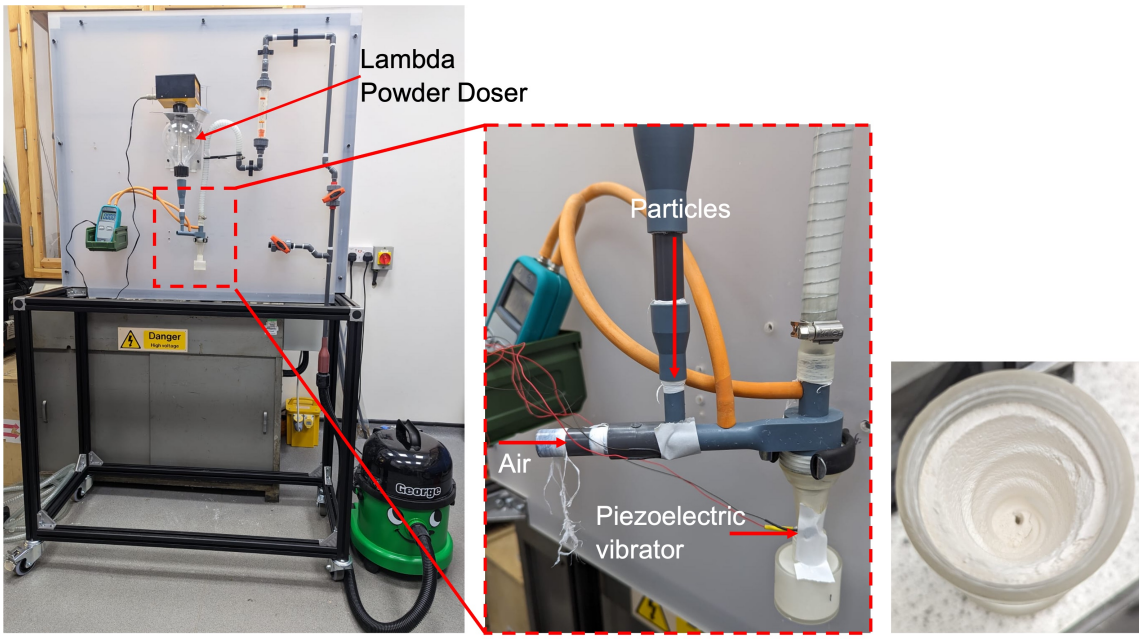


Figure B.1: Free fall of particles into the flowing stream of air results in accumulation of particles on the cyclone walls.

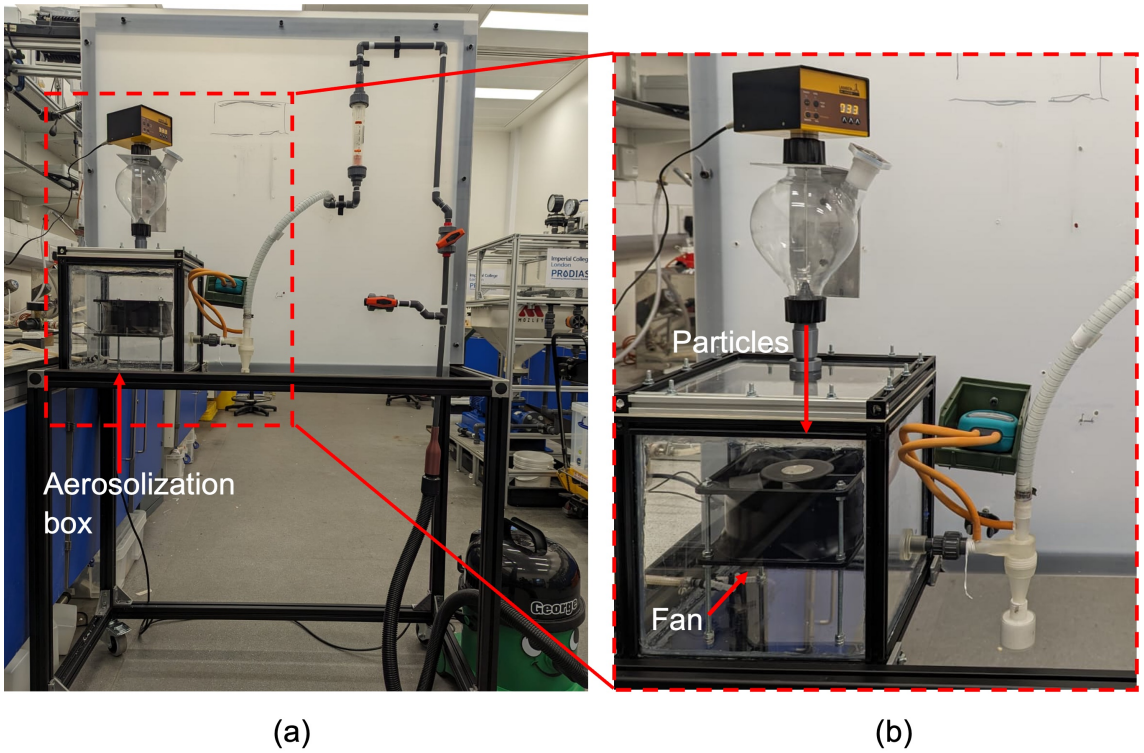


Figure B.2: A particle dispersion chamber is incorporated before the cyclone inlet to generate an aerosol for dispersing solids in air. However, particles tend to adhere to the chamber walls and accumulate in the dead zones.

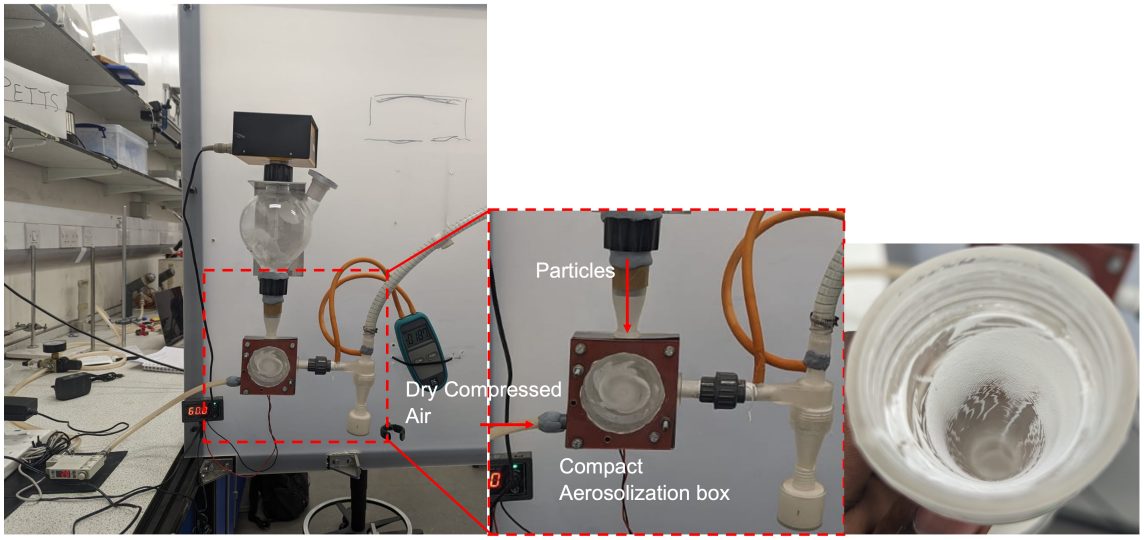


Figure B.3: A compact aerosolization chamber eliminates the problem of particle agglomeration along the walls. However, the pressure inside the system could not be maintained due to hair-line leaks.



Figure B.4: Figure depicting the novel method to capture the particles exiting through the dust outlet using expandable chamber.

Appendix C

Supplemental Data for Chapter 5: "Influence of Conic Shape on Bypass and Cut-Size in Hydrocyclones"

C.1 Empirical Models from Industrial Data:

In this section the discuss the developmental emprical model to predict the separation metric of 650 mm hydrocyclone. All the experiments were performed by Anglo American on standard and novel convex-bottom hydrocyclone designs. Using the experimental data, predictive models were developed to evaluate both standard and novel hydrocyclones using input design variables; dimensions, and operating conditions of a hydrocyclone to predict the parameters such as bypass, cut size, sharpness of classification, flowrate, and recovery ratios. While empirical models in literature (Plitt [232] and Nageswararao *et al.* [233]) were initially tested, the results were unsatisfactory for some quantities, leading to develop a own non-linear regression models for sharpness and feed flowrates. The final models were then subjected to Monte Carlo simulations within the design space to explore possible outcomes.

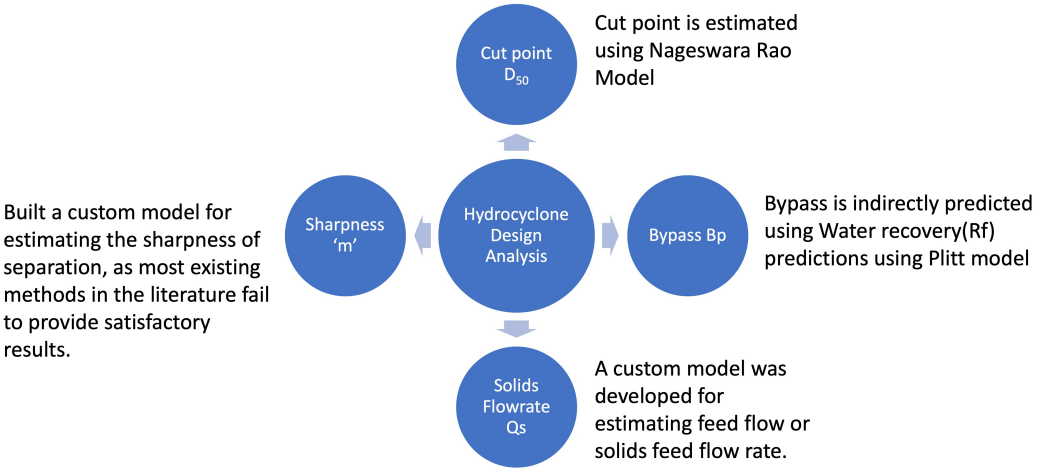


Figure C.1: Parameters used to predict hydrocyclone performance and the models/methodology used for their prediction.

C.1.1 Plitt Model: For prediction of Bypass through underflow recovery.

$$
\begin{aligned}
d_{50c} &= \frac{50.5 D_c^{0.46} D_i^{0.6} D_o^{1.21} \exp[6.3\phi]}{D_u^{0.71} h^{0.38} Q^{0.45} \left(\rho_s - \rho_l\right)^{0.5}} \\
S &= \frac{3.28 \left(D_u/D_o\right)^{331} h^{0.54} \left(D_u^2 + D_o^2\right)^{0.36} \rho_p^{0.24} \exp[0.54\phi]}{P^{0.24} D_c^{1.11}} \\
R_v &= \frac{S}{1+S} \\
m &= 1.94 \exp\left[-1.58 R_v\right] \left[\frac{D_c^2 h}{Q}\right]^{0.15} \\
P &= \frac{1.88 Q^{1.78} \exp[0.55\phi]}{D_c^{0.37} D_f^{0.94} h^{0.28} \left(D_{\mathrm{u}}^2 + D_o^2\right)^{0.87}}
\end{aligned}
\tag{C.1}
$$

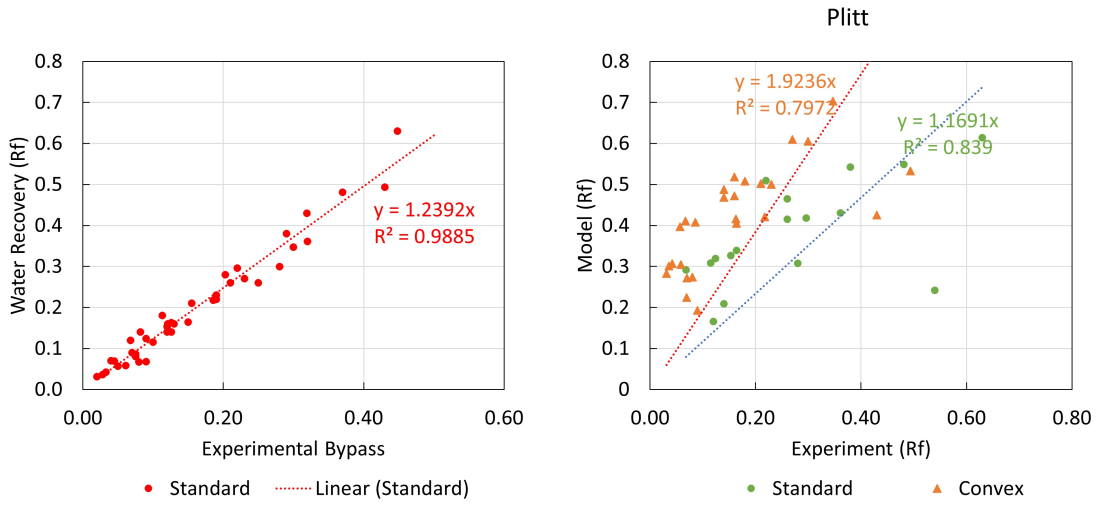
Plitt mentions that due to the interdependency of the recovery of solids and the flow split, the calculation of R has to be done iteratively. However, it has been shown that this is not required and that this calculation can be done directly. By calculating the total volumetric recovery from equation 3.33, and the solids recovery due to classification from,

$$R_c = \sum_i^n c_i f_i$$

the water recovery, $\mathrm{R_f}$, can be calculated from

$$R_f = \frac{R_v - \phi R_c}{1 - \phi R_c}$$

Note that in the above Equations, the units are: $D_{\mathrm{c}}, D_{\mathrm{i}}, D_{\mathrm{o}}, D_{\mathrm{u}}, h(\ \mathrm{cm}); Q(\mathrm{l/\ m}); P(\mathrm{kPa}); \eta_{\mathrm{p}}(\mathrm{cP})$; $C_{\mathrm{V}}(\%); d_{50\mathrm{c}}(\mu\mathrm{m}); \rho_{\mathrm{s}}, \rho_1\ (\ \mathrm{g/cm^3})$.



(a) Bypass versus water recovery (Rf) **(b)** Prediction of water recovery by Plitt model

Figure C.2: Bypass model: Bypass is predicted indirectly using water recovery (Rf) using Plitt model

C.1.2 Nageswara Rao Model: For Cut size determination

$$
\begin{aligned}
\frac{Q}{D_{\mathrm{c}}^2\sqrt{P/\rho_{\mathrm{p}}}} &= K_{Q_{\mathrm{o}}}\left\{D_{\mathrm{c}}^{-0.10}\right\}\left(\frac{D_{\mathrm{o}}}{D_{\mathrm{c}}}\right)^{0.68}\left(\frac{D_{\mathrm{i}}}{D_{\mathrm{c}}}\right)^{0.45}\left(\frac{L_{\mathrm{c}}}{D_{\mathrm{c}}}\right)^{0.20}\theta^{-0.10}\\
\frac{d_{50\mathrm{c}}}{D_{\mathrm{c}}} &= K_{D_{\mathrm{o}}}\left\{D_{\mathrm{c}}^{-0.65}\right\}\left(\frac{D_{\mathrm{o}}}{D_{\mathrm{c}}}\right)^{0.52}\left(\frac{D_{\mathrm{u}}}{D_{\mathrm{c}}}\right)^{-0.50}\left(\frac{D_{\mathrm{i}}}{D_{\mathrm{c}}}\right)^{0.20}\\
&\times\left(\frac{L_{\mathrm{c}}}{D_{\mathrm{c}}}\right)^{0.20}\theta^{0.15}\left(\frac{P}{\rho_{\mathrm{p}}gD_{\mathrm{c}}}\right)^{-0.22}\lambda^{0.93}\\
R_{\mathrm{f}} &= K_{W_{\mathrm{o}}}\left\{D_{\mathrm{c}}^{0.00}\right\}\left(\frac{D_{\mathrm{o}}}{D_{\mathrm{c}}}\right)^{-1.19}\left(\frac{D_{\mathrm{u}}}{D_{\mathrm{c}}}\right)^{2.40}\left(\frac{D_{\mathrm{i}}}{D_{\mathrm{c}}}\right)^{0.50}\\
&\times\left(\frac{L_{\mathrm{c}}}{D_{\mathrm{c}}}\right)^{0.22}\theta^{-0.24}\left(\frac{P}{\rho_{\mathrm{p}}gD_{\mathrm{c}}}\right)^{-0.53}\lambda^{0.27}\\
R_{\mathrm{V}} &= K_{V^0}\left\{D_{\mathrm{c}}^{0.00}\right\}\left(\frac{D_{\mathrm{o}}}{D_{\mathrm{c}}}\right)^{-0.94}\left(\frac{D_{\mathrm{u}}}{D_{\mathrm{c}}}\right)^{1.83}\left(\frac{D_{\mathrm{i}}}{D_{\mathrm{c}}}\right)^{0.25}\\
&\times\left(\frac{L_{\mathrm{c}}}{D_{\mathrm{c}}}\right)^{0.22}\theta^{-0.24}\left(\frac{P}{\rho_{\mathrm{p}}gD_{\mathrm{c}}}\right)^{-0.31}
\end{aligned}
\tag{C.2}
$$

Note that in above Equation, the units are:
$D_{\mathrm{c}}, D_i, D_0, D_{\mathrm{u}}, L_{\mathrm{c}}(\mathrm{m}); \theta$ (degrees); $Q\ (\mathrm{m^3/h})$; $P(\mathrm{kPa}); g\ (\mathrm{m/s^2})$; $\eta(\mathrm{cP}); R_{\mathrm{V}}, R_f, C_{\mathrm{V}}$ (fraction); $d_{s0\mathrm{c}}\ (\mu\mathrm{m}); \rho_{\mathrm{p}}\ (\mathrm{t/m^3})$

C.1.3 Feed Flowrate model: Non-linear regression model

$$
Q_s = 37.03\left(\frac{D_c^2}{D_o D_u}\right)^{-0.193}(Eu * Fr)^{0.575}\left(\frac{\mu_s}{\mu_w}\right)^{0.611} \tag{C.3}
$$

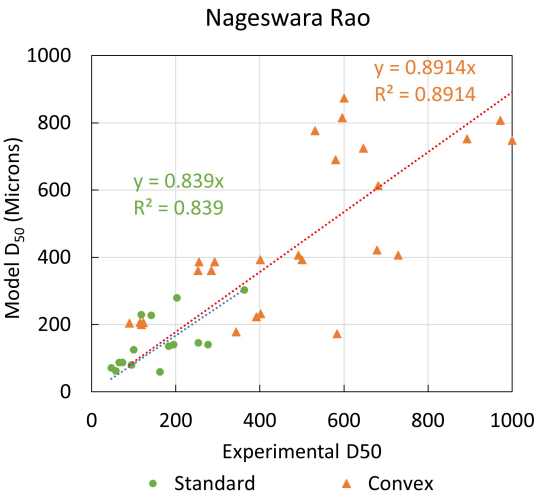


Figure C.3: Cut size as a function of hydrocyclone design is modelled using Nageswara Rao model

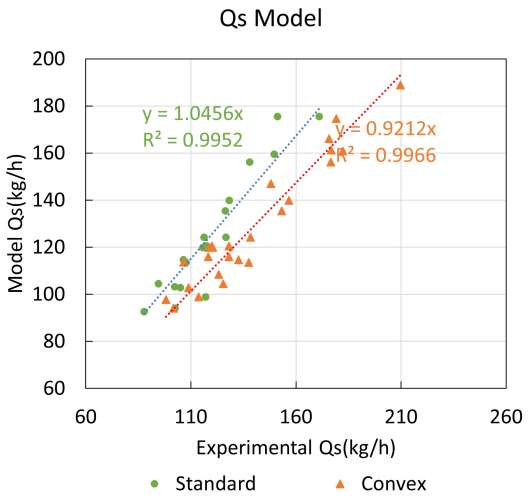


Figure C.4: Feed solids flowrate is modeled using our own Non-linear regression model as a function of hydrocyclone design is modelled using Nageswara Rao model

Table C.1: Statistics of non-linear regression model for feed solids flowrate

Regression Statistics			
Multiple R	0.96069		
R Square	0.922925		
Adjusted R Square	0.90751		
Standard Error	0.053321		
Observations	19		
	Coefficients	**Standard Error**	**P-value**
Intercept	3.611824	0.267627	8.55E-10
ln(Dc2/(DoDu)	-0.19332	0.071003	0.015725
ln(gamma)	0.575153	0.091711	1.5E-05
ln(viscosity)	0.611235	0.046386	1.19E-09

C.2 Experimental Conditions

C.3 Hydrocyclones Predictive models for Monte Carlo simulations

Table C.2: Design and operating conditions for the plant trails

Test No.	Apex/VF Ratio	VF diameter (Do-mm)	Apex diameter (Du-mm)	Pressure	Mass Loading (%)	Design
1	0.81	260	210	110	65	Standard
2	0.75	280	210	110	45	Standard
3	0.63	240	150	80	65	Standard
4	0.58	260	150	80	45	Standard
5	0.54	280	150	95	45	Standard
6	0.88	240	210	95	65	Standard
7	0.79	240	190	95	55	Standard
8	0.63	240	150	110	55	Convex
9	0.68	280	190	80	65	Convex
10	0.79	240	190	110	45	Convex
11	0.75	280	210	80	55	Convex
12	0.79	240	190	95	55	Convex
13	0.75	280	210	110	45	Convex
14	0.79	240	190	95	55	Convex
15	0.88	240	210	80	45	Convex
16	0.54	280	150	110	65	Convex
17	0.63	240	150	110	55	Convex
18	0.75	280	210	80	55	Convex
19	0.75	280	210	110	45	Convex
201	0.63	240	150	110	55	Standard
202	0.63	240	150	80	65	Standard
203	0.79	240	190	95	65	Standard
206	0.54	280	150	80	65	Standard
207	0.63	240	150	110	40	Convex
208	0.68	280	190	80	40	Convex
209	0.68	280	190	80	45	Convex
210	0.68	280	190	95	45	Convex
211	0.68	280	190	80	55	Convex
212	0.63	240	150	95	55	Convex
213	0.63	240	150	80	55	Convex
214	0.88	240	210	130	65	Convex
215	0.63	240	150	110	65	Convex
216	0.54	280	150	80	65	Convex
217	0.68	280	190	95	65	Convex
218	0.68	280	190	110	65	Convex
219	0.63	240	150	110	40	Standard
220	0.68	280	190	80	40	Standard
221	0.68	280	190	80	45	Standard
223	0.68	280	190	80	55	Standard
224	0.63	240	150	95	55	Standard
225	0.63	240	150	80	55	Standard
226	0.63	240	150	80	65	Convex
227	0.79	240	190	95	65	Convex

Table C.3: Monte Carlo model input variables and output predictions

Hydrocyclone Predictive Models	
Inputs:	**Predict:**
Hydrocyclone type	Cut size
Hydrocyclone dimensions	Sharpness
Operating Pressure	Fines Bypass
Feed solids concentration	Flowrate (solids & liquid)
Feed size distribution	

Appendix D

Publications

Publication 1

A. K. Pukkella, J. J. Cilliers and K. Hadler, 'A comprehensive review and recent advances in dry mineral classification,' *Minerals Engineering*, vol. 201, p. 108 208, 2023

Publication 2

A. K. Pukkella, J. Cilliers and K. Hadler, 'Design of parabolic conic gas cyclones for coarse particle classification: A cfd study with response surface methodology,' *Powder Technology*, vol. 433, p. 119 217, 2024

Publication 3

A. K. Pukkella, D. Vega-Garcia, K. Hadler and J. Cilliers, 'Influence of conic shape on bypass and cut-size in hydrocyclones,' *Separation and Purification Technology*, vol. 361, p. 131 224, 2025

Publication 4

A. K. Pukkella, D. Vega-Garcia, K. Hadler and J. Cilliers, 'The influence of surface-wall roughness on hydrocyclone performance,' *Separation and Purification Technology*, vol. 360, p. 131 109, 2025

Publication 5

A. K. Pukkella, J. Rasera, K. Hadler and J. Cilliers, 'Impact of conic curvature and wall roughness on gas cyclones: A computational and experimental study,' *Powder Technology*

- *Under Review*,

Minerals Engineering 201 (2023) 108208

Contents lists available at ScienceDirect

Minerals Engineering

journal homepage: www.elsevier.com/locate/mineng

A comprehensive review and recent advances in dry mineral classification

Arjun Kumar Pukkella [a,b,*], Jan J. Cilliers [a], Kathryn Hadler [a,c]

[a] Imperial College London, Department Earth Sciences and Engineering, Exhibition Road, London, SW7 2AZ, United Kingdom
[b] TCS Research, Tata Research Development and Design Centre, Pune, 411013, India
[c] European Space Resources Innovation Centre (ESRIC), Luxembourg Institute of Science and Technology (LIST), 5 Avenue des Hauts-Fourneaux, L-4362, Luxembourg

ARTICLE INFO

Keywords:
Dry classification
Centrifugal classifiers
Gravitational classifiers
Inertial classifiers

ABSTRACT

Dry particle classification is an important step in dry particle processing. A thorough literature review is conducted on the available dry particle classification technologies. A detailed discussion is presented on each class of equipment based on the active forces (including centrifugal, gravity, and inertial) that cause particle segregation. Special attention is given to centrifugal classifiers because of their adaptability to a wide range of cut sizes and high throughputs. Interestingly, literature studies on gas cyclones show that they are conventionally used as gas-solid separators with cut sizes d_{50} less than 3 μm rather than as a particle classifier. Further, throughput rate and cut size (d_{50}) data were collated for all the equipment reviewed. A new graphical illustration of throughput rate vs cut size is used to identify the major gaps in dry classification technology and to recommend research directions.

1. Introduction

Water is critical to the performance of most mineral processing circuits. Huge quantities of water are consumed daily in various unit operations like comminution (grinding), flotation, slurry transportation, and all hydrometallurgical operations (Napier-Munn and Morrison, 2003). It has been estimated that around 1 kiloliter of water is required to process a tonne of ore (Brown, 2002). There is a significantly increased demand for water for the basic needs of a growing population, agriculture, and other industries. These needs, combined with growing water scarcity due to climate change, and stricter regulatory standards for water abstraction and disposal places the future of water-based mineral processing under scrutiny.

Dry mineral processing offers reduced mining water demand. It is considered to be economically viable due to lower capital and operational costs with a smaller plant footprint (Napier-Munn and Morrison, 2003). Franks et al. (2015) have reported that Dry Sand Fluidized Bed (DSFB) only in combination with heap leaching may have economic benefits with reduced energy and water requirements in a copper ore processing flow sheet. Dry mineral processing methods are classified broadly into size reduction (comminution) and separation. Dry separation uses forces generated by gravity, centrifuges, magnetics, electricity, and so forth to separate a collection of particles into groups of different sizes and compositions. Classification is a specific operation that deals solely with particle separation into sized fractions. Size classification is affected by particle physical properties such as size, shape, and density. Particle size classification is broadly grouped into two classes; those that take advantage of carrier fluid to create differences in particle trajectory, which is strongly dependent upon the size and density of the particles because of fluid dynamic interaction forces. In dry separation, this fluid is generally air. The second class of classifier is based on the particle's ability (or probability) to pass through an aperture, such as a screen. This is not generally efficient for fine particles, and will not be reviewed in detail.

Size classification can be carried out wet or dry. In mineral processing, wet classification techniques are generally preferred over dry technologies (Wills and Napier-Munn, 2005). However, with an increasing focus on reducing water consumption in the minerals industry, dry technologies are receiving more attention. Dry separation technologies present a range of challenges, including low throughput rates, narrow cut size ranges, high operating costs, and the need for dust mitigation. Furthermore, efficient dry classification requires low powder moisture content to avoid blocking equipment. Although wet classification technologies address many of the above challenges it also presents difficulties. There are significant costs associated with accessing water and water handling, tailings dams and their management and the elimination of harmful chemicals before their disposal. Wet processing is often not possible in very arid climates and sub-zero conditions.

Dry size-based particle classification has important applications in a variety of industries, such as minerals and cement, agriculture, food processing, pharmaceuticals, and resource recycling. The world

* Corresponding author at: Imperial College London, Department Earth Sciences and Engineering, Exhibition Road, London, SW7 2AZ, United Kingdom.
E-mail address: a.pukkella20@imperial.ac.uk (A.K. Pukkella).

https://doi.org/10.1016/j.mineng.2023.108208
Received 29 January 2023; Received in revised form 15 June 2023; Accepted 19 June 2023
Available online 4 July 2023
0892-6875/© 2023 The Author(s). Published by Elsevier Ltd. This is an open access article under the CC BY-NC-ND license (http://creativecommons.org/licenses/by-nc-nd/4.0/).

Powder Technology 433 (2024) 119217

Contents lists available at ScienceDirect

Powder Technology

journal homepage: www.journals.elsevier.com/powder-technology

Design of parabolic conic gas cyclones for coarse particle classification: A CFD study with Response Surface Methodology

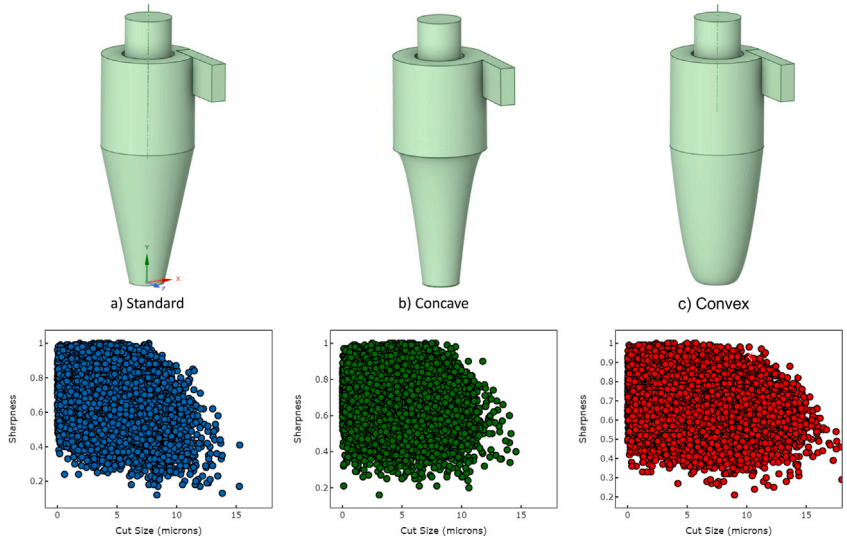
Arjun Kumar Pukkella [a,b,*], Jan Cilliers [a], Kathryn Hadler [a,c]

[a] Imperial College London, Department Earth Sciences and Engineering, Exhibition Road, London, SW7 2AZ, United Kingdom
[b] TCS Research, Tata Research Development and Design Centre, Pune, 411013, India
[c] European Space Resources Innovation Centre (ESRIC), Luxembourg Institute of Science and Technology (LIST), 5 avenue des Hauts-Fourneaux, L-4362, Luxembourg

HIGHLIGHTS

- Effect of conic curvature on particle classification is studied using CFD simulations.
- CFD model validates predictions for standard design with reported experimental results.
- Coarser cut-sizes are observed for curved conic designs (Parabolic convex and concave).
- Particle tracks, flow profiles, and TKE contours provide a plausible explanation.
- D-optimal design and Response surface methods analyze variable interaction effects.

GRAPHICAL ABSTRACT



ARTICLE INFO

Keywords:
Cyclone classifier
Parabolic conic
CFD
Particle tracking
Monte Carlo simulations

ABSTRACT

Gas cyclones have traditionally been used as particle separators to remove dust from gas streams, with the goal of achieving a dust-free gas flow at the exit pipe and recovering particles to the dust outlet. Typically, the particle size for removal to the dust outlet is less than 1 μm. However, gas cyclones can also be targeted for particle classification rather than particle removal. In this study, the effect of the shape of the curved conical wall, specifically the parabolic concave and convex conic designs, on particle classification in a 31 mm diameter gas cyclone was evaluated using Computational Fluid Dynamics (CFD). The CFD model predictions for standard small-scale gas cyclones were validated using experimental data available in the literature for various inlet flow rates. The curvature of the conical wall varied from convex to concave, resulting in the observation of sharper and coarser cut sizes for the parabolic conic designs. The cut size increases to 4.91 μm for the concave design at a flow rate of 30 liters per minute, compared to 3.38 μm and 2.65 μm for the convex and standard design cyclones, respectively. The axial, tangential, pressure, and turbulent kinetic energy profiles were used to provide an explanation for the observed results. The interaction effects between the parameters

* Corresponding author at: Imperial College London, Department Earth Sciences and Engineering, Exhibition Road, London, SW7 2AZ, United Kingdom.
E-mail address: a.pukkella20@imperial.ac.uk (A.K. Pukkella).

https://doi.org/10.1016/j.powtec.2023.119217
Received 19 September 2023; Received in revised form 22 November 2023; Accepted 26 November 2023
Available online 28 November 2023
0032-5910/© 2023 The Author(s). Published by Elsevier B.V. This is an open access article under the CC BY-NC-ND license (http://creativecommons.org/licenses/by-nc-nd/4.0/).

Manuscript

Click here to view linked References

Impact of Conic Curvature and Wall Roughness on Gas Cyclones: A Computational and Experimental Study

Arjun Kumar Pukkella[a,b,*], Joshua Rasera[a], Kathryn Hadler[a,c] and Jan Cilliers[a]

[a]Imperial College London, Department Earth Sciences and Engineering, Exhibition Road, London, SW7 2AZ, United Kingdom
[b]TCS Research, Tata Research Development and Design Centre, Pune, 411013, India
[c]European Space Resources Innovation Centre (ESRIC), Luxembourg Institute of Science and Technology (LIST), 5 avenue des Hauts-Fourneaux, L-4362, Luxembourg,

ARTICLE INFO

Keywords:
Cyclone
CFD Modelling
Convex conic
Cut-size
Solids recovery
Surface-roughness

ABSTRACT

This study investigates experimentally the influence of conic curvature and surface-wall roughness on the separation performance of gas cyclones. Computational Fluid Dynamics (CFD) modeling was employed to explain the underlying physics. Gas cyclones (31 mm diameter) were 3D printed with different surface textures. A novel dust particle collection technique was developed to measure the particle size distribution of the sample from the dust outlet. Experimental analysis comparing standard and convex design cyclones revealed that increased flow rates improved overall solids recovery for both designs. However, the convex design consistently exhibited lower solids recoveries with coarser cut sizes resulting in a classification effect. Particle separation efficiency was shown to increase with flow rate and particle size, with a characteristic fish-hook trend observed for particles under 2 microns that diminished at higher flow rates.

CFD simulations revealed that axial and tangential velocities, as well as static pressure profiles, were influenced by surface-wall roughness, resulting in lower tangential velocities and shorter natural vortex lengths for rough designs. Rough wall surfaces were associated with decreased collection efficiency for both cyclone designs. These findings highlight the significance of cyclone geometry and surface conditions on separation performance and suggest that roughness could be leveraged as a design variable for optimizing classification efficiency.

1. Introduction

Gas cyclones are widely used in industrial processes for separating particles from gas streams due to their simple design, low maintenance, and ability to handle large volumes of gas under harsh conditions. Traditionally, the primary objective of gas cyclones is the complete removal of solid particles from the gas stream (separation), which is critical in applications such as pollution control, material recovery, and gas purification [1, 2]. The separation efficiency of a cyclone is influenced by several design factors, including the cyclone's geometry and the operating conditions [3, 4]. Conventional cyclone designs feature a cylindro-conical section where centrifugal forces drive particle separation, with the goal of minimizing the cut-size, thereby removing as many fine particles as possible [5].

Extensive research has been conducted on the influence of design and operational parameters on the performance efficiency of gas cyclones. Investigations into inlet dimensions, including height and width, have underscored the significance of design choices in influencing pressure drop and cut-off diameter, highlighting the need for optimization in cyclone design [6]. The use of innovative inlet configurations, such as double spiral and angular helical roof, have been shown to improve flow symmetry, suggesting that alternative geometries can enhance separation efficiency [7–9]. Vortex finder design modifications, including changes in angle and shape (converging and diverging), have also been explored, indicating that careful consideration of these elements can impact particle separation performance [10, 11]. The ratio of cylinder length to conic section length has been noted as a critical factor, with implications for separation efficiency [12]. More recently, investigations into conic curvature have highlighted its role in influencing design outcomes, emphasizing the need for a nuanced understanding of how geometric variations can affect overall cyclone performance [13, 14]. These studies collectively illustrate the importance of design implications in optimizing cyclone functionality.

While most studies focus on gas cyclones as particle separators achieving smaller cut sizes, some research has explored their classification capabilities. Yoshida [15] examined how apex cone angle and clearance can enhance classification efficiency through blow-up flow, achieving cut sizes between 2 and 38.07 µm. Oshitari et al. [16, 17] found that blow-up flow improves classification sharpness, resulting in cut sizes of 18 to 29 µm. Additionally, Caliskan et al. [18] demonstrated a cyclone design with internal collector rings capable of classifying particles into four size classes. These studies suggest a growing interest in the potential of gas cyclones to function as classifiers.

However, the need for coarser cut-sizes in gas cyclones is becoming increasingly important not only due to industrial applications [19–22] but also due to the challenges associated with water usage in separation processes. Hydrocyclones, which are widely used in wet classification, depend on water for particle separation. However, in regions with arid or cold climates, dry classification presents a viable

*Corresponding authors
a.pukkella20@imperial.ac.uk (A.K. Pukkella)
ORCID(s):

Influence of Conic Shape on Bypass and Cut-Size in Hydrocyclones

Arjun Kumar Pukkella[a,b,*], Dennis Vega Garcia[c], Kathryn Hadler[a,d] and Jan Cilliers[a]

[a]*Imperial College London, Department Earth Sciences and Engineering, Exhibition Road, London, SW7 2AZ, United Kingdom*
[b]*TCS Research, Tata Research Development and Design Centre, Pune, 411013, India*
[c]*Sustainable Minerals Institute's International Centre of Excellence, Las Condes, Apoquindo 2929, Santiago,*
[d]*European Space Resources Innovation Centre (ESRIC), Luxembourg Institute of Science and Technology (LIST), 5 avenue des Hauts-Fourneaux, L-4362, Luxembourg,*

ARTICLE INFO

Keywords:
Hydrocyclones
CFD Modelling
Convex conic
Bypass
Cut-size

ABSTRACT

Hydrocyclones in ball-mill classifier circuits have traditionally faced the challenge of fines bypass, driving the exploration of alternatives such as Derrick screens. However, our study demonstrates that optimizing hydrocyclone design, specifically with convex-conic geometry, can achieve lower bypass with coarser cut sizes. Through a combination of Computational Fluid Dynamics (CFD) simulations and lab-scale experiments, we consistently observed that convex-conic hydrocyclones deliver coarser cut sizes and lower bypass rates compared to standard hydrocyclones across a range of flow rates.

CFD results revealed that convex designs exhibit distinct flow characteristics, such as higher axial velocities near the apex and lower radial velocities at the center, and lower tangential velocities creating a favorable environment for particle classification and reducing fines bypass with coarser cut size. Experimental findings confirmed these trends, with the convex design achieving lower underflow recoveries and reduced bypass at all tested flow rates. For instance, at a flow rate of 1000 mL/s, the convex hydrocyclone reduced fines bypass to 18.6%, compared to 24.6% for the standard design, while producing a coarser cut size of 94 µm versus 78 µm. These findings prove that convex-conic hydrocyclones offer superior performance, making them a cost-effective alternative to Derrick screens.

1. Introduction

Hydrocyclones have established themselves as integral components in a wide range of industrial processes, facilitating efficient particle separation and classification. These devices find applications in ore processing, chemical engineering, and mineral beneficiation due to their simple design and capability to separate solid particles from liquid suspensions [1, 2]. Hydrocyclones are employed in mill-classifier circuits in mineral industries; where, the coarse fraction (*i.e.*, underflow) is sent back for further milling. Nonetheless, within a conventional hydrocyclone, the intricacies of the internal flow field invariably result in a compromised classification process, whereby fine particles become entrained in the underflow. These fine particles, evading proper separation and finding themselves misallocated to the underflow, are known as 'bypass'. Importantly, the presence of these bypassed fine particles enhances the yield of particles in the underflow, while reducing water recovery. This aspect holds particular significance for dewatering operations. Roldanvillasana et al. assert that the bypass effect should be regarded as a prevalent occurrence rather than an incidental anomaly [3].

Bypass reduction in hydrocyclones in mill-classifier closed circuits can improve separation efficiency, reduce power consumption, and improve product quality by restricting the flow of fine particles to the underflow stream. Research has shown that bypass reduction can lead to significant improvements in mill circuit performance and should be considered an important operational parameter in such circuits [4]. As noted by Napier-Munn et al., reducing the bypass can increase the circuit capacity and improve the grinding performance in a closed circuit.

From past research, it is understood that the bypass is influenced by the change in either operating conditions or by the design modifications. Cilliers et al. have studied the effect of temperature on the classification and dewatering characteristics of 10 mm hydrocyclones. They reported that the bypass increased with the temperature of the suspension (studied range: 10-60°C) [5]. Frachon and Cilliers [6] observed that bypass increases with an increase in pressure and stays relatively constant at higher feed flowrates. Banerjee et al. also observed that bypass increases with feed pressure and decreases with solids loading [7].

The separation of particles in the hydrocyclone primarily begins in the conical section. For a conventional straight-cone hydrocyclone, Fu et al. has investigated the effects of cone angle, and was observed that separation efficiency was influenced more strongly for a fixed cylindrical diameter than for a fixed total hydrocyclone length [8]. Yang et al. have reported that tapering the cylindrical body can effectively reduce the fine particle's misplacement to the underflow [9]. Jiang et al. increased the cone angle to 180°, creating a flat-bottomed, cylindrical hydrocyclone. It was observed that the flat-bottomed structure had lower axial velocities and increased particle residence times, thereby reducing the bypass behavior [10]. Jiang et al. have reported that the effect of the 'W'-shaped apex structure reduced the bypass by increasing the axial velocity of the inner vortex while reducing the outer vortex [11]. According to Hou et al. [12], enlarging the upper diameter of the spigot in a cylindrical hydrocyclone has been found to reduce the

*Corresponding authors
a.pukkella20@imperial.ac.uk (A.K. Pukkella)
ORCID(s):

The Influence of Surface-Wall Roughness on Hydrocyclone Performance

Arjun Kumar Pukkella[a,b,*], Dennis Vega-Garcia[c], Kathryn Hadler[a,d] and Jan Cilliers[a]

[a]Imperial College London, Department Earth Sciences and Engineering, Exhibition Road, London, SW7 2AZ, United Kingdom
[b]TCS Research, Tata Research Development and Design Centre, Pune, 411013, India
[c]Sustainable Minerals Institute's International Centre of Excellence, Las Condes, Apoquindo 2929, Santiago,
[d]European Space Resources Innovation Centre (ESRIC), Luxembourg Institute of Science and Technology (LIST), 5 avenue des Hauts-Fourneaux, L-4362, Luxembourg,

ARTICLE INFO

Keywords:
Hydrocyclones
CFD Modelling
Wall roughness
Bypass
De-watering
Underflow recovery

ABSTRACT

The impact of hydrocyclone design and operation on particle separation has been extensively studied. However, scant attention has been paid to wall surface roughness, despite its relevance to industrial scenarios. This study investigates the influence of surface-wall roughness on hydrocyclone performance through Computational Fluid Dynamics (CFD) modelling and experimental analysis. Flow properties and particle separation characteristics between smooth and rough-surfaced hydrocyclones at various flow rates were investigated. CFD analysis reveals a threshold surface-wall roughness above which underflow water recovery significantly increases. Additionally, the axial, tangential, and radial velocities, as well as pressure distribution profiles, exhibit distinct trends for smooth and progressively rough hydrocyclones.

Experimental studies were conducted on 75 mm diameter hydrocyclones, 3D-printed with three different degrees of surface roughness for water-only and 5% solids conditions. The experimental observations support the trends predicted by CFD. Rough-surfaced hydrocyclones demonstrate significantly higher underflow solids recoveries, with values increasing up to 58%, compared to 46% for smooth-surfaced hydrocyclones at a flow rate of 1000 mL/s. At the highest flow rate of 1500 mL/s, rough-surface hydrocyclones show a 27% higher underflow solids recovery than smooth designs. Additionally, rough-surfaced hydrocyclones achieved higher underflow solids concentration at increased flowrates compared to smooth hydrocyclones, with concentration ratios ranging from 1.36% to 2.2% compared to 1.44% to 1.93% for smooth surfaces.

These findings underscore the complex interplay between flow dynamics and particle separation in hydrocyclones, highlighting the potential of surface-wall roughness to enhance separation performance. These findings are important in maintaining and improving hydrocyclone performance in industrial applications requiring dewatering applications and high solids recovery.

1. Introduction

Hydrocyclones play a crucial role in various industrial processes, offering efficient particle separation and classification in applications such as ore processing, waste-water and effluent treatment, catalyst recovery operations, and mineral beneficiation [1, 2]. In prior research on hydrocyclones, the focus has predominantly been on understanding the impacts of design geometry and operational parameters on key performance metrics such as cut size, recovery, separation efficiency, pressure, and capacity. However, these studies typically operate under the assumption of smooth wall surfaces, overlooking the practical reality of wall roughness as changing internal wall surface roughness due to wear during operation. Despite its significant influence on the hydrocyclone's flow field, wall roughness effects have not been studied comprehensively.

Fontein et al. first documented the influence of wall roughness on the reduction in tangential velocities and pressure drop. In his study involving 30 mm diameter hydrocyclones, he compared the smooth cyclone with an artificially roughened cyclone (roughness height parameter (ks) = 110-150 microns). It was observed that, for a constant pressure drop the flow rate increased from 13.2 lpm to 18.8 lpm with an increase in underflow solids recovery from 10.4% to 24.3% [3]. Bradley reported that no differences were observed between 'machined' and 'highly polished' hydrocyclones. This finding suggests that wall roughness must surpass a certain threshold to have a significant effect on cyclone performance [2]. Zhao et al. studied the effect of surface wall roughness in hydrocyclones under equal flow rate and equal inlet pressure conditions. Their CFD model was validated experimentally on a hydrocyclone with a 150 mm diameter and a roughness height of 117 microns. It is reported that equal pressure conditions can provide superior separation results with higher capacity than equal flow rate conditions. However, the roughness adversely affects the separation and flow field in both cases [4]. Hou et al. studied the effect of wall roughness on a flat-bottom 200 mm cylindrical hydrocyclone using CFD simulations. It was observed that as the wall structure changes from smooth to rough-wall, with a roughness height of 100 microns, the fines bypass increases from 9 to 12%, making the cut size coarser, from 77 to 88 microns [5].

Though surface roughness in hydrocyclones has not been explored extensively, it has been well-researched in gas cyclones. Initial attempts to incorporate surface roughness

*Corresponding authors
a.pukkella20@imperial.ac.uk (A.K. Pukkella)
ORCID(s):